The University of Nottingham

UNITED KINGDOM · CHINA · MALAYSIA

Centrifuge Modelling and Analytical Solutions for the Cone Penetration Test in Layered Soils

by

Pin-Qiang Mo BEng , MSc

Thesis submitted to The University of Nottingham for the degree of Doctor of Philosophy

May 2014

Dedictation

I would like to dedicate this thesis to my loving parents.

Abstract

The interpretation of measurements from the cone penetration test is still predominately based on empirical correlations, which can be attributed to the lack of understanding of penetration mechanisms, that involve severe stress-strain and shear dilatancy close to the probe. Even so, it remains one of the most widely used in-situ tools for site characterisation, and several methods for displacement pile design have been developed using CPT data. This research investigates the response of penetrometers and the behaviour of layered soils during installation of probes using geotechnical centrifuge modelling and cavity expansion analysis.

Two series of centrifuge tests were performed in stratum configurations of silica sand in a 180° axisymmetric model, allowing the observation of the induced soil deformation through a Perspex window. The variations of penetration resistance and soil deformation with penetration depth, soil density, stress level and soil layering are examined from the results of the centrifuge tests. The quantified soil displacements and the resulting strains in the axisymmetric model have provided an effective approach for investigation of penetration mechanisms with soil element trajectories, strain paths and rotations of principal strain rate. The effects of layering on both resistance and soil deformation are shown with dependence of the relative soil properties and profiles. The results presented also serve as a base for applications of cavity expansion solutions, back analyses and further studies.

Analytical solutions for cavity expansion in two concentrically arranged regions of soil are developed using a non-associated Mohr-Coulomb yield criterion for large strain analysis of both spherical and cylindrical cavities. The solutions are validated against finite element simulations and a detailed parametric study of the layered effects on the pressure-expansion curves is performed. To apply the proposed solutions to pen-

etration problems, a simplified combination approach is suggested to eliminate the discrepancy between concentric layering and horizontal layering. The analytical study of penetration in two-layered and multi-layered soils is therefore achieved, with comparisons to elastic solutions and numerical simulations provided.

The back analyses based on the resistance and soil deformation emphasise the influences of small-strain stiffness, soil-probe interface friction angle, and relative density/state parameter. The correlation between the cone tip resistance and the pile bearing capacity is also discussed, and the scale effects are examined through the ground surface effect and the layering effect by the developed cavity expansion solutions. The penetration mechanisms are summarised from the aspects of soil stress-strain history, particle breakage, soil patterns, and penetration in layered soils. The layered effects emphasised in this research indicate that the penetration resistance is strongly dependent on the soil properties within the influence zones above and below the probe tip, and also related to the in-situ stress gradient along the penetration path. It is also suggested that correlations from calibration chamber tests using uniform soil and a constant stress field may not be suitable for direct interpretation of CPT data. Finally, the averaging technique for pile design is suggested based on the transition curve of tip resistance in layered soils with consideration of the scale effects.

Acknowledgements

The research described in this thesis was carried out at the University of Nottingham during the period of October 2010 to May 2014, and would not have been possible without the support of many individuals and numerous organisations.

First and foremost, I would like to sincerely thank Dr. Alec Marshall, my main research supervisor for his constant guidance and assistance. He helped me a lot with his advice and encouragement on both academic and personal aspects. I am indebted to Prof. Hai-Sui Yu, my second research supervisor for the insights and helpful comments throughout these years. He always provided me valuable time and advice as I found my way. My deepest gratitude also extends to Prof. Glenn McDowell. As my MSc supervisor and PhD internal examiner, his advice has been helpful for my research.

Moreover, I would like to thank all technicians of the Department of Civil Engineering for the contribution they offered for my centrifuge tests. In particular, I am grateful to Craig Cox and Jim Meakin for their patience to improve my experimental apparatus and address my endless equipment queries. My tests were only possible with their help. To my colleagues in the Nottingham Centre for Geomechanics (NCG), I must acknowledge your continued enthusiasm, support and friendship over these years.

Special thanks go to the financial support from The University of Nottingham, Dean of Engineering Research Scholarship for International Excellence, which is greatly appreciated.

Finally, but most importantly, I would like to thank my family; my parents, sister and brother for your endless encouragement and support throughout this long and challenging period of my life.

Table of Contents

List of Figures

List of Tables

Nomenclature

Roman Symbols

a_0, a	radii of cavity
b_0, b	radii of Soil A/B interface
c_{0A}, c_A	radii of plastic boundary in Soil A
c_{0B}, c_B	radii of plastic boundary in Soil B
d_{50}	grain diameter for which 50 % of the sample (by weight) is smaller
e	void ratio of sand sample
f_s	sleeve friction
g	earth gravity, $\approx 9.8 m/s^2$
h	vertical position of soil element relative to probe shoulder
k	parameter to combine spherical and cylindrical analysis
q_b	pile end bearing capacity
q_c	cone tip resistance
q_{c1N}	stress-normalised cone tip resistance
r_0, r	radial positions of soil element in the model
s_u	undrained shear strength for clay
t_{shear}	thickness of shear zone for soil-probe interaction
u	radial displacement
z	depth of penetration

A_b	base area of probe
A_s	embedded shaft area of probe
B	diameter of probe or pile
C	cohesion of soil
D	diameter of centrifuge container; radius of Soil B in Finite element models
D_R	relative density of soil
E	Young's modulus of soil
G, G_0	shear modulus and small-strain shear modulus of soil
G_s	specific gravity
H	distance to soil interface
H_t	thickness of sandwiched soil layer
K_0	coefficient of at-rest earth pressure
K_H	correction factor for thin-layer effects
N	ratio of centrifuge acceleration and earth gravity
N_q, N_c	cone factors for cohesionless soils and cohesive soils
P_0	initial cavity pressure and in-situ hydrostatic stress
P_a, P_b	radial stress at the cavity and the boundary of two soil layers
P_{c_A}, P_{c_B}	radial stress at the plastic boundary of Soil A and Soil B
P_{lim}	limit pressure of cavity expansion
Q	normalised cone tip resistance
Q_{total}, Q_{tip}, Q_s	total penetration load, tip load, shaft frictional load
R	radius of probe or pile
R_s	state parameter as a ratio of stresses

X, Y	horizontal and vertical locations of soil elements
Z	normalised penetration depth, $= z/B$
Z_s, Z_w	size of influence zones in strong and weal soils

Greek Symbols

α_c	roughness at the penetrometer-soil interface
δ	soil-probe interface friction angle
ε	strain
η'	cone tip resistance ratio in layered soils
η'_0	cavity pressure ratio in layered soils
η'_{max}, η'_{min}	maximum and minimum resistance ratio in thin-layer profiles
ν	Poisson's ratio of soil
$\overline{\beta}$	average shaft friction over vertical stress
ϕ	friction angle of soil
ψ	dilation angle of soil
σ'_{v0}, σ'_{h0}	initial vertical and horizontal stress
σ_r, σ_θ	radial and tangential stresses
σ_0	in situ total stress
σ_{atm}	atmospheric pressure, as the reference pressure
τ_s, $\overline{\tau_s}$	local shaft friction and average shaft friction
$\xi'_{\Delta x}$, $\xi'_{\Delta y}$	horizontal and vertical deformation ratios in layered soils
Δx, Δy	horizontal and vertical displacements

Ψ	state parameter

Abbreviations

ALE	Arbitrary Lagrangean-Eulerean formulation
CEM	Cavity Expansion Method
CNS	constant normal stiffness interface shear test
CPT	Cone Penetration Test
CSL	critical state line
DAS	Date acquisition system
DEM	Discrete Element Method
FEM	Finite Element Method
FOV	field of view
GeoPIV	geotechnical Particle Image Velocimetry
NCG	Nottingham Centre for Geomechanics

Chapter 1

Introduction

1.1 Overview

It has been increasingly significant for geotechnical engineers to determine parameters and engineering properties of soil using in situ testing methods, which avoid the difficulties in retrieving undisturbed samples, owing to the two inherent merits compared to laboratory tests: less expensive and less time consuming. As one of the most versatile devices for in situ soil testing, the cone penetration test (CPT) has been widely used in geotechnical engineering practice to obtain soil profiles and measure in situ soil properties based on the reliability and repeatability of the CPT measurements. The CPT tool has also been extensively developed for CPT-based design methods for piles and for evaluation of liquefaction. The analogues between a penetrometer and a displacement pile in both geometry and installation method make the study of penetration mechanisms attractive.

However, over the years, many correlations between CPT measurements and soil properties have been proposed empirically for soil identification and classification. Penetration induces large strains within the ground, that has inevitable influence on surface structures and subsurface infrastructure. The severely distorted soil around the penetrometer makes the analysis of the mechanical process complicated, and the soil stress/strain history associated with pile/probe installation and the distribution of the load on the probe are still not well understood. In addition, with respect to the fact that the subsoil always consists of layered deposits (in contrast to a homogeneous material), the layered effects during penetration are not addressed sufficiently in the literature.

1.2 Research Aims and Objectives

Since the mechanical behaviour of soil within penetration problems is not well understood, this research aims to investigate soil deformation as well as penetration resistance, with particular interests on the layered effects. To improve the interpretation of CPT data and the design of pile foundations, it is essential to understand the relationship between soil behaviour and penetrometer response.

In this research, the centrifuge tests and the analytical approaches were carried out with the objectives as follows:

1. to improve the testing methodology for CPT modelling within the geotechnical centrifuge;
2. to investigate the penetration resistance with variation of soil conditions;
3. to quantify the soil deformation associated with the probe penetration from the centrifuge tests;
4. to extend the solutions of cavity expansion in two concentric regions of soil;
5. to examine the layered effects of CPT by using the proposed analytical solutions;
6. to establish correlations between CPT measurements and soil behaviour, and consequently to better understand the penetration mechanisms.

1.3 Outline of the Thesis

This thesis consists of eight chapters as outlined below, including this introduction (Chapter 1). The literature about cone penetration testing in layered soils is reviewed in Chapter 2. The methods of centrifuge modelling, soil deformation measurement and the theory of cavity expansion for geomechanics are also provided in Chapter 2. Chapter 3 describes the methodology of the centrifuge testing, where the experimental apparatus and instrumentation are detailed followed by the description of soil model preparation, testing programme and procedure. The results of centrifuge tests are presented in Chapter 4. The measurements of penetration resistances and the induced soil deformation are investigated separately with analyses of the layering effects. In Chapter 5, analytical solutions for cavity expansion in two concentric regions of soil are

proposed for both spherical and cylindrical cavities in elastic-perfectly plastic soils. After validation with finite element simulations, the parametric study investigates the influence of soil layering during cavity expansion. One of the applications of the analytical solutions is the analysis of cone penetration in layered soils, as performed in Chapter 6. The results of layering effects and the thin-layer effects are compared with experimental data, elastic solutions, and numerical results. Chapter 7 provides an analysis and discussion related to the outcomes of this research, and the penetration mechanisms are summarised for geotechnical design. Finally, Chapter 8 draws conclusions of the research and provides some suggestions for further research on this topic.

Chapter 2

Literature Review

2.1 Introduction

The cone penetration test has been in use and undergone tremendous development as an in-situ geotechnical probing technique for subsurface exploration since the 1930s. The high repeatability of the test data and the simplicity of the test procedure have contributed to make it one of the most popular in-situ tools used for soil investigation worldwide. According to the International Reference Test Procedure for the CPT / CPTU (IRTP, 1994), the standard cone penetrometer is cylindrical in shape having a cone in front with a base area of $10\,cm^2$ and 60° tip apex angle. The friction sleeve, located behind the conical tip, has a standard area of $150\,cm^2$. The continuous measurements of tip resistance (q_c) and sleeve friction (f_s) are measured simultaneously to estimate continuous profile of soil properties. Other sensors can also be incorporated into the cone penetrometer system to measure seismic velocity, electrical resistivity, PH, temperature, and specific ion concentration; based on the detection of pollutants, concentrations, and distributions (Mitchell et al., 1998). In brief, three main aspects of applications of CPT have been concluded by Jacobs (2004) as below:

1. to determine the soil profile and identify the soils present
2. to interpolate ground conditions between control boreholes
3. to evaluate the engineering parameters of soils and to assess the bearing capacity and settlement of foundations

Despite of the advantages of CPT (e.g. continuous profile, cheaper, faster), it still has deficiencies, like no sample for inspection and unreliable for cemented soils or soils

with significant gravel content. From the interpretation point of view, despite the advances in equipment design and the variety of tests performed by CPT, a rigorous theoretical understanding of quantitative interpretation techniques is still not available. Hitherto, the correlations between test data and soil properties still rely very heavily on empirical relationships due to the complexity of soil behaviour and the complicated boundary conditions. In addition, the penetration problem coupled with the large strains and significant rotations of soil particles makes the evaluation more difficult, especially for implication in non-uniform soil deposits with in-situ conditions.

A review of the literature about cone penetration testing is provided in this chapter. The methods on analysis of cone tip resistance are first presented in Section 2.2 with assessment of the limitations and advantages of each theory. The interpretation of CPT data is also described for both cohesionless and cohesive soils. In addition, the previous research on penetration in layered soils is covered with both experimental and numerical approaches. The relevant techniques that will be used for the experimental tests are introduced and discussed in Section 2.3, where previous centrifuge studies on CPT are also outlined. The development of the cavity expansion theory and the applications to geotechnical problems are then presented in Section 2.4, with particular focus on the interpretation of penetration and solutions for layered media.

2.2 Previous Research of Cone Penetration Test

Generally, cone factors are derived to evaluate the relationships between cone resistance and soil properties by experimental and analytical approaches. The correlations can be expressed in Equation (2.1) for both cohesionless soils and cohesive soils.

$$\begin{aligned} q_c &= N_q \times \sigma'_{v0} && \text{(Cohesionless soils)} \\ q_c &= N_c \times s_u + \sigma_0 && \text{(Cohesive soils)} \end{aligned} \tag{2.1}$$

where N_q and N_c are the cone factors for sand and clay respectively (Yu, 2006); σ'_{v0} is the effective vertical stress; s_u is the undrained shear strength and σ_0 is the in situ total stress (either vertical or mean total stress depending on the type of theory used for cone penetration analysis).

2.2.1 CPT analysis methods

2.2.1.1 Experimental testing

Calibration chamber testing

Calibration chamber testing is generally accepted as the main approach to calibrate and evaluate in situ testing devices under controlled conditions to correlate the obtained raw data with the engineering parameters (e.g. Holden, 1971; Houlsby and Hitchman, 1988; Kurup et al., 1994). It has been designed and constructed to develop empirical but reliable correlations in primarily cohesionless materials since the 1970s. In principle, the cone penetration test is conducted in a chamber filled with soil samples (with known density and consolidated to desired stresses). In terms of Schnaid and Houlsby (1990), the inherent merits of calibration chamber tests can be summarised as follows:

- Ability to produce soil models similar to natural deposits
- Homogeneity and repeatability of the samples under a wide range of relative densities
- Capability of controlling vertical and horizontal stresses of the samples
- Ability to simulate stress and strain history of the sample

The main limitation of calibration chamber testing is the influence of boundary conditions, which has been investigated by Parkin and Lunne (1982); Schnaid and Houlsby (1991); Salgado et al. (1998); Pournaghiazar et al. (2012). Effectively, a chamber with rigid boundaries results in higher penetration resistance which needs to be reduced by a certain correction factor; whereas a chamber with constant confining stress releases the created stress by insertion, especially for tests with dense sand. Hence, the correlations of calibration chamber tests and free-field tests have to be used to correct the difference caused by the chamber size and boundary condition effects. For instance, the ratio of chamber to field penetration resistance would vary between approximately 0.5 and 0.9 for heavily dilatant samples of Ticino sand. Therefore, the considerable uncertainty about boundary effects would preclude the use of calibration chamber results with great confidence (Salgado et al., 1998). Another deficiency of calibration chamber tests is that the effects of stress gradient and ground surface are not included.

Centrifuge modelling

Geotechnical centrifuge modelling has the ability of scaling down a full-scale prototype model to a small-scale centrifuge model, with replication of in-situ stress field. Particularly, many researchers have conducted centrifuge modelling of the cone penetration test (e.g. Gui et al., 1998), and the repeatability and reliability of CPTs in the centrifuge have resulted in this method becoming another option for laboratory testing. In recent years, centrifuge testing has played an important role in both verifying and establishing correlations between cone resistance and soil properties. Bolton and Gui (1993) also noted that it is essential to perform soil tests in the centrifuge, which provides the analogous stress field for boundary value problems. Thus, this is also adopted in the present study, and more details can be found in Section 2.3.

2.2.1.2 Analytical solutions

Bearing capacity method

In geotechnical engineering, bearing capacity theory is used to determine the maximum pressure a foundation can support based on plasticity theory as developed by Prandtl (1921). Hence, for the cone penetration process, the failure load of a deep circular foundation in soil is assumed to be equal to the cone resistance. For the limit equilibrium method (e.g. Terzaghi, 1943 and Meyerhof, 1951), different types of failure mechanisms for deep penetration are selected based on behaviour of soil, and the collapse load is then calculated by applying the global equilibrium of the soil mass. In the slip-line method, a yield criterion is introduced to give plastic equilibrium within the slip-line network region, which could provide more precise results.

This approach has been widely used by engineers owing to its simplicity. Nevertheless, it is not appropriate or adequate for the analysis of deep penetration problems which should accommodate the cone into the deformed soil rather than adopting a failure mechanism. In addition, the failure mechanisms are not compatible with the boundary conditions. The assumption of no deformation of the soil (rigid-plastic soil model) leads to the largest limitation comparing with the behaviour of real soil.

Cavity expansion method

Based on the early suggestion of Bishop et al. (1945) and Hill (1950), cavity expansion

methods are used to predict the tip resistances and shaft capacities of cone penetrometers and piles in soil and rock (Yu, 2000). Limit pressures of spherical and cylindrical cavities obtained at large strains can be related to cone penetration resistance. Based on the assumption of Gibson (1950), Randolph et al. (1994) noted that the correlation between end bearing pressure (q_b) and limit pressure of spherical cavity expansion (P_{lim}) is generally accepted, as shown in Equation (2.2).

$$q_b = P_{lim} \times (1 + \tan\phi \times \tan\alpha) \tag{2.2}$$

where ϕ is the friction angle, and α is the angle of the rigid zone at the pile tip. More details about cavity expansion theory and the application to penetration problems will be provided in Section 2.4.

Strain path method

The strain path method, first proposed by Baligh (1985), provides a systematic framework for the steady state analysis of cone penetration in soil. In this method, the soil is regarded as a viscous fluid with a steady flow past a fixed penetrometer. The velocities of soil particles around the penetrometer were approximated by the flow field of an inviscid fluid. In addition, the strain path method can also be used to derive the normalised pore pressure distribution associated with Henkel's empirical equation ($\Delta u = \Delta\sigma_{oct} + \alpha_f \times \Delta\tau_{oct}$, where $\Delta\sigma_{oct}$ is the change in octahedral mean normal stress, $\Delta\tau_{oct}$ is the change in octahedral shear stress, and α_f is a parameter related to the Skempton's pore pressure) which showed good qualitative agreement with field and laboratory test data (Teh, 1987).

However, the assumptions of the method are based on incompressible behaviour of soil and the flow field is derived from classical fluid mechanics. It works well for undrained cohesive soil, but is not suitable for drained frictional soil and deep penetration conditions. In spite of its limitations, the strain path method has been used by many authors to analyse the cone penetration test. The simple pile model has been developed by van den Berg (1994) using a perfectly plastic von Mises soil model without consideration of cone geometry and roughness (Equation 2.3).

$$N_c = 1.51 + 2\ln\frac{G}{s_u} \tag{2.3}$$

In order to take into account of cone geometry, roughness, shear stress, and anisotropic in-situ stress effects, Teh and Houlsby (1991) used a number of methods to extend the expression using the strain path method, and yielded the following expression:

$$N_c = \frac{4}{3}\left(1+\ln I_R\right)\left(1.25+\frac{I_R}{2000}\right)+2.4\,\alpha_c-0.2\,\alpha_s-1.8\,\Delta \tag{2.4}$$

where I_R is the rigidity index, $= G/s_u$, Δ is the anisotropic in-situ stress parameter, α_c is the roughness at the cone-soil interface, and α_s is the roughness at the shaft-soil interface (α_s is normally taken as identical to α_c due to the same material used in the shaft and cone).

2.2.1.3 Numerical simulations

Finite element analysis

Finite element analysis has been used widely for the study of geotechnical problems, including the cone penetration test. Compared with the strain path method, the advantages of the finite element method are concluded and listed by Walker (2007):

- The equilibrium equations are fully satisfied without any equilibrium imbalance
- The cone geometry can be taken into account in the finite element approach
- Capability of controlling vertical and horizontal stresses of the samples
- It can be easily modified for application to frictional-dilatant soils

Due to the complexity of soil behaviour with the large strains of cone penetration, two FE approaches are used to deal with problems of large deformation, namely Lagrangean and Eulerean formulations. van den Berg (1994) presented a Eulerean type model to analyse the cone penetration test in both clay and sand (Figure 2.1). However, no correlation of cone factors and soil properties has been given for analysis or comparison.

A novel finite element formulation for the analysis of steady state cone penetration in undrained clay was developed by Yu et al. (2000) using both the von Mises and the modified Cam Clay models. Walker (2007) proposed an explicit finite element model with an adaptive mesh to simulate the cone penetration test in undrained clay. Figure

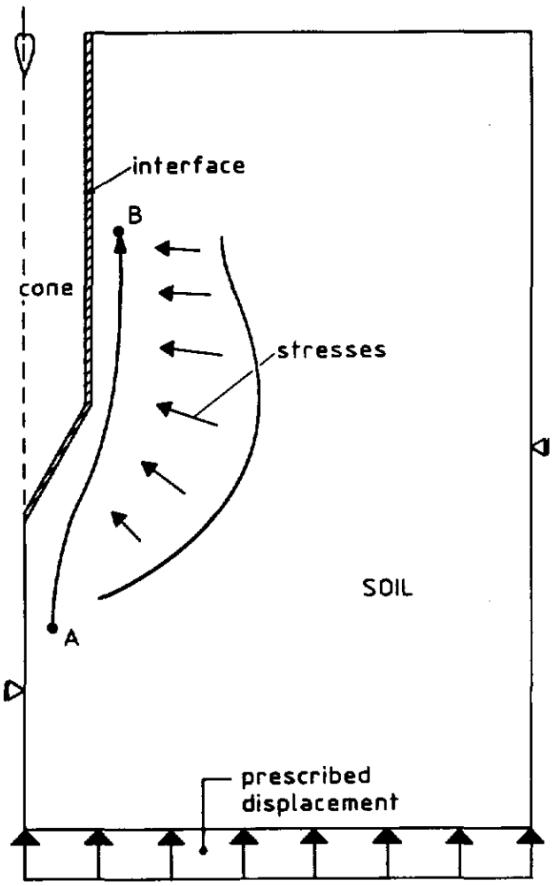

Figure 2.1 Schematic view of Eulerean approach of cone penetration problem; after van den Berg (1994)

2.2 shows the schematic of the model, and Equation (2.5) could be used to relate the cone factor to the soil properties, where α_c is the roughness at the penetrometer-soil interface.

$$N_c = 2.19 \ln (I_R) + 2.275 {\alpha_c}^2 - 1.146 \alpha_c - 0.1867 - 1.95 \Delta \tag{2.5}$$

Discrete element method

Recently, in order to simulate the fundamental behaviour of granular materials, the discrete element method (DEM) proposed by Cundall and Strack (1979) has been widely used. Cone penetration has also been simulated since Huang and Ma (1994), and the authors focused their attention on the effect of soil-penetrometer interface friction. Jiang et al. (2006) have carried out simulation of deep penetration in granular soils using a two-dimensional discrete element method.

Figure 2.3 shows the model of the cone penetration in the DEM analysis by Jiang et al. (2006). A standard penetrometer with radius R of $18\,mm$ and apex angle of 60° is

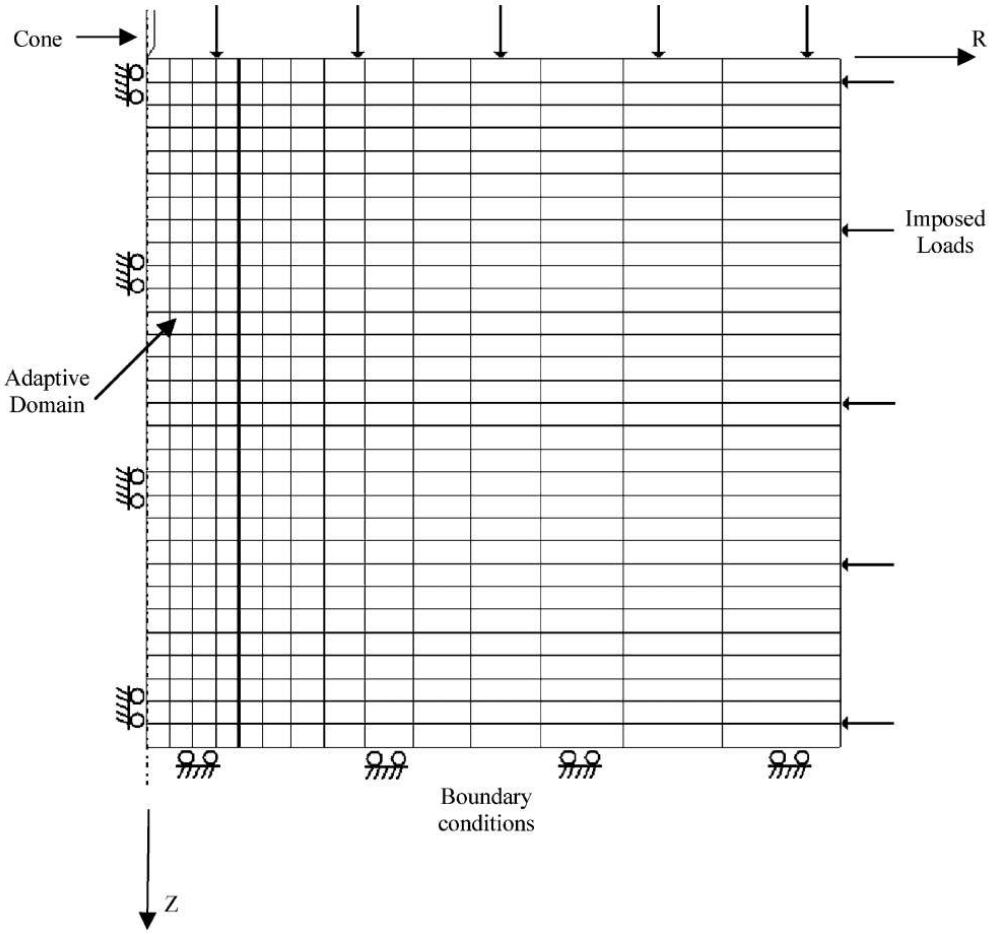

Figure 2.2 Schematic of the model with adaptive domain; after Walker (2007)

described with three rigid walls: frictional tip boundary, frictional sleeve boundary, and frictionless sleeve boundary. The granular material was simulated by 20 types of disks with an average grain diameter $d_{50} = 2.925\,mm$. Over 10000 particles composed a ground with a depth and width of $16R$ and $17.5R$, respectively, using a multi-layer under-compaction method.

The numerical results investigated the tip resistances in the penetration tests and the penetration mechanisms from the viewpoints of the deformation pattern, velocity fields, stress fields and stress paths were discussed in detail. Despite the main limitation of DEM to simulate a great number of particles with current PCs, the results show some similarity with that of field and laboratory tests. In addition, the obtained penetration mechanisms are helpful for understanding axisymmetric CPT tests.

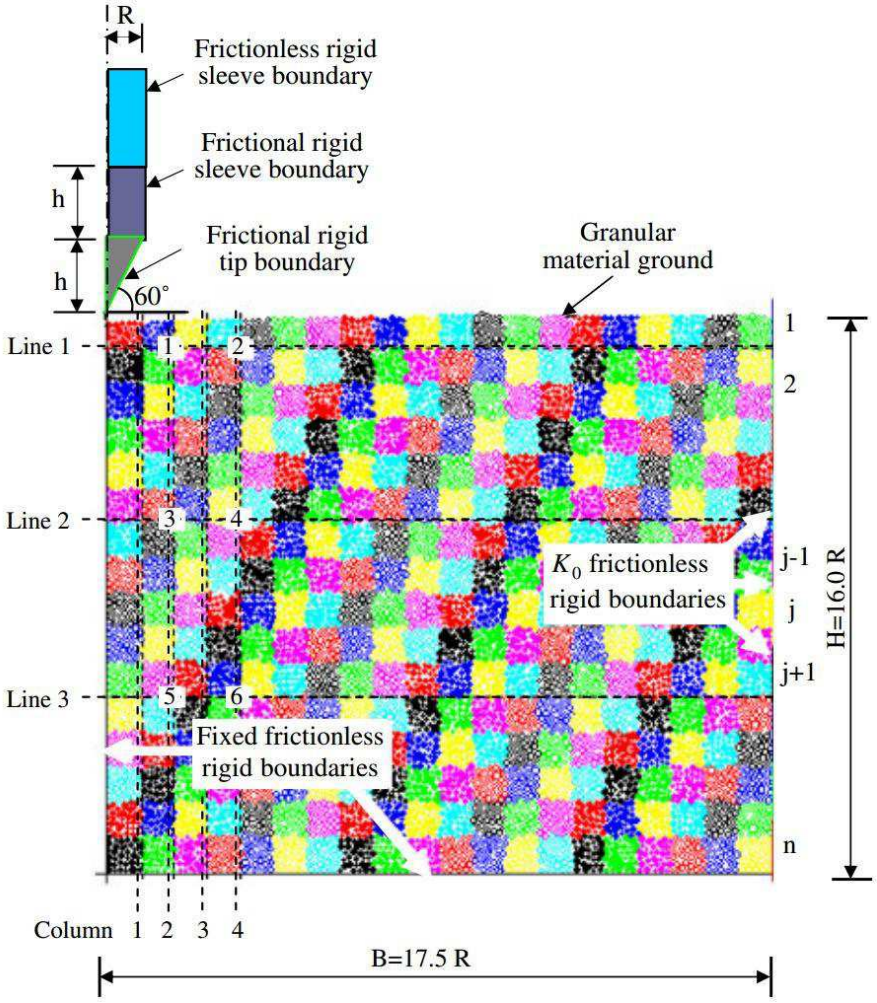

Figure 2.3 The CPT model in the DEM analysis; after Jiang et al. (2006)

2.2.2 CPT in layered soils

Natural soil deposits consist of layers with varying thickness and mechanical properties. An objective of CPT data interpretation is the delineation of interfaces between soil layers in order to produce an accurate profile of subsurface soil features. The interpretation of CPT data in layered soils is complicated by the fact that readings are influenced not only by the soil at the location of the cone tip but also by layers of soil at some distance beneath and above it.

A near continuous data profile is an advantage of the CPT for interpretation of stratigraphic details. However, the influence zone effect makes delineation of soil layers difficult. The size of the influence zones is dependent on the soil properties (Yang, 2006). Therefore, for penetration in layered soils, the distance to sense a lower layer differs with the properties of both soil layers and the relative distance to the soil in-

terface. For multi-layered soils, the layered effects become more complicated and important, especially for thin-layer deposits. As a result, CPT data (e.g. q_c, f_s) does not solely represent the soil at the location of cone tip, and makes soil classification difficult. This can also impact on the ability of CPT to determine liquefaction potential of soil zones (e.g. Robertson, 1982; Tseng, 1989; Moss et al., 2006).

There has been relatively little research done on the effect of soil layering on CPT measurements. A small number of experiments (e.g. Treadwell, 1976; Silva and Bolton, 2004; Xu, 2007) have been carried out that provide observations of the transition through soil layers. Numerical simulations (e.g. van den Berg et al., 1996; Ahmadi and Robertson, 2005; Xu and Lehane, 2008; Walker and Yu, 2010) have been conducted for the analysis of layered effects and influence zones around soil interfaces. The first analytical solution for penetration in layered soils was proposed by Vreugdenhil et al. (1994), which is an approximate solution for simple linear-elastic media.

2.2.2.1 Gui and Bolton (1998)

It was reported by Gui and Bolton (1998) that penetrating into a new soil layer has a significant impact on CPT profile and therefore pile design. As can be seen from Figure 2.4, the CPT profile can deviate from a uniform soil (ideal result) profile by detecting the soil lying beneath it, and some distance (Z_s) is required to develop a new tip resistance once entering a new soil layer. For pile design, the influence zones are determined by the surrounding soil profiles, thus the end-bearing capacity is significantly affected by the soil layering that may be present near the pile tip.

In order to study the effect of penetration depth (Z_s), a set of cone uplift tests (i.e. pull-out tests where the penetrometer is pulled out of the soil after a penetration test) in the centrifuge (Gui and Bolton, 1998) showed that it takes a distance of about 5 cone diameters to develop the full resistance of a given sand layer.

2.2.2.2 van den Berg et al. (1996)

van den Berg et al. (1996) presented a Eulerean large-strain finite element solution for penetration in layered soil which is characterized by a non-associated Drucker-

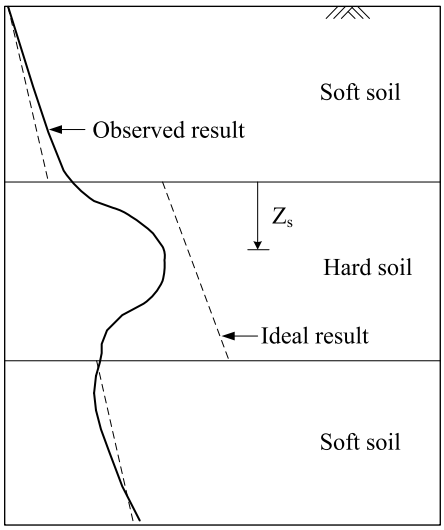

Figure 2.4 Layered effects of development on CPT profiles; after Gui and Bolton (1998)

Prager criterion. Large plastic deformations were taken into account by using a meshing re-adaptivity technique, called Arbitrary Lagrangean-Eulerean formulation (ALE), in which nodal point displacements and velocities and material displacements and velocities are decoupled. The adopted Eulerean framework is a special case of ALE with fixed element nodes. For a layered system, the material properties near the interfaces could be modified to subtract the convected stresses and strains due to the physical movement of material particles.

For a material constitutive model, the Drucker-Prager plasticity model with isotropic strain hardening assumption and a non-associated flow rule were adopted to model strength of sand with the yield function and plastic potential function as shown in Equation (2.6). J_2 is the second invariant of the deviatoric stress tensor, p is the hydrostatic pressure; α and κ are material strength parameters; β is a dilatancy factor. In addition, a von Mises criterion was used to model the undrained clay behaviour.

$$\begin{aligned} f &= \sqrt{3J_2} + \alpha\, p - \kappa \\ g &= \sqrt{3J_2} + \beta\, p \end{aligned} \tag{2.6}$$

A typical cone penetrometer with diameter of $35.7\,mm$ was modelled to penetrate into the subsoil at a speed of $2\,cm$ per second. Two subsoil systems were studied in a qualitative nature: 'clay on sand' and 'sand on clay'. The results in Figure 2.5 show that the cone in sand layer can sense the underlying clay layer at a distance of about $3B$, whereas it takes about $5B$ to develop the full resistance for an advancing cone from

soft layer to sand layer. However, as the author emphasized, the material properties adopted had a great effect on the results and the study was mainly focused on the qualitative assessment of the finite element solution in a layered soil. Therefore, more precise data should be obtained from in-situ tests and more parameter studies should be undertaken to apply to analyse the case of cone penetration test.

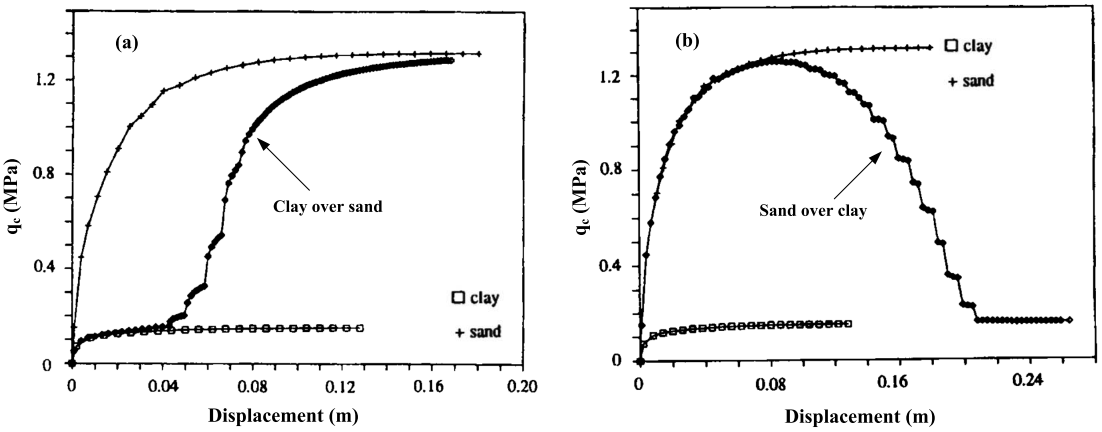

Figure 2.5 Load-displacement curves for: (a) clay on sand; (b) sand on clay; after van den Berg et al. (1996)

2.2.2.3 Ahmadi and Robertson (2005)

The CPT tip resistance (q_c) in layered soil was simulated by the finite differential method using the commercial computer program FLAC. The layering effect for penetration in both sand and clay was investigated using simple constitutive models. The Mohr-Coulomb elastic-plastic model was selected as the constitutive law for sand. The Mohr-Coulomb parameters were tested to model the mechanical properties of Ticino sand. For constitutive law of clay, the Tresca failure criterion was used with the undrained shear strength of clay (s_u). Due to the undrained behaviour of the clay, Poisson's ratio was taken as 0.49.

Before the investigation of the thin-layer effects, a numerical analysis of two-layered soil was carried out to examine the effects of soil layering on the penetration resistance. Figure 2.6 presents the results of numerical simulations. The distance that the cone senses the approaching layer is larger for penetration from dense sand to loose sand, $4.5B$ for subplot (a) and $18B$ for subplot (b) respectively. The cone resistance in the clay layer is only slightly influenced by the sand layer both above and below,

i.e. 1.7B from subplot (c) and 2B from subplot (d).

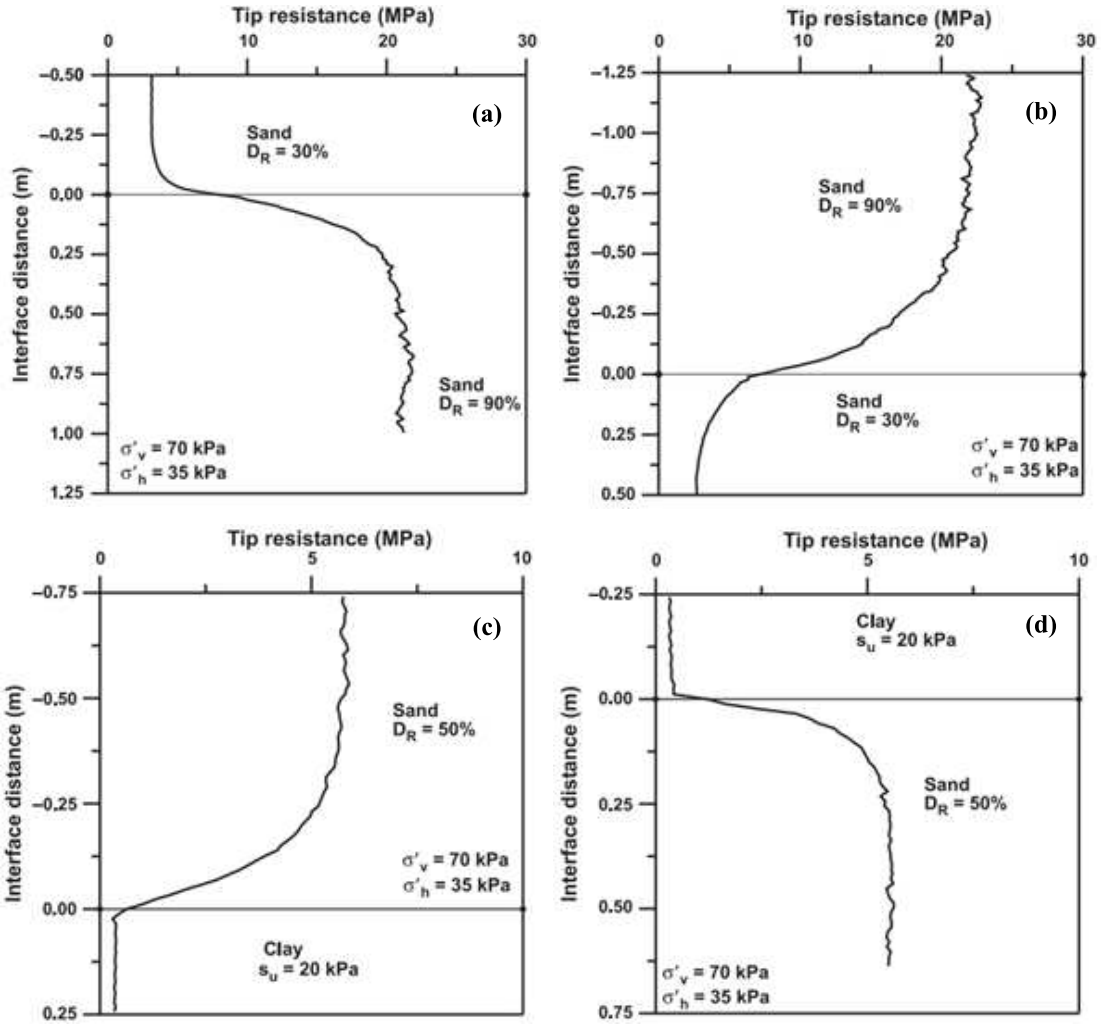

Figure 2.6 Penetration analysis: (a) loose sand overlying dense sand; (b) dense sand overlying loose sand; (c) medium dense sand overlying soft clay; (d) soft clay overlying medium dense sand (after Ahmadi and Robertson, 2005)

During the analysis of a multi-layer system, different thicknesses of sand layer sandwiched by the other two layers of soft clay (assuming that the surrounding layers have the same soil properties) were carried out to present the thin-layer effects. Both dense sand layer and loose sand layer tests were performed. For the former, a thickness of 28B for the middle sand layer was required to develop a steady-state penetration resistance. Otherwise, the tip resistance would be affected by the soft clay layer below before it reaches its true value of tip resistance. For the latter, the required distance reduced to 7B, which is due to the relative density. The results showed that the tip resistance and the layering effect (including the thin-layer effect) are influenced sig-

nificantly by the relative stiffness and strength of each soil type. As depicted in Figure 2.7, in order to address the problem of the thin dense sand layer (q_{cA}) embedded in soft clay (q_{cB}), the correct cone resistance (q_c^*) was defined as $q_c^* = K_H \times q_{cA}$, where K_H is a correction factor and is a function of the ratio of layer thickness to cone diameter (H/B).

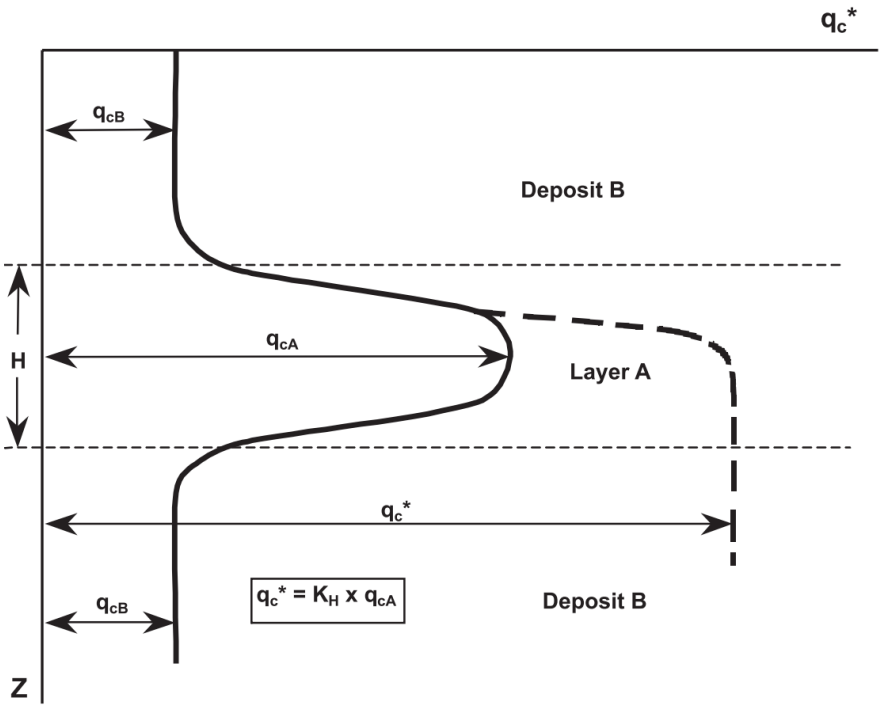

Figure 2.7 Thin-layer correction factor K_H; after Ahmadi and Robertson (2005)

2.2.2.4 Xu (2007)

Centrifuge tests of penetration tests in layered soil samples (superfine silica sand and kaolin clay) were conducted by Xu (2007), using jacking model piles of $6\,mm$, $9.5\,mm$ and $16\,mm$ in diameter, as shown in Figure 2.8. The transition from one soil layer to the other showed that the influence zone in the stronger layer was larger (about five times the pile diameter), and the tip resistance was more sensitive to be affected by the weaker soil layer. The scale effect resulted in the larger pile reacting more slowly to changes in soil stratigraphy, and the influence zones around the soil interface were relatively larger. However, it was expected that the normalised distance to the interface (H/B) eliminated the scale effect, and the equations based on numerical results were proposed to describe the variation of resistance ratio in two-layer soil profiles, according only to the resistance ratio ($q_{c,w}/q_{c,s}$).

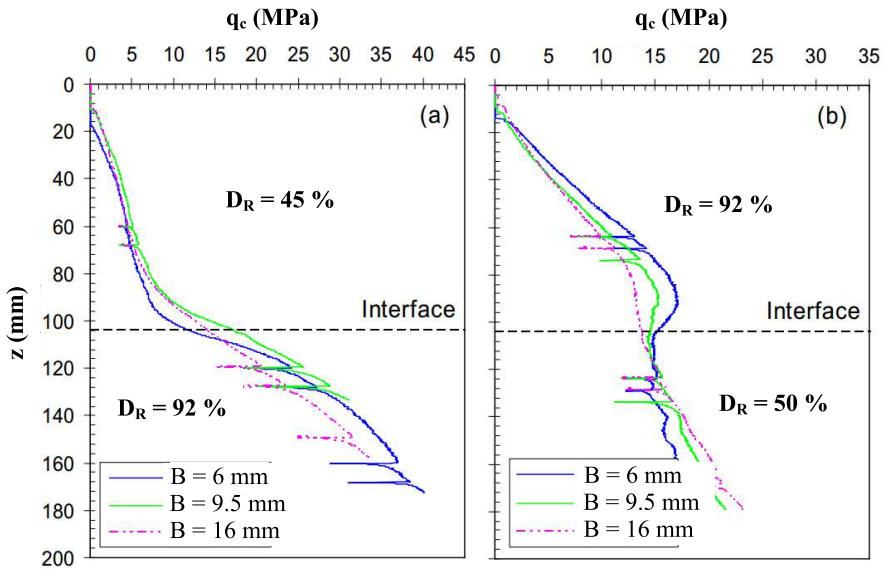

Figure 2.8 Centrifuge results of pile penetration in layered soils; after Xu (2007)

2.2.2.5 Walker and Yu (2010)

An analysis of the cone penetration test in multi-layered clay was presented by Walker and Yu (2010), using the commercial finite-element code Abaqus/Explicit. Similar to van den Berg et al. (1996), the von Mises yield criterion and its associated flow rule were assumed to model the plastic behaviour of elastoplastic undrained clays. An arbitrary Lagrangian-Eulerian scheme and an enhanced hourglass algorithm were adopted to preserve the quality of mesh throughout the numerical simulation. The behaviour of the penetration resistance when a cone passes between soil layers was investigated, and the distribution of soil deformation around the penetrometer provided insights into the understanding of penetration mechanisms.

Figure 2.9 exhibits the constraints and surface interactions that were imposed in the dual-layered soil model. In Abaqus / Explicit, the contact algorithm is based on the concept of a master surface and a slave surface. The interface hard kinematic condition provides the transmission of any contact pressure between two surfaces. The tie conditions at the both sides of the interface are necessary to prevent the top layer from sliding off the bottom layer, to prevent the soil domains splitting along the interface and to prevent the soil buckling when the cone passes the interface.

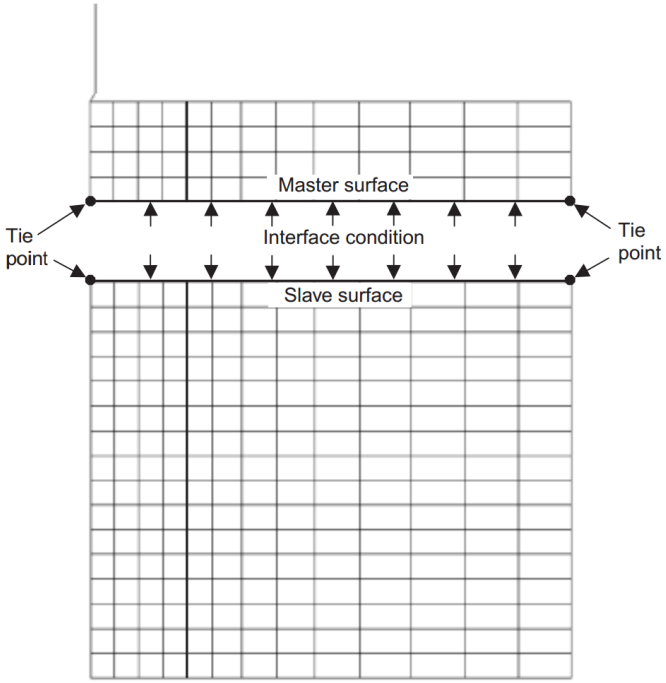

Figure 2.9 Boundary constraints and interface conditions of the dual-layered soil model; after Walker and Yu (2010)

Figure 2.10 signifies the change of the penetration resistance when the cone was pushed from a strong layer to a weaker layer. It was found that the penetration resistance was influenced significantly by both upper layer and lower layer. Apparently, the distance of influence depends heavily on the relative strength of the layers. The results reveal that the cone senses the approaching layer at 2.1 $\sim$ 2.6 cone diameters above the interface and the influence of the upper layer extends for 2.0 $\sim$ 2.2 cone diameters into the bottom layer respectively.

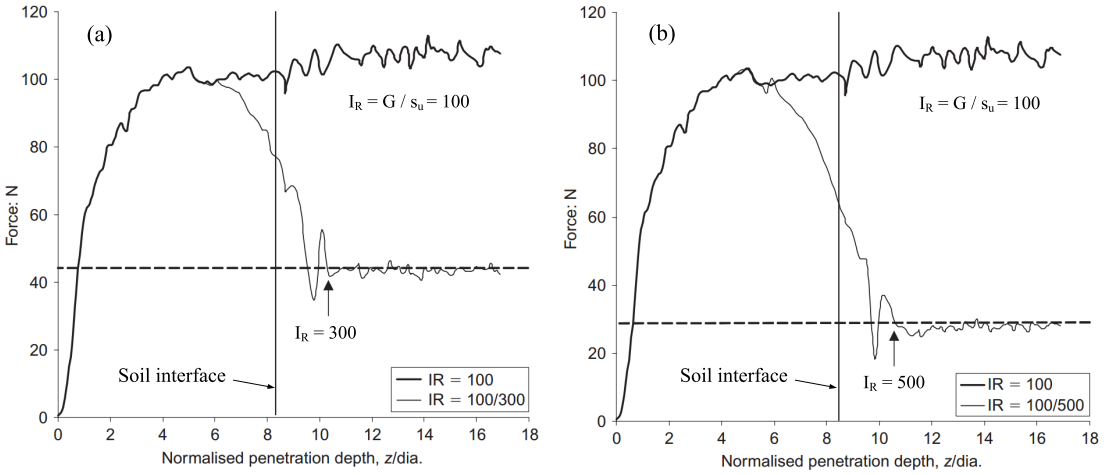

Figure 2.10 Penetration resistance in a dual-layered soil; after Walker and Yu (2010)

The analysis of three layers of clay was also presented to investigate the influence of the relative strength, as illustrated in Figure 2.11. Comparing the two stages when the cone passes the interfaces, the height of influence of the layers is larger when the penetrometer is pushed through a strong layer into a softer layer. In contrast, the lower strong layer has very little effect on the penetration resistance, while it increases sharply to its steady-state penetration resistance after the cone passes to the bottom layer.

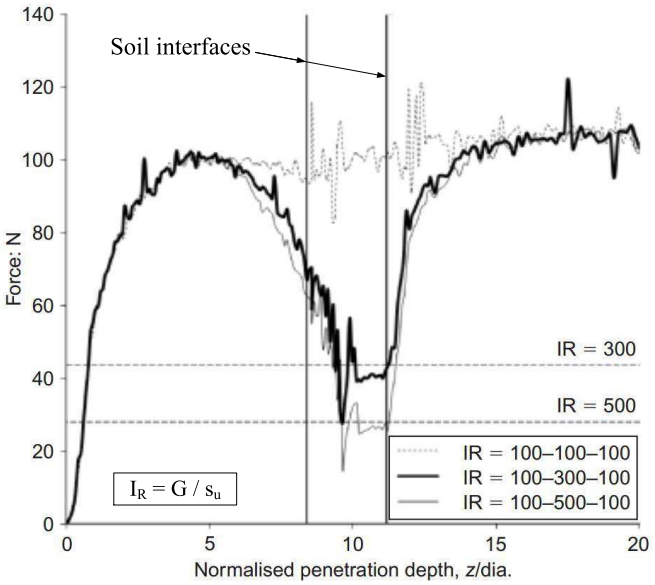

Figure 2.11 Penetration resistance in a multi-layered soil; after Walker and Yu (2010)

In addition, the effect of layer thickness on the penetration resistance was examined by altering the thickness of the middle layer to $5\,cm$, $10\,cm$, $15\,cm$ and $30\,cm$. The behaviour of the penetration resistance was studied in relation to the thickness and relative strength of the soil layers. The results revealed that the layer thickness has no impact on the penetration resistance while the cone is in the top layer. A thickness of two cone diameters was required to drop to the steady-state penetration resistance when inserting the cone into a thin weaker soil layer.

2.3 Centrifuge Modelling and Soil Deformation Measurement

2.3.1 Centrifuge modelling and NCG geotechnical centrifuge

Soil behaviour is complex and non-linear, with dependence on the current stress conditions and stress/strain histories. For large-scale boundary value problems, a traditional

scaled physical model would not be able to replicate the stress field, and the boundary effects are arguably considerable. However, the construction of a full-scale model which provides the actual in-situ conditions increases the cost significantly and reduces the efficiency of the examination. On the other hand, tests conducted at site also have limitations due to uncontrollable site conditions and inadequate measurements. Alternatively, the investigation based on experimental tests benefits from the precise control of variables, and the stress conditions can be provided by the centrifuge rather than a traditional physical model.

Centrifuge testing has proven to be a particularly useful tool for the study of geotechnical engineering (Taylor, 1995). The applied acceleration of many times earth gravity enables the full scale prototype situation to be scaled down to a relatively small physical model. The centrifugal force is generated by the inertia from Newton's second law of motion ($F = M \cdot r \cdot \omega^2$; where M is the mass, r is the rotational radius, and ω is the angular rotational velocity of the centrifuge), which is equal and opposite to the centripetal force. A main advantage of centrifuge modelling lies in the replication of the stress level and the stress gradient with depth, thus the model testing results can be extrapolated to full prototype scale. It is important to recognise that the full-scale prototype does not exactly match the full-scale problem under investigation, but that the modelling can provide an effective approach to explore the general mechanisms involved.

2.3.1.1 Scaling laws

While the physical model is scaled down to represent the prototype, the relationship between the model and the prototype is governed by a number of scaling criteria. For the basic scaling law of centrifuge modelling, the uniform acceleration field is assumed to apply to the model by selecting an effective centrifuge radius R_e which will minimise the scaling errors due to the nonlinear stress distribution and the difficulty of representing sufficient detail. Thus, the inertial acceleration field of N times earth gravity (g, $\approx 9.8\,m/s^2$) is provided in accordance with Equation (2.7).

$$N = \frac{\omega^2 R_e}{g} \tag{2.7}$$

For the centrifuge model, the vertical stress at depth h_m is given by the expression: $\sigma_{v,m} = \rho \cdot N \cdot g \cdot h_m$, whereas the vertical stress at depth h_p is given by $\sigma_{v,p} = \rho \cdot g \cdot h_p$ for the prototype. Due to the similarity, $\sigma_{v,m} = \sigma_{v,p}$, $h_m = h_p \cdot N^{-1}$. Therefore, the scale factor (prototype : model) for linear dimensions is $N : 1$, as depicted in Figure 2.12. The comparison of the distributions of vertical stress in the centrifuge model and its corresponding prototype is shown in Figure 2.13. In order to minimise the error on stress distribution, the effective centrifuge radius, R_e, is equal to $R_t + h_m/3$, where R_t is the radius to the top of the model; the radius where the vertical stress in model and prototype are identical is given by $R_t + h_m \times 2/3$. Based on the physical relationships and dimensional analyses, the scale factors for quasi-static models relevant to common geotechnical applications of centrifuge modelling can be derived as listed in Table 2.1. A more detailed description can be found in Taylor (1995), as well as the effects of consolidation, seepage, and particle size.

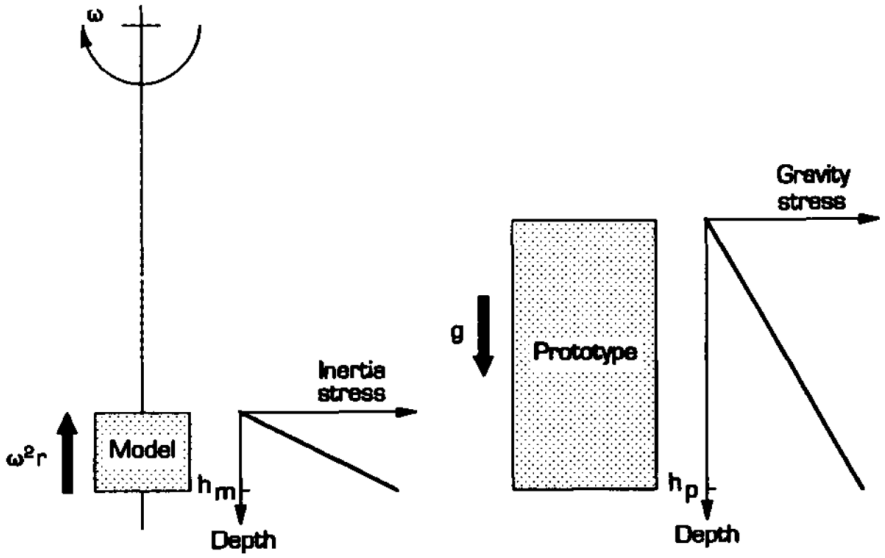

Figure 2.12 Schematic of prototype and centrifuge model; after Taylor (1995)

2.3.1.2 NCG geotechnical centrifuge

The Nottingham Centre for Geomechanics (NCG) geotechnical centrifuge, manufactured by Broadbent G-Max, is a $50\,g$-T machine, with $2.0\,m$ platform radius. It is a typical medium-size beam centrifuge with one swinging platform, and a payload capacity of $500\,kg$ at a nominal radius of $1.70\,m$ can be spun up to $100\,g$. More centrifuge specification is provided in Table 2.2, and Figure 2.14 shows the main components of

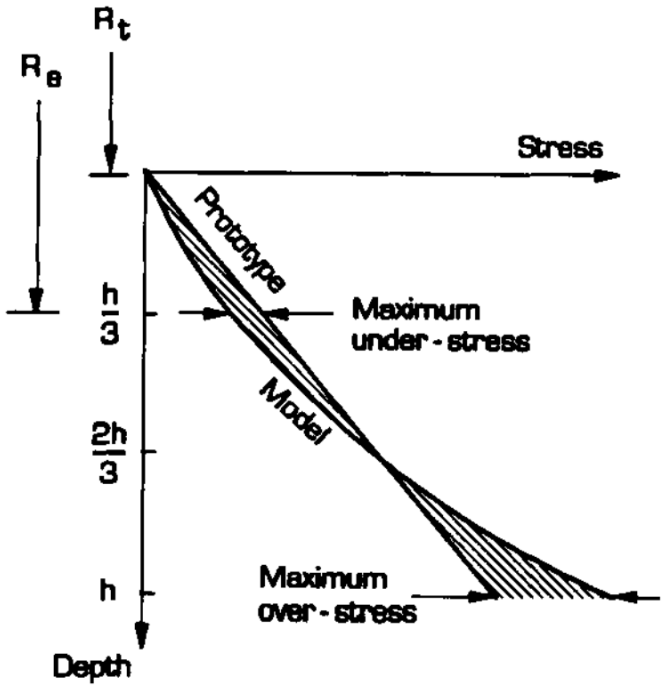

Figure 2.13 Comparison of stress variation with depth in a centrifuge model and its corresponding prototype; after Taylor (1995)

the centrifuge, as described in Ellis et al. (2006). A fixed counterweight, whose position is manually adjustable using a detachable screw jack prior to centrifuge flight, is used to coarse balance the swing platform. This can provide a payload mass between 200 and 500 kg for primary balancing. In addition, an automatic 'in-flight' balancing system allows correcting the imbalance of $\pm 50\,kN$ by the movement of oil in the centrifuge arms. In view of safety, the centrifuge automatically shuts down when the tolerable out-of-balance load of $\pm 30\,kN$ is exceeded.

Date acquisition system (DAS), developed by G-Max and supplied by Broadbent, provides normal functions, including control systems, data acquisition and transmission (Ellis et al., 2006). The DAS cabinet is mounted above the centrifuge arms close to the central axis, as shown in Figure 2.14. It has a capacity of 128 channels for transducer interfacing, and each channel with transducer can digitise and transfer the data to a fibre optic link to the control room PC network. 36 power slip rings and a fibre optic rotary joint provide link the top of the DAS cabinet for AC power distribution and DC supplies on the model. Two PCs located in the control room are used to control the operation of the centrifuge, data acquisition and experiment control system based on Remote Desktop over the university TCP / IP based LAN network.

Table 2.1 Scale factors for centrifuge modelling of quasi-static problems

Quantity	metric unit	Scaling factor (prototype / model)
Gravity / Acceleration	m/s^2	$1/N$
Density	kg/m^3	1
Unit weight	N[1]$/m^3$	$1/N$
Length / Displacement	m	N
Area	m^2	N^2
Volume	m^3	N^3
Stiffness	N/m^2	1
Stress / Pressure	N/m^2	1
Strain	–	1
Force	N	N^2
Velocity	m/s	1

[1] N in units means the unit of force: newton.

Table 2.2 Specification of the NCG geotechnical centrifuge (Ellis et al., 2006)

Platform radius	$2.0\,m$
Assumed effective radius of payload	$1.7\,m$
Maximum size of payload	$0.8\,m$ wide (vertical in flight) $0.6\,m$ wide (circumferential in flight) $0.9\,m$ high (radial in flight)
Maximum payload	$850\,kgm$ ($500\,kg$ at $1.7\,m$) up to $100\,g$
Maximum acceleration	$150\,g$ (at $1.7\,m$)
In-flight balancing	$\pm 50\,kgm$
Motor	$75\,kW$ three phase induction motor

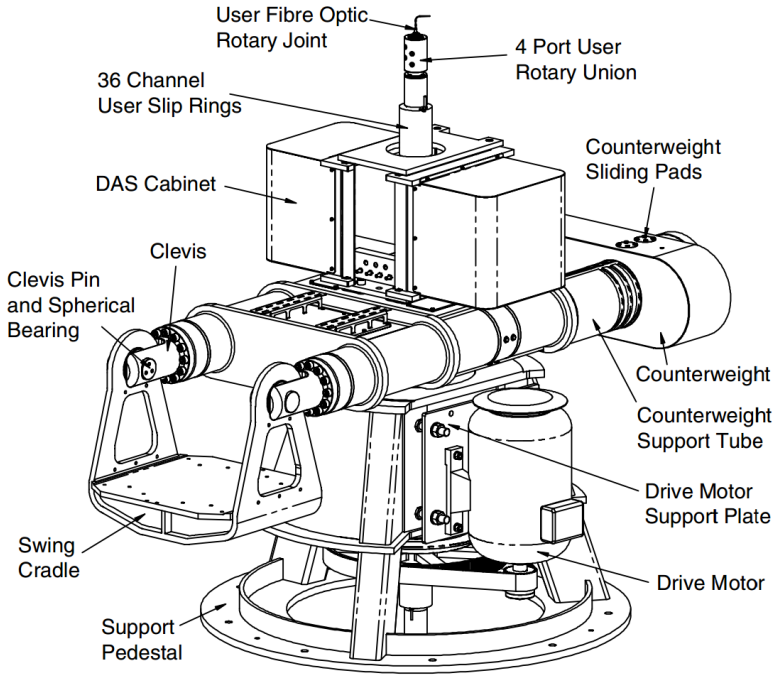

Figure 2.14 Schematic of the NCG geotechnical centrifuge; after Ellis et al. (2006)

2.3.2 Previous centrifuge modelling of CPT

Over 50 centrifuge tests were conducted by Lee (1990) to investigate the cone penetration test in cohesionless soils. It was reported that the penetration resistance is largely dependent on the stress level and soil density, and the results were plotted to relate the tip resistance with the two parameters, as shown in Figure 2.15. The tip resistance increased linearly with the vertical stress, except for the penetration near the ground surface. The growth of q_c was also found to be sharper in soil with higher relative density. The grain size effect was observed for smaller penetrometers: $B/d_{50} < 12$, and the effect of probe surface roughness was negligible, as well as the effect of penetration rate (varying from $3.5\,mm/s$ to $27\,mm/s$). The bottom boundary effect was also evaluated, and a theoretical solution for deep penetration was proposed by using a modified spherical cavity expansion approach.

Thereafter, more penetration tests were carried out at the Cambridge Geotechnical Centrifuge Centre (Bolton and Gui, 1993; Gui and Bolton, 1998; Gui et al., 1998; Bolton et al., 1999), and the guidelines for CPT in sand were developed after investigating the tests using Fontainebleau sand (a typical silica sand with $d_{50} = 0.22\,mm$) from five European centrifuge centres. The interpretation of centrifuge results was provided with a proposed normalisation of cone resistance and penetration depth. After

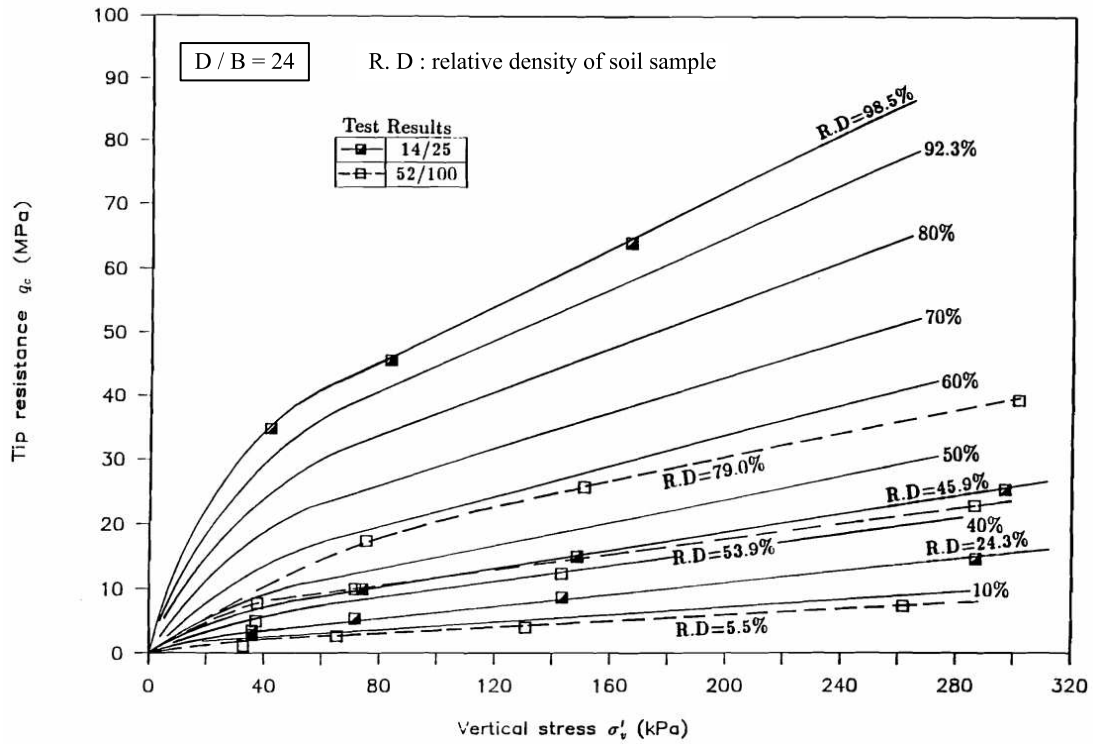

Figure 2.15 Typical results of Lee (1990) to correlate q_c with σ'_{v0} and relative density for $D/B = 24$

illustrating the repeatability of the results from the five laboratories (Figure 2.16), the effects of container size (D/B), stress level, and grain size ratio (B/d_{50}) were examined as presented in Figure 2.17 and Figure 2.18. A more conservative D/B ratio (40) was suggested to eliminate the boundary effects, and the stress level effect was attributed to the sand particle crushing although no evidence was provided from the results. The grain size of fine particles did not affect the Q-Z curves for B/d_{50} in the range 28 to 85. Coarse particles had more effect on the cone resistance, and the grain size effect was generally negligible for $B/d_{50} > 20$. The slight decrease of Q after the peak value was presumably attributed to the enhanced tendency of crushing. Centrifuge modelling of shaft friction of non-displacement piles conducted by Fioravante (2002) also indicated that the scale effects on the shaft friction for $B/d_{50} > 30$ to 50 can be neglected.

Centrifuge tests were performed by McDowell and Bolton (2000) for penetration of a probe with $10\,mm$ diameter into calcareous Quiou sand at a gravitational acceleration of $70\,g$. The effects of particle size distribution were examined by tests with uniform soil and well-graded soil. Particle crushing was also evaluated by retrieving the soil adjacent to the probe at various depths for particle size analysis. Significant crushing was observed for deep sand with deep penetration mechanism, and the crushing was

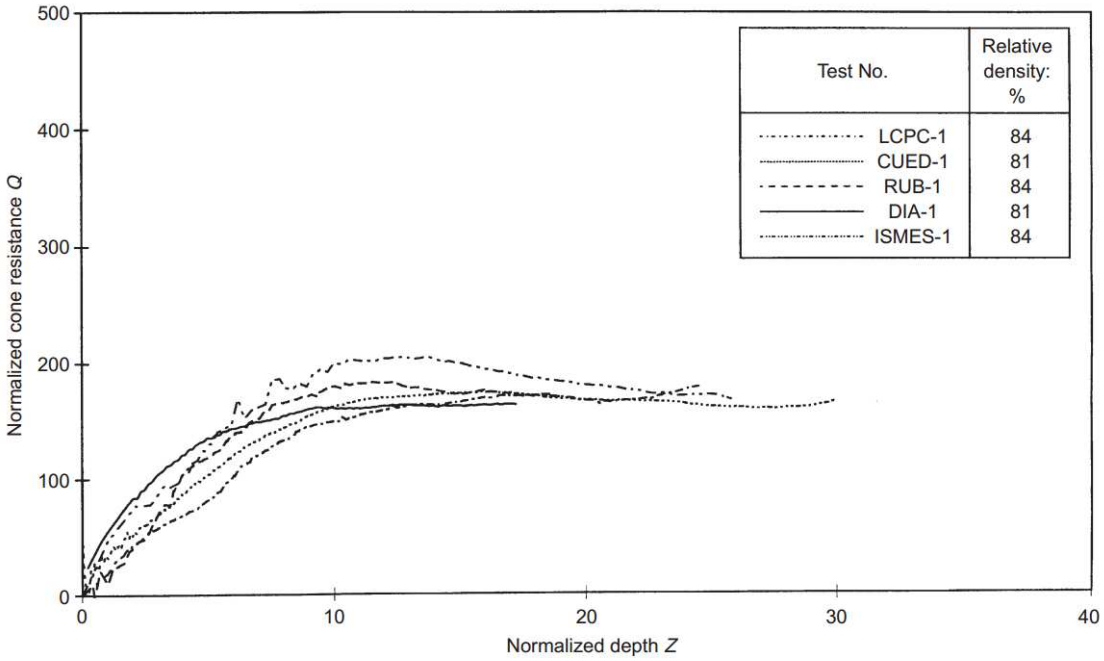

Figure 2.16 Results of normalised cone resistances for five laboratories; after Bolton et al. (1999)

attributed to the large soil compressibility for calcareous sand.

Silva and Bolton (2004) carried out centrifuge penetration tests in saturated layered sands. A piezocone with 12 mm diameter was inserted into layered silica sands (Fraction E sand layer was sandwiched by two layers of Fraction B sand) at 50 g, for investigation of the effects of penetration rate, fluid viscosity, and soil layering. The tip resistance sensed the interface at three cone diameters ahead, whereas the magnitude of the layered effects was small for both tip resistance and excess pore water pressure.

Centrifuge tests were conducted by Xu (2007) to study the performance of pile end-bearing capacity in uniform and layered soil profiles. Both silica sand and kaolin clay were used in the centrifuge models for jacked pile installation tests and static load tests at different g levels. The results of normalised resistance Q and relative density were provided in Figure 2.19 with comparisons with centrifuge results from Bolton and Gui (1993) and a correlation proposed by Tatsuoka et al. (1990). The ratio of pile capacity and installation resistance (q_b/q_c) was concluded at approximately 0.9. Significant layered effects were observed from the results of penetration resistance. The transition of q_c was evaluated with the distance to the soil interface, and the size of influence zone was related with the relative penetration resistances in uniform soils.

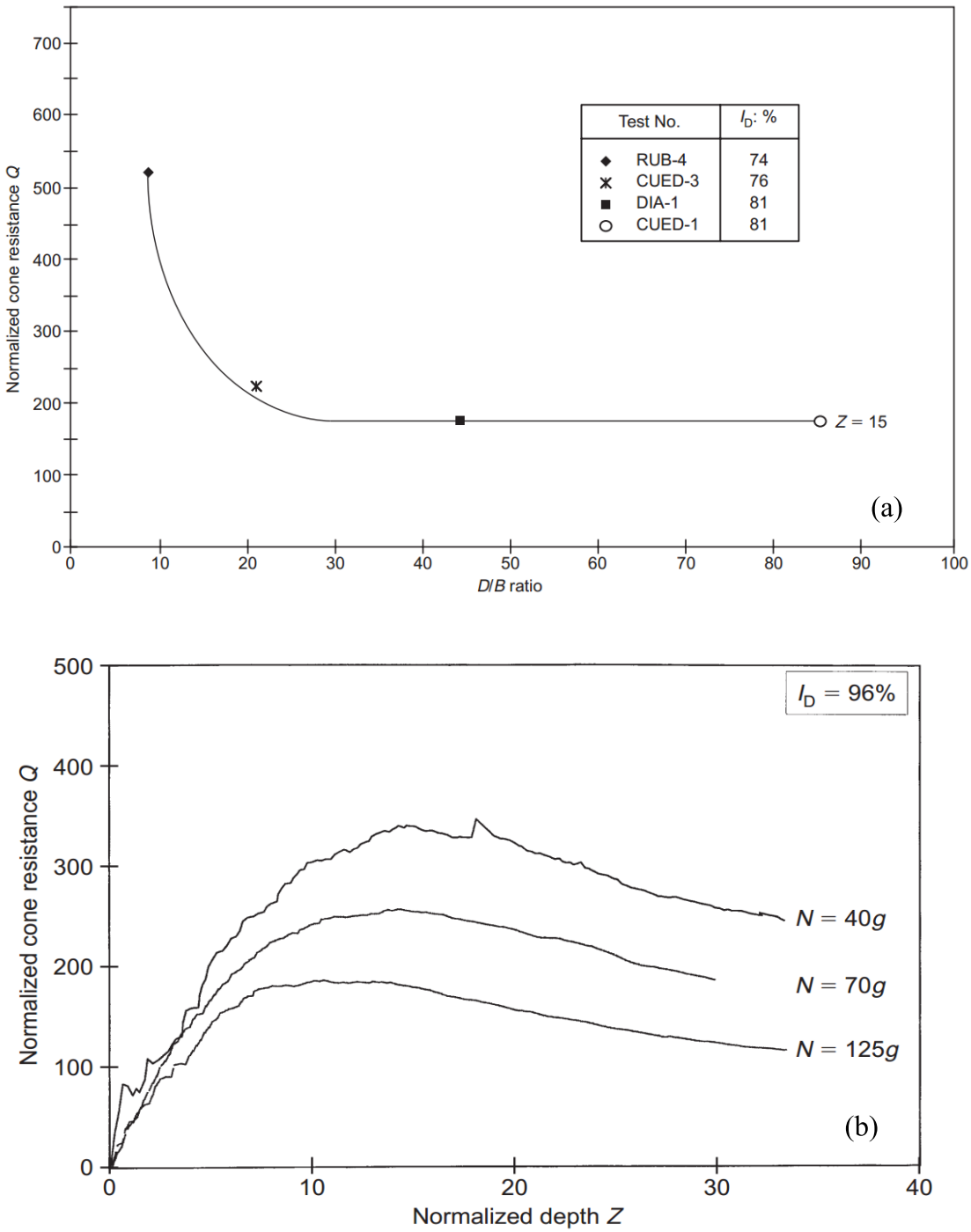

Figure 2.17 Effects of: (a) D/B ratio; (b) stress level N; after Bolton et al. (1999)

Centrifuge modelling of axial pile jacking into sand was performed by Deeks (2008). Static load tests conducted after pile installation showed that the load-displacement and stress-strain response are self-similar at varying stress levels. The performance of the strength and stiffness of the pile was illustrated in the back analysis of the centrifuge results, including the parabola curve of CPT rigidity ratio, dilation at the soil-pile interface, and cyclic loading during penetration.

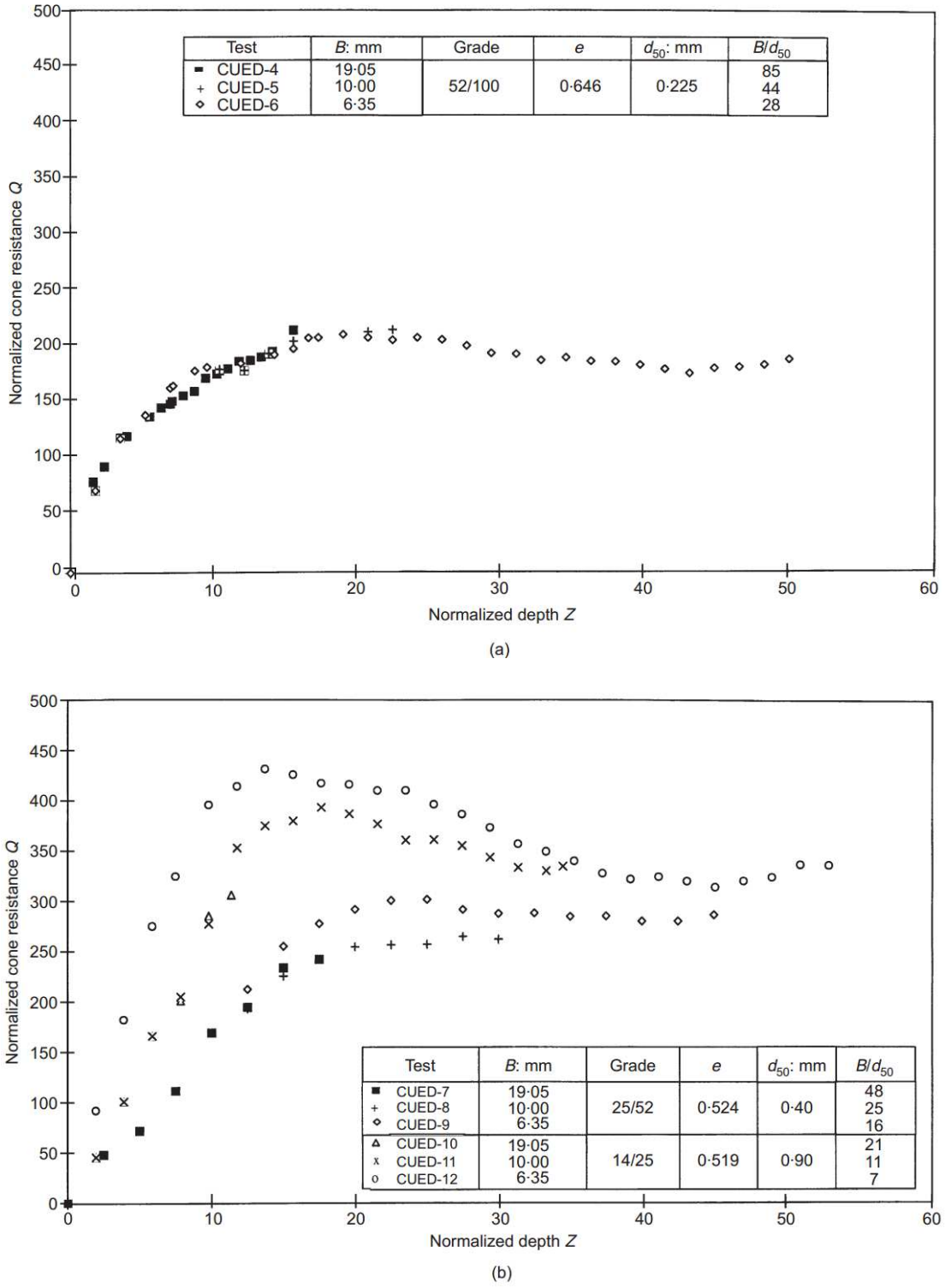

Figure 2.18 Effects of grain size ratio (B/d_{50}): (a) fine particles; (b) medium and coarse particles; after Bolton et al. (1999)

Yi (2009) studied the changes of radial stresses and pore pressures during installation of piles in soft clays. The effect of set-up had been emphasized with the dissipation of excess pore pressures during penetration. Substantial strength enhancements were

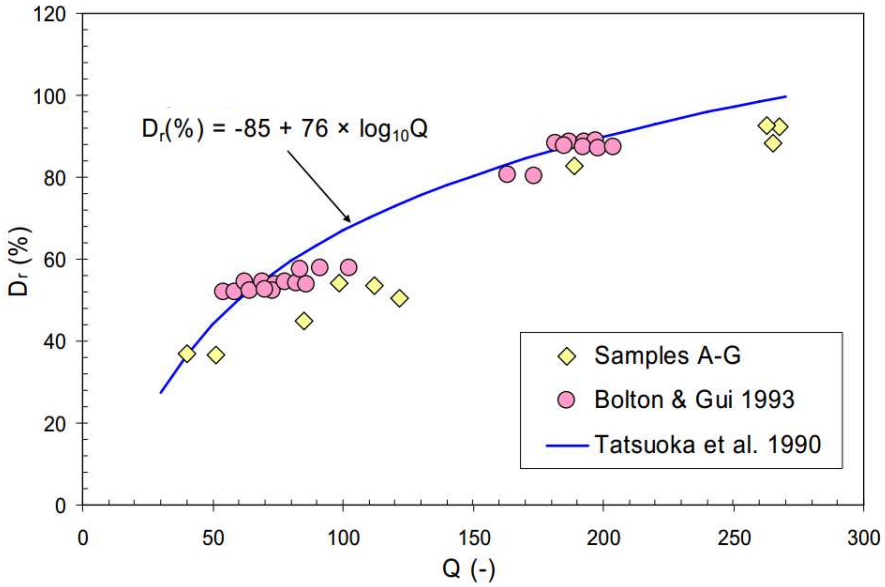

Figure 2.19 Correlation between normalised resistance Q and relative density; after Xu (2007)

observed in the soil after pile installation.

A 180° axisymmetric model of CPT was performed by centrifuge modelling by Liu (2010) to measure the soil deformation during penetration, as illustrated in Figure 2.20. The effects of soil density, g level, probe tip shape, and re-driving were investigated for penetrating a probe with 12 mm diameter in Fraction C sand. Soil displacements, trajectories, and strain paths were obtained to compare with the deformation pattern reported by White and Bolton (2004) in a plane-strain calibration chamber. No significant difference was found for penetration in sand with different relative density.

2.3.3 Soil deformation measurement technology

The measurement of soil deformation plays an important role to study the geotechnical problems and the failure mechanisms involved. Many attempts have been made to improve the technologies to visualise and quantify the deformation associated with geotechnical problems, as reviewed by White (2002). A traditional method is X-ray imaging technique, which is to obtain a series of radiographs following the movement of lead shot embedded in the soil model. Although this technique has been developed with much progress since the late 1920s (Gerber, 1929), the precision of the field of view is still limited by the inherent disadvantages, e.g. shrinkage and swelling of the X-ray film, non-planar movement of the lead shot, and specific equipment re-

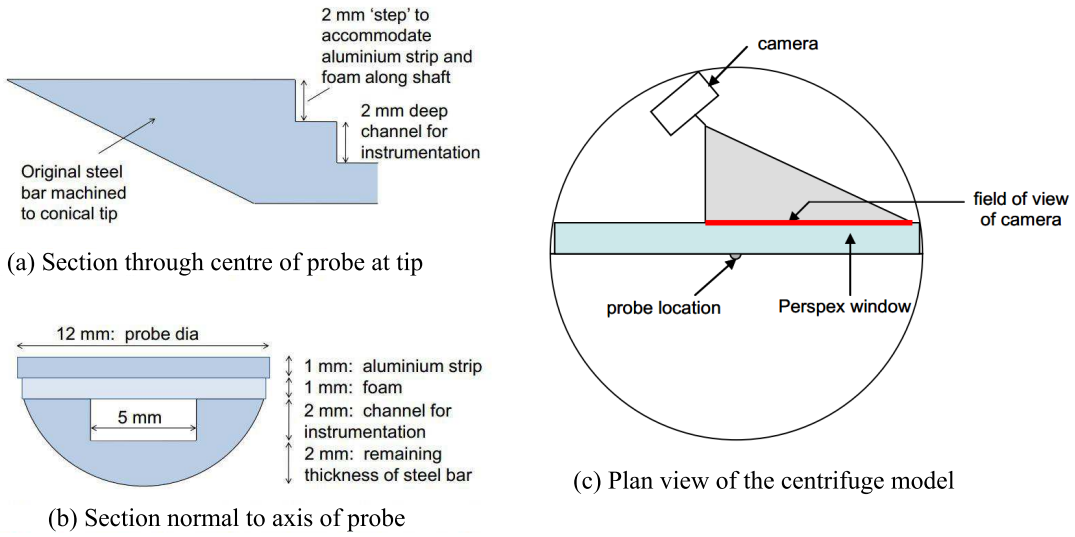

(a) Section through centre of probe at tip

(b) Section normal to axis of probe

(c) Plan view of the centrifuge model

Figure 2.20 Centrifuge model for penetration of half-probe with measurement of soil deformation; after Liu (2010)

quired. With the assistance of a transparent window, the development of photogrammetric techniques enhanced the precision of measurements and provided an easier and more effective approach for physical modelling. The typical methods include stereo-photogrammetry (Butterfield et al., 1970), photoelastic technique (Allersma, 1987), and video-photographic method (Chen et al., 1996). After analysing and comparing the performances of the available techniques by White (2002), a more precise measurement of soil deformation was required, and consequently the author developed a new system combining three technologies: digital still photography, Particle Image Velocimetry, and close-range photogrammetry. The performance of the proposed measurement system have been assessed by three indicators: accuracy, precision and resolution, as detailed in White (2002) and Take (2003).

2.3.3.1 Particle Image Velocimetry

Particle Image Velocimetry (PIV) is a velocity-measuring technique based on images by digital still cameras, which was originally used in fluid mechanics. White et al. (2003) have applied this displacement measurement technique to geotechnical models, together with the description of basic theory and algorithms. A series of calibration tests was carried out to investigate the performance of PIV for the field of geotechnics with influences of soil appearance, particle displacements, and test patch size.

For PIV analysis, Figure 2.21a presents the schematic of the analysis process for a pair of images. A mesh of test patches is determined for the image 1. The autocorrelation function is used to find the displacement vector of each patch between successive images. For each test patch, $I_{test}(\underline{U})$ is the image matrix with size of $L \times L$ pixels which contains all of the colour information within the patch region. A search patch $I_{search}(\underline{U}+\underline{s})$ is extracted from image 2 to search the location of the test patch. The Fast Fourier transform (FFT) of each patch and the convolution theorem are applied to obtain the resulting normalised correlation plane $R_n(s)$ through the sequence of the digitally-captured images (White et al., 2003).

With regards to the precision and accuracy of the measurement system, the texture of the soil must be sufficient to allow patches of soil to be effectively distinguished (Marshall, 2009). Natural texture for sand particles can help to identify and track the movement of patches of pixels in low-velocity flow field, while artificial texture provided by the coloured 'flock' material needs to be scattered onto the surface of clay sample.

The empirical equation proposed by White et al. (2003) gives the precision error corresponding to the test patch size (Equation 2.8). The larger patches selected with smaller errors can provide more precise results, while reducing the number of patches. Therefore, the selection of an optimum patch size needs to be balanced based on the properties of digital still cameras used.

$$\rho_{pixel} = \frac{0.6}{L} + \frac{150000}{L^8} \tag{2.8}$$

where ρ_{pixel} is the precision error and L is the test patch size in *pixels*.

2.3.3.2 Close-range photogrammetry

Close-range photogrammetry offers the conversion from image-space (*pixels*) into object-space (*mm*). The basic transformation model is the linear scaling of pinhole camera model. As a single scaling factor used across the image, errors can occur due to the spatial variation. Also this image distortion requires the cameras validation tests for correction. As concluded from White (2002), the sources of image distortion

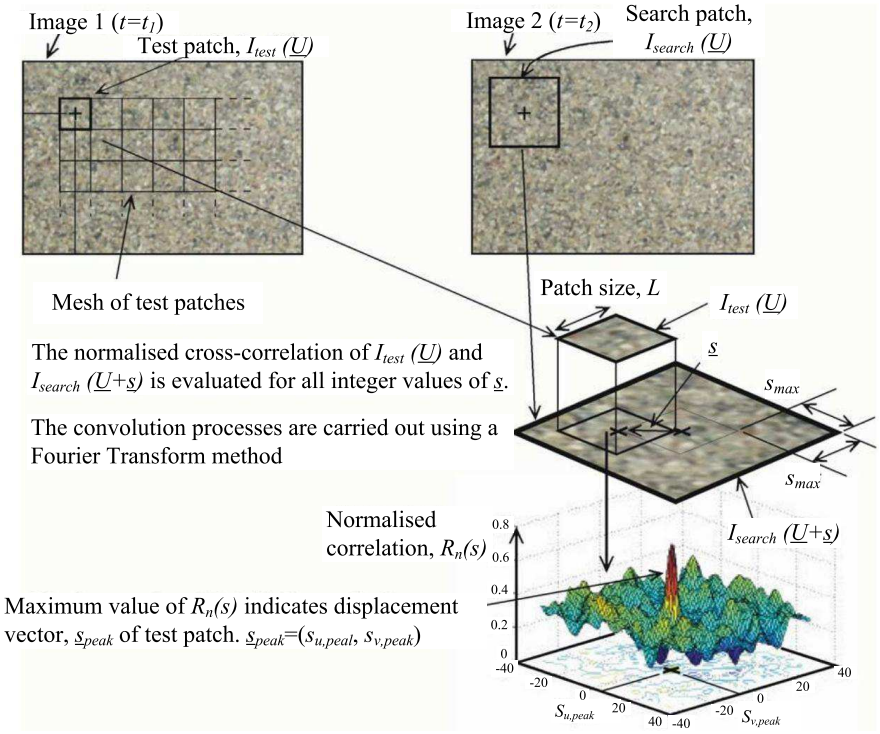

(a) displacement measurement from the PIV analysis (after White, 2002)

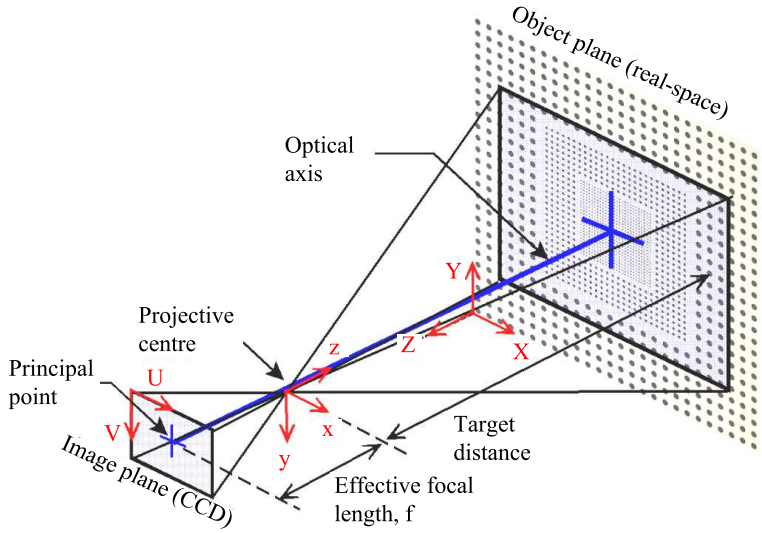

(b) the pinhole camera model for close-range photogrammetry (after Take, 2003)

Figure 2.21 Schematics of GeoPIV analysis; after White (2002) and Take (2003)

mainly come from: non-coplanarity, lens distortion, CCD non-squareness, and refraction.

Non-coplanarity between the image and object planes is considered as an inevitable phenomenon, owing to any tiny movement in the spinning centrifuge model. The Euler angles θ^*, ϕ^* and φ^* are employed to relate the coordinate systems of the CCD and the object plane. Radial and tangential lens distortion, which would lead to 'fish-eye'

and 'barrelling', can be corrected by four parameters (k_1, k_2 for radial lens distortion; p_1, p_2 for tangential lens distortion). CCD non-squareness is eliminated by CCD pixel aspect ratio α. Finally, the refraction through a viewing window depends on the thickness and refractive index of the window. In terms of Snell's law ($\sin\alpha = n\sin\beta$), an iterative process is optimised to weaken the magnitude of the refraction errors.

2.4 Cavity Expansion Solutions in Soils

Cavity expansion plays an important role as a fundamental problem in geotechnical engineering. The applications of this theory involve many aspects of geotechnical problems (e.g. pile foundations, in-situ soil testing, tunnelling and mining). This section first reviews the development of the theory for geotechnical materials and the associated applications (Section 2.4.1). The studies about the interpretation of CPT measurements using cavity expansion are detailed in Section 2.4.2 and cavity expansion in layered media is briefly reviewed in Section 2.4.3.

2.4.1 Cavity expansion theory and applications

Cavity expansion is a classical model with investigation of the cavity pressure-expansion behaviour, the stress/strain field around the cavity and the soil development during process of expansion and contraction. As shown in Figure 2.22, the initial cavity with radius of a_0 is expanded to a, with the increasing of cavity pressure from P_0 to P_a. The typical result of the analysis is the cavity pressure-expansion curve (Figure 2.22b), while the limit pressure P_{lim} is always obtained from the solutions for examining a particular problem. Cavity expansion theory has been extensively developed and widely used for the study of many engineering problems since its first application to the analysis of indentation of ductile materials (Bishop et al., 1945), while the application to geotechnical problems was first brought up in the 1960s. Gibson and Anderson (1961) adopted the theory of cylindrical cavity expansion for the estimation of soil properties from pressuremeter test data. Thereafter, numerous analytical and numerical solutions have been proposed using increasingly sophisticated constitutive soil models by using the principles of continuum mechanics. The development of the theory and its application to geomechanics were described in detail in Yu (2000).

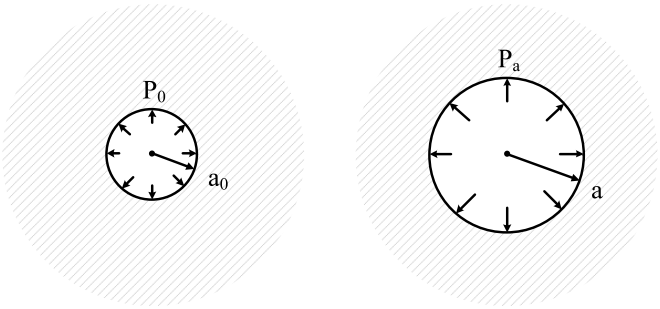

(a) cavity expansion

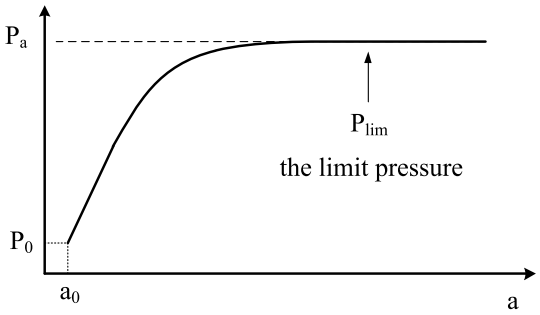

(b) cavity expansion-pressure curve

Figure 2.22 Cavity expansion model and the pressure-expansion curve

Many existing solutions are available from the literature, including linear/nonlinear elastic solutions, elastic-perfectly plastic solutions, critical state solutions, and elasto-plastic solutions. Besides the fundamental elastic solutions in finite/infinite isotropic media, expansion of cavities in a cross-anisotropic elastic material was presented by Lekhnitskii (1963); and solutions in a semi-infinite half-space were provided by Verruijt and Booker (1996) (cylindrical) and Keer et al. (1998) (spherical).

Hill (1950) presented a large strain solution for both spherical and cylindrical cavities in a Tresca material. Chadwick (1959) reported a quasi-static expansion of a spherical cavity in ideal soils using Mohr-Coulomb yield criterion with associated flow rule. Vesic (1972) gave an approximate solution for spherical cavity expansion in an infinite soil mass using a compressible Mohr-Coulomb material. The analysis was applied to evaluate the bearing capacity factors of deep foundations in the same paper. Carter et al. (1986) derived closed-form solutions for cavity expansion from zero initial radius in an ideal cohesive-frictional material with a small-strain restriction. The deformations in the elastic region were assumed to be infinitesimal, and the convected term of the stress rate was neglected in the governing equation, which provided an approxi-

mate limit pressure solution.

Yu and Houlsby (1991) presented a unified analytical solution of cavity expansion in dilatant elastic-perfectly plastic soils, using the Mohr-Coulomb yield criterion with a non-associated flow rule. The complete large-strain analysis, with the aid of a series expansion, was introduced to derive a rigorous closed-form solution without any additional restrictions or assumptions. The typical results of pressure-expansion curves for both spherical and cylindrical cavities are shown in Figure 2.23 with variation of dilation angle ψ. The application to piling engineering was pointed out, and the limitation of their analysis was that the material properties were assumed to be constant and independent of stress-strain history. Salgado et al. (1997) and Salgado and Prezzi (2007) reported a cylindrical cavity expansion solution and produced a stress rotation analysis for the interpretation of the cone penetration test (CPT). A nonlinear elastic region and a numerical formulation in the plastic region were used to achieve a variable stiffness, friction angle, and dilation angle, which will be discussed more in Section 2.4.2.

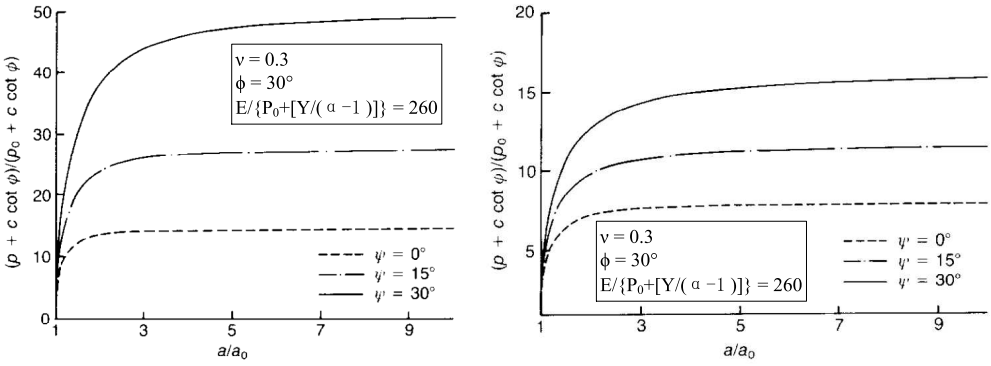

(a) Typical expansion-pressure curves for spherical cavities (b) Typical expansion-pressure curves for cylindrical cavities

Figure 2.23 Typical pressure-expansion curves for both spherical and cylindrical cavities; after Yu and Houlsby (1991)

The critical state based plasticity models of cavity expansion were developed in the last three decades. Davis et al. (1984) presented an undrained cylindrical expansion in a rate-type clay from zero initial radius, and the yield surface was implied based on the modified Cam Clay model (Roscoe and Burland, 1968). The application to predict the behaviour of driven piles in clay was also provided in the same paper. Collins and Yu (1996) provided analytical and semi-analytical solutions for undrained expansion of cylindrical and spherical cavities from a finite initial radius. Original Cam Clay (Schofield and Wroth, 1968) and modified Cam Clay (Wood, 1990)

were adopted to simulate both normally and over-consolidated clays, and the typical pressure-expansion curves for normally consolidated clay ($n_p = 1.001$, where n_p is the over-consolidation ratio in terms of the mean effective stress) are shown in Figure 2.24. A brief application to prediction of excess pore pressures during pile installation in over-consolidated clays was presented to confirm its potential and usefulness in geotechnical practice.

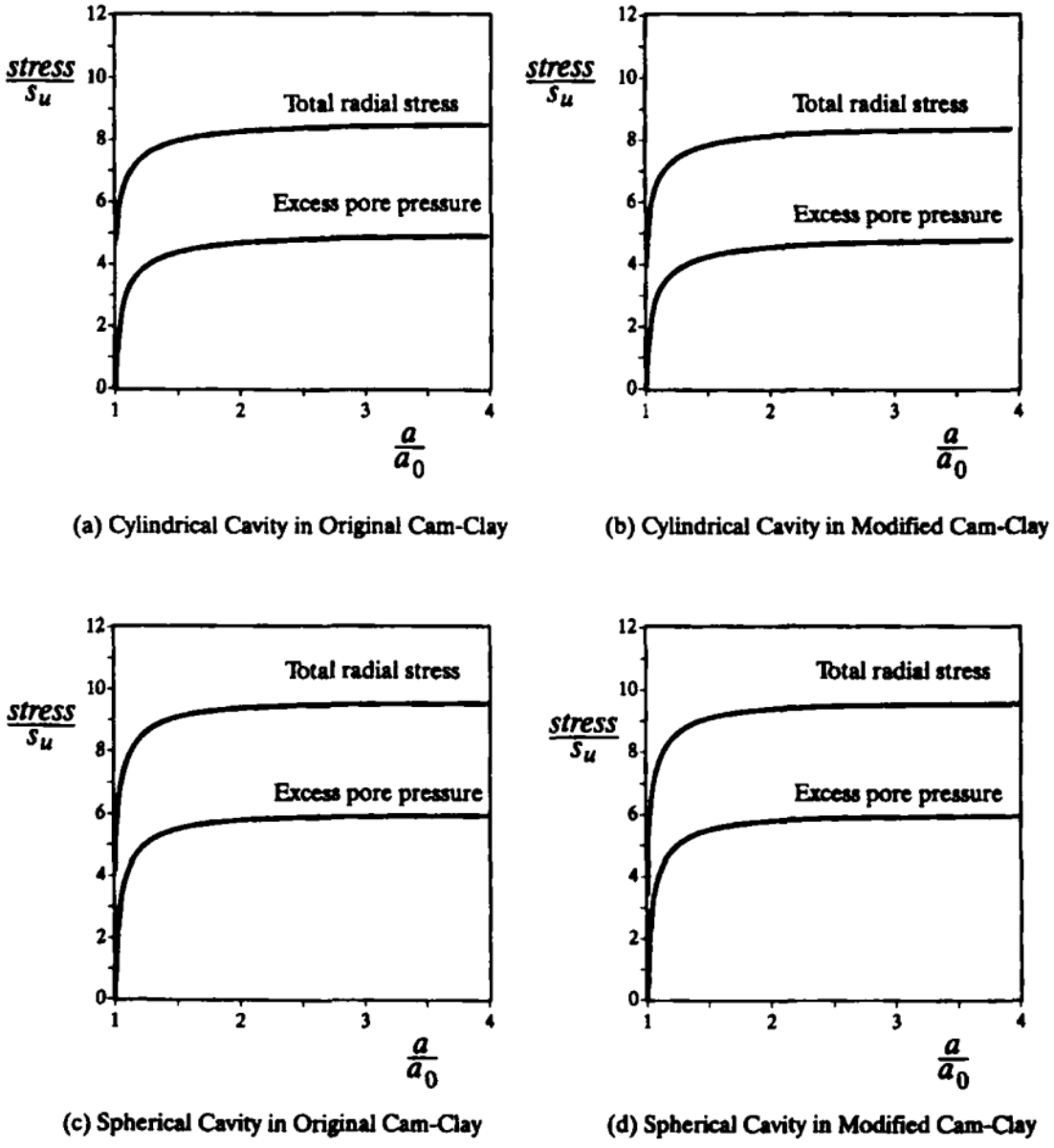

Figure 2.24 Typical pressure-expansion curves for both spherical and cylindrical cavities using original Cam clay and modified Cam clay; after Collins and Yu (1996)

Drained expansion in NC clays (Palmer and Mitchell, 1971; for cylindrical cavities) and heavily OC clays (Yu, 1993) were also provided by small strain analyses of critical

state based models. Collins et al. (1992) developed a semi-analytical solution using a state parameter-based critical state model for sands; the Mohr-Coulomb model was also used to describe sand behaviour.

A series of 2D numerical simulations of cavity expansion was carried out in an elasto-plastic solid by Rosenberg and Dekel (2008), and used to apply to long-rod penetration mechanics. Steel, aluminium, and lead were simulated within Autodyn by using a simple von-Mises yield criterion. The resulting critical pressures had a good agreement with analytical model predictions for the compressible solid (Figure 2.25a), and the normalised cavity pressure for three materials has been concluded with a single quadratic curve (Figure 2.25b). Tolooiyan and Gavin (2011) performed finite element simulations of spherical cavity expansion in sand using Mohr-Coulomb and Hardening Soil models, and applied the method to extrapolate the cone tip resistance.

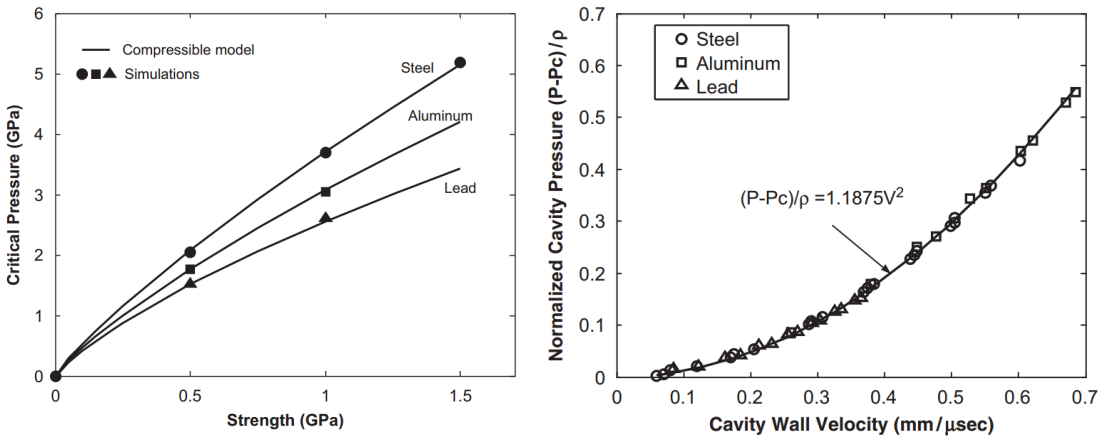

(a) Comparison of critical pressure between simulation and analytical solution

(b) Normalised cavity pressure curve

Figure 2.25 Numerical simulation of cavity expansion in three materials; after Rosenberg and Dekel (2008)

Geng et al. (2013) carried out simulations of cylindrical cavity expansion in granular materials using the discrete element method (DEM). The study investigated the effect of particle shape and micro-properties, which provided the micro mechanical insights into the soil behaviour, and the results compared well with pressuremeter test data. A sample of two-ball clumps and the typical results pressure-expansion curves with comparison with experimental data are shown in Figure 2.26.

As reviewed by Yu (2000), the cavity expansion theory has mainly been applied in

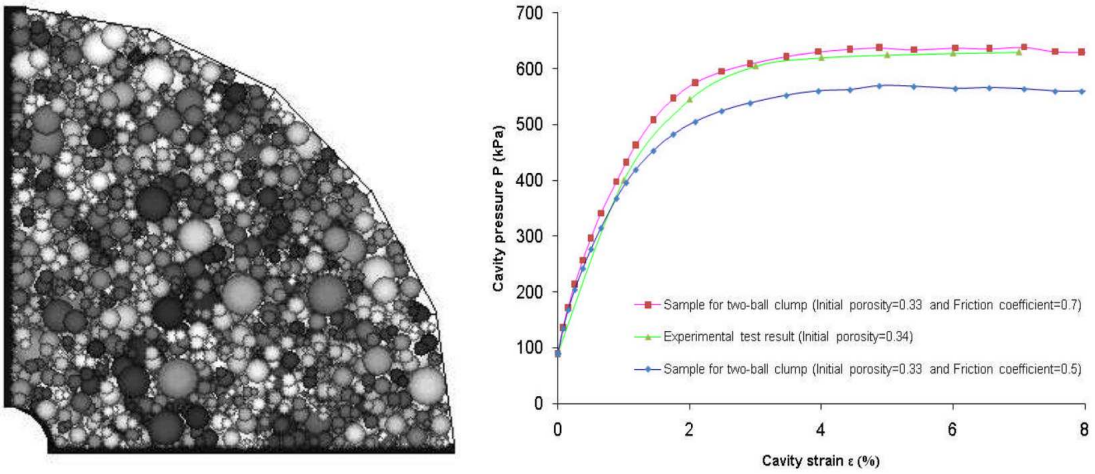

(a) A sample of two-ball clumps

(b) Comparison of DEM simulation with experimental data

Figure 2.26 DEM simulation of cylindrical cavity expansion, and comparison with pressuremeter testing; after Geng (2010)

the geotechnical engineering areas of in-situ soil testing (Wroth, 1984; Clarke, 1995; Lunne et al., 1997; Salgado et al., 1997; Yu and Mitchell, 1998; Salgado and Prezzi, 2007), deep foundations (Davis et al., 1984; Randolph et al., 1994; Yasufuku and Hyde, 1995; Collins and Yu, 1996), tunnels and underground excavations (Hoek and Brown, 1980; Mair and Taylor, 1993; Yu and Rowe, 1999) and recently for an interaction analysis between tunnels and piles (Marshall, 2012; 2013).

The cylindrical cavity expansion method is adopted for the interpretation of pressuremeter tests owing to the similar geometry and loading history, especially for self-boring pressuremeter. Figure 2.27a implies the model of pressuremeter and the analogue of the pressure-expansion curve and the pressuremeter curve. Many correlations have been proposed for testing in undrained clay and drained sand, to predict soil properties, e.g. shear modulus, undrained shear strength/angles of friction and dilation, in-situ horizontal stress and state parameters (Ladanyi, 1963; Palmer, 1972; Hughes et al., 1977; Houlsby and Hitchman, 1988; Houlsby and Yu, 1980; Yu et al., 1996; Ajalloeian and Yu, 1998; Yu and Mitchell, 1998). The applications to pile foundations and cone penetration testing (Figure 2.27b and c) have been studied since Bishop et al. (1945). The analysis of cone resistance has been reviewed by Yu and Mitchell (1998), and more literature about application to CPT or piles will be discussed in the next section.

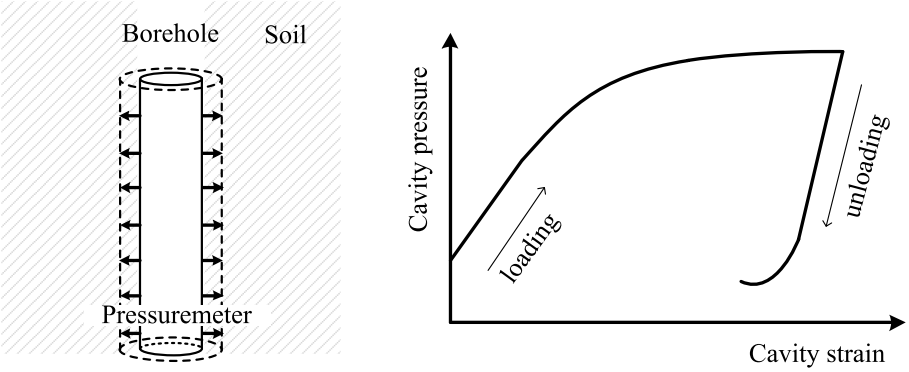

(a) Pressuremeter testing

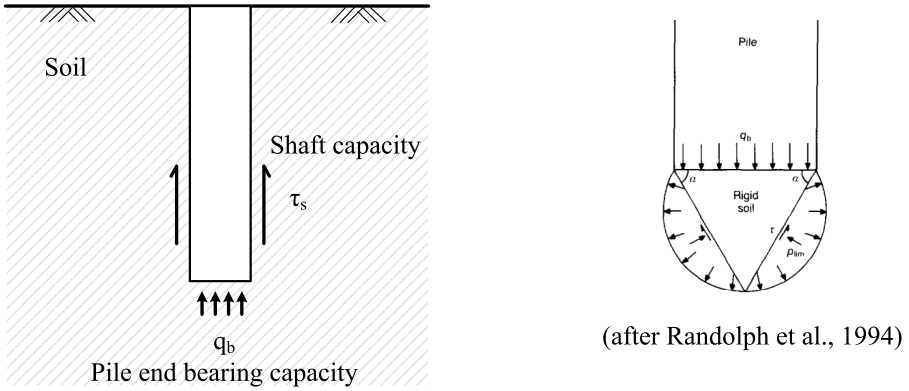

(after Randolph et al., 1994)

(b) Pile foundations

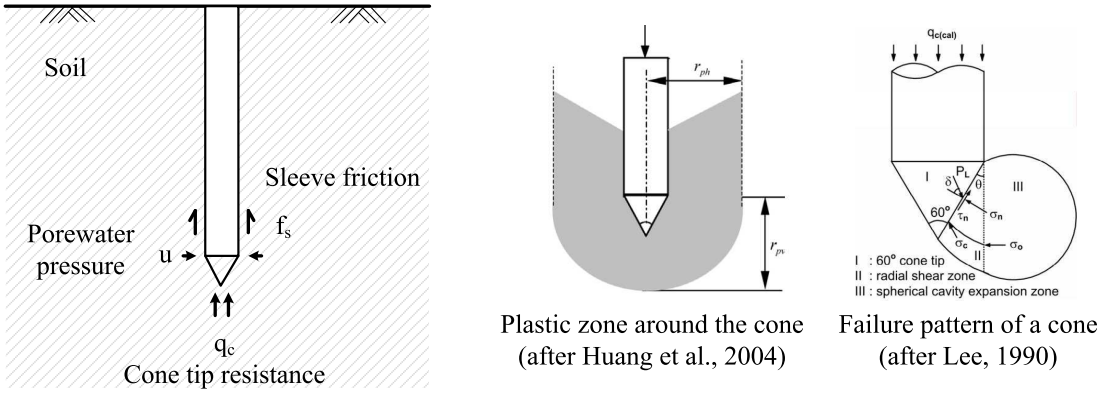

Plastic zone around the cone (after Huang et al., 2004)

Failure pattern of a cone (after Lee, 1990)

(c) Cone penetration testing

Figure 2.27 Applications to (a) pressuremeter testing; (b) pile foundations; (c) cone penetration testing

2.4.2 Application to interpretation of CPT

The application of cavity expansion analyses to penetration problems was first reported by Bishop et al. (1945) who noted that the penetrating force is proportional to the cavity expansion pressure. Since that time, a considerable amount of research has been carried out to improve the theoretical solutions relating to cavity pressure (particularly the limit pressure) and to investigate the correlation between the cavity pressure and

penetrometer resistance (e.g. Yu and Mitchell, 1998).

The solutions for both cohesive and cohesionless soils have been developed significantly since the 1970s. Spherical cavity expansion from zero radius in a nonlinear viscoelastic-plastic soil has been applied for predicting bearing capacity of deep circular footings by Ladanyi and Johnston (1974), with the failure model shown in Figure 2.28. The cone factors are expressed in Equation (2.9).

$$N_c = 3.06 + 1.33 \times \ln \frac{G}{s_u} \qquad \text{(cohesive soils)}$$
$$N_q = \frac{(1+2K_0)\,A}{3}\left[1+\sqrt{3}\,tan\left(\lambda\,\phi'\right)\right] \qquad \text{(cohesionless soils)} \tag{2.9}$$

where N_c and N_q are cone factors; G is shear modulus and s_u is undrained shear strength; K_0 is the coefficient of lateral earth pressure at rest, ϕ' is the friction angle of cohesionless soil, A is the ratio of the effective spherical cavity limit pressure to the initial mean effective stress (P_{lim}/P_0), and λ is the cone roughness indicator (1 for a rough cone and 0 for a smooth cone).

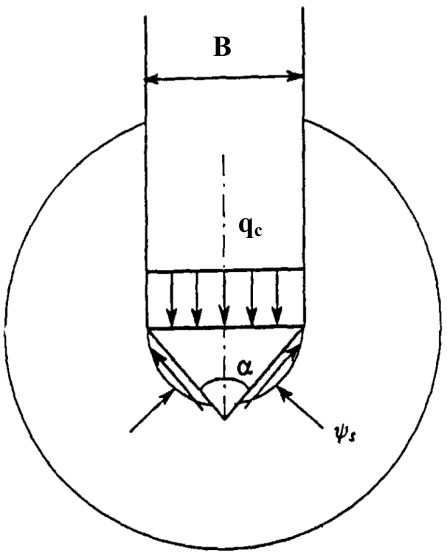

Figure 2.28 Failure model of deep circular footings by using assumption of spherical cavity expansion; after Ladanyi and Johnston (1974)

Vesic (1977) proposed a failure pattern under a flat-bottom pile to estimate the end bearing capacity. As illustrated in Figure 2.29a, Zone I is a wedge below the pile that moves with the pile (this phenomenon was also observed by White, 2002); Zone II is an area with significant radial shearing; Zone III has a pattern similar to a spherical cav-

ity expansion. When relating the end bearing capacity (q_b) to cone tip resistance (q_c), the cone factors for both both cohesive and cohesionless soils are given in Equation (2.10). Lee (1990) extended this model for a cone with 60° apex angle, where Zone I is replaced by the rigid cone, as shown in Figure 2.29b. The method was adopted by Gui and Jeng (2009) to predict cone tip resistance from centrifuge tests.

$$N_c = 3.90 + 1.33 \times \ln \frac{G}{s_u} \qquad \text{(cohesive soils)}$$

$$N_q = \left(\frac{1+2K_0}{3-sin\,\phi'} \right) exp\left[(\pi/2 - \phi') \times tan\,\phi' \right] \times tan^2 (45^\circ + \phi'/2) \times I_{rr}^{\frac{4sin\,\phi'}{3(1+sin\,\phi')}} \qquad \text{(cohesionless soils)} \tag{2.10}$$

where I_{rr} is a proposed reduced rigidity index to account for soil compressibility.

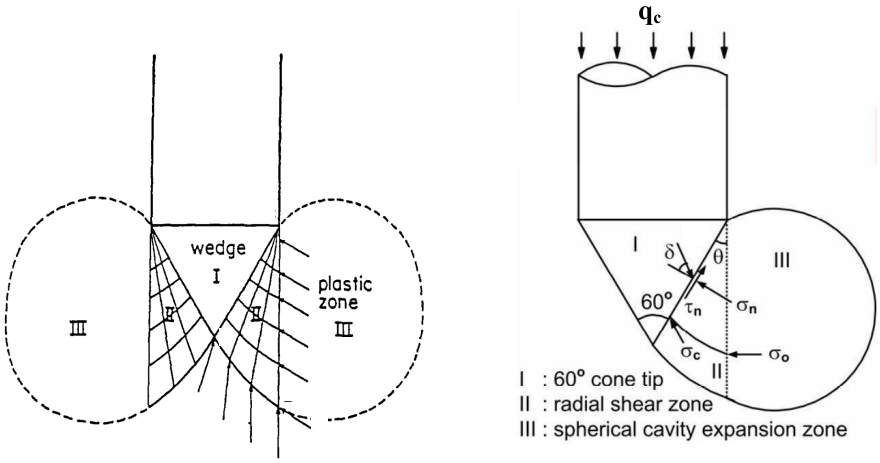

(a) assumed failure pattern under a pile; after Vesic (1977)

(b) assumed failure pattern of a cone; after Lee (1990) (from Gui and Jeng, 2009)

Figure 2.29 Failure pattern around (a) pile (after Vesic, 1977) and (b) cone (after Lee, 1990)

A spherical cavity expansion solution refined and simplified from the solution of Vesic (1977) was proposed by Yasufuku and Hyde (1995) to predict the pile end bearing capacity. The schematic of cavity expansion under the pile is provided in Figure 2.30. The soil was modelled by Mohr-Coulomb failure criterion, and the friction angle was related to the mean stress. After taking into account the soil crushability, the cone factor for sand was obtained in Equation (2.11).

$$N_q = \frac{(1+2K_0)\,A}{3\,(1-sin\,\phi')} \tag{2.11}$$

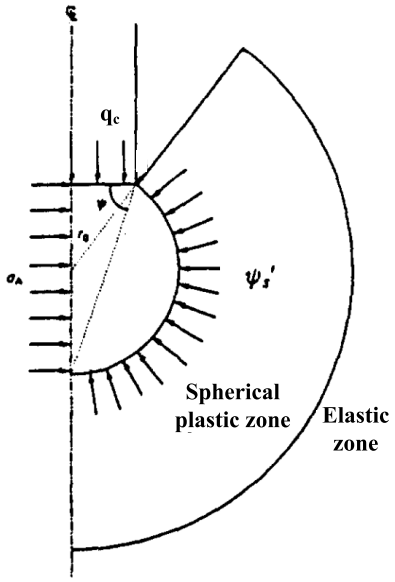

Figure 2.30 The proposed failure mechanism of a pile in crushable sands; after Yasufuku and Hyde (1995)

Salgado et al. (1997) proposed a cylindrical cavity expansion solution for evaluation of penetration resistance in sand, together with stress rotation analyses. Since experimental observations indicated the importance of the initial lateral effective stress (σ'_{h0}) from calibration chamber tests, the scenario of cylindrical cavity expansion was adopted in a nonlinear elastic-plastic material, and the slip pattern with a logarithmic spiral under the probe was assumed to determine the stress rotation after Salgado (1993), as shown in Figure 2.31. The variation of soil properties was achieved by a nonlinear elastic zone and dividing the plastic zone into many concentric thin layers with different soil properties. The solution was compared with the results of about 400 calibration chamber tests with relative differences of less than $\pm 30\,\%$. An alternative approach to estimate q_c using the calculated limit pressure was carried out by Salgado and Prezzi (2007), and the proposed correlation between q_c and soil relative density (D_R), critical-state friction angle (ϕ_{cs}), and initial stress state (σ'_{h0}) is expressed in Equation (2.12) (σ_{atm} is the atmospheric pressure).

$$\frac{q_c}{\sigma_{atm}} = 1.64\,exp\left[0.1041\,\phi_{cs} + (0.0264 - 0.0002\,\phi_{cs})\,D_R\right] \times \left(\frac{\sigma'_{h0}}{\sigma_{atm}}\right)^{0.841-0.0047\,D_R} \tag{2.12}$$

2.4.3 Cavity expansion in layered media

Despite the wide application of the theory to geotechnical problems, very little work has been done to consider the effect of distinct soil layers within the framework of cav-

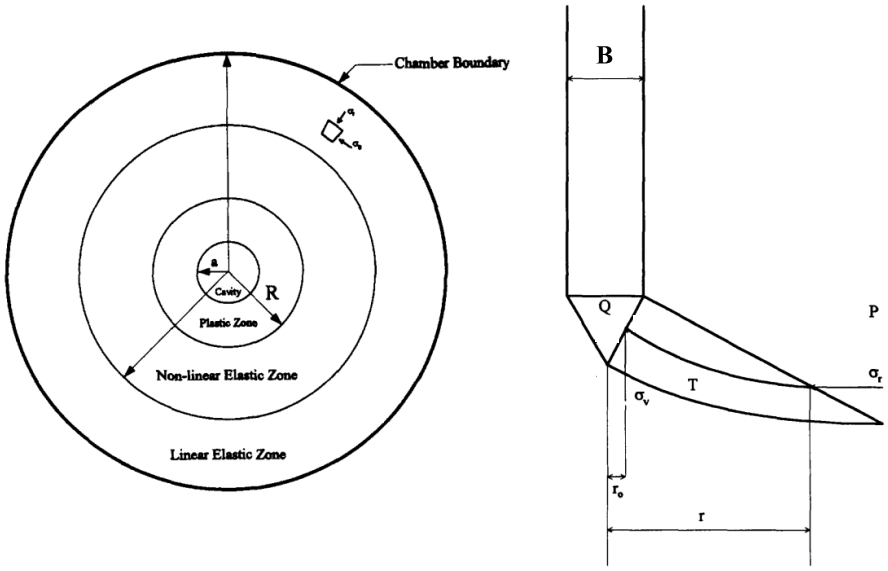

(a) Cylindrical cavity expansion model (b) Slip mechanism for penetration in sand

Figure 2.31 Cylindrical cavity expansion model and slip pattern for stress rotation, after Salgado et al. (1997)

ity expansion analyses. Analytical cavity expansion solutions for two concentrically layered media were developed by Bernard and Hanagud (1975) and Bernard (1976) for the study of projectile penetration, as shown in Figure 2.32. The analysis considered an incompressible material as well as the assumption of a compressible locking strain (i.e. a 'locking strain' was introduced to the analytical model to consider some effect of volume change where the plastic zone is assumed to be uniformly compressed) and was used to solve for dynamic solutions of penetration depth and impact velocity.

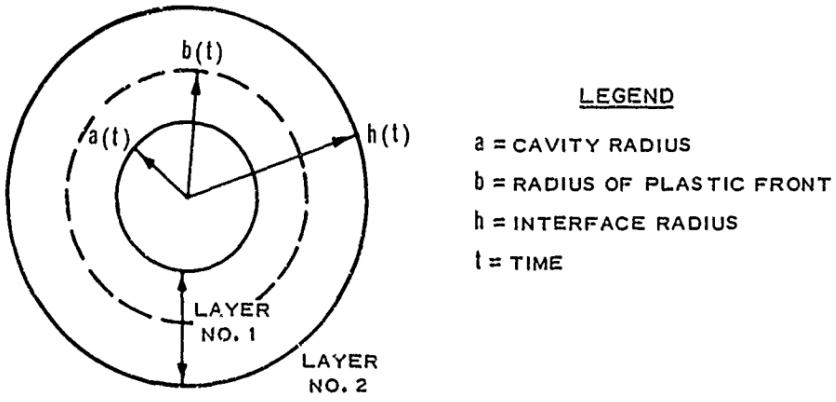

Figure 2.32 Spherical cavity model surrounded by concentric layers; after Bernard and Hanagud (1975)

Sayed and Hamed (1987) were the first to apply analytical cavity expansion analyses of concentrically layered media to the field of geomechanics. The elastic solutions for both spherical and cylindrical cavities in layered mass were presented by using the

model in Figure 2.33. The method of spherical case was applied to evaluate pile settlement in soil layers, and a cylindrical analysis was used to investigate the effect of a remoulded annulus on the stress-strain behaviour and deformation response of the intact soil. However, in their analysis the medium was assumed to be a frictionless linear-elastic solid (i.e. only E and ν was used to capture the soil behaviour) and did not account for the plastic behaviour of soils.

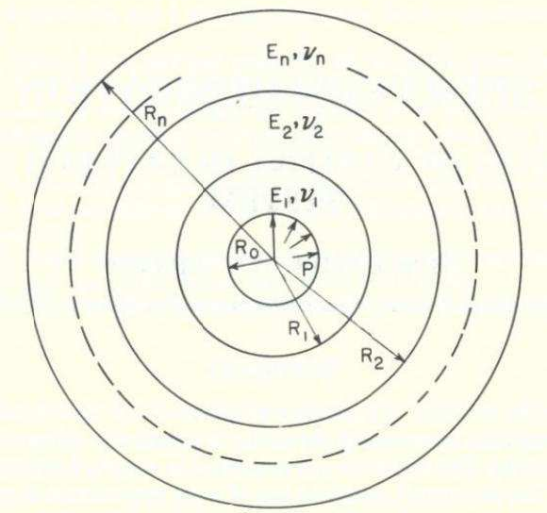

Figure 2.33 Expansion of cavity in layered elastic system; after Sayed and Hamed (1987)

Xu and Lehane (2008) used a numerical analysis of spherical cavity expansion to investigate pile or probe resistance in two-layered soil profiles. The PLAXIS finite element code was employed for using a nonlinear elastic hardening soil model (H-S model, as described in Schanz et al., 1999), and axisymmetric conditions were used for spherical cavity expansion, as shown in Figure 2.34. After verification of results of numerical simulations by the closed-form analytical solutions of Yu and Houlsby (1991), cavity expansion in two-layered soil profiles (shown in Figure 2.35) were performed by the variation of the soil interface location (H_{cavity}). The initial cavity ($a_0 = 0.1\,m$) was expanded to $a = 0.2\,m$, and the corresponding cavity pressure was taken as the limit pressure P_{lim}. The results of a typical test with a drained dense sand ($D_R = 97\%$) overlying a undrained soft clay are shown in Figure 2.36. A resistance ratio $\eta = q_b/q_{b,s}$ was proposed to evaluate the layered effects and the influence zones in both layers. In addition, a series of centrifuge tests with piles jacked into layered soils was carried out to confirm the suitability of the proposed correlations based on the numerical analysis of expansion in two layered soils. Since the analytical solution about cavity expansion

in layered media has not previously been presented in the literature, the development of an analytical cavity expansion method for application to geotechnical problems in layered soils is the main motivation for the work described in Chapter 5.

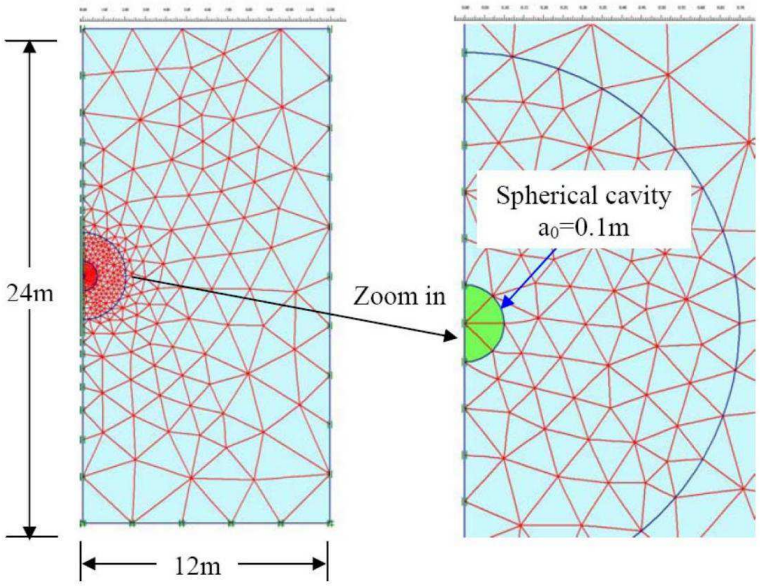

Figure 2.34 Finite element model of spherical cavity expansion in PLAXIS; after Xu and Lehane (2008)

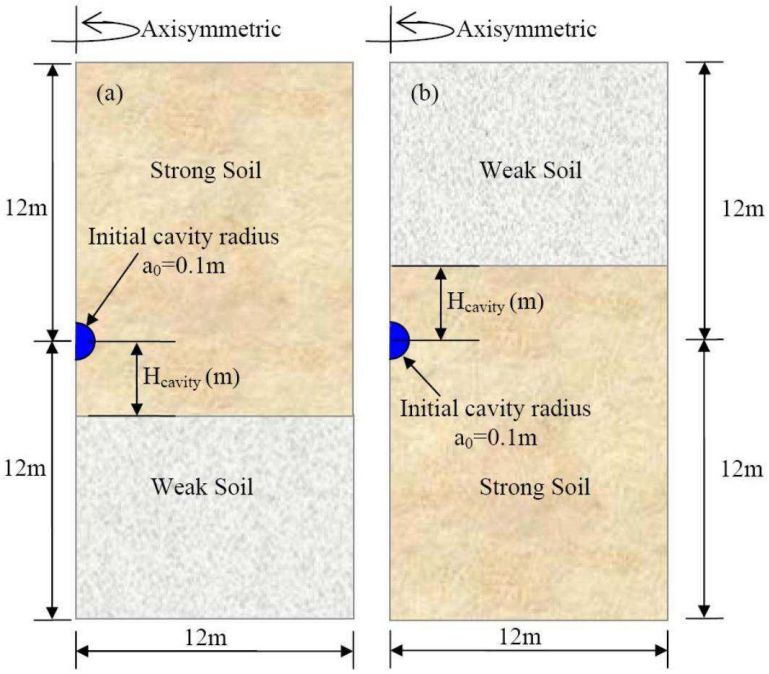

Figure 2.35 Cavity expansion in two-layered soil profiles: (a) strong soil overlying weak soil; (b) weak soil overlying strong soil; after Xu and Lehane (2008)

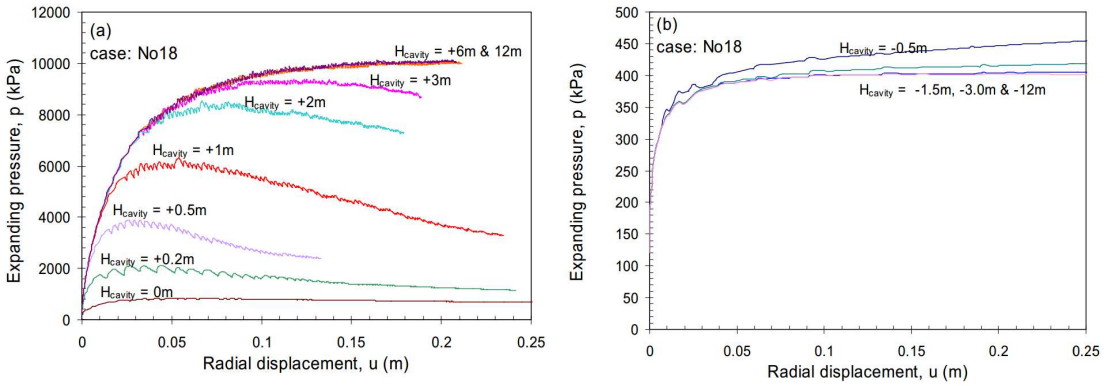

Figure 2.36 Normalised pressure expansion curves of a typical test with dense sand overlying soft clay: (a) cavity in dense sand; (b) cavity in soft clay; after Xu and Lehane (2008)

2.5 Chapter Summary

Previous research on cone penetration testing was outlined in this chapter, and the relevant methods adopted in this research were presented in detail to provide insights into the penetration mechanisms. The literature review can be summarised as follows:

- The cone penetration testing has become an effective and economical in-situ tool for soil investigation and site characterisation, whereas the interpretation of CPT measurements still rely heavily on empirical relationships owing to the complexities of the penetration problem. Soil heterogeneity, compressibility, variability of soil properties, and soil-probe interactions make the understanding of penetration mechanisms difficult.

- The experimental, analytical and numerical methods on the analysis of cone tip resistance have been reviewed respectively, and some of the proposed correlations of cone factors were provided with emphasised limitations.

- Previous research on CPT in layered soils was also presented. The layered effects observed from the field and laboratory tests were usually investigated by numerical approaches. The influence of layering was found to be largely dependent on the soil properties of both soil layers and stress conditions.

- The advantages of centrifuge modelling were highlighted, and the scaling laws between the centrifuge model and the prototype model were outlined. The description of the NCG geotechnical centrifuge was also provided with specifications and schematics. Previous centrifuge studies of penetration problems were reviewed to provide the guidelines for CPT in sand (Gui et al., 1998) and im-

provements for soil deformation measurement during penetration (Liu, 2010).

- The technology for soil deformation measurement (White et al., 2003) was then introduced after reviewing other methods. The developed system combining digital still photography, Particle Image Velocimetry, and close-range photogrammetry provide a good performance of soil deformation measurement with accuracy, precision and resolution.

- The theory of cavity expansion has wide applications to geotechnical engineering. Numerous analytical and numerical solutions have been proposed using increasingly sophisticated constitutive soil models, and many applications like piled foundations, and in-situ soil testing were discussed, especially for cone penetration tests.

- Previous research of cavity expansion in layered media was reviewed, which mainly used elastic solutions and numerical simulations. An analytical solution of cavity expansion in layered soils was shown to be required for the evaluation of the layered effects more effectively.

Chapter 3

Centrifuge Modelling Methodology

3.1 Introduction

The literature review presented in Chapter 2 gave the background and an overview of the previous research on cone penetration testing, with particular interest in stratified soils. The current interpretation of CPT data is mainly based on empirical correlations, attributed to the complexity of the problem and the uncertainty of the penetration mechanism. Centrifuge modelling replicates the field stress magnitude and gradient, and the image analysis technology for measurement of soil deformation in axisymmetric models provides an effective method for investigation of probe performance and soil movements during penetration. All of the centrifuge tests in this research were carried out on the NCG geotechnical centrifuge, as introduced in Section 2.3.1.

This chapter describes the details of the centrifuge modelling methodology. The experimental apparatus that was adopted to perform the centrifuge tests is first detailed in Section 3.2 with instrumentation of the probe described in Section 3.3. The method of soil model preparation is presented in the subsequent Section 3.4, before the chapter is concluded by a summary of the testing programme and procedure (Section 3.5).

3.2 Experimental Apparatus

3.2.1 Container and Perspex window

Due to the geometry of a cone penetrometer, it is more reasonable to simulate the penetration problem using a three-dimensional model or axisymmetric model, rather than

a plane strain/stress model. The benefits of a 3D model mainly lie in the geometric consistency and the similarity of stress/strain conditions around the probe. One of the main advantages of the conducted centrifuge tests is the ability to obtain soil deformation associated with penetration, but this requires a plane of symmetry within the model. Therefore, a half-cylinder axisymmetric model was used with a transparent window at the plane of symmetry for observation, following the design of Liu (2010).

The centrifuge container, made from steel, is shown in Figure 3.1, with inner diameter (D) of 500 mm and depth of 500 mm. The effects of wall friction have been examined to be relatively small for penetration tests in a calibration chamber (White and Bolton, 2004) and in centrifuge tests (Klotz and Coop, 2001). For the purpose of soil observation, two pieces of Perspex window with thickness of 50 mm and 25 mm which offer sufficient optical clarity, were placed at the centre of the container to form the axisymmetric model. The considerable Perspex window thickness was required to provide sufficient strength and stiffness to retain the high pressure of soil in the centrifuge model and limit horizontal strains, together with three braces, as shown in Figure 3.1. Although the glass window offers less surface friction, the Perspex has a higher allowable stress as discussed by White (2002) and the negligible difference with respect to measured displacements between the two types of window has been observed by Liu (2010). In addition, the effect of refraction has been considered within the GeoPIV analysis to account for the refractive distortion by Snell's Law (White, 2002).

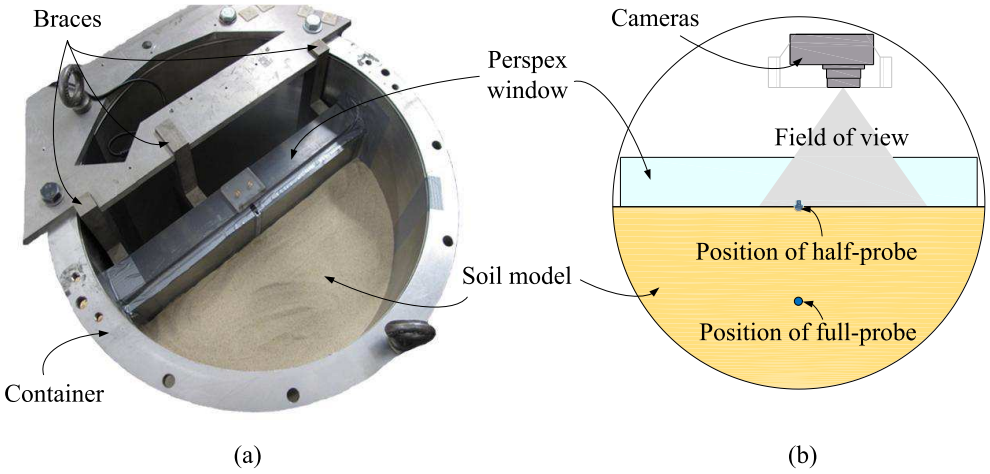

Figure 3.1 The centrifuge container with Perspex window

3.2.2 Actuator

The driving mechanism was the same as that used by Liu (2010). Figure 3.2 illustrates the actuator and reaction system for driving the probe into the soil. The actuator, positioned above the container, was able to drive the probe a maximum displacement of 220 mm at any speed up to 5 mm/s by means of a motor acting through a gearbox and lead screw. The displacement control method was used for all of the centrifuge tests at a speed of approximately 1 mm/s. A potentiometer was fixed to the moving connector to record the travel of the penetrometer, which was then used to control the penetration speed via the power supplied for the motor. The connection between the half-probe and the actuator was set up by two steel wires. This design attempts to eliminate the eccentricity of the probe from the connector in the actuator, which would generate bending moments within the probe. The details about the probe will be presented in the following Section 3.2.3.

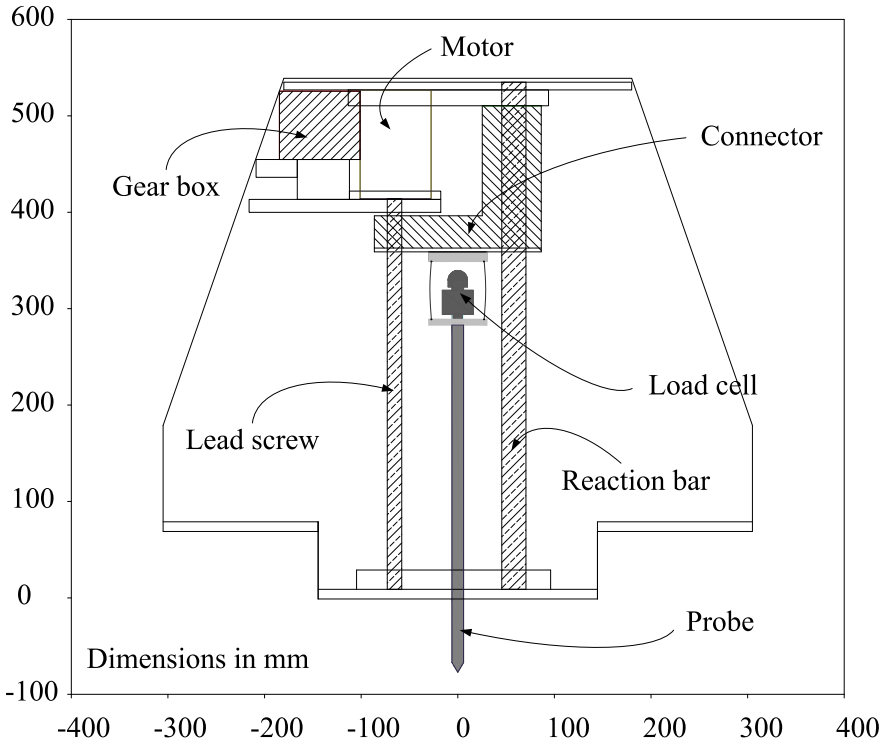

Figure 3.2 Schematic of the actuator driving mechanism

3.2.3 Model penetrometer design

Rather than the standard cone penetrometer (diameter 35.7 mm), probes with 12 mm diameter (B) and an apex angle of 60°, manufactured from aluminium alloy (relative sur-

face roughness: $R_n \approx 5 \times 10^{-3}$), were used for the centrifuge tests. The relative surface roughness is defined as $R_n = R_t/d_{50}$, where R_t is the maximum height of the surface profile; and d_{50} is the average grain size (Fioravante, 2002). The value $R_n \approx 5 \times 10^{-3}$ for aluminium alloy was suggested by Zhao (2008) for Fraction E sand ($d_{50} = 0.14\,mm$, as shown in Table 3.1). The probe, representing a miniature CPT, can also be regarded as a pre-cast pile in prototype model due to the analogy between piles and penetrometer behaviour (Gui and Bolton, 1998; White and Bolton, 2005). For the half-probe the ratio of container to probe diameter (D/B) is $500/12 = 42$, which is greater than the proposed ratio (40) to minimise the boundary effects for dense sand suggested by Gui et al. (1998) and Bolton and Gui (1993). Also, the ratio of probe diameter to the mean grain size (B/d_{50}) is $12/0.14 = 86$, larger than the minimum acceptable value (20) for Leighton Buzzard sand (Bolton et al., 1993). The full-probe tests were also performed in the same samples after the half-probe test, as indicated in Figure 3.1 and Figure 3.14, aiming to validate the results of penetration resistance. The boundary effects are limited according to Gui et al. (1998), and the discussion about the effects will be presented later in Section 4.2 and Section 7.3.1.

Attempts have been made by previous researchers (Liu, 2010; Marshall, 2009) to accurately model half-axisymmetric probes in the centrifuge. However, any intrusion of sand particles between the half-probe and the window will force the probe to deviate from the window, as observed by Liu (2010). Consequently the images would not capture the soil deformation on the plane of symmetry and hence the penetration mechanism is no longer achieved. In addition, any trapped sand would abrade or deteriorate the window and the half-probe. This is arguably the greatest challenge for using a 180° axisymmetric model for these types of tests, and is why many experiments use a plane strain model (e.g. Berezanysev et al., 1961; Yasufuku and Hyde, 1995; White, 2002).

In order to maintain contact between the probe and the window, a steel guiding bar was connected to the penetrometer in parallel to the probe, and an aluminium channel ($8\,mm$ wide by $8\,mm$ depth) was fixed into the middle of the Perspex window, as shown schematically in Figure 3.3a and b. As the penetrometer slides along the Perspex face, the guiding bar slides into the aluminium channel. This method prevented sand grain

ingress between the probe and the Perspex and ensured that the probe maintained contact with the Perspex as it was driven into the soil. Figure 3.3c gives the cross sectional schematic of the channel with dimensions. Using the aluminium channel means that displacement data within a small region directly ahead of the penetrometer can not be obtained. This small region close to the probe experiences extreme distortion and rotation during penetration, which invalidates the results from GeoPIV.

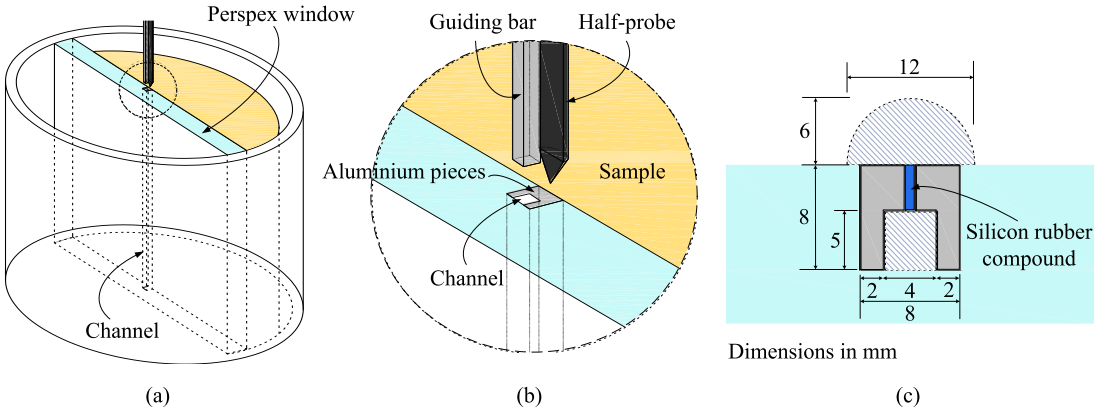

Figure 3.3 Schematic of aluminium channel for half-probe

As illustrated in Figure 3.4 and Figure 3.5, the schematics present the details of the probe design for both half-probe and full-probe. For half-probe assembly shown in Figure 3.4, five '12BA' screws (*BS* 93 : 2008) were used to fix the gap between the probe and the guiding bar due to the slenderness of the guiding bar. This meant that the aluminium channel had to be slotted to accommodate the screws, which is shown in Figure 3.3c. This slot was then filled with silicone rubber compound (flowable fluid) to prevent soil particles from entering the aluminium channel during tests.

In an attempt to exclude the load caused by the silicon rubber and friction from the guiding bar, a centrifuge test using the half-probe with no sand was conducted to estimate the effective penetration load for all half-probe tests. In addition, to minimise friction along the back of the probe and the guiding bar, these surfaces were also coated with silicon grease. A load cell with a loading cap was located at the head of the half-probe to record the total penetration load. Three strain gauges ('SG1', 'SG2' and 'SG3'), together with the strain gauge tabs and the wires, were embedded inside the body of the half-probe, attempting to measure tip resistance and shaft friction.

The full-probe had a similar size and length as the half-probe. As illustrated in Figure 3.5, it was manufactured from an aluminium tubing with outer diameter of half inch ($\approx 12.7\,mm$) and inner diameter of about $9.5\,mm$. The hollow cylinder was selected to accommodate the wires of strain gauges, and the end was manufactured for connection with a 60° conical tip component. Rather than single strain gauge in the half-probe, a pair of strain gauges ('SG45') were installed on the tip component of the full-probe to compensate for the bending effect, which will be presented in details in Section 3.3.1.

3.3 Instrumentation

3.3.1 Load cell and strain gauges

As the probe resistance is one of the main measurements for in-situ CPT, a load cell with capacity of $10\,kN$ provided by Richmond Industries Ltd (Figure 3.6a) was installed at the top of the penetrometer to measure the total penetrating resistance (see Figure 3.4 and Figure 3.5). For half-probe tests, the load cell was situated along the probe centroid to minimize the bending effect. To allow examination of the probe tip resistance and shaft friction, the probes were instrumented with strain gauges to measure the axial response during penetration. The strain gauges were installed inside the probes, as shown in Figure 3.4 and Figure 3.5. The foil strain gauges 'FLA-3-350-23' were supplied by Tokyo Sokki Kenkyujo Co., Ltd (Figure 3.6b), with gauge length of $3\,mm$; gauge resistance of $350 \pm 1.0\,\Omega$; temperature compensation factor of $23 \times 10^{-6}/^\circ C$; and gauge factor of $2.13 \pm 1\%$. They were used in general Wheatstone bridge configurations with an excitation voltage (V_{EX}) of $12\,V$. Figure 3.7a shows the circuit plate for the Wheatstone bridge, and the connections are illustrated in Figure 3.7b and c for half-probe and full-probe, respectively. A quarter-bridge circuit was used for each strain gauge in the half-probe by measuring the output voltage (V_O) with change in electrical resistance of the active strain gauge. However, to avoid the influence of bending moment, the tip resistance of the full-probe was measured by using a half-bridge circuit which allows bending compensation. From the circuits, it is conceivable that the component of resistance caused by bending is included in the total change of resistance in quarter-bridge; whereas the positive and negative bending moments are able to be compensated in half-bridge to provide a more reliable effect of ΔR_p. Calibrations of instrumented probes were carried out on a loading machine. The

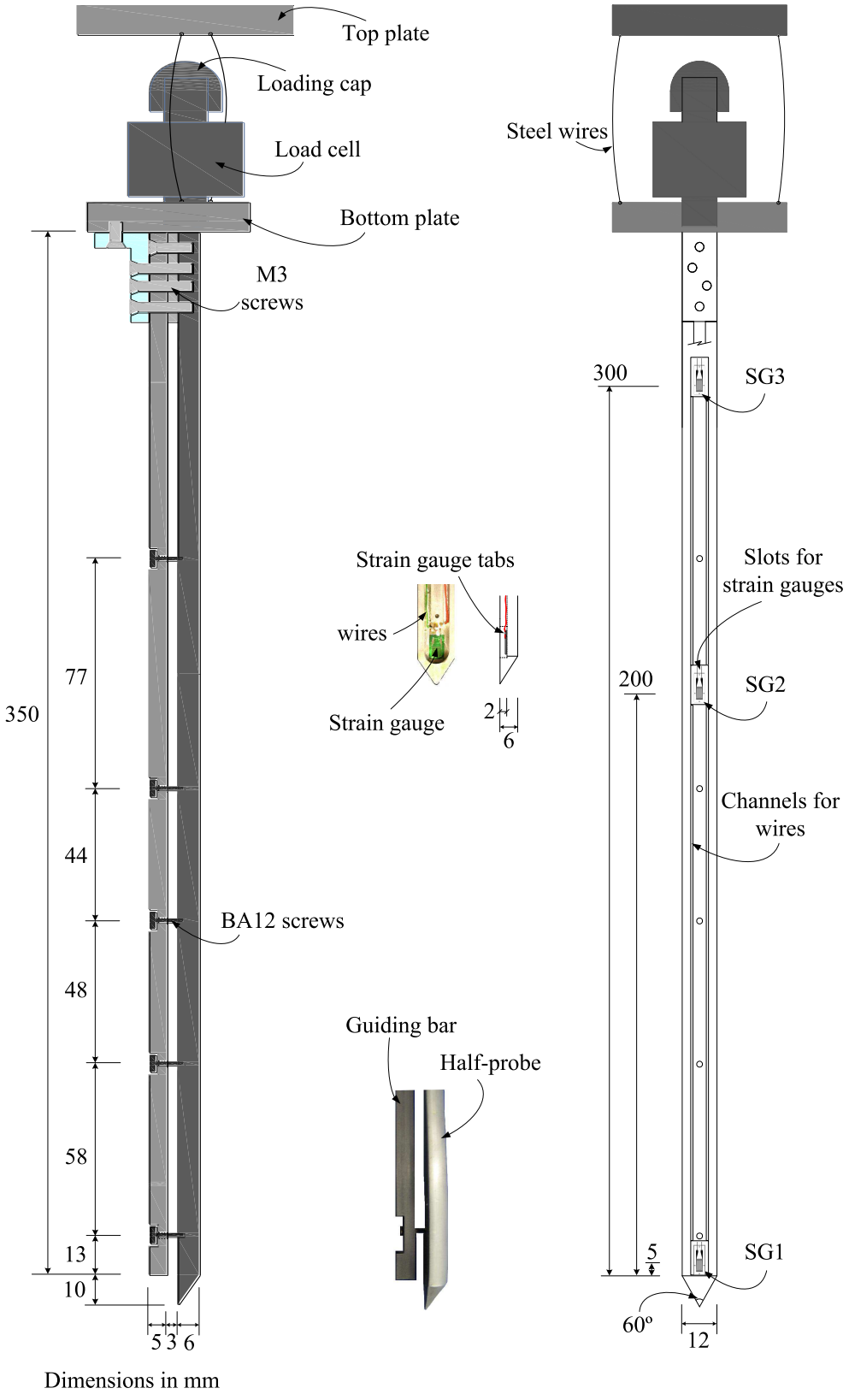

Figure 3.4 Schematic of the half-probe assembly

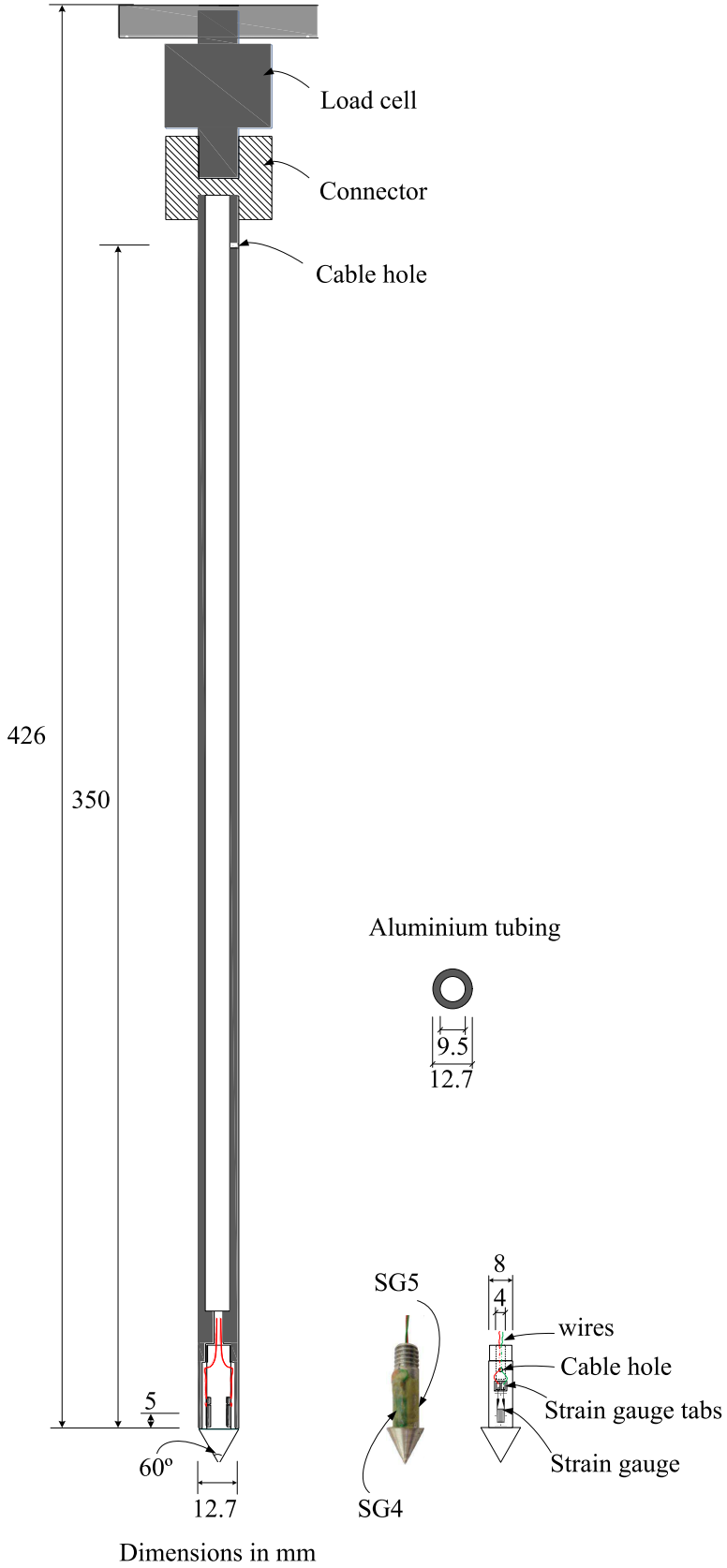

Figure 3.5 Schematic of the full-probe assembly

results of the strain gauge calibration tests are provided in Figure 3.8. The output signals from the strain gauges showed some non-linearity and were somewhat susceptible to the effects of zero-shifting, temperature, hysteresis and electrical interference; however linear curve fitting was used to determine the calibration factor for each measurement.

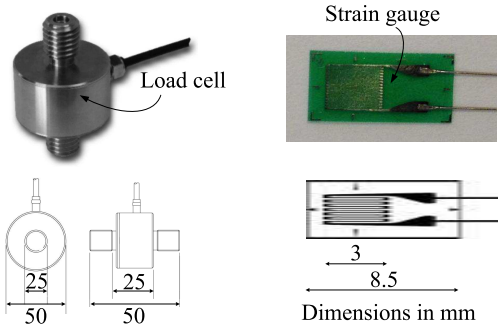

(a) Load cell (b) Strain gauge

Figure 3.6 Schematic of load cell and strain gauge

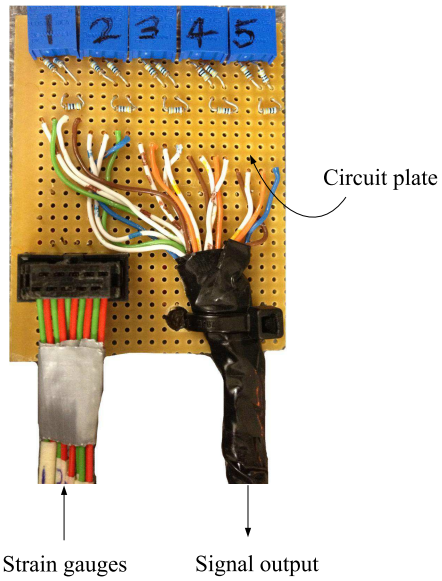

(a) Circuit plate for Wheatstone bridge

R_{SG} : Strain gauge resistance ($R_0 = R_{SG} = 350\ \Omega$)
ΔR_p : Change of resistance caused by pressure
ΔR_{bm} : Change of resistance caused by bending moment

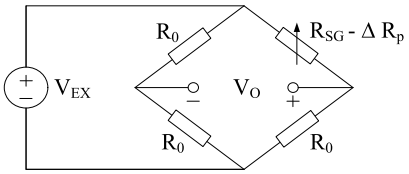

(b) Quarter-Bridge Circuit for strain gauges in half-probe

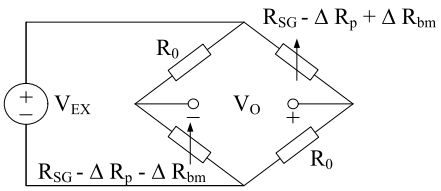

(c) Half-Bridge Circuit for strain gauges in full-probe

Figure 3.7 The circuit plate for Wheatstone bridge and the connections for both probes

3.3.2 Digital cameras

The deformation of the soil model when advancing miniature probes was observed by digital still cameras through the transparent Perspex window. Two 14.7 mega-pixel digital cameras (Canon PowerShot G10) with high pixel resolution were mounted in the container to obtain sub-surface soil movement data. The image-space field-of-

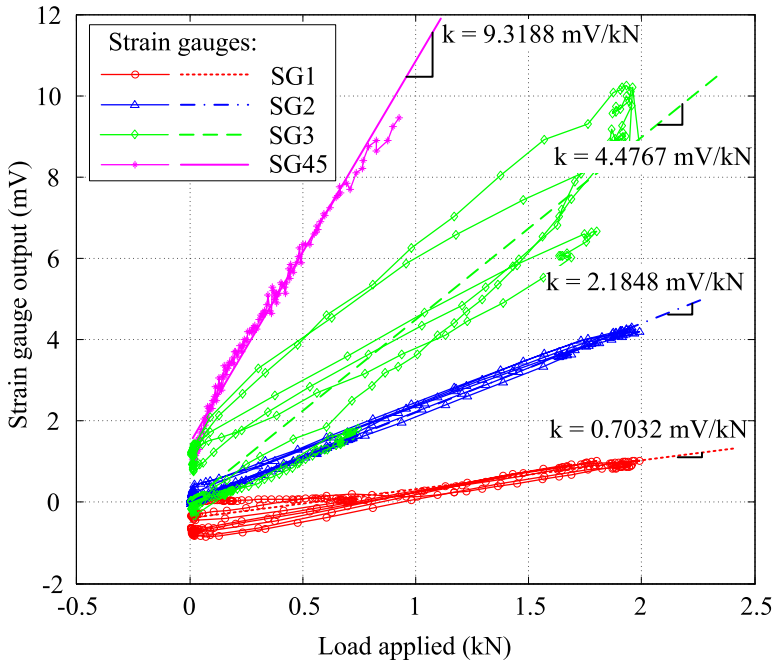

Figure 3.8 The results of strain gauge calibration tests for determination of calibration factors

view (FOV) of each camera was 4416×3312 pixels, while the FOV in object-space was about $163\,mm \times 115\,mm$. According to the theoretical GeoPIV precision proposed by White (2002), the precision error is less than $4 \times 10^{-4}\,mm$ when using a patch size of 80×80 pixels.

The locations of the cameras can be seen in Figure 3.1b and Figure 3.9. The cameras faced perpendicularly to the plane of the Perspex window, and the centre of the lenses pointed at approximately $5B$ (B is diameter of probe) to the left of the centreline of the window. This design attempts to ensure that the concerned area in the left-hand side was observed, and distortion of images in this area was minimised. As illustrated by Liu (2010), due to the axisymmetric nature of the model, the displacements on both sides of the probe are essentially similar, therefore measuring displacements on one side of the probe is sufficient. This reduced field of view results in better quality and resolution of the captured images. Figure 3.9a shows the elevation view that the two cameras. The cameras capture approximately $190\,mm$ of probe penetration when the heights of the cameras are $140\,mm$ and $250\,mm$ from the bottom of the tub.

The cameras interfaced with a rack mounted PC using a USB connection and were controlled using the PSRemote Multi-Camera software. This software offers functions like remote and simultaneous shooting, adjustment, and downloading of images. During

tests, the captured images were stored on the cameras $16\,GB$ memory card after digitization, compression and transmission, while the centrifuge rack PC was controlled remotely from the control room using Windows Remote Desktop. The frame rate was set to $0.2\,FPS$ (FPS: frames per second), which means that consecutive images represent a penetration of $4 \sim 6\,mm$. Two aluminium blocks were used to prevent the lenses from tilting caused by centrifugal force.

In order to provide bright and stable lighting conditions, a halogen light was installed above the container and a mirror placed at the bottom (see Figure 3.9a) to illuminate the viewing window. An array of 8×5 control points with spacing of approximately $30\,mm$, were painted onto the Perspex window within the cameras' FOV, as presented in Figure 3.9b. A fixed frequency grid distortion target sheet printed on Mylar and manufactured by Edmund Industrial Optics was used as the calibration target to precisely calculate the locations of the control points, as introduced by Take (2003). The control points were then used to determine the transformation parameters from each image (White, 2002).

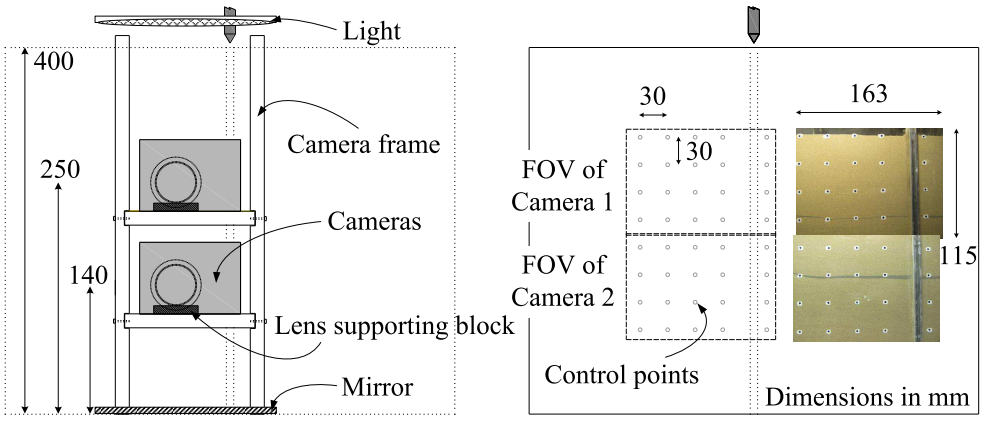

(a) Front view of cameras and lighting system (b) Control points on the Perspex window

Figure 3.9 Schematic of cameras, lighting and control points

3.4 Soil Model Preparation

3.4.1 Material properties

Due to the advantages of grain strength and its appropriate particle size, Fraction E silica sand, supplied by David Ball Ltd U.K., was used throughout the centrifuge tests.

It is a naturally occurring silica sand, sometimes referred to as Leighton Buzzard sand. The Fraction E sand is also referred to as 100/170 (Tan, 1990), which is named after British Standard sieves ($No.100$ sieve has aperture size of $150\,\mu m$, and the size of $No.170$ sieve is $90\,\mu m$). As reported by Prakongkep et al. (2010), scanning electron microscope (SEM) is a reliable method to examine the size and shape of grains. The SEM picture from Cabalar et al. (2010) (Figure 3.10a) shows that the sand grains are quite angular. According to *BS* 1881-131 : 1998 for Fraction E sand, at least 70% by weight falls between 90 and $150\,\mu m$, which is also validated by the particle size distribution curve from Tan (1990) using the dry sieving method (*BS* 1377 : 1990), as shown in Figure 3.10b. The properties of Fraction E sand are listed in Table 3.1 from Tan (1990). The void ratio is determined by $e = G_s \rho_w / \rho_d - 1$, and the relative density (D_R) is defined as $D_R = [(e_{max} - e)/(e_{max} - e_{min})] \times 100\,\%$, where ρ_d is the dry density of a sample and ρ_w is the density of water. The mechanical behaviour of Fraction E sand has been investigated by many previous researchers (e.g. Tan, 1990 and Bui, 2009).

As illustrated in Section 2.3.3, the deformation of soil is measured by tracking the soil element patches, which contains sufficient texture, in the subsequent image. Albeit the natural sand has inherent texture itself, the grain size is very small and the colour of sand particle is light brown, which result in little discernable texture for analysis using GeoPIV. To overcome this defect, approximately 5% of dyed Fraction E sand was mixed with clean sand to offer sufficient texture for tracking, as suggested by White (2002).

Table 3.1 Properties of the Friction E silica sand (Tan, 1990)

Property	Fraction E sand
Grain size d_{10} (mm)	0.095
Grain size d_{50} (mm)	0.14
Grain size d_{60} (mm)	0.15
Specific gravity G_s	2.65
Maximum void ratio (e_{max})	1.014
Minimum void ratio (e_{min})	0.613
Friction angle at constant volume (ϕ'_{cv})	32°

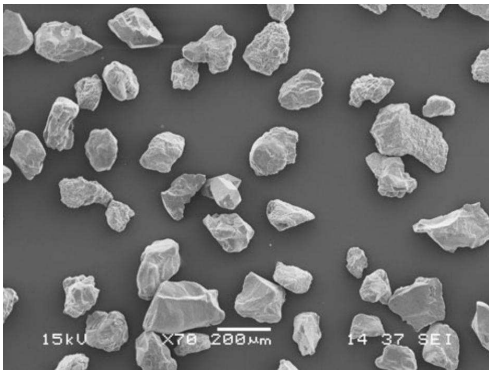

(a) SEM picture

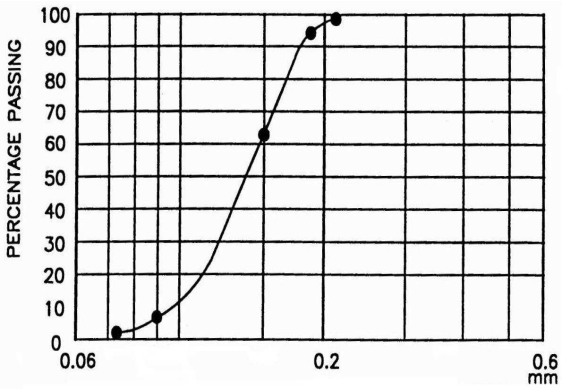

(b) Particle size distribution

Figure 3.10 (a) SEM picture (from Cabalar et al., 2010) and (b) particle size distribution (from Tan, 1990) for Fraction E silica sand

3.4.2 Soil preparation

To achieve granular soil models with certain uniform densities, a method of sand pouring was adopted to prepare soil samples for the centrifuge tests. In this project, the multiple-sieving air pluviation method (Miura and Toki, 1982; Zhao, 2008) was employed, with an achievable range of relative density between 50% and 90%. The single-holed sand pourer consists of sand hopper, nozzle and multiple sieves, as shown in Figure 3.11. The sand hopper can move vertically to adjust the drop height and horizontally to fit the size of container. The nozzle is a plate with a single hole, which can control the flow rate of sand pouring by adjusting size of hole. The flow rate is defined as the weight of sand which passes through the nozzle per unit time. Generally for a fine, uniformly graded silica sand, soil model with higher density is obtained with lower flow rate and larger drop height (Zhao, 2008).

Calibration tests were carried out by varying both the size of orifice and pouring height to check the uniformity and repeatability of the resulting samples. Two types of single-holed nozzle with hole diameters of $5\,mm$ and $9\,mm$ were used with average flow rates of $0.239\,kg/min$ and $1.048\,kg/min$, respectively. In Figure 3.12, a proposed relationship between flow rate and nozzle diameter is compared with the data provided by Zhao (2008).

It has been shown that the method of sand pouring has a high quality and repeatable soil preparation, in spite of some unavoidable experimental uncertainties (e.g. uniformity

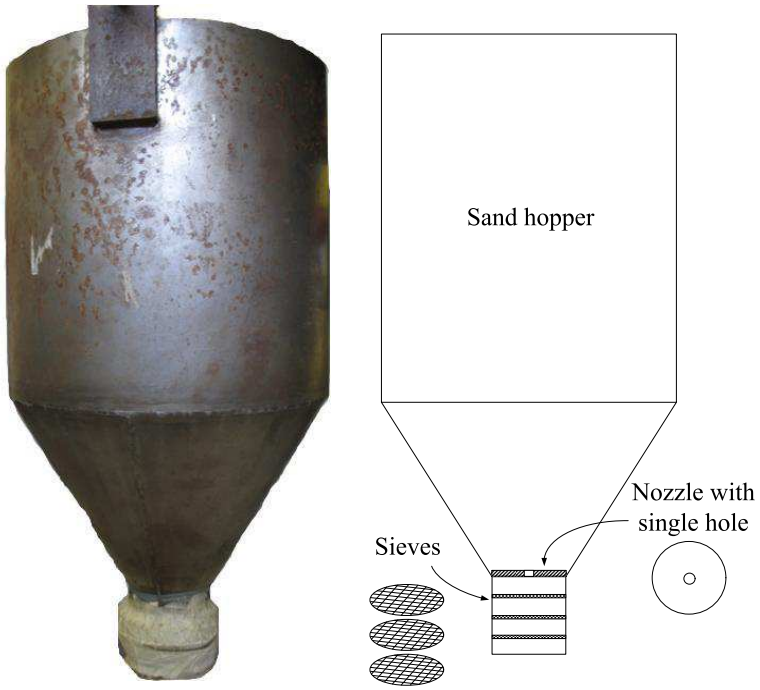

Figure 3.11 Schematic of the single-holed sand pourer

and heterogeneity of sample). Loose samples ($D_R = 50\,\% \pm 10\,\%$) were prepared using the large nozzle with pouring height of $0.5\,m$, while dense samples ($D_R = 90\,\% \pm 5\,\%$) could be achieved with the small nozzle with $1\,m$ of pouring height. The corresponding void ratios (e) for dense and loose sample are 0.653 and 0.814 respectively. It is worthwhile noting that the loose sample falls within the 'Medium dense' range ($D_R = 35\,\% \sim 65\,\%$) and the dense sample within the 'Very dense' range ($D_R = 85\,\% \sim 100\,\%$), based on *BS EN ISO* 14688-2 : 2004. The layered sand samples with different densities were also prepared in the same manner to form the stratified soil layers. Furthermore, the sand sample would be densified when placing the model onto the centrifuge platform and when increasing the acceleration levels. By calculating the depth of sample before and during flight, the dense samples were found to experience a volume densification of $0.4\,\% \sim 0.5\,\%$ (around $2\,\%$ increasing of D_R for dense sand), while the loose samples tended to be densified by $1.1\,\% \sim 1.3\,\%$ of volume, which had a increase of D_R at approximately $10\,\%$. The stress error between the centrifuge model and the prototype at $50\,g$ is under $4\,\%$ for both dense sand and loose sand samples with depth of $320\,mm$ and therefore considered acceptable (see Figure 3.13a). The predicted vertical stresses for dense sand ($D_R = 90\,\%$) and loose sand ($D_R = 50\,\%$) under $1\,g$ are also presented in Figure 3.13b.

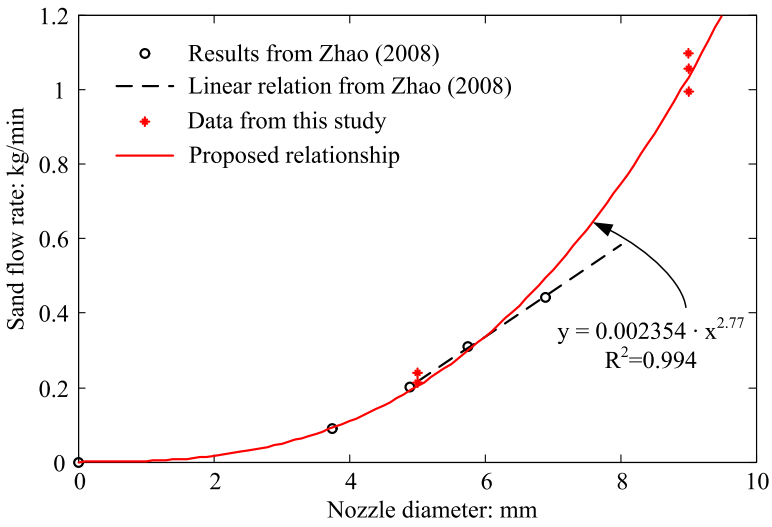

Figure 3.12 Sand pouring flow rate against nozzle diameter

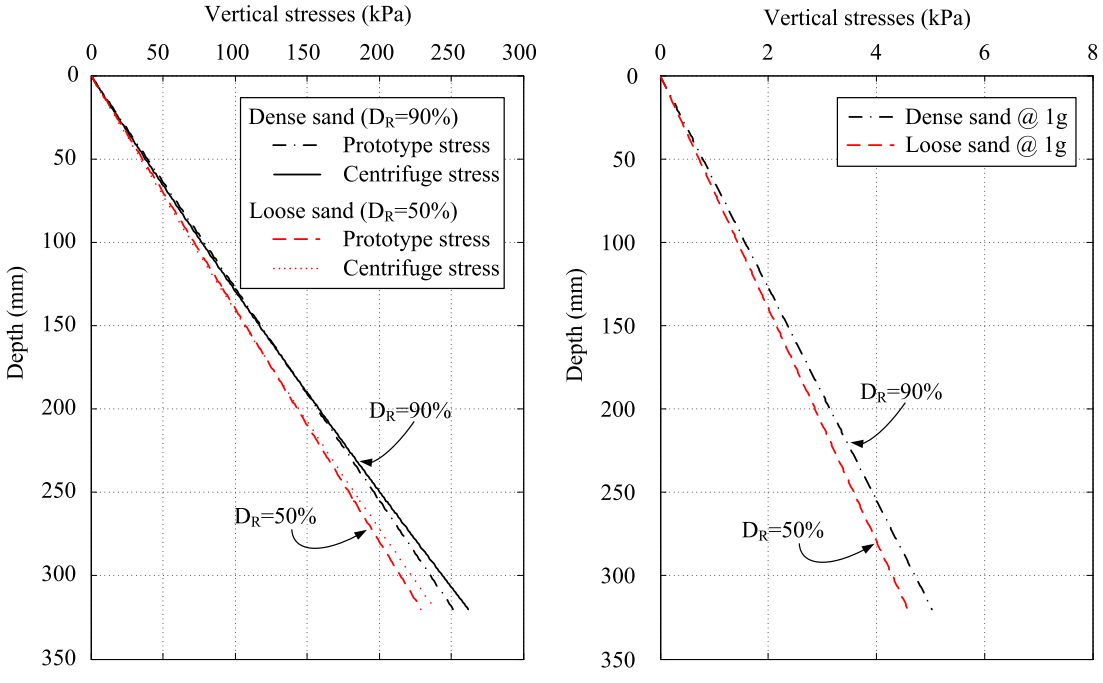

(a) Stress error in centrifuge (50g) (b) Predicted vertical stress @ 1g

Figure 3.13 Stress field at centrifuge and 1g condition

3.5 Testing Programme and Procedure

3.5.1 Testing programme

A summary of the two series of centrifuge tests is listed in Table 3.2. All of the penetration tests were performed at a constant speed of approximately $1\,mm/s$, corresponding to a quasi-static press-in process. The first stage, referred to as 'MP I', consists of five tests with different soil conditions tested at $50\,g$. Only half-probe tests with measurement of total penetration resistance were carried out during this stage. Some tests with similar soil profiles were conducted to validate the repeatability of the centrifuge tests. The tests in this stage differed slightly with each other due to the incrementally improved equipment. The quality of images for soil deformation measurement was improved through the camera settings and lighting during this stage. After manufacturing of the half-probe and the full-probe instrumented with strain gauges, the second stage 'MP II' started with a $1\,g$ test (MP II-01), validating the design of new probes and providing the effects of stress level. Following that, six centrifuge tests at $50\,g$ were carried out with half-probe test ('-HP'), full-probe tests ('-FP'), and then full-probe tests at $1g$ ('-FP-1g'). The test layout is shown in Figure 3.14, where full-probe tests were located to try to reduce the boundary and interaction effects.

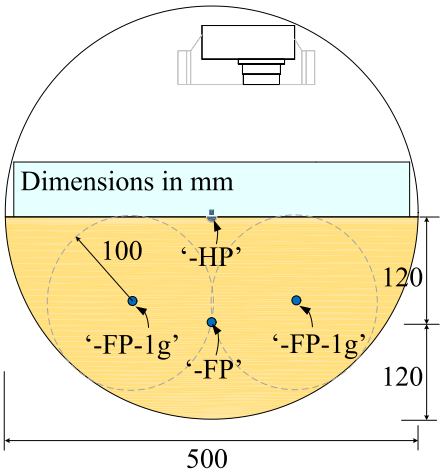

Figure 3.14 Test locations in plane view of the container

The soil samples of the centrifuge tests in both stages had different soil profiles, aiming to explore the layered effects during penetration. The details of layered samples with various densities and depths are summarised in Table 3.3, including two 3-layered samples with thin layers (MP II-06 and MP II-07). The uniform samples (e.g. MP II-

02 and MP II-03) served as references for the layered sample tests. In addition to penetration tests, all tests using the full-probe included a process of pull-out after a penetration of about 190 *mm*. The pull-out test for half-probe was only carried out for MP II-01-HP-1g and MP II-02-HP, owing to the tension strength of steel wires.

During stage 'MP I' three failed tests with bad quality of images are not included within the testing programme. For stage 'MP II' the results of penetration resistance of the half-probe suffered from one or more disabled signals from the strain gauges. The strain gauges 'SG2' and 'SG3' in Figure 3.4 were the most problematic ones, and were abandoned for the last four tests. In addition, some tests had problems due to bending moment at the head of half-probe, which meant the total load data was unusable. The details about the results of penetration resistance will be presented in Section 4.2.

Table 3.2 Summary of the centrifuge tests

Test ID	Testing Date	Soil Description	Half-Probe Test	Full-Probe Test	Full-Probe Test @ 1g
MP I-01	2011.10.06	Uniform Dense	MP I-01-HP	-	-
MP I-02	2011.11.28	Loose over Dense	MP I-02-HP	-	-
MP I-03	2012.01.18	Dense over Loose	MP I-03-HP	-	-
MP I-04	2012.02.21	Uniform Dense	MP I-04-HP	-	-
MP I-05	2012.03.20	Loose over Dense	MP I-05-HP	-	-
MP II-01	2012.11.21	Uniform Dense-1g	MP II-01-HP-1g	-	MP II-01-FP-1g
MP II-02	2013.04.03	Uniform Dense	MP II-02-HP	MP II-02-FP	-
MP II-03	2013.05.16	Uniform Loose	MP II-03-HP	MP II-03-FP	-
MP II-04	2013.07.31	Loose over Dense	MP II-04-HP	MP II-04-FP	MP II-04-FP-1g
MP II-05	2013.07.31	Dense over Loose	MP II-05-HP	MP II-05-FP	MP II-05-FP-1g
MP II-06	2013.08.14	Thin Dense Layer	MP II-06-HP	MP II-06-FP	MP II-06-FP-1g
MP II-07	2013.08.21	Thin Loose Layer	MP II-07-HP	MP II-07-FP	MP II-07-FP-1g

Table 3.3 Details of sample for each centrifuge test

Test ID	Soil Description	D_R of Soil 1 (%)	Depth of Soil 1 (*mm*)	D_R of Soil 2 (%)	Depth of Soil 2 (*mm*)	D_R of Soil 3 (%)	Depth of Soil 3 (*mm*)
MP I-01	Uniform Dense	81	320	-	-	-	-
MP I-02	Loose over Dense	88	179	61	134	-	-
MP I-03	Dense over Loose	41	188	92	130	-	-
MP I-04	Uniform Dense	90	317	-	-	-	-
MP I-05	Loose over Dense	93	228	48	90	-	-
MP II-01	Uniform Dense-1g	84	297	-	-	-	-
MP II-02	Uniform Dense	91	301	-	-	-	-
MP II-03	Uniform Loose	50	298	-	-	-	-
MP II-04	Loose over Dense	82	205	57	85	-	-
MP II-05	Dense over Loose	37	201	78	97	-	-
MP II-06	Thin Dense Layer	56	142	95	65	50	87
MP II-07	Thin Loose Layer	88	153	55	57	93	90

3.5.2 Testing procedure

All centrifuge tests were carried out at a constant acceleration of $50g$, and the general centrifuge test procedure is summarised as follows:

1. Prepare the container with three support braces and the first layer of Perspex window;
2. Affix the aluminium pieces into the channel in the second layer of Perspex window with control points using Loctite super glue;
3. Fill the slot of aluminium channel with silicone rubber compound;
4. Place the window into the container, seal the gaps with duct tape, and prepare for sand pouring;
5. Weigh the container, place under the hopper, set the nozzle size and pouring height;
6. Pour the sand to a desired depth, calculate the true value by averaging the measured depths at different locations, and measure the gross weight;
7. Repeat the steps 5 and 6 to pour layered sand sample after adding some dyed sand to identify the interface;
8. Move the container with the prepared sample onto the centrifuge platform, place camera assembly and light components;
9. Install the required instrumented probe into the actuator, and mount the actuator onto the container;
10. Connect the cables for cameras, lights, instruments (load cell, strain gauge, potentiometer) and actuator motor;
11. Adjust the settings of cameras using PSRemote Multi-Camera, and set up the programmes 'Acqlipse^{TM}' and 'LabVIEW' for data acquisition;
12. Spin the centrifuge package up to $160rpm$ (rpm: revolutions per minute) and keep the speed constant;
13. Take pictures simultaneously every 5 seconds, and penetrate the probe into the soil by about $190mm$. Conduct the pull-out process for relevant tests;

14. Slow down the centrifuge. Repeat some steps to carry out full-probe test and '-FP-1g' test;
15. Disconnect assemblies and take the container off from the swinging platform;
16. Empty the container and clean the aluminium channel for the next sample preparation;
17. Copy the images from the camera memory cards and data files from the Data Acquisition system for post analyses.

3.6 Chapter Summary

The centrifuge modelling methodology was described in this chapter for performing two series of centrifuge tests as part of this research. After introducing the experimental apparatus, the development of the instrumented probes for the axisymmetric model was detailed in Section 3.2 and 3.3. The properties of Fraction E sand were then presented and the method of sample preparation was described in Section 3.4. Finally, details of the two series of centrifuge tests and the testing procedure were described in Section 3.5.

Chapter 4

Results of Centrifuge Tests

4.1 Introduction

The results of centrifuge tests in uniform and layered soils (Section 3.5.1) are presented in this chapter. The experimental apparatus used for centrifuge testing were described in Section 3.2 and the procedure was detailed in Section 3.5.2. The main objectives of these tests with measurements of penetration resistance and soil deformation are to investigate the response of the penetrometer during installation and to identify the displacement mechanisms observed within the soil. The results of penetration resistance are provided in Section 4.2 and the results of soil displacements are presented in Section 4.3, followed by the results of strains during penetration (Section 4.4) and layered effects on soil deformation (Section 4.5). The effects of stress level, soil density and soil layering are investigated throughout the results. The investigation of soil displacements demonstrates the soil strain history during penetration for better understanding of the relevant mechanisms with penetration in layered soils.

The schematics of penetration resistance and soil deformation during installation are depicted in Figure 4.1. The total penetration load (Q_{total}) consists of two main parts: probe tip load (Q_{tip}) and shaft frictional load (Q_s). The cone tip resistance (q_c) equals Q_{tip} divided by the base area (A_b), and the average shaft friction ($\overline{\tau_s}$) is Q_s over the embedded shaft surface area (A_s), as illustrated in Equation (4.1). The depth of penetration is denoted as 'z' (see Figure 4.1a). Before measuring the soil deformation using GeoPIV, the location of soil elements around the probe is defined in a Cartesian coordinate system (XY) at the symmetric plane (i.e. window surface), as shown in Figure 4.1b. The origin is set at the surface of the soil where the probe enters the soil. Soil

horizontal and vertical displacements are referred to as Δx and Δy respectively, and soil displacements moving downwards and outwards from the probe are taken as positive. With regards to soil strains, a compression positive notation is used in this chapter, which is in contrast to that in Chapter 5. More details about the strains in an axisymmetric model are provided in Section 4.4. Unless stated otherwise, all results in this chapter are presented in model scale.

$$Q_{total} = Q_{tip} + Q_s = q_c \times A_b + \int_0^z \tau_s \times \pi B \, \mathrm{d}z = q_c \times A_b + \overline{\tau_s} \times A_s \tag{4.1}$$

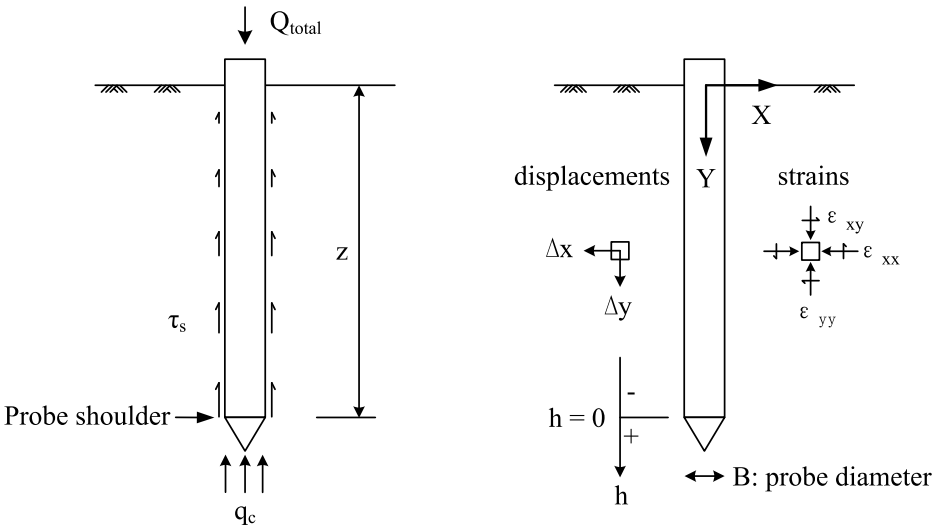

(a) penetration resistance (b) soil deformation

Figure 4.1 Schematics of penetration resistance and soil deformation

4.2 Results of Penetration Resistance

4.2.1 Variation with penetration depth

As described in Section 3.5, a prepared soil sample could be used for 'half-probe test','full-probe test' and '1g test'. Each test may consist of penetration and pull-out process, using a constant speed of approximately $1\,mm/s$. The results of an example test with uniform soil (MP II-02) are presented first to illustrate the data processing procedure. The penetration loads recorded by the load cell and strain gauges are given in Figure 4.2 for half-probe test (MP II-02-HP) and full-probe test (MP II-02-FP), respectively. Both penetration and pull-out tests were carried put in a uniform dense sand ($D_R = 91\,\%$) under $50\,g$. 'Load cell' provides the data of total penetration load (Q_{total}), whilst 'SG1', 'SG2' and 'SG45' are from the data recorded by the strain gauges (see

Figure 3.4 and Figure 3.5). 'SG1' represents the half-probe tip load, while the combined 'SG45' gives the full-probe tip load. However, 'SG2' and 'SG3' were affected by bending effects and did not provide sufficient resolution to evaluate the loads along the shaft. Care should be taken to evaluate the raw data from the strain gauges, as some scattered results contaminated by unpredictable factors were removed or smoothed.

As the probe is inserted into the soil, it is notable that both total load and tip load for '-HP' and '-FP' tests generally increase linearly with time (i.e. depth). 'Load cell' and 'SG2' are consistent with each other until significant bending occurs at a later penetration stage. After the process of penetration, the load reduces to a stabilised value by approximately 10 %. This part of reduced load implies the dissipation of stresses at the cone tip and shaft surface. It is likely due to the effect of motion at a constant speed when the probe comes to a halt. The redistribution of stresses around the probe and creep effects would also reduce the loads during the stop. The pull-out test starts with an immediate disappearance of compressional loads, whereas 'SG2' in half-probe test and 'Load cell' in full-probe test experience tensional loads, which attribute to the reverse of friction along the embedded shaft. The tensional loads decrease with the reduction of horizontal stress on shaft and the effective shaft area.

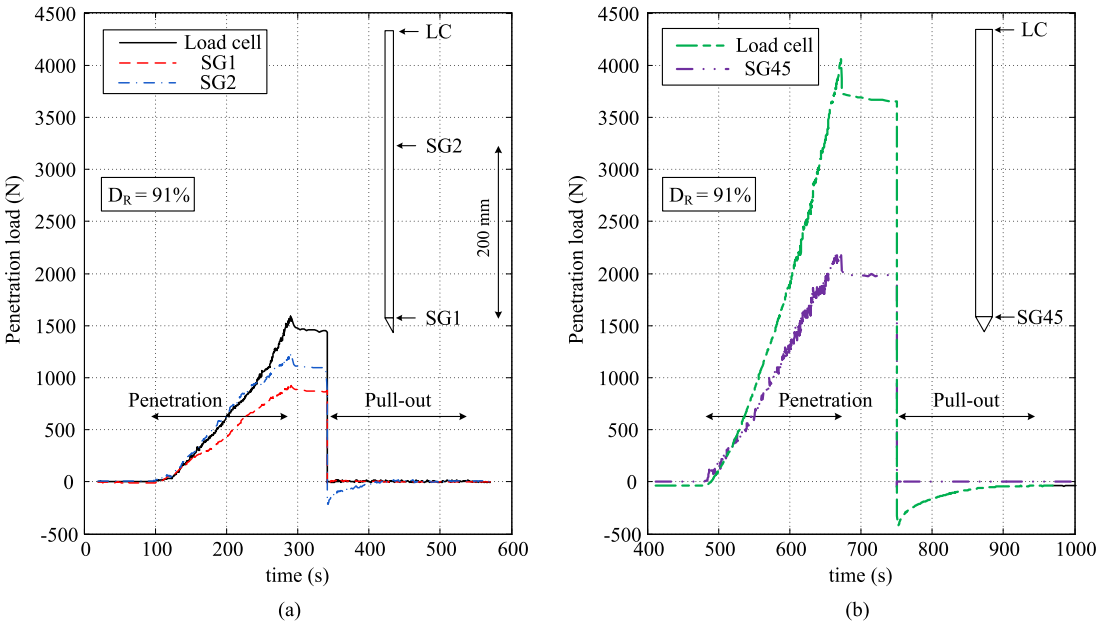

Figure 4.2 Penetration loads against time: (a) MP II-02-HP; (b) MP II-02-FP

Similarly, the load-displacement curves are shown in Figure 4.3a for both half-probe

test and full-probe test. For the total load from full-probe test, the magnitude of compression and tension recorded by the load cell is comparable with the results provided by Deeks and White (2006), as shown in Figure 4.3b. The typical test carried out by Deeks and White (2006) used a '12 *mm*' probe in Fraction E sand ($D_R = 105\,\%$) under the same stress condition ($50\,g$). The results from two centrifuge models are essentially identical, which in turn verify the consistency and reliability of the load measurements. On the other hand, the boundary effect for full-probe test ($D/B = 20$) is shown to be limited, as D/B is about 26 in Deeks and White (2006).

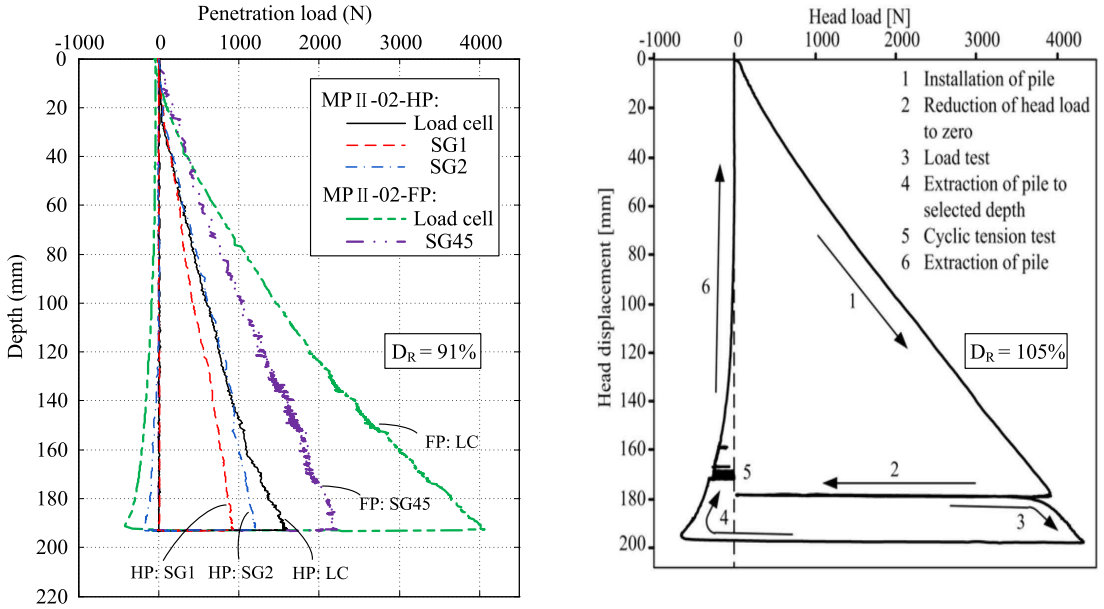

(a) results from MP II-02

(b) results from Deeks & White (2006)

Figure 4.3 Penetration resistance for tests of MP II-02, and a comparison with a typical test from Deeks and White (2006)

To evaluate the relevance between resistance and in-situ stress, dividing the tip loads by corresponding base areas gives the tip resistances, as shown in Figure 4.4. The results of half-probe test and full-probe test have good agreement with each other. The resistance of full-probe is slightly larger than that of half-probe, owing to the boundary effects at the centre of the sample and the slightly densified sample caused by the insertion of the half-probe and spin-down / up of the centrifuge. During the first penetration of half-probe, the soil stress state is increased around the half-probe. The locked-in stress condition (rather than the initial stress) in turn influences the results of the second penetration of the full-probe. Approximately $5 \sim 10\,\%$ larger tip resistance was found for tests of 'MP II-02' (Figure 4.4). The difference between total penetration

load and tip load rests with the shaft friction, which is further explored in Section 4.2.2.

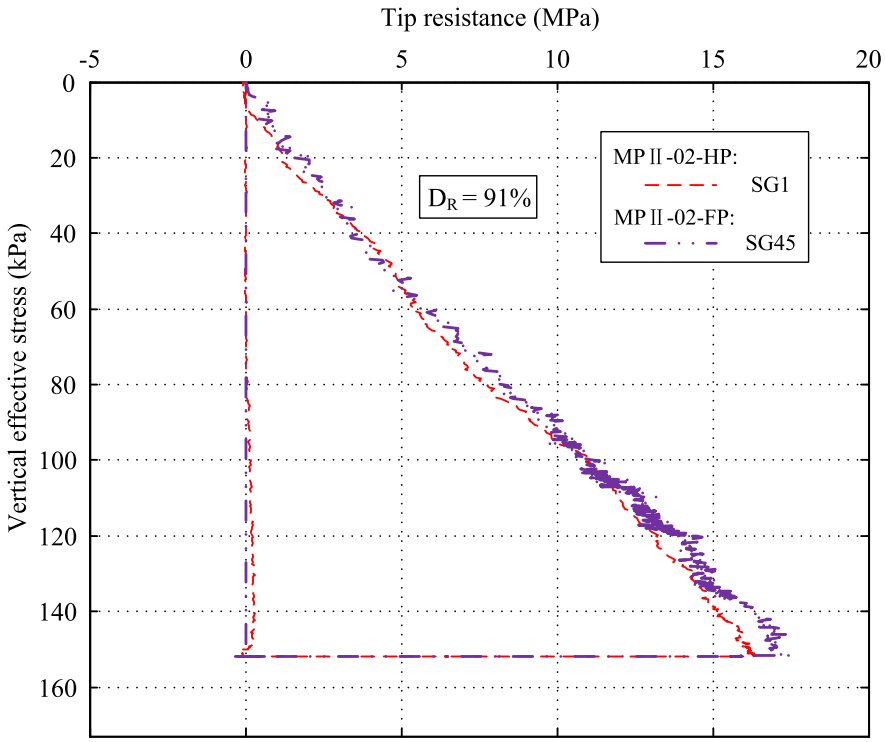

Figure 4.4 Tip resistance against vertical effective stress for tests of MP II-02

4.2.2 Variation with soil density

Apart from the effect of stress gradient, soil density is one of the important parameters affecting the results of penetration resistance, as reported by Jamiolkowski et al. (2003); Tatsuoka et al. (1990); Gui et al. (1998). The relative density of soil, associated with soil behaviour (e.g. compressibility, dilatancy), leads to the pattern of distorted stress/strain field around the probe and consequently the penetration resistance. Although the steady state of penetration resistance was not achieved for stiff silica sand in the centrifuge tests, the variation with soil density is examined by the two series of centrifuge tests. Figure 4.5 shows the results of total load (Q_{total}) for all half-probe tests. The soil samples are dry sand with different relative densities and layered profiles, as described in Table 3.3 (Section 3.5.1). In spite of the effects of friction from the guiding bar and the window boundary, the results from tests with similar D_R (e.g. MP I-01-HP, MP I-04-HP and MP II-02-HP) exhibit essential consistency, illustrating the repeatability of penetration and the homogeneity of the sample. Both dense sand and loose sand have linear increases of total load with depth. However, the value of dense

sand ($D_R = 90\,\%$) is about $2 \sim 3$ times that for loose sand ($D_R = 50\,\%$). For layered soils, the curves are influenced by the soil beneath and above the cone tip as the probe penetrates through the interface. More about the layered effects will be presented in Section 4.2.4.

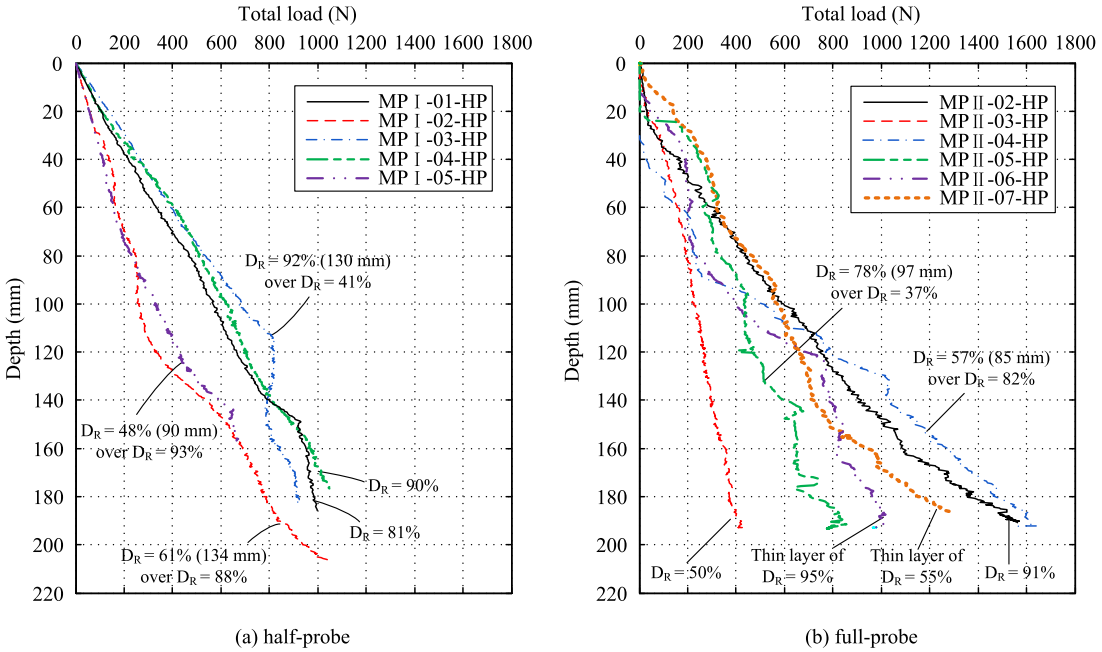

Figure 4.5 Total load using half-probe for penetration tests: (a) MP I; (b) MP II

4.2.2.1 Tip resistance

Tip resistance (q_c), as a direct indication of the strength and stiffness of the soil, is shown in Figure 4.6 with comparisons of half-probe test and full-probe test in the same soil samples. For the tests with uniform soil, the linearly increasing q_c is also observed for both half-probe test and full-probe test. The layered effects from q_c in half-probe tests can be observed. However, comparing to the uniform soil tests (MP II-02-HP and MP II-03-HP), the trends from one layer to another overstate the curves from uniform soils, which serve as references. It may be attributed to the single strain gauge ('SG1') in the half-probe, which is susceptible to ambient changes of soil behaviour. On the other hand, the full-probe tests provide more reliable results of q_c, for both uniform and layered samples. Therefore the analysis of penetration resistance later is based on the tests using the full-probe.

With the assumption of linear increase of tip resistance q_c, loose sand ($D_R = 50\,\%$)

exhibits a rate of roughly $26.3\,kPa/mm$ and dense sand ($D_R = 90\,\%$) increases at approximately $84.2\,kPa/mm$. It should be noted that the increase rate for loose sand decreases after about $90\,mm$ of penetration, whereas the gradient for dense sand increases gradually to a small extent, also shown in Figure 4.7. The concave shape of q_c-$depth$ curves for dense sand was also observed by White (2002), for Fraction B sand in a surcharged calibration chamber (plane strain model). The effect was attributed to the influence of the rigid bottom boundary, as reported by Klotz and Coop (2001). As to centrifuge tests, Lee (1990) proposed a relationship for the limit bottom effect ($X/B = 0.1139 \times D_R + 1.238$). The distance from the cone tip to the bottom (X) is approximately $110\,mm$, which is smaller than $146\,mm$, as required by Lee (1990) for $D_R = 90\,\%$. On the contrary, no bottom effect occurs for loose sand, as the required distance is $88\,mm$ for $D_R = 50\,\%$.

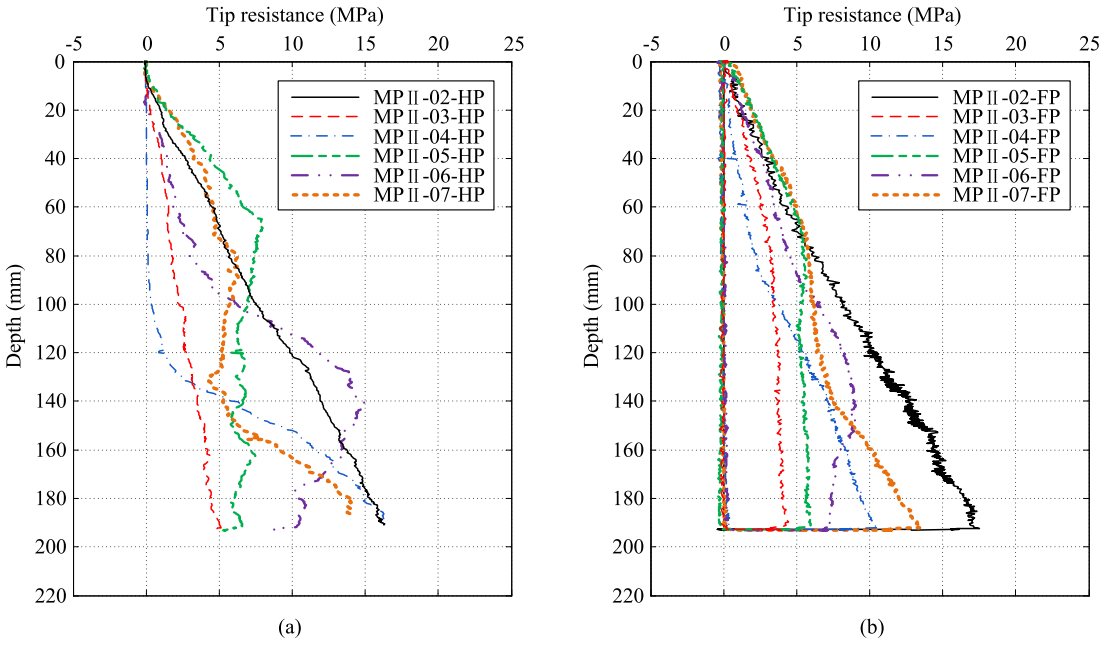

Figure 4.6 Tip resistance for tests of MP II using: (a) half-probe; and (b) full-probe

Bolton et al. (1993) proposed a dimensional analysis of CPT results from centrifuge tests, based on the observed linear relationship between the tip resistance (q_c) and vertical effective stress (σ'_{v0}), consistent with the cone factor in sand from bearing capacity analysis ($N_q = q_c/\sigma'_{v0}$). Similar trends were also found in Bolton et al. (1999); Deeks and White (2006); Xu (2007). The normalised cone tip resistance (Q) and the normalised penetration depth (Z) are defined in Equation (4.2) and (4.3).

$$Q = \frac{q_c - \sigma'_{v0}}{\sigma'_{v0}} \tag{4.2}$$

$$Z = \frac{z}{B} \tag{4.3}$$

Nevertheless, non-linear relationships between q_c and σ'_{v0} obtained from calibration chamber tests are widely accepted for CPT interpretation (e.g. Baldi et al., 1986; Kokturk, 1993; Robertson and Wride, 1998; Jamiolkowski et al., 2003). One of the popular definitions of stress-normalised cone tip resistance is q_{c1N}, as illustrated in Equation (4.4) (after Robertson and Wride, 1998), indicating that q_c increases at a decreasing rate with depth.

$$q_{c1N} = \frac{\left(q_c - \sigma'_{v0}\right)/\sigma_{atm}}{\left(\sigma'_{v0}/\sigma_{atm}\right)^{0.5}} \tag{4.4}$$

where σ_{atm} is the reference pressure $= 100\,kPa$; sometimes the net tip resistance ($q_c - \sigma'_{v0}$) is replaced by q_c in the literature.

Figure 4.7 presents the normalised cone tip resistance using both definitions. Compared to q_{c1N}, Q is a more appropriate normalisation to achieve a constant value, despite some curvature for uniform sand tests. Nevertheless, it is likely that loose sand without bottom effect reaches a constant value in q_{c1N}-Z curve. Generally, Q for loose sand ($D_R = 50\,\%$) varies between $30 \sim 60$, and dense sand ($D_R = 90\,\%$) has $2 \sim 3$ times greater value with $Q \approx 90 \sim 110$. Taking the results of uniform sand tests as references, layered effects are noticeable from the Q-Z curves for layered tests, as will be discussed in Section 4.2.4.

4.2.2.2 Shaft friction

Shaft friction load (Q_s) can be achieved by subtracting cone tip load Q_{tip} from total load Q_{total}, as defined in Equation (4.1). $\overline{\tau_s}$ represents the average shaft friction over the embedded shaft surface area. Figure 4.8 exhibits the results for uniform sand tests (MP II-02-FP and MP II-03-FP). Figure 4.8a shows Q_s-$depth$ curves for both penetration and pull-out tests. The trend increases linearly for loose sand, with a rate of

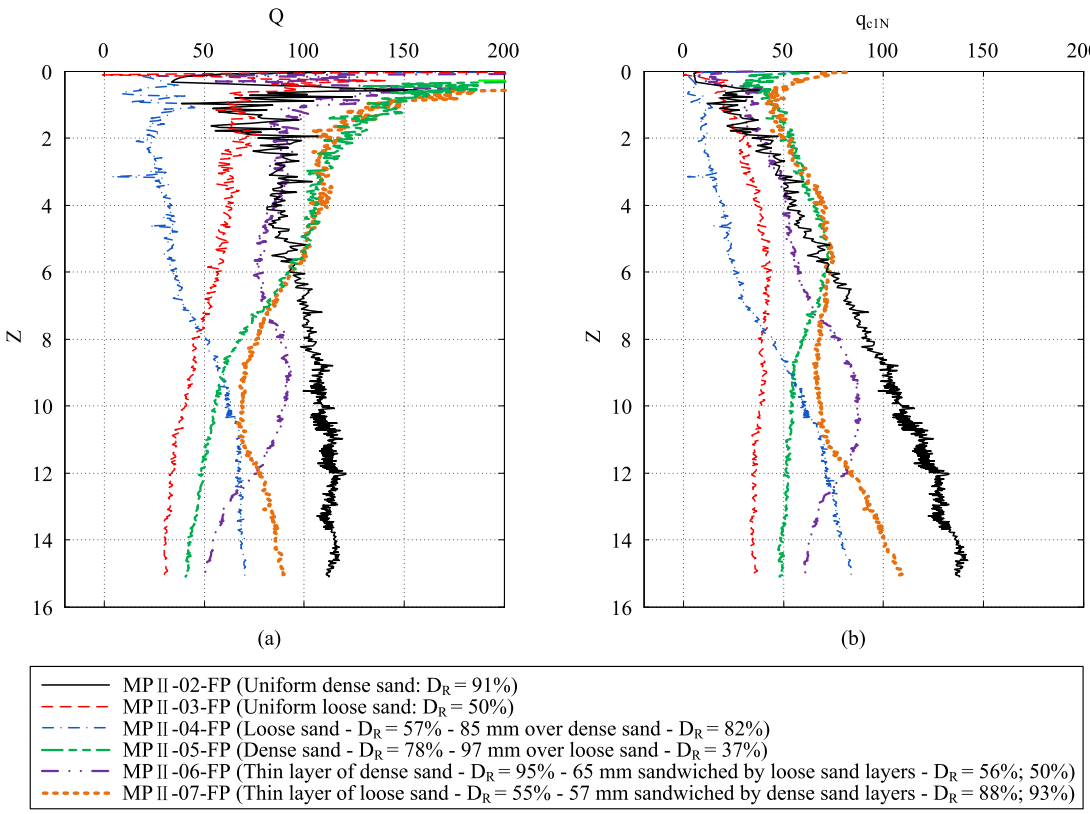

Figure 4.7 Normalised cone resistance for tests of MP II using full-probe

$1.84 N/mm$. However, dense sand has a concave shape, and the magnitude of Q_s is over 3 times larger than that of loose sand. The friction load percentage (Q_s/Q_{total}) shown in Figure 4.8b, varies between $20 \sim 40\,\%$, where dense sand has a slightly larger value than loose sand. This ratio is essentially comparable to that found in the results of Deeks (2008), where $Q_s/Q_{total} \approx 23\,\%$. The average shaft friction $\overline{\tau_s}$ in Figure 4.8c gives development of the frictional resistance. Similar to tip resistance shown in Figure 4.6b, loose sand tends to level off and dense sand gradually increases.

4.2.3 Variation with stress level

As presented in Section 4.2.2, the results indicate that q_c of a penetration test is proportional to σ'_{v0}, in some manner. The centrifuge increases the stress level by a factor of N, compared to geostatic stress by earth gravity. The effect of stress level ($50g$ and $1g$) is investigated in this section. Figure 4.9 exhibits the comparisons of Q_{total} and q_c of full-probe tests in $50g$ and $1g$. The magnitude of $50g$ tests is around $10 \sim 12$ times that from $1g$ tests, which is less than the centrifuge factor ($N = 50$). The resistances increase with stress level at a decreasing rate, as reported by Lee (1990). This

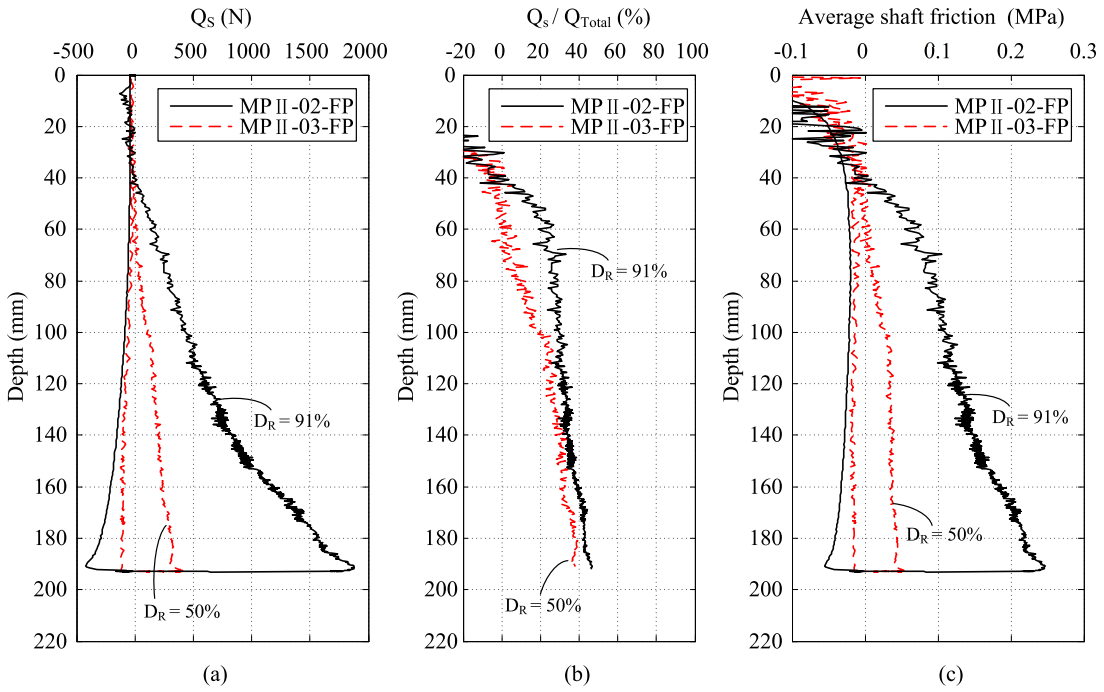

Figure 4.8 Shaft friction for uniform sand tests: MP II-02-FP and MP II-03-FP

phenomenon was also observed by Gui et al. (1998), where Q fell as g-level rose. This is presumably attributed to the effects of dilatancy and particle crushing as high stress level is applied. As mentioned by Lee (1990), dilatancy effect is suppressed under high confining stress, as well as the operative friction angle. Particle breakage around the cone tip is enhanced with stress level, as illustrated by Jamiolkowski et al. (1985) and observed by White and Bolton (2004). The results indicate that the penetration resistance is not proportional to the stress level, although the resistance at each stress gradient increases linearly with depth (Figure 4.7).

4.2.4 Layered effects on penetration resistance

Section 2.2.2 outlined the layered effects when inserting a probe into stratified soils. The transition of cone tip resistance from one soil layer to another is evaluated by the cone tip resistance ratio, η', as defined in Equation (4.5), where $q_{c,w}\,(Q_w)$ and $q_{c,s}\,(Q_s)$ represent the resistances in uniform weak soil (i.e. loose sand) and strong soil (i.e. dense sand). Figure 4.10 exhibits the interpretation of MP II-04-FP. The normalised resistance curve for uniform soil is modified from the results of MP II-02-FP and MP II-03-FP (Figure 4.10a). η' from loose sand ($D_R = 57\,\%$) to dense sand ($D_R = 82\,\%$) is shown in Figure 4.10b against the relative distance to the soil interface

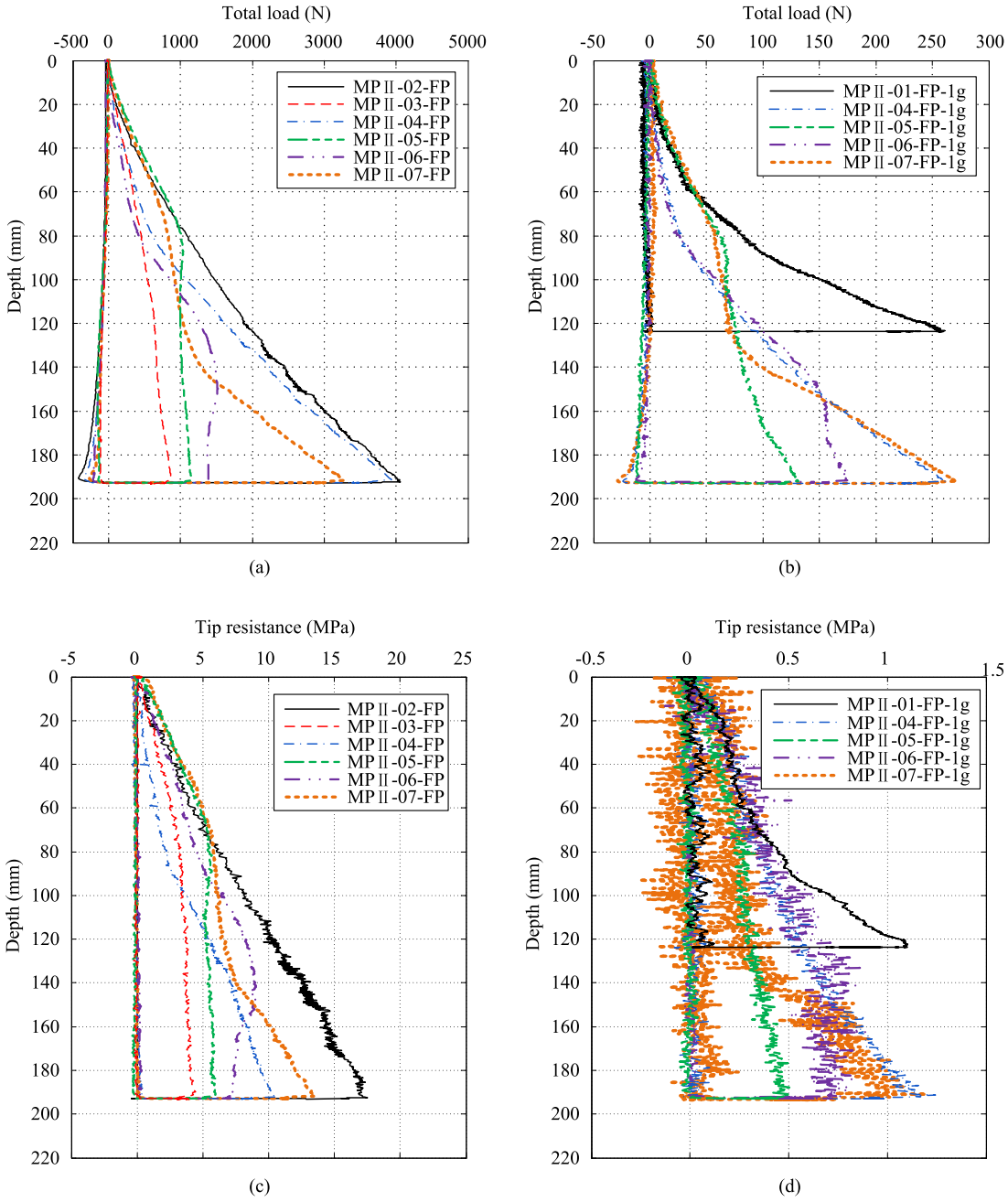

Figure 4.9 Comparisons of total load and tip resistance of full-probe tests in: (a, c) 50g; and (b, d) 1g

(H/B). The normalised resistance is scattered near the surface as shown in Figure 4.7a, which results in the unreasonable value of η' (e.g. η' is less than 0 for MP II-04-FP). In spite of the surface effects, the general transformation of η' from 0 to 1 is observed. In addition, a smoothed curve is obtained by curve fitting using Equation (4.6), which varies between 0 and 1. The influence zones above and below the interface (Z_w and Z_s) are defined as 5% beyond the uniform soil resistance (i.e. the influence zone in η' curve is $0.05 < \eta' < 0.95$). For MP II-04-FP, the zone of influence in loose sand is about $2B$ and $Z_s \approx 4B$. It is apparent that the transition zone in stronger soil is larger

than that in weak soil, which means that it takes a greater distance to develop the resistance in a dense sand than in a loose sand. Also, when penetrating a probe from a dense sand into a loose sand, the resistance is affected by the underlying soil at a longer distance above the soil interface, indicating that the loose sand layer is relatively more sensitive to be detected.

$$\eta' = \frac{q_c - q_{c,w}}{q_{c,s} - q_{c,w}} \approx \frac{Q - Q_w}{Q_s - Q_w} \tag{4.5}$$

$$\eta' = \frac{1}{1 + S_1 \times exp\,(S_2 \times H/B)} \tag{4.6}$$

where S_1 and S_2 are curve fitting parameters which are related to the soil properties of both soil layers. Due to the limited centrifuge tests, the correlations of S_1 and S_2 are not available; however, the range of the parameters can be provided as: $1.7 < S_1 < 5.4$ and $-0.5 < S_2 < -0.3$. Both S_1 and S_2 increase with the relative density of dense sand layer and decrease with the relative density of loose sand layer.

Figure 4.11 presents the curves of cone tip resistance ratio for both two-layered soils (MP II-04-FP and MP II-05-FP) and three-layered soils (MP II-06-FP and MP II-07-FP). The curving fitting lines are provided in Figure 4.11a. When the probe is pushed from dense sand into loose sand, η' transforms from 1 to 0, and the transition zone is located more to the side of the dense sand ($Z_s \approx 5B$; and $Z_w \approx 1B$). This contrasts with the test from loose sand to dense sand, where $Z_s \approx 4B$ and $Z_w \approx 2B$. The layered effects in multi-layered soils are notable in Figure 4.11b, where H_t is the thickness of the sandwiched soil layer. MP II-06-FP is the test with dense sand sandwiched by loose sand layers. Because of the large influence zone in stronger soil, the resistance in dense sand is affected by both of the loose sand layers, resulting in the maximum resistance ratio smaller than 1 ($\eta'_{max} \approx 0.6$). By contrast, for MP II-07-FP, the sandwiched thin layer is loose sand, and the minimum resistance ratio is slightly larger than 0, owing to the relatively small transition zone in weak soil.

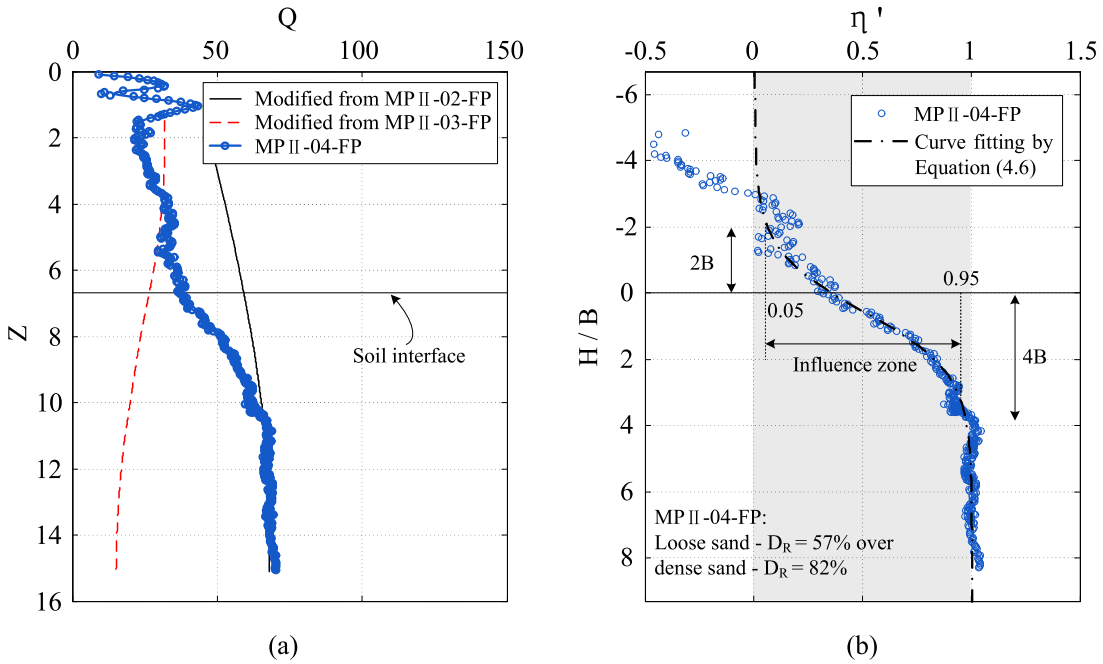

Figure 4.10 Layered effects for test: MP II-04-FP

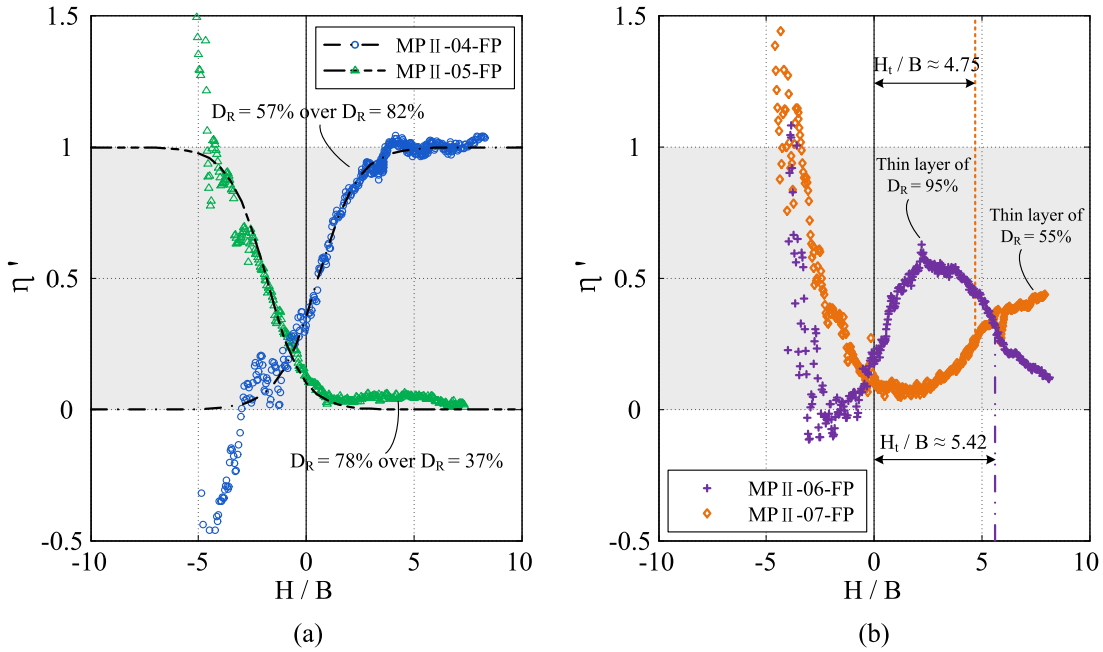

Figure 4.11 Layered effects for tests with: (a) two-layered soils; and (b) three-layered soils

4.3 Results of Soil Displacements

One of the main objectives of the centrifuge tests presented in this chapter is to evaluate the distribution of displacements and strains associated with the installation of probes in uniform and layered soils. The distributions of soil deformation around the penetrometer provide insights into the mechanisms that are responsible for the probe resistance data as the cone passes between soil layers.

As introduced in Section 2.3.3, soil deformation caused by the penetration is precisely measured based on a series of digital images. The cameras and relevant components were detailed in Section 3.3.2. A Matlab-based programme 'GeoPIV', developed by White et al. (2003), is adopted to analyse the soil displacements in object-space (along the symmetric plane), as discussed in this section.

Using the GeoPIV analysis, soil element patches were created by meshing within the field of view in image-space. A patch size of 80 pixels represents a nominal size of $2 \sim 3\,mm$ in object space, according to a particular transformation. As a result the location and size of each patch in object-space is disordered and inconsistent corresponding to the coordinate system defined in Figure 4.1. In addition, due to the full cycle of consecutive shooting (image capture, conversion, compression, transmission), images were not taken at strictly identical pace (every penetration of approximately $4 \sim 6\,mm$).

Therefore, in order to normalise for convenient deformation analysis, the raw GeoPIV data was interpolated to a regular soil mesh in the 'XY' system with a grid spacing of $1 \times 1\,mm$ ($X = -6 \sim -120\,mm; Y = 0 \sim 200\,mm$), as well as the process of penetration with $1\,mm$ per step. Strains were then deduced from the displacements based on this re-established mesh. The results of soil displacements are shown in this section and strains are subsequently presented in Section 4.4, followed by the analysis of layered effects on soil deformation (Section 4.5).

As a probe advances into ground, soil particles are pushed away to accommodate the probe and are simultaneously dragged downwards owing to shearing at the soil-probe interface. The soil around the probe is squeezed or dilated, and consequently the con-

fining stress is built up to in turn act on the probe. The results of displacements in this section are focused on the tests with uniform sand (MP II-02 and MP II-03), which give the effects of variation with penetration depth and relative density of soil, and also serve as reference for later investigation of stress level effects and layered effects on soil deformation. The profiles of displacements are illustrated separately as: cumulative displacement field; instantaneous displacement field; soil element trajectories; streamlines and soil element paths.

4.3.1 Cumulative displacement field

A good indication of soil deformation is to describe the displacement pattern around the penetrometer, which involves large horizontal and vertical movements. The contours of cumulative displacements around the penetrometer are plotted in Figure 4.12 and Figure 4.13 to reveal the displaced soil fields after 160 mm of penetration for dense sample and loose sample. As the cameras were faced to the left side of the penetrometer (Section 3.3.2), the results are focused in this concerned area within the 'X Y' coordinate system. The area close to the centreline of the probe ($X = 0 \sim -6\,mm$) is not included due to the existence of the aluminium channel (Section 3.2.3) and the approached probe. Since very little displacement was observed in the far field ($X/R > 10$, as noted by White, 2002; R is the probe radius, $= B/2$), only the contours in the near field around the centreline of the probe are presented ($X = -6 \sim -60\,mm$). Horizontal displacement (Δx), vertical displacement (Δy), and total displacement are shown separately in these two figures, with labels indicating the corresponding displacement in mm. Total displacement on the symmetric plane is simply calculated by $\sqrt{\Delta x^2 + \Delta y^2}$.

In Figure 4.12, both horizontal and vertical displacements differ slightly with depth around the probe shaft, except for the surface effects at the shallow soil ($Y < 90\,mm$). The profile of total displacement around the probe has a similar shape with the plastic zone sketched by Huang et al. (2004) using finite element analysis of cone penetration in cohesionless soil. This deformation pattern shows reasonable similarity to cylindrical cavity expansion around the shaft, and spherical expansion around the cone, as discussed by Lunne et al. (1997) and Yu (2006).

When the results of dense sand (Figure 4.12) and loose sand (Figure 4.13) are com-

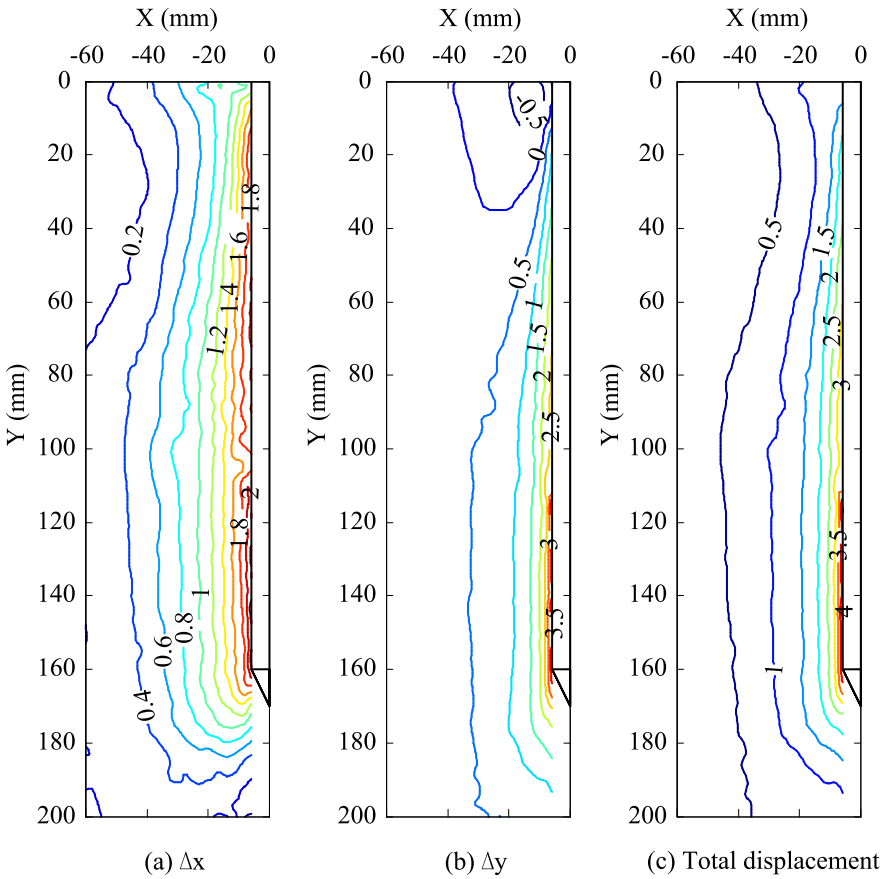

Figure 4.12 Cumulative displacement contours of MP II-02 (160 *mm* of penetration in dense sand: $D_R = 91\%$): (a) Δx; (b) Δy; (c) total displacement

pared, a similar deformation pattern is observed though the magnitude of displacement in loose sand is slightly smaller. The influence zone of displacement in dense sand is larger than that in loose sand. In consideration of the same size of penetrated probe, the total displacing soil equals the volume of the probe. It is conceivable that more significant displacement occurs immediately adjacent to the probe in the loose sample, and the soil within the smaller influence zone is more compressed than dense sand. The contours in loose sand (Figure 4.13) vary with depth more than that in dense sand, owing to the less uniform soil in the loose sample. One of the large differences between contours of dense and loose sample is the surface effects. It takes about 90 *mm* ($7.5B$) to reach a steady displacement profile in dense sand, whereas the distance in loose sand is relatively less, around 60 *mm* ($5B$).

Another significant difference can also be observed from the axial displacement (Δy). Soil is heaved near surface with penetration for the dense sample, as the elements above the contour line '$\Delta y = 0$' (area: $|X| < 40\,mm$; $Y < 35\,mm$) move upwards. In contrast,

no upwards movement is observed in the loose sand test; but indentation occurs near the surface. It is conceivable that the difference of surface effects can be attributed to the fact that dense sand tends to be displaced (compression is somehow compensated by the dilatant behaviour) and loose sand is relatively more compressible. The large deformation zone in Δy is found in deep location for dense sand, whilst this zone is more concentrated on the upper soil ($Y < 90\,mm$) for loose sample.

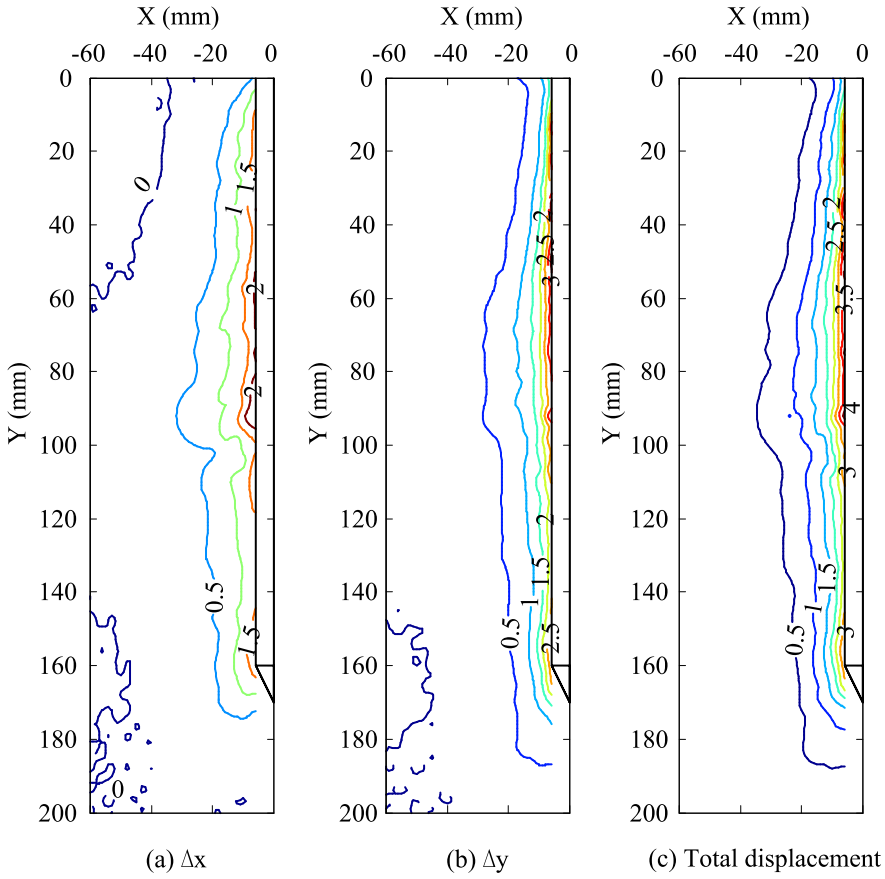

Figure 4.13 Cumulative displacement contours of MP II-03 (160 *mm* of penetration in loose sand: $D_R = 50\,\%$): (a) Δx; (b) Δy; (c) total displacement

Figure 4.14 offers the profiles of Δx and Δy for columns of soil elements with different distances to the centreline of the probe. The distance has been normalised by the probe radius (6 *mm*), and the five columns are noted as $X/R = 2, 3, 4, 5, 6$. The results of displacements are also normalised by R, which exhibit the relative radial and axial displacements ($\Delta x/R$; $\Delta y/R$) away from the probe. The downwards displacement $\Delta y/R$ on the left side of the figure is shown as negative in order to distinguish from $\Delta x/R$ presented on the right side. The results of both dense sand and loose sand are shown in Figure 4.14 with cumulative displacements after 160 *mm* of penetration.

Apparently, soil closer to the probe has greater lateral and axial displacements. For soil elements near the surface, displacements increase with depth, and $\Delta y/R$ in dense sand grows sharper than the others which reverses from heave to downwards movement. Steady displacement profiles of dense sand are again shown here below $90\,mm$. For soil below $160\,mm$ where probe has not passed, the influence zone ahead of the cone extends beyond this field of view ($200\,mm$), and the size of influence zone for dense sand is larger than loose sand. It also shows that for dense sand Δy is fully developed for soil approximately $2\,R$ below the probe shoulder and Δx is fully developed for soil less than $1\,R$ below the probe shoulder, whereas no clear trend of fully displaced soil is found for loose sand.

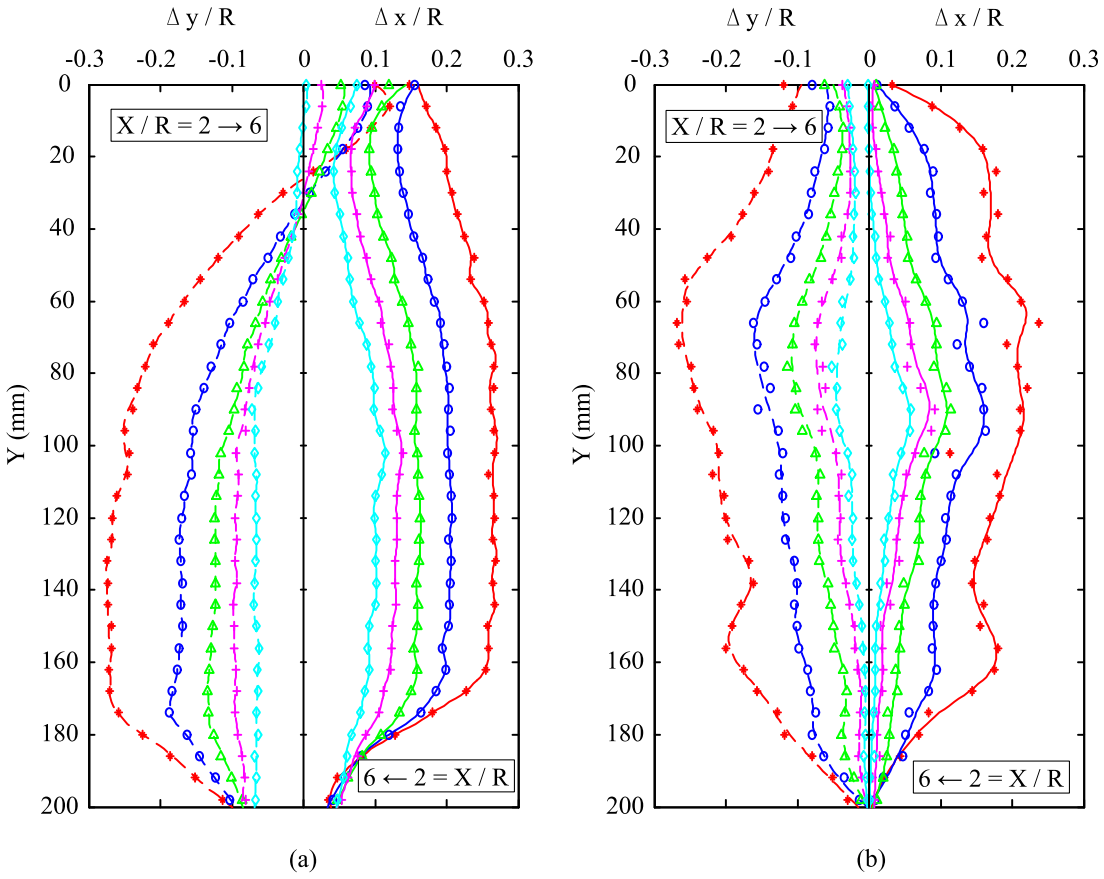

Figure 4.14 Cumulative displacement profiles with variation of horizontal distance to the probe after $160\,mm$ of penetration: (a) Dense sand: $D_R = 91\,\%$; (b) Loose sand: $D_R = 50\,\%$

The histories of the soil displacements for a single column of soil elements ($X/R = 2$) during different stages of penetration are illustrated in Figure 4.15. The variation of penetration depth is described as Z ($Z = z/B$, as defined in Equation 4.3 in Section

4.2.2), which varies as $Z = 2.5, 5.0, 7.5, 10.0, 12.5$. This figure offers the developments of the displacements during penetration. It is notable that most of the displacements are generated before the probe passes, and the displacement developed after probe passes can hardly be observed. With relatively shallower penetration, the influence zone ahead of the probe can also be measured. For dense sand, over 80 *mm* below the cone is affected to experience vertical displacement, and radial displacement starts to occur at 50 *mm* below the probe shoulder. In contrast, for loose sand with smaller influence zone, the size is about 70 *mm* and 40 *mm* for Δy and Δx respectively.

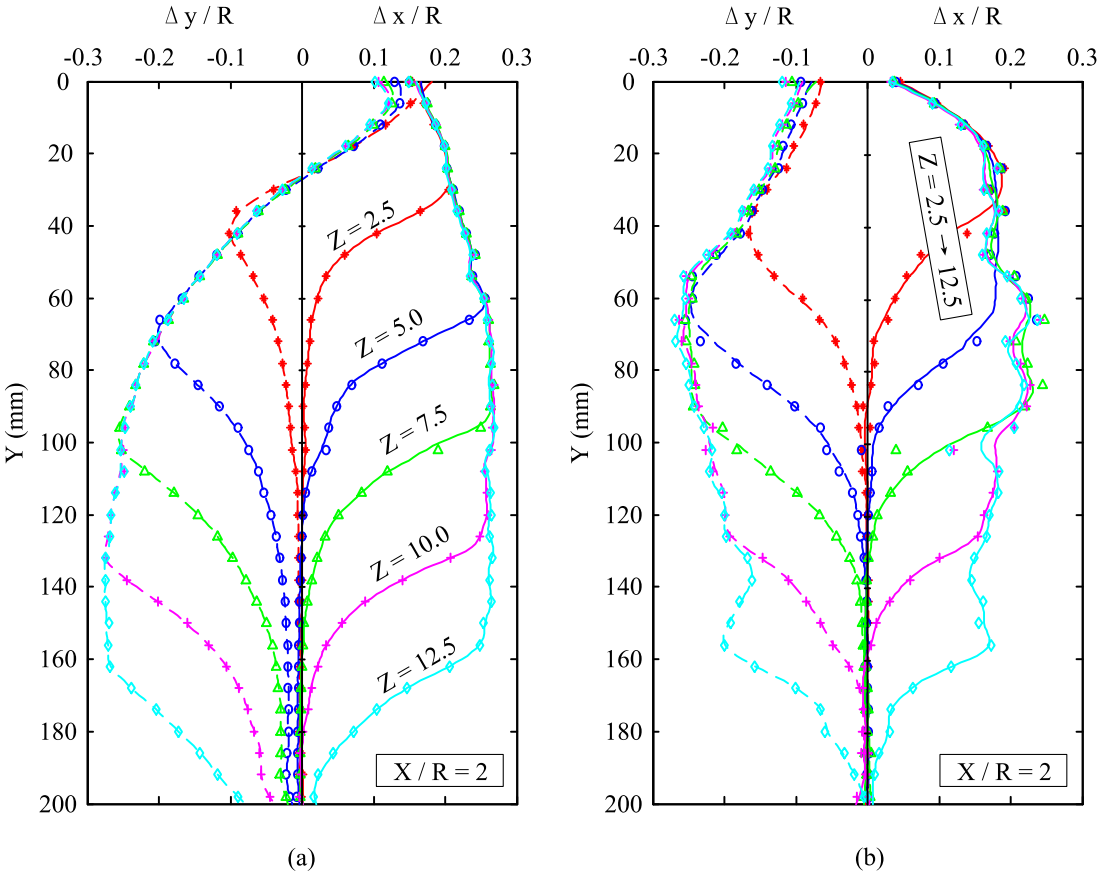

Figure 4.15 Cumulative displacement profiles with variation of penetration depth for $X/R = 2$: (a) Dense sand: $D_R = 91\%$; (b) Loose sand: $D_R = 50\%$

'h' is defined as the vertical position relative to the probe shoulder, as illustrated in Figure 4.1b. As the probe approaches and passes a given horizon, h varies from negative to positive. For instance, when the probe is penetrated to $z = 120\,mm$, h/B for soil element at $Y = 60\,mm$ equals 5, and $h/B = -5$ for soil at depth of 180 *mm*. As soil element is deformed primarily before the probe shoulder reaches the same level as the element location, and the displacements during this stage ($h < 0$) are named as the net

soil displacement (White, 2002).

Figure 4.16 presents the distributions of the net displacements: $\Delta x/R$ and $\Delta y/R$ with offset from the centreline of the probe X/R during the stage $h < 0$, as the probe is pushed from $Z = 2.5$ to 12.5. Both lateral and downwards displacements decrease exponentially with horizontal distance from the probe, which is comparable to the results of cavity expansion analysis. This curvature also illustrates the decay of influence on distant elements. The horizontal size of influence zone during $h < 0$ is $X/R \approx 10$ for dense sand, and slightly smaller size is found for loose sand ($X/R \approx 7$).

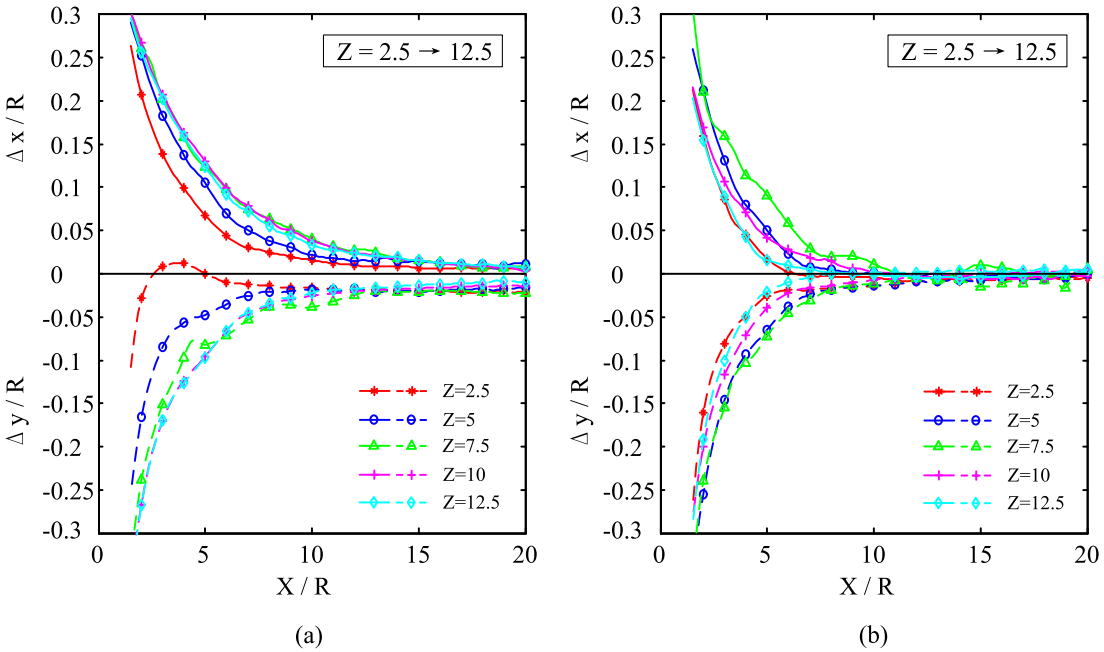

Figure 4.16 Displacement distributions ($h = 0$) with variation of penetration depth: (a) Dense sand: $D_R = 91\,\%$; (b) Loose sand: $D_R = 50\,\%$

4.3.2 Instantaneous displacement field

Instantaneous displacement field is the displacement developed over an interval of penetration distance (Δz), which directly illustrates the mechanism of penetration. For example, $\Delta x|_{\Delta z} = \Delta x|_{z+\Delta z/2} - \Delta x|_{z-\Delta z/2}$, denotes the instantaneous displacement which may represent the velocity field at a given penetration stage. Thus the results of contours are superimposed with displacement vectors to illustrate the direction of movement throughout this interval. It is worthwhile noting that all vectors (with spaces of $4\,mm$) are plotted at a scale factor of 5, which means that a vector with length of $5\,mm$

in the coordinate system represents a total displacement of $1\,mm$.

Figure 4.17 and Figure 4.18 exhibit the results of dense sand and loose sand for different interval distances ($\Delta z = 2\,mm$, $6\,mm$, $12\,mm$) when the probe is pushed to $150\,mm$ of depth. The contours are plotted only for values from the colour-bar (from 0.05 to 1.0), and the displacement vectors are eliminated for total displacement less than $0.1\,mm$, which represent soil that has hardly deformed during the penetration interval. It is observed that the influence zone in the instantaneous displacement field is a bulb around or a bit ahead of the cone tip. Soil elements adjacent to the probe shaft have little deformation, which is mainly caused by the shaft friction. During this interval, the soil in this bulb is displaced horizontally and vertically, and the displacement vectors grow radially, which seems comparable to a spherical cavity expansion. Intuitively, the failure mode is very similar to that proposed by Lee (1990) (Figure 2.29b), where zone III is the spherical cavity expansion zone based on Vesic (1977). This phenomenon urged the analyses of the correlation between cone penetration and spherical cavity expansion (e.g. Randolph et al., 1994; Yu and Mitchell, 1998; Gui and Jeng, 2009), and the developed analytical solutions in this research provided in Chapter 5 for spherical case are also applied to investigate the penetration problem in layered soils, as presented in Chapter 6.

The results of instantaneous displacements show that the influence portion extends to a larger field as the interval increases, while the extent of the zone is always below the probe shoulder. Comparing with the results of dense sand, the displaced zone in loose sand is smaller (i.e. the displacement is concentrated closer to the cone tip). More downward movements are observed in loose sand than dense sand, whereas dense sand tends to have more lateral displacement than loose sample. It is also notable that the upper boundary of the influence zone in dense condition is close to an inclination line at 60° from vertical, whereas the loose sand has a boundary that inclines at approximately 45° from vertical.

Similarly, the instantaneous displacement fields with different depth of penetration ($Z = 2.5, 5.0, 7.5, 10.0, 12.5$) during an interval of $6\,mm$ are shown in Figure 4.19 and Figure 4.20 for dense sand and loose sand respectively. The size of the influence por-

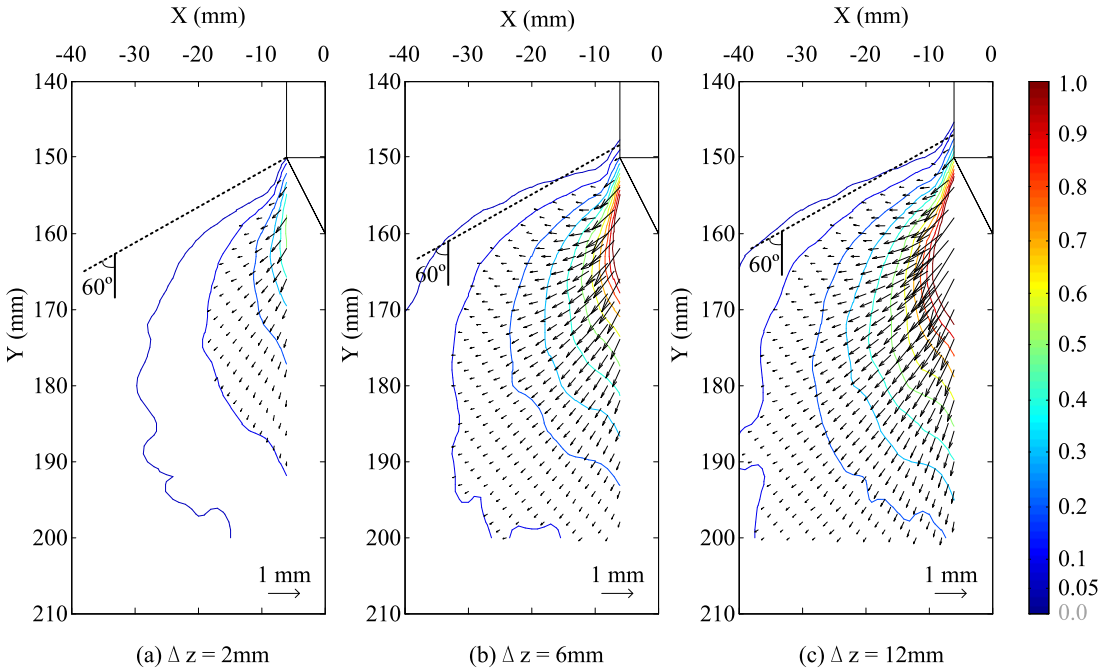

(a) Δ z = 2mm (b) Δ z = 6mm (c) Δ z = 12mm

Figure 4.17 Instantaneous displacement contours of MP II-02 (150 *mm* of penetration in dense sand: $D_R = 91\,\%$): (a) $\Delta z = 2\,mm$; (b) $\Delta z = 6\,mm$; (c) $\Delta z = 12\,mm$

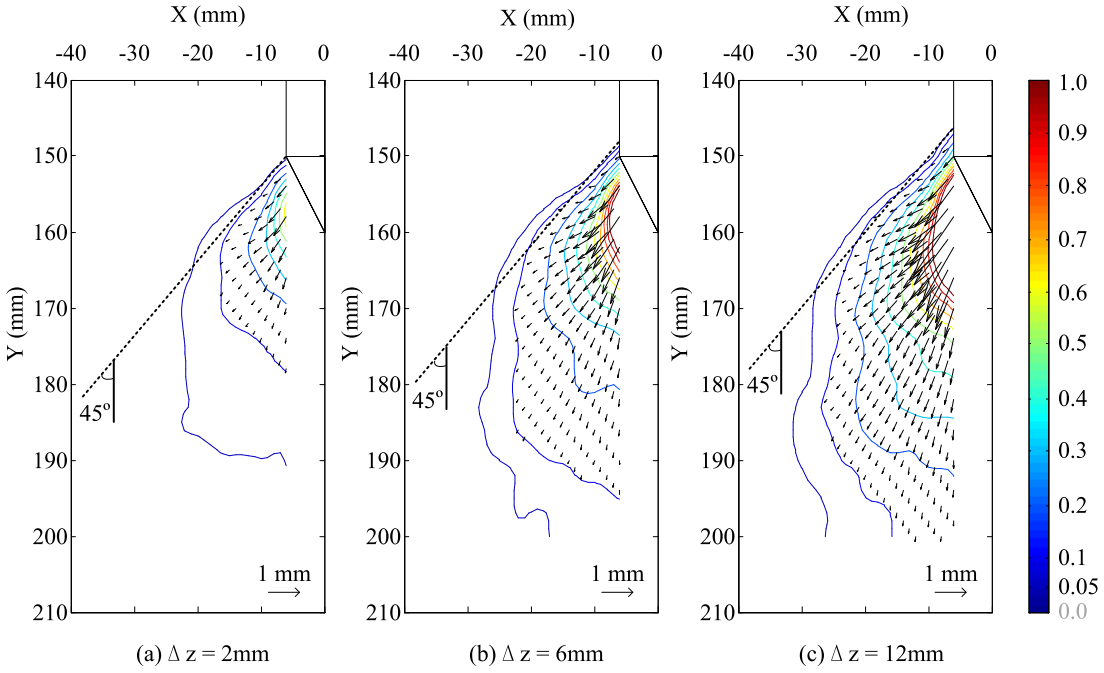

(a) Δ z = 2mm (b) Δ z = 6mm (c) Δ z = 12mm

Figure 4.18 Instantaneous displacement contours of MP II-03 (150 *mm* of penetration in loose sand: $D_R = 50\,\%$): (a) $\Delta z = 2\,mm$; (b) $\Delta z = 6\,mm$; (c) $\Delta z = 12\,mm$

tion differs slightly as probe goes deeper. The shallow penetration ($z = 30\,mm$) in dense sand extends the zone over the level of probe shoulder, and experiences more upward movements owing to the heave effect. This upwards movement is then constrained with depth when initial stress condition is increased. As no heave is observed for loose

sample, the influence zone and the displacement direction vary little with depth.

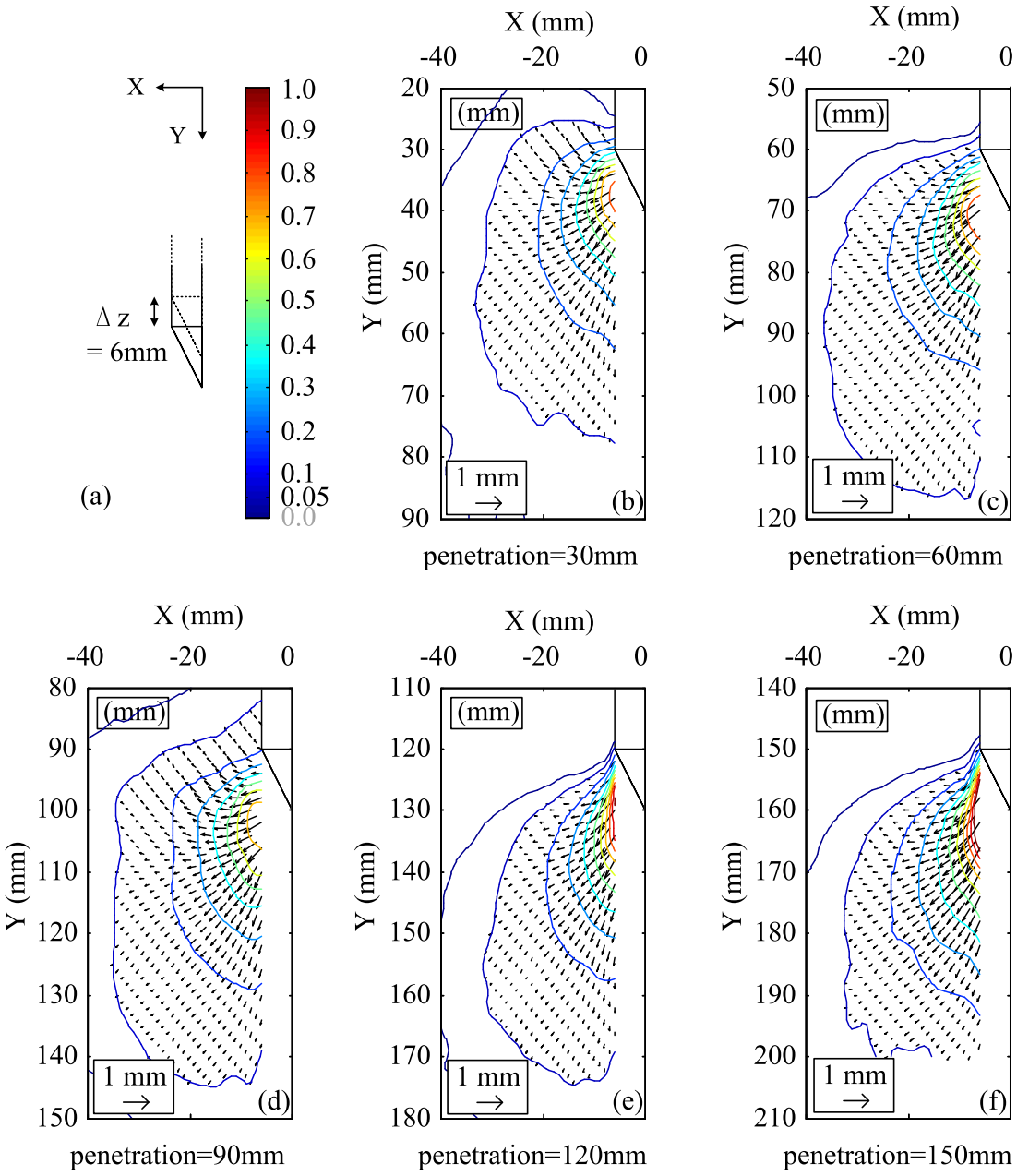

Figure 4.19 Instantaneous displacement contours of MP II-02 (Dense sand: $D_R = 91\,\%$): variation with depth ($30\,mm \rightarrow 150\,mm$)

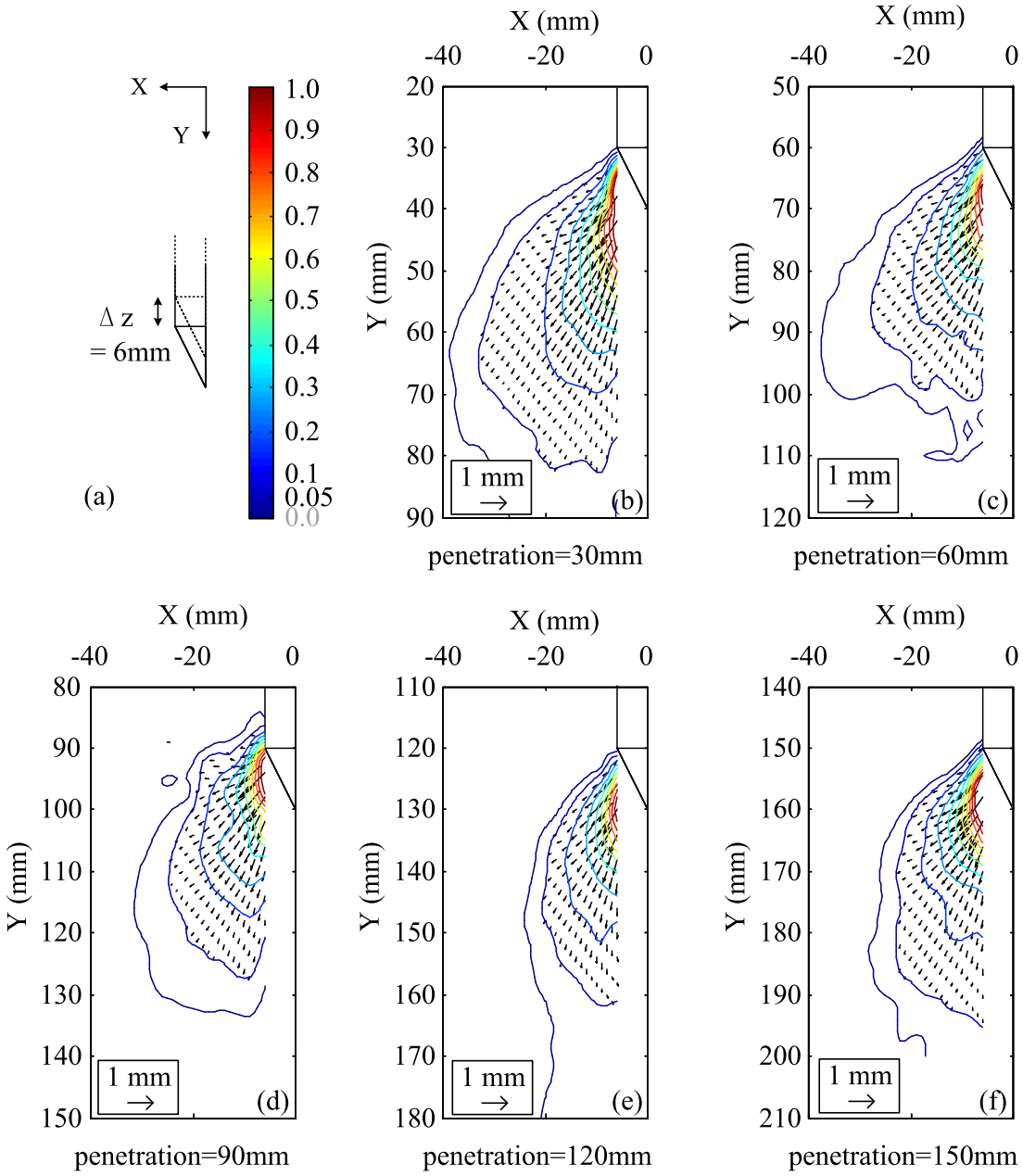

Figure 4.20 Instantaneous displacement contours of MP II-03 (Loose sand: $D_R = 50\,\%$): variation with depth ($30\,mm \rightarrow 150\,mm$)

4.3.3 Soil element trajectories

Full trajectories of soil elements that describe the displacement path during penetration provide a good insight into the penetration mechanism. Figure 4.21 offers the curvature of the element paths with normalised horizontal displacement against normalised vertical displacement for 5 soil elements at depth of 120 mm with variation of offset from the probe ($X/R = 2, 3, 4, 5, 6$). Generally, for each soil element, the curve starts from the origin point where no penetration is applied. As the probe approaches, the element is mainly displaced downwards and then curves to deform more laterally. At the final state, the ratio between radial and axial movement ($\Delta x/\Delta y$) increases with offset from the probe centreline.

When the probe shoulder reaches the elevation of the element ($h = 0$), the triangle mark '$\triangle$' is denoted on the curve. After 160 mm of penetration, the star mark '$*$' is denoted to represent the end of penetration. It is clear to note that the major proportion of the displacement occurs in the stage when $h < 0$ (i.e. the net displacement), and little contribution is made during $h > 0$. More specifically, the displacement in stage $h > 0$ goes slightly further away from the probe, which is in contrast with that observed by White (2002). The data of White (2002) showed that the direction of movement reverses back towards the pile with about 1% of pile diameter after the soil element passes the pile tip, which relaxes stress and consequently the shaft friction. However, for the data obtained here, this horizontal relaxation is not observed in stage $h > 0$, but in the stage as h approaches zero (from negative). A slight relaxation occurs just before the probe shoulder passes, as shown in Figure 4.22.

Comparing the results of dense sand and loose sand, the final horizontal displacement of dense sand is generally a little larger than the vertical displacement; more vertical displacement is observed within loose condition. The magnitude of displacement within loose condition is also smaller than in dense sand. The ratio between displacement in loose sand and dense sand decreases from 64% ($X/R = 2$) to 33% ($X/R = 6$) with increasing offset from the probe.

The trajectories of the same soil elements are plotted against h/B in Figure 4.22. The soil displacement path illustrates how the soil element flows around the probe dur-

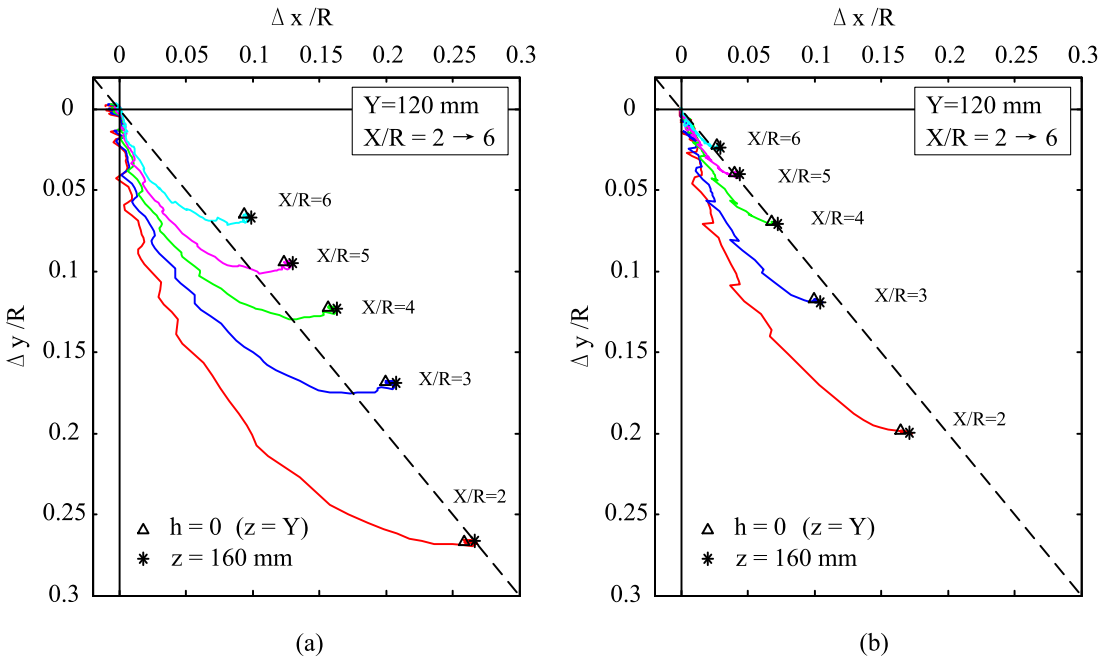

Figure 4.21 Trajectories of soil elements at depth $Y = 120\,mm$ with variation of X/R: (a) Dense sand: $D_R = 91\,\%$; (b) Loose sand: $D_R = 50\,\%$

ing installation. The maximum displacements are observed to occur before the probe passes. For $\Delta y/R$, the maximum value is reached at $h/B \approx -1$, while $\Delta x/R$ has the maximum value when $h/B \approx -0.5$. A little amount of horizontal relaxation is observed just after the peak value in $\Delta x/R$ for dense sand; nearly no relaxation occurs in loose conditions.

The trajectories of a single column of soil elements ($Y/B = 2.5, 5, 7.5, 10, 12.5$) at $X/R = 2$ are shown against the penetration depth (Z) in Figure 4.23. For shallow penetration, the displacement profiles at $h = 0$ increase with depth, especially for Δy. The reduction of Δy for dense sand before the probe passes indicates the relative heave as the soil flows around the probe shoulder. The effect of heave vanishes gradually as the probe is pushed to deeper soil. By contrast, the relaxation of horizontal movement is not obvious for both dense sand and loose sand.

4.3.4 Streamlines and distorted soil elements

The streamlines after penetration describe the soil deformation patterns around the penetrometer. Figure 4.24a exhibits the soil distortions in a uniform flow field for dense sand (left-hand side) and loose sand (right-hand side) after $150\,mm$ of penetra-

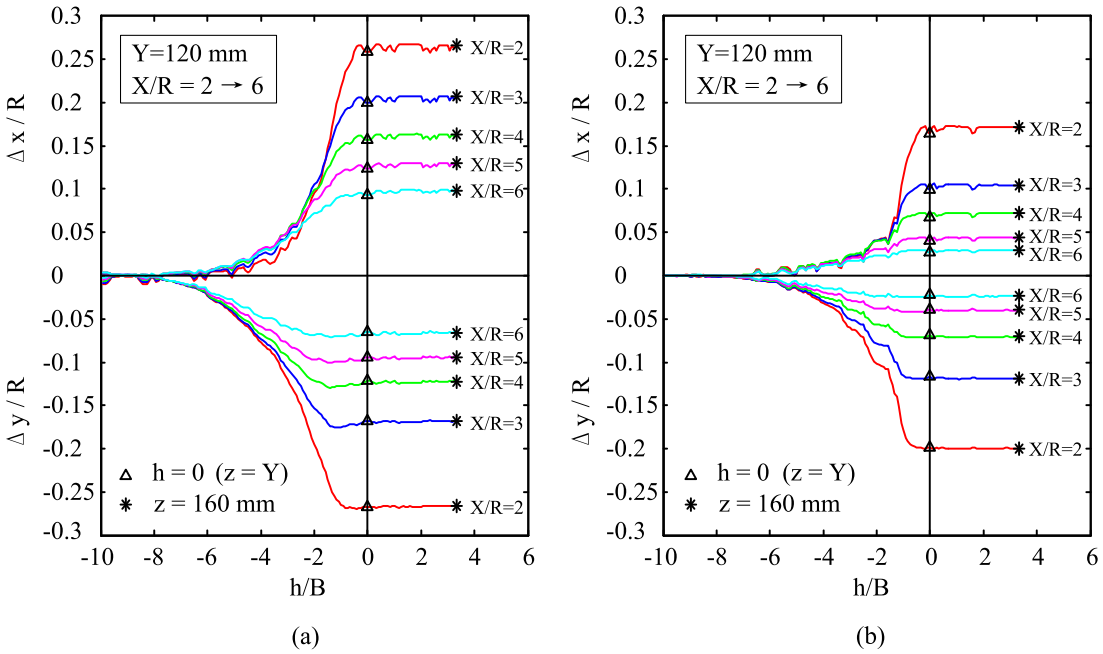

Figure 4.22 Normalised Δx and Δy of soil elements at depth $Y = 120\,mm$ with variation of X/R: (a) Dense sand: $D_R = 91\,\%$; (b) Loose sand: $D_R = 50\,\%$

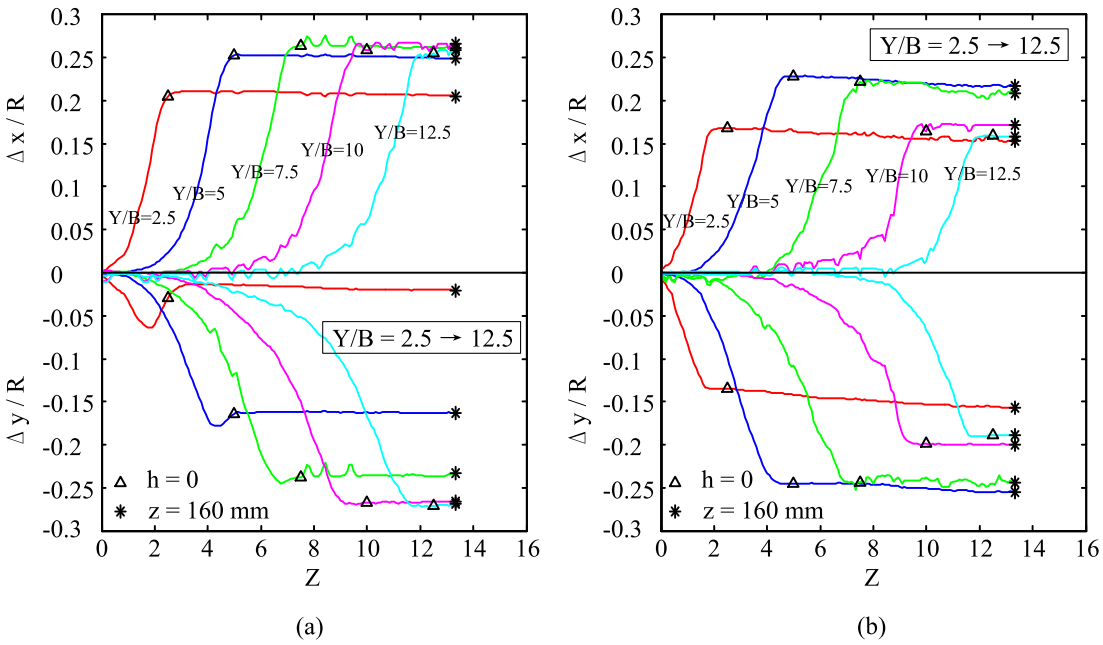

Figure 4.23 Normalised Δx and Δy of soil elements at $X/R = 2$ with variation of vertical location Y/B: (a) Dense sand: $D_R = 91\,\%$; (b) Loose sand: $D_R = 50\,\%$

tion. The streamlines adjacent to the probe are found to be denser for loose sand, and the pattern near surface is different to dense sand. Figure 4.24b and c provide details of the profiles of displacement at the surface and the elevations of the probe shoulder and probe tip using displacement vectors (no scale factors are applied for the vectors). It is notable that the surface of dense sand heaves while loose sand tends to be dragged

downwards with penetration. The magnitude and the direction of displacement around the cone are clearly shown for sand with different relative density.

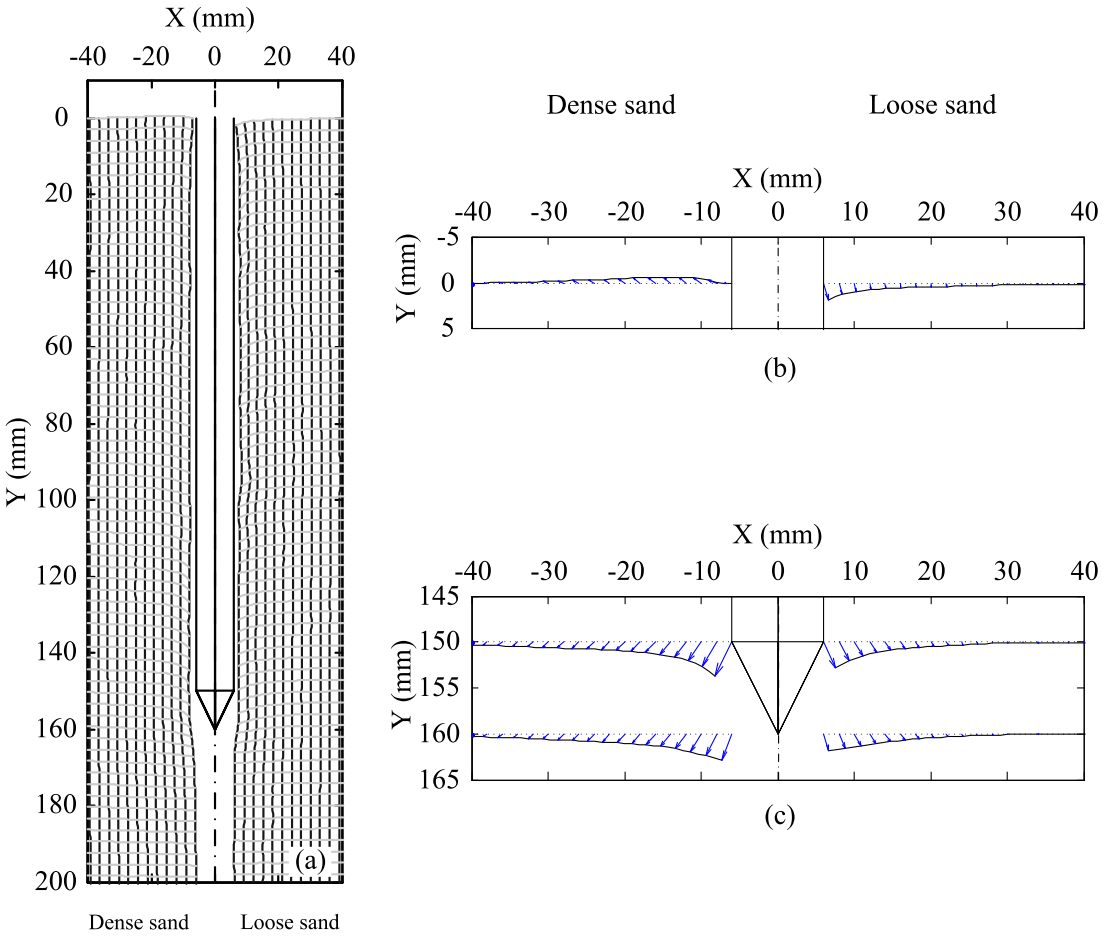

Figure 4.24 Profiles of (a) streamlines of the soil flow, (b) displacement at the surface, and (c) displacement around the cone tip for both dense sand and loose sand

Figure 4.25 is an alternative illustration of the soil element path during penetration. The soil elements near the probe are described as standard squares with size of $1\,mm \times 1\,mm$. The deformed square elements with different distance to probe centreline indicate the deformation patterns with offset. After the original element is plotted as red patch, the same element is superimposed with a darker element for every $5\,mm$ of penetration. The blue patch represents $h = 0$; the green patch nearly overlaps the blue one, as the displacements for $h > 0$ is limited. The series of soil element patch clearly record the shape of the deformed element, and the comparison of the element paths between dense sand and loose sand is straightforward.

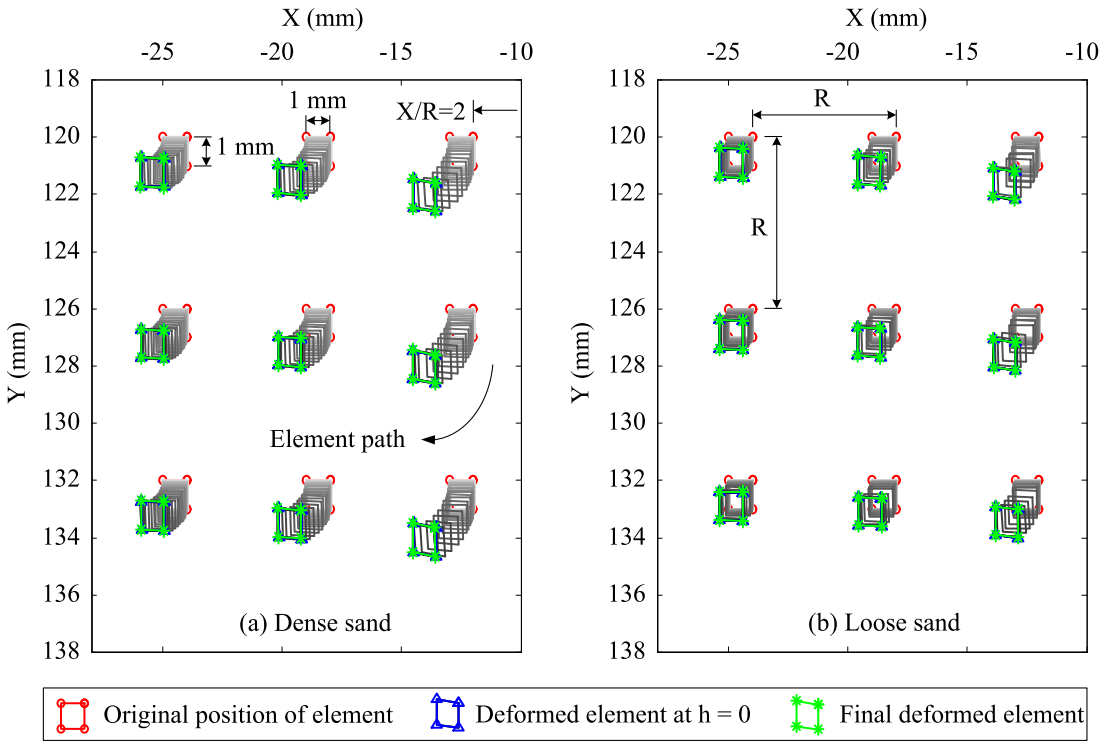

Figure 4.25 Soil element path during 150 *mm* of penetration: (a) Dense sand: $D_R = 91\%$; (b) Loose sand: $D_R = 50\%$

4.4 Results of Soil Strains

Soil strains derived from the results of the incremental displacements (presented in Section 4.3) are quantified and presented in this section. To determine the strains in an axisymmetric model, radial symmetry around the probe is assumed as illustrated in Figure 4.1. With compression positive notation, the definitions of strain components is the 'XY' system are listed as follows based on Cauchy's infinitesimal strain tensor with small deformation assumption:

$$\begin{aligned} \varepsilon_{xx} &= -\frac{\partial \Delta x}{\partial |X|} \qquad \varepsilon_{yy} = -\frac{\partial \Delta y}{\partial Y} \qquad \varepsilon_{xy} = -\frac{1}{2}\left(\frac{\partial \Delta x}{\partial Y} + \frac{\partial \Delta y}{\partial |X|}\right) \\ \varepsilon_{\theta\theta} &= -\frac{\Delta x}{|X|} \qquad \varepsilon_{x\theta} = \varepsilon_{y\theta} = 0 \qquad \varepsilon_{volume} = \varepsilon_{xx} + \varepsilon_{yy} + \varepsilon_{\theta\theta} \end{aligned} \tag{4.7}$$

where $|X|$ means the horizontal distance to centreline of probe; θ is the direction perpendicular to the 'XY' plane; ε_{xx}, ε_{yy} and $\varepsilon_{\theta\theta}$ are axial strains in x, y and θ directions; ε_{xy} is the shear strain in XY plane and ε_{volume} is the volumetric strain. The correlated strains in 'XY' plane are plotted in the Mohr circle of strains in Figure 4.26. The small strain assumption within the strain analysis makes the data very close to the probe ($X/R < 2$) unreliable. The calculation of strains was processed by importing the dis-

placement field into a corresponding mesh within FLAC (Itasca, 2005) for each step of penetration, as suggested by Marshall (2009). It has been mentioned by White (2002) and Marshall (2009) that large errors in the deduced strains are likely to be produced by small errors of the displacements. Therefore, the scatter of strains is relatively large, and some smoothing was applied to reduce the noise.

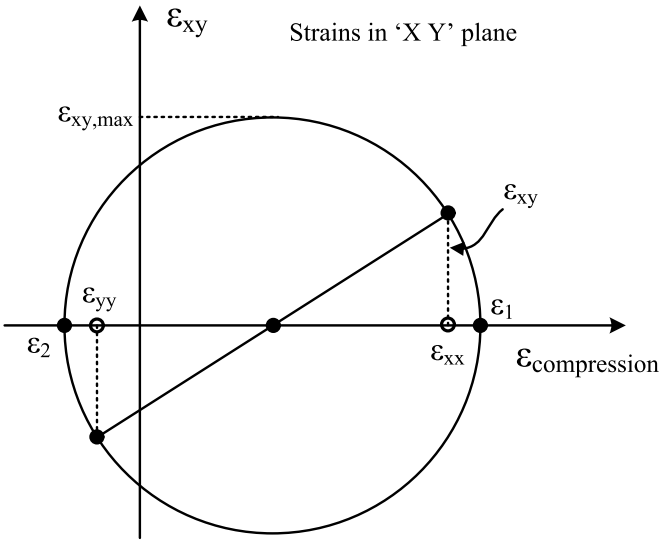

Figure 4.26 Mohr circle of strains in the '*X Y*' plane

Shearing dilatancy describes the change of volume when the material is distorted. At any shearing mode, the angle of dilation (ψ) defines the ratio of plastic volume change to plastic shear strain rate (Equation 4.8), where ψ is taken as positive when there is volume expansion and $\dot{\gamma}$ is the engineering shear strain rate (i.e. $\dot{\gamma}_{xy} = 2 \times \dot{\varepsilon}_{xy}$). In practice, total strains are dominated by the plastic components due to the relatively high elastic stiffness. Thus the elastic components are sufficiently small to be removed from the equation ($\dot{\varepsilon}_{total} = \dot{\varepsilon}^e + \dot{\varepsilon}^p$), as deduced in the right part of Equation (4.8). The principal strains in the 'X Y' plane (shown in Figure 4.26) can be derived by $\varepsilon_1, \varepsilon_2 = (\varepsilon_{xx} + \varepsilon_{yy})/2 \pm \sqrt{(\varepsilon_{xx} - \varepsilon_{yy})^2 + (2 \cdot \varepsilon_{xy})^2}/2$. Together with the strain in the θ direction, the three principal strains are ε_1, ε_2 and $\varepsilon_{\theta\theta}$. Therefore, the maximum value of shear strain rate in 3D strain space is then evaluated by the octahedral shear strain (i.e. the deviatoric component in π-plane), as expressed in Equation (4.9). For calculation of dilation angle, the incremental strains are estimated by strains developed over an interval of penetration (Δz), e.g. $\dot{\varepsilon}|_{\Delta z} = \varepsilon|_{z+\Delta z/2} - \varepsilon|_{z-\Delta z/2}$.

$$\sin\psi = -\frac{\dot{\varepsilon}^{\,p}_{volume}}{\left|\dot{\gamma}^{p}_{max}\right|} \approx -\frac{\dot{\varepsilon}_{volume}}{|\dot{\gamma}_{max}|} \tag{4.8}$$

$$|\dot{\gamma}_{max}| = \dot{\gamma}_{oct} = \frac{2}{3} \cdot \sqrt{(\dot{\varepsilon}_1 - \dot{\varepsilon}_2)^2 + (\dot{\varepsilon}_1 - \dot{\varepsilon}_{\theta\theta})^2 + (\dot{\varepsilon}_2 - \dot{\varepsilon}_{\theta\theta})^2} \tag{4.9}$$

4.4.1 Contours of cumulative strains

The cumulative strains after 160 *mm* of penetration exhibit the strain state of the distorted soil elements around the probe. Figure 4.27 and Figure 4.28 give the contours of the cumulative horizontal strain (ε_{xx}), vertical strain (ε_{yy}) and shear strain (ε_{xy}) for dense sand (MP II-02) and loose sand (MP II-03). Compared with the contours of displacements, strains have more scatter owing to the amplified error from the GeoPIV data, especially for soil at depth around 110 *mm* where the data is combined from two pictures. Hence the results of strains are analysed avoiding this area.

For soil ahead of the probe cone, ε_{xx} is negative and ε_{yy} is positive, indicating the soil below the probe shoulder is undergoing vertical compression and horizontal extension. In contrast, the soil around the probe shaft experiences vertical extension and horizontal compression. This shows the different deformation patterns around the probe, and similar phenomenon was also observed by White (2002) and Liu (2010). Severe shear strain (ε_{xy}) appears in soil adjacent to the probe cone and shaft, where shearing mode dominates the deformation pattern. Comparing the results of dense sand and loose sand, the magnitude of strains in loose sand seems to be greater, attributed to the higher compressibility of the loose sample.

4.4.2 Contours of instantaneous strains

Similar to displacement, the instantaneous results provide a straightforward illustration of the penetration mechanisms. The instantaneous strain also represents the incremental strain (strain rate) during that incremental penetration stage; Δz is taken as probe radius, $= 6\,mm$. The contours of penetration at depth of 150 *mm* for dense sand and loose sand are shown in Figure 4.29 and Figure 4.30 respectively. The shared colourbar is given in subplot (a), and the strain rates in the 'X Y' plane and the volumetric strain rate are then presented in subplot (b $\sim$ f).

The positive and negative bulbs in $\dot{\varepsilon}_{xx}$ and $\dot{\varepsilon}_{yy}$ reveal the compression zones and the

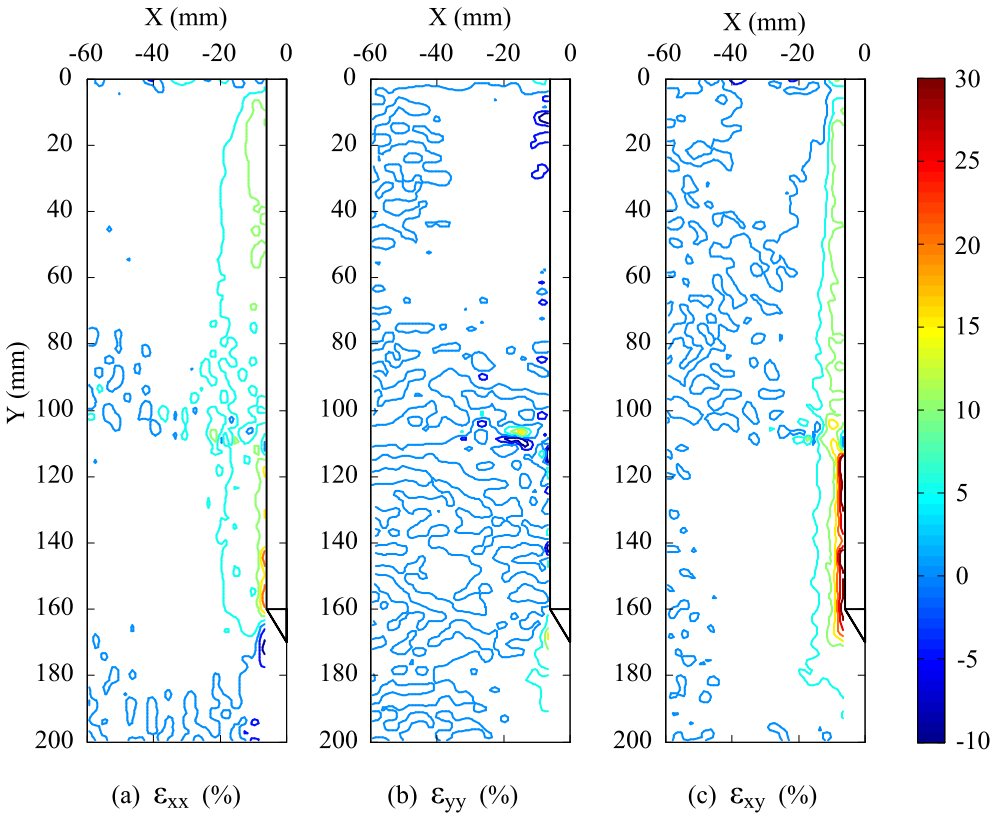

Figure 4.27 Cumulative strain contours of MP II-02 (160 *mm* of penetration in dense sand: $D_R = 91\,\%$): (a) ε_{xx} (%); (b) ε_{yy} (%); (c) ε_{xy} (%)

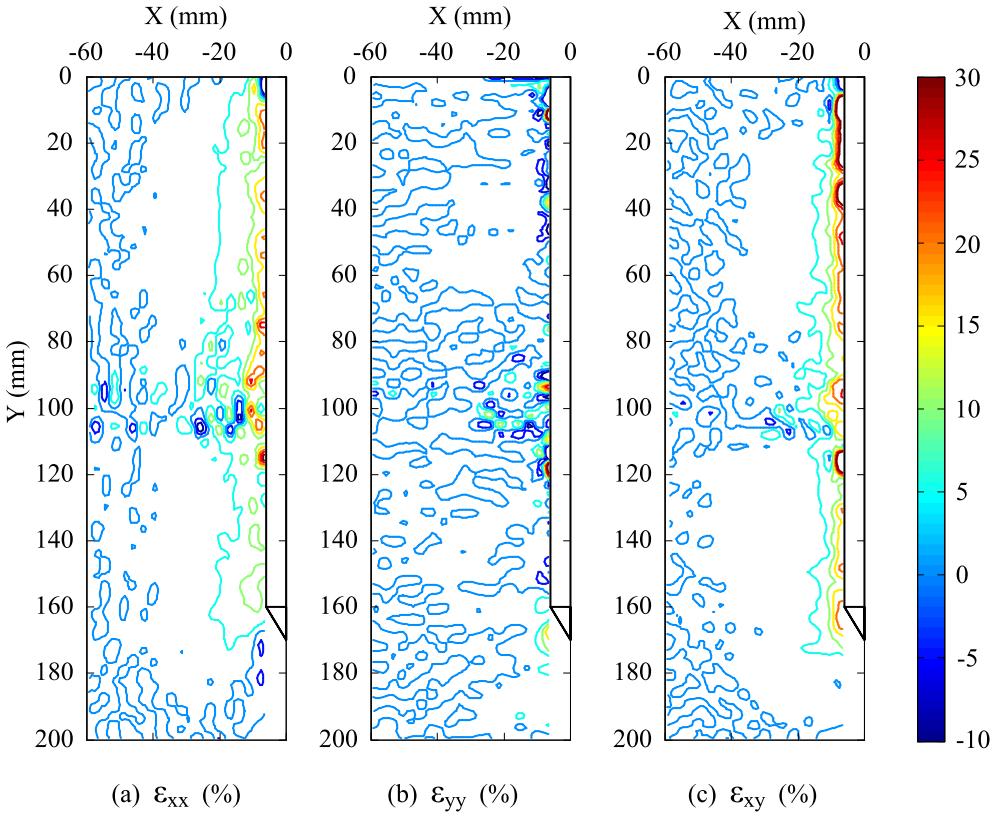

Figure 4.28 Cumulative strain contours of MP II-03 (160 *mm* of penetration in loose sand: $D_R = 50\,\%$): (a) ε_{xx} (%); (b) ε_{yy} (%); (c) ε_{xy} (%)

extension zones. The boundaries where $\dot{\varepsilon}_{xx}$ and $\dot{\varepsilon}_{yy}$ are close to zero seem to be a line that extends from the probe shoulder and inclined at about $30^\circ \sim 35^\circ$ from the vertical. Soil below this line experiences incrementally horizontal extension and vertical compression, whereas the strain rates reverse for the soil above the line. In contrast to the contour of cumulative shear strain, the shear strain rate $\dot{\varepsilon}_{xy}$ is a bulb shaped zone extending down to $3B$ below the probe; a little negative zone exists as the soil is rolled up around the probe shoulder. The high shear strain zone is also evident in the contour of $\dot{\varepsilon}_{xy,max}$, where the soil is under horizontal extension and vertical compression. The contour of $\dot{\varepsilon}_{volume}$ offers the zones of volumetric contraction (positive) and dilation (negative). It is notable that dilation with significant shear occurs below the cone and the contraction zone close to the probe shoulder is relatively small. When the contours are compared between dense and loose sand, smaller zones and magnitudes of $\dot{\varepsilon}_{xy}$ and $\dot{\varepsilon}_{volume}$ are observed for the loose sand. This implies that loose sand tends to be less sheared and dilated than dense sand.

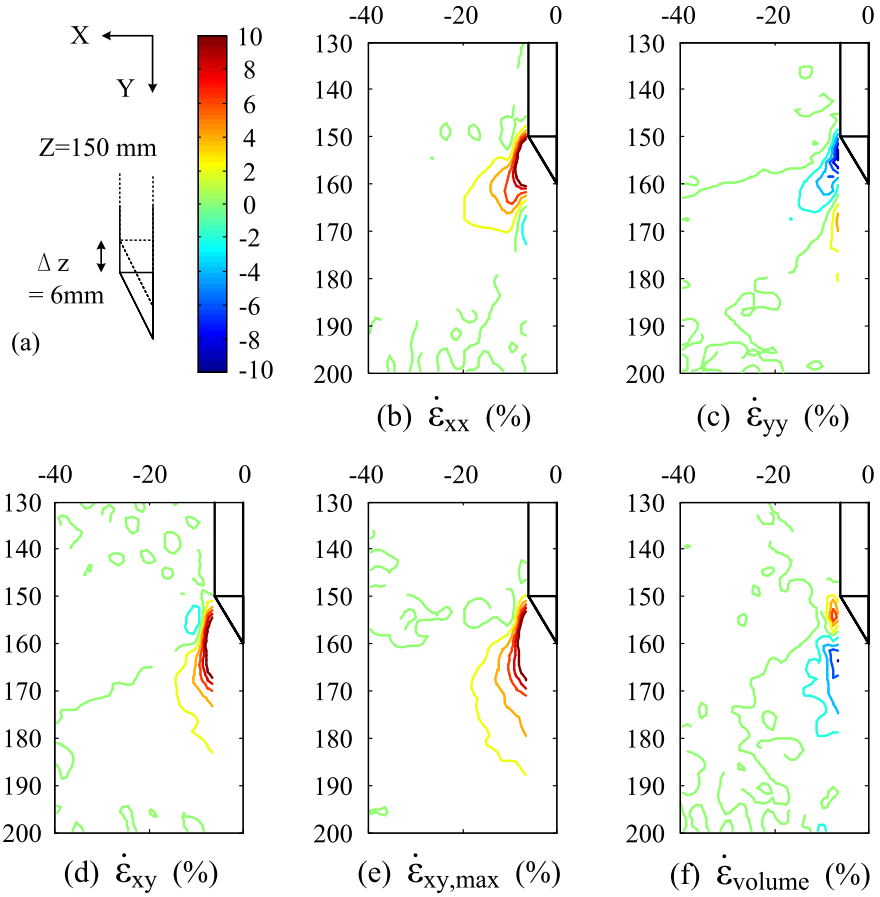

Figure 4.29 Instantaneous strain contours ($\Delta z = 6\,mm$) of MP II-02 ($150\,mm$ of penetration in dense sand: $D_R = 91\%$): (b) $\dot{\varepsilon}_{xx}$ (%); (c) $\dot{\varepsilon}_{yy}$ (%); (d) $\dot{\varepsilon}_{xy}$ (%); (e) $\dot{\varepsilon}_{xy,max}$ (%); (f) $\dot{\varepsilon}_{volume}$ (%)

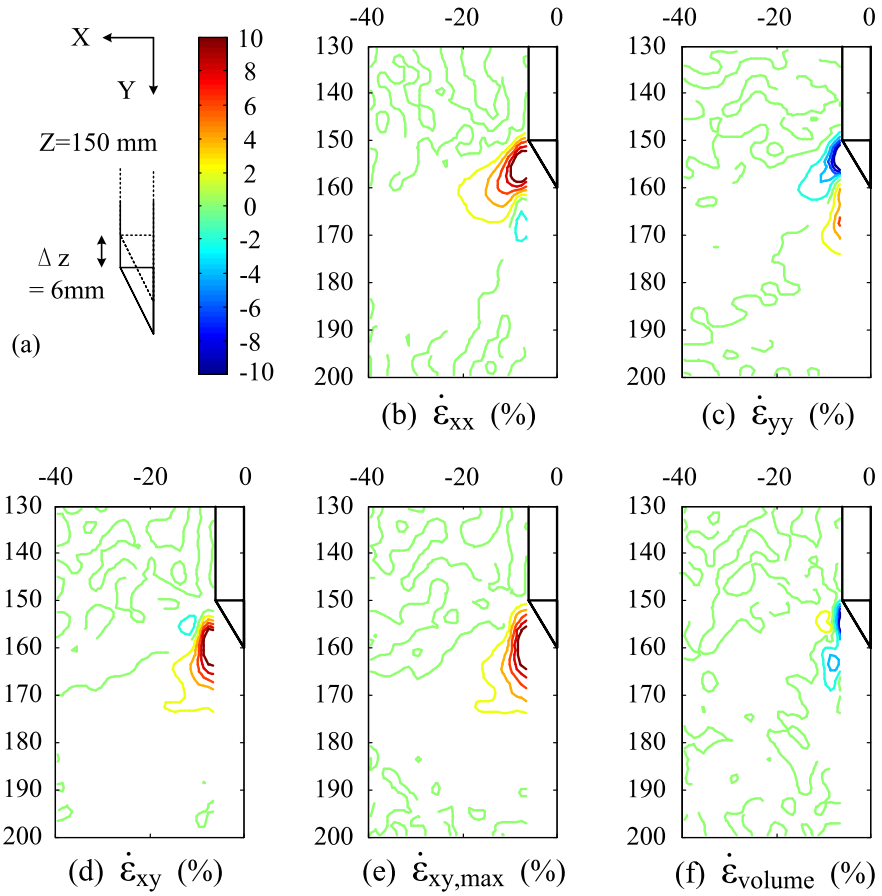

Figure 4.30 Instantaneous strain contours ($\Delta z = 6\,mm$) of MP II-03 (150 *mm* of penetration in loose sand: $D_R = 50\,\%$): (b) $\dot{\varepsilon}_{xx}$ (%); (c) $\dot{\varepsilon}_{yy}$ (%); (d) $\dot{\varepsilon}_{xy}$ (%); (e) $\dot{\varepsilon}_{xy,max}$ (%); (f) $\dot{\varepsilon}_{volume}$ (%)

4.4.3 Principal strain rates

Figure 4.31 and Figure 4.32 offer an alternative view of the instantaneous strain field, with the magnitude and the direction of principal strain rate at various depths of penetration ($z = 30\,mm \sim 150\,mm$). The principal strain rates are focused on $\dot{\varepsilon}_1$ and $\dot{\varepsilon}_2$ in the 'X Y' plane (Figure 4.26), where $\dot{\varepsilon}_1$ is compression and $\dot{\varepsilon}_2$ is tension. The magnitude of strain rate is illustrated by the size of the crossing lines (a standard length for 10 % of strain rate is given in the plots). The main principal strain rate is directed from the cone tip, and decays significantly with relative distance. Despite the fact that sand is known to behave in a non-coaxial manner, the large strain around the probe cone leads to a reduced effect of non-coaxiality (Roscoe, 1970). Hence the directions of the principal strain rate provides some clues for estimation of directions and distributions of the principal stress rate. There is no obvious trend with variation of depth for both dense and loose sand. The directions of the principal strain rate between dense sand and loose sand are observed to be essentially similar, with slightly smaller inclination from vertical for loose sample.

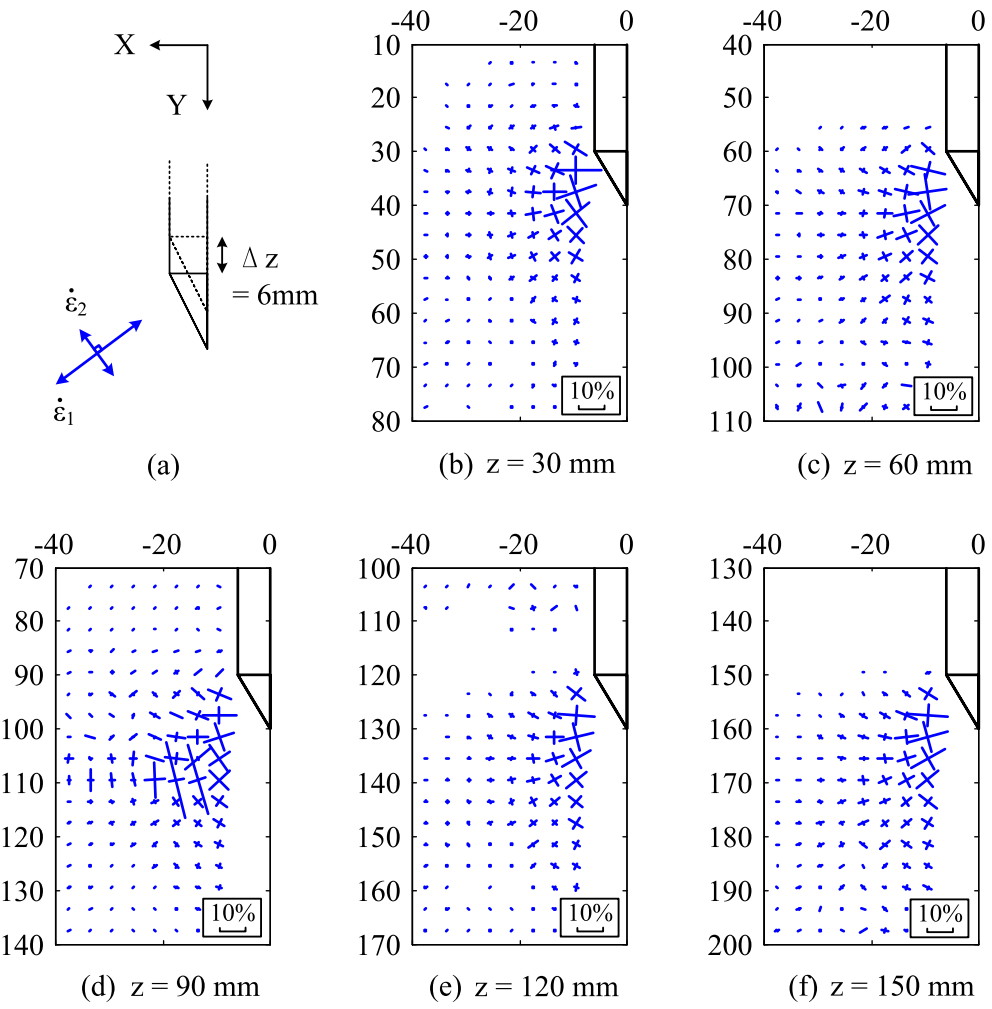

Figure 4.31 Principal strain rates in dense sand ($D_R = 91\,\%$): variation with depth ($30\,mm \rightarrow 150\,mm$)

4.4.4 Variation of strains with offset from probe

The variation of strains with offset from the probe centreline (X/R) is examined in this section. The distribution of cumulative strains (ε_{xx}, ε_{yy}, ε_{xy} and ε_{volume}) of soil elements at two different depths ($Y = 60\,mm$; $150\,mm$) are given in Figure 4.33 for both dense sand and loose sand. Consistent with the results of displacements, the distributions decrease quickly with horizontal distance from the probe. Horizontal strain in loose sand is generally larger than that of dense sand, and more concentrated close to the probe. Compared with ε_{xx}, the amount of vertical strain is much smaller; somewhat tensile ε_{yy} is evident in shallow dense sand and in deep loose sand. The decay of ε_{xy} is apparently sharper than that of ε_{xx}, and the influence zone is then slightly narrower. As the hoop strain $\varepsilon_{\theta\theta}$ is derived from Δx, the resulting volumetric strain implies that for dense sand, dilation occurs for $X/R < 4$ that is surrounded by contraction zone with

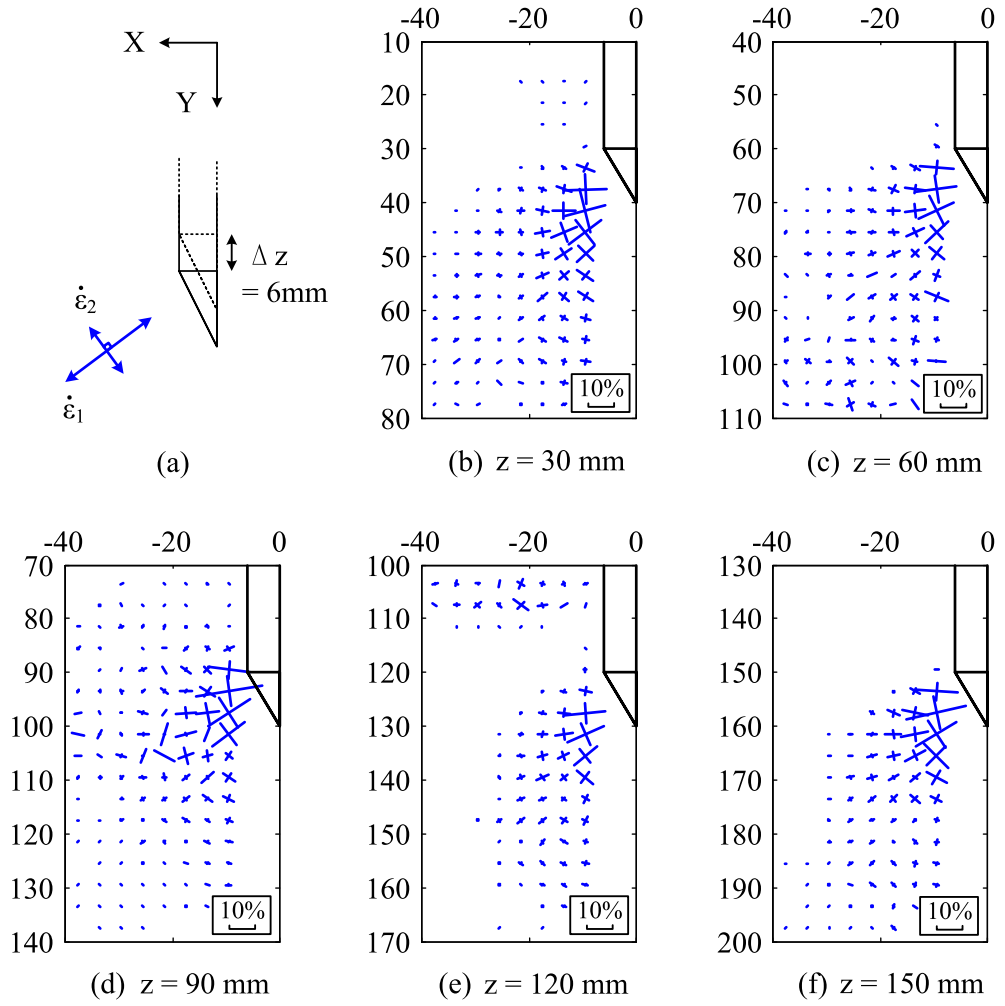

Figure 4.32 Principal strain rates in loose sand ($D_R = 50\,\%$): variation with depth ($30\,mm \rightarrow 150\,mm$)

an influence portion of $X/R \approx 10$. By comparison, loose sand experienced smaller volumetric expansion owing to the lower dilatancy of loose sand compared to dense.

As previously presented on the bulbs of incremental strains, both horizontal and vertical strains reverse as the soil flows past the probe which is considered as stationary. As the soil element transitions from vertical compression and horizontal extension to horizontal compression and vertical extension, the maxima and minima of the strain histories are provided in Figure 4.34. The extension zone of ε_{xx} is located very close to the probe ($X/R < 2$), and the magnitude of ε_{yy} is relatively smaller. Comparison of dense sand and loose sand shows again that soil with higher density has larger influence region and the strains drop more gently with offset from the probe.

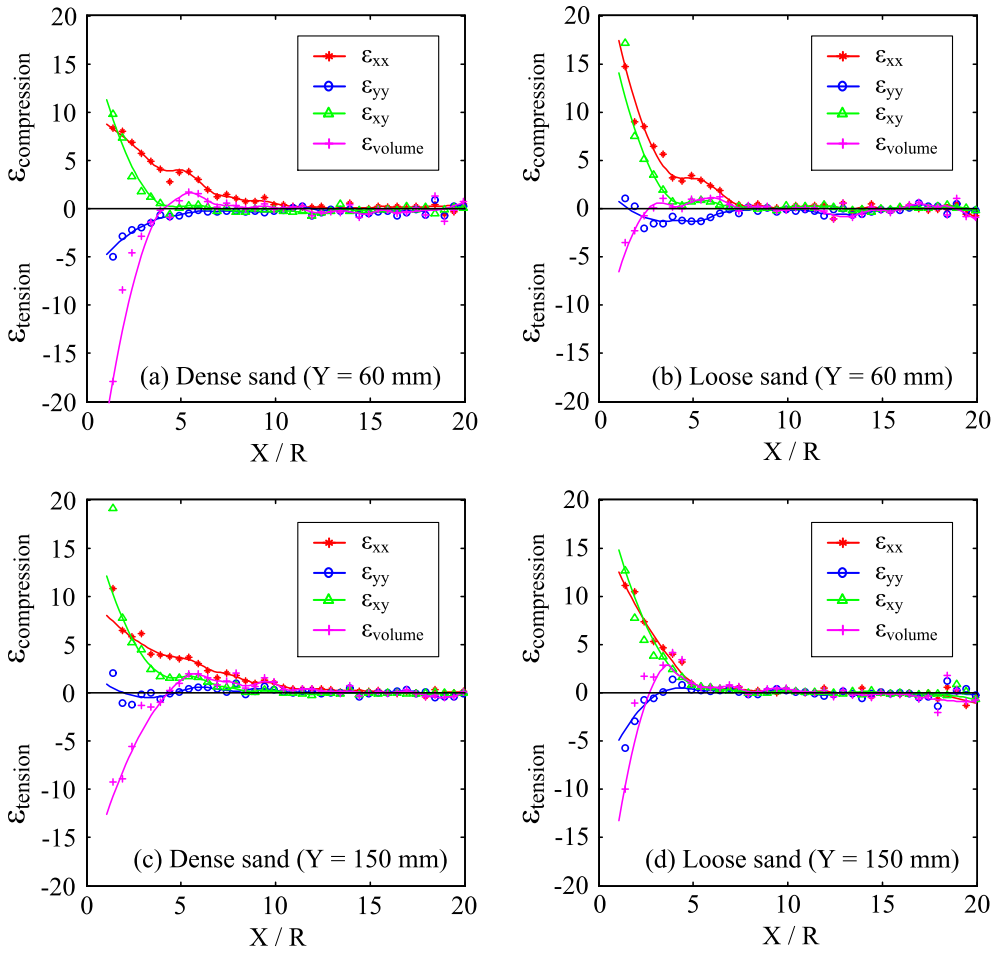

Figure 4.33 Distributions of strains ($h = 0$): (a) Dense sand ($z = Y = 60\,mm$); (b) Loose sand ($z = Y = 60\,mm$); (c) Dense sand ($z = Y = 150\,mm$); (d) Loose sand ($z = Y = 150\,mm$)

4.4.5 Strain paths of soil elements

Strain paths shown in Figure 4.35 $\sim$ Figure 4.37 reveal the evolution of strains (ε_{xx}, ε_{yy}, ε_{xy}, ε_{volume}, $\varepsilon_{\theta\theta}$, ε_1, ε_2) during probe installation. In Figure 4.35, the strain histories are plotted against the relative position to probe shoulder (h/B) for soil elements in the near field ($X/R = 2$) at a depth of $60\,mm$ and $150\,mm$ for both dense sand and loose sand. Clearly the majority of the strain is developed before the probe shoulder passes, and the strain remains nearly constant when $h > 0$.

It is notable that the strain reversal of ε_{xx} and ε_{yy} occurs before the probe shoulder passes. With penetration, ε_{xx} gradually drops to the minima at $h/B \approx -2$, which is slightly earlier than when ε_{yy} reaches the maxima, followed by the phase of strain reversals. The strain changes direction, crosses the zero strain line, and reaches an opposite peak at $h/B \approx -0.5$. The location where these two curves intersect suggests that the relatively small compressive strains (ε_{xx} and ε_{yy}) occur at $h/B \approx -1$, where

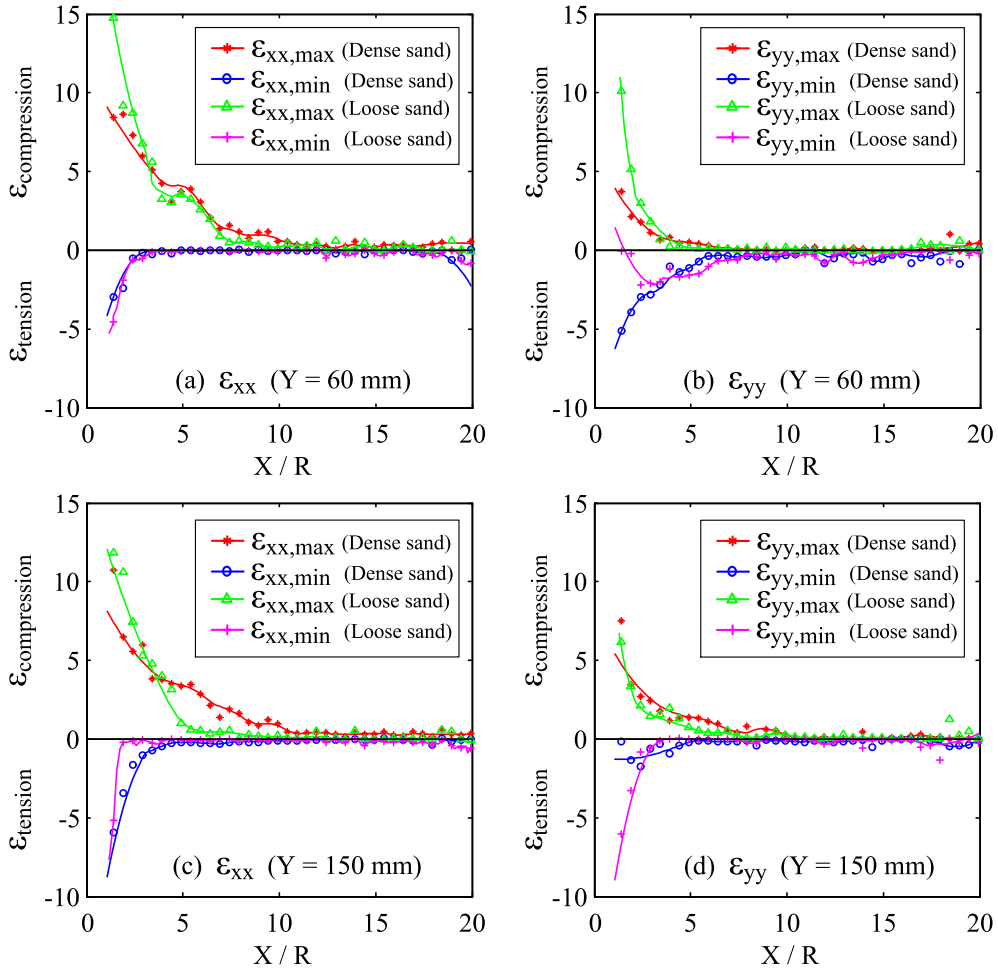

Figure 4.34 Distributions of maximun and minimun strains: (a) ε_{xx} ($Y = 60\,mm$); (b) ε_{yy} ($Y = 60\,mm$); (c) ε_{xx} ($Y = 150\,mm$); (d) ε_{yy} ($Y = 150\,mm$)

ε_{xy} grows sharply to the maxima. There is no obvious difference on the strain reversal for both dense and loose sand in both depths. The sensing distances of ε_{xx} and ε_{yy} are about $5\,B$ and $8\,B$, which match the observation of Liu (2010).

The phenomenon of strain reversal was also reported by Baligh (1985) and White and Bolton (2004). However, the former was an analytical solution that is only suitable for undrained clay; and the latter was from calibration chamber tests in a plane strain model. Therefore, it is essential to quantify the strain reversal during penetration in an axisymmetric model of sand with severe volumetric strain.

The phase from $h/B = -0.5$ to 0 exhibits a small proportion of strain reduction, among which the reduction of ε_{xy} is the most notable. The two principal strains (ε_1 and ε_2) represent the size of the Mohr circle in 'X Y' plane. Extensive ε_{zz} continuously grows until the probe approaches, and is the minimum principal strain. Consequently, the negative

volumetric strain indicates the dilatant behaviour of soil near the probe, whereas the final state of loose sand appears to have nearly no dilation; this can be attributed to the relatively high compressive ε_{xx}.

Comparing the results to that from 'far' field ($X/R = 6$ in Figure 4.36), the general trends also apply to the strain paths with lower magnitude. The difference appears to be the strain reversal that only occurs for ε_{yy} at shallower depth. Higher proportion of ε_{xx} is observed, which dominates ε_1 in the Mohr circle, and shear strain is mainly less than 1% except for dense sand at deep position ($\varepsilon_{xy} < 2\%$). Another contrast is ε_{volume}, the soil located far from the probe has volumetric contraction rather than dilation in the near field.

The variation of ε_{volume} with offset from the probe centreline is shown in Figure 4.37. The eventual state of ε_{volume} also signifies the distribution of density after penetration. For dense sand, soil at $X/R = 2 \sim 4$ experiences dilation after the probe passes while contraction appears for soil further than $X/R = 5$. The peak dilation is observed when the probe is just above the soil element ($h/B = -1 \sim -2$), and the peak value comes later for soil closer to the probe. There is no systematic trend in loose sand; more contraction is observed, especially for loose sand at deep locations.

4.4.6 Rotations and dilation

Due to the inserting probe with a cone shape, the soil elements around the probe are severely distorted, including both translation and rotation. The translation of soil element has been quantified horizontally and vertically through the GeoPIV analysis, as shown in Section 4.3. Although the rotation cannot be directly obtained from the GeoPIV data, displacements of a network of triangular elements were used to evaluate the soil rotation by White (2002). The results showed that high rotation ($> 20^\circ$) was observed for soil adjacent to the probe, and the magnitude of soil rotation decreased significantly with the offset from the probe centreline. Similar trends can also be found from the distorted element patches in Figure 4.25, and the rotation of dense sand and loose sand are of comparable magnitude.

An alternative illustration of the soil rotation is the change of the direction of the prin-

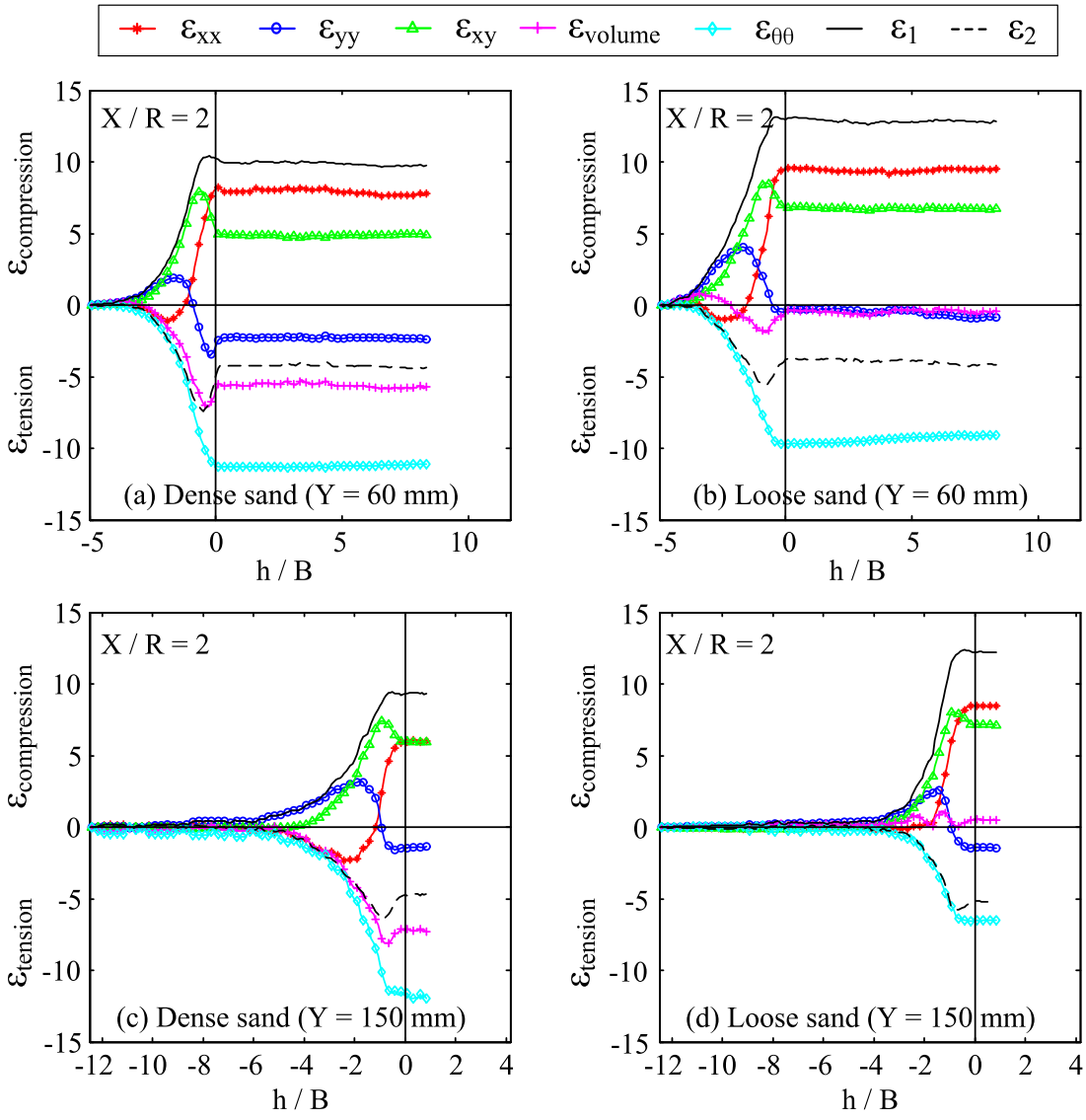

Figure 4.35 Strain paths of soil element at $X/R = 2$ against h/B: (a) Dense sand ($Y = 60\,mm$); (b) Loose sand ($Y = 60\,mm$); (c) Dense sand ($Y = 150\,mm$); (d) Loose sand ($Y = 150\,mm$)

cipal strain. Section 4.4.3 presents the directions of principal strain rates for both dense and loose samples. Here the cumulative principal strain (ε_1) is considered to track the rotation path during the penetration, as shown in Figure 4.38. Both dense and loose sand at depth of $60\,mm$ (subplots a, b) and $150\,mm$ (subplots c, d) are provided in variation with offset from probe centreline ($X/R = 2 \rightarrow 6$). It is worthwhile noting that the angle (θ) is evaluated by the inclination from the vertical direction in degrees. In essence, when a probe is far ahead of the soil element, vertical compression effect dominates the strain state; thus the direction of ε_1 begins with a small inclination, and the initial inclination increases with offset. With the probe approaching, this angle increases gradually to a steady level when the probe shoulder passes.

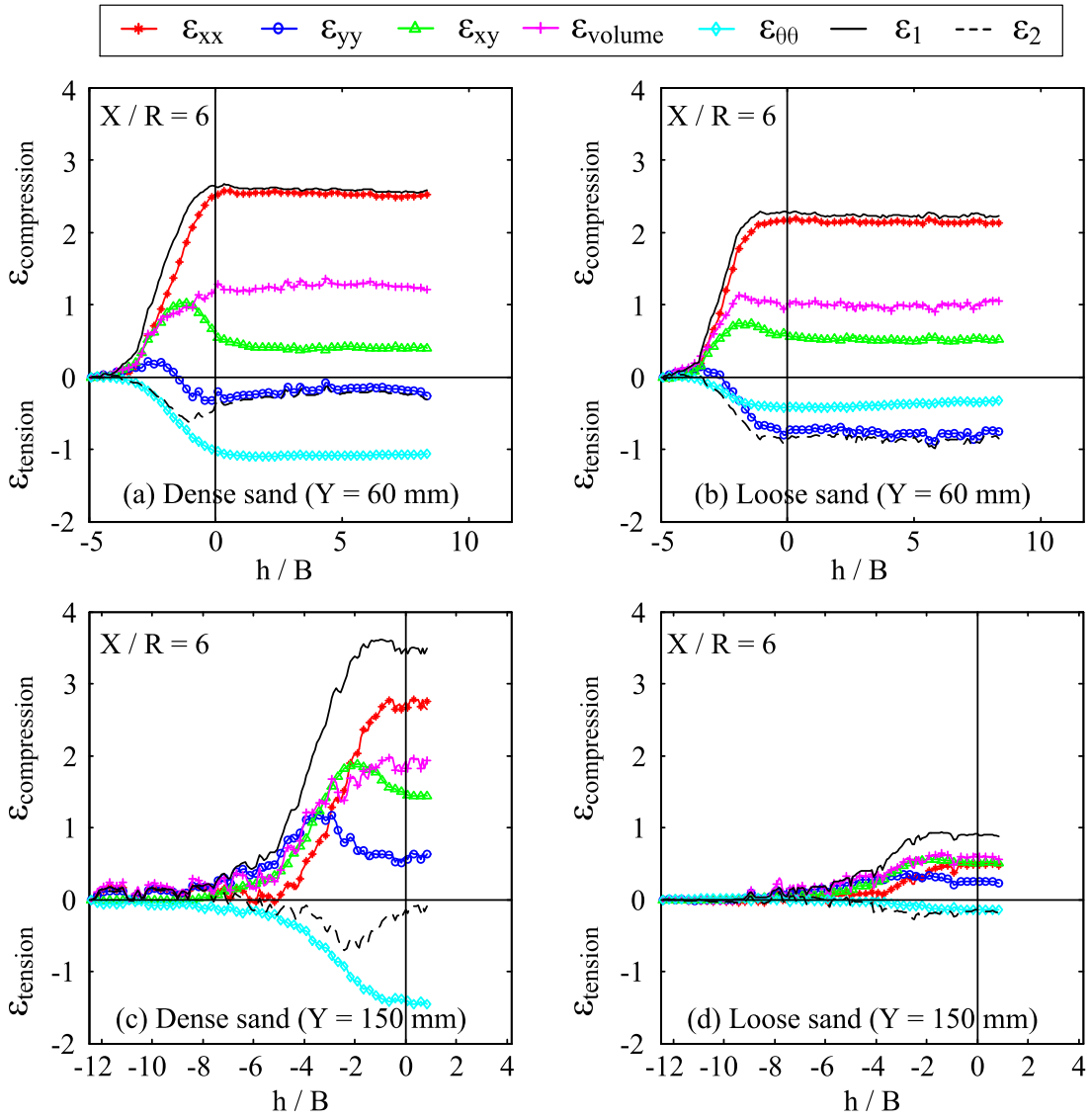

Figure 4.36 Strain paths of soil element at $X/R = 6$ against h/B: (a) Dense sand ($Y = 60\,mm$); (b) Loose sand ($Y = 60\,mm$); (c) Dense sand ($Y = 150\,mm$); (d) Loose sand ($Y = 150\,mm$)

The large scatter at the early stage is believed to be attributed to the large proportion of strain error for soil elements that are slightly distorted. The scatter is also more obvious for soil farther away from the probe, in which ε_1 is more affected or even dominated by horizontal strain (ε_{xx}). Despite the strain error, the general trends of rotation of ε_1 are apparent since the probe is getting closer ($h/B > -5$). Eventually for dense sand at depth of $60\,mm$, the inclination of ε_1 is approximately 68° for $X/R = 2$, whilst θ_{ε_1} is close to 90° for $X/R = 4,\ 5$, indicating the nearly horizontal ε_1 after probe passes. Mostly, the ultimate value of θ_{ε_1} increases with the offset from the probe centreline, which is in contrast with the decreasing rotation of soil element with offset. In addition,

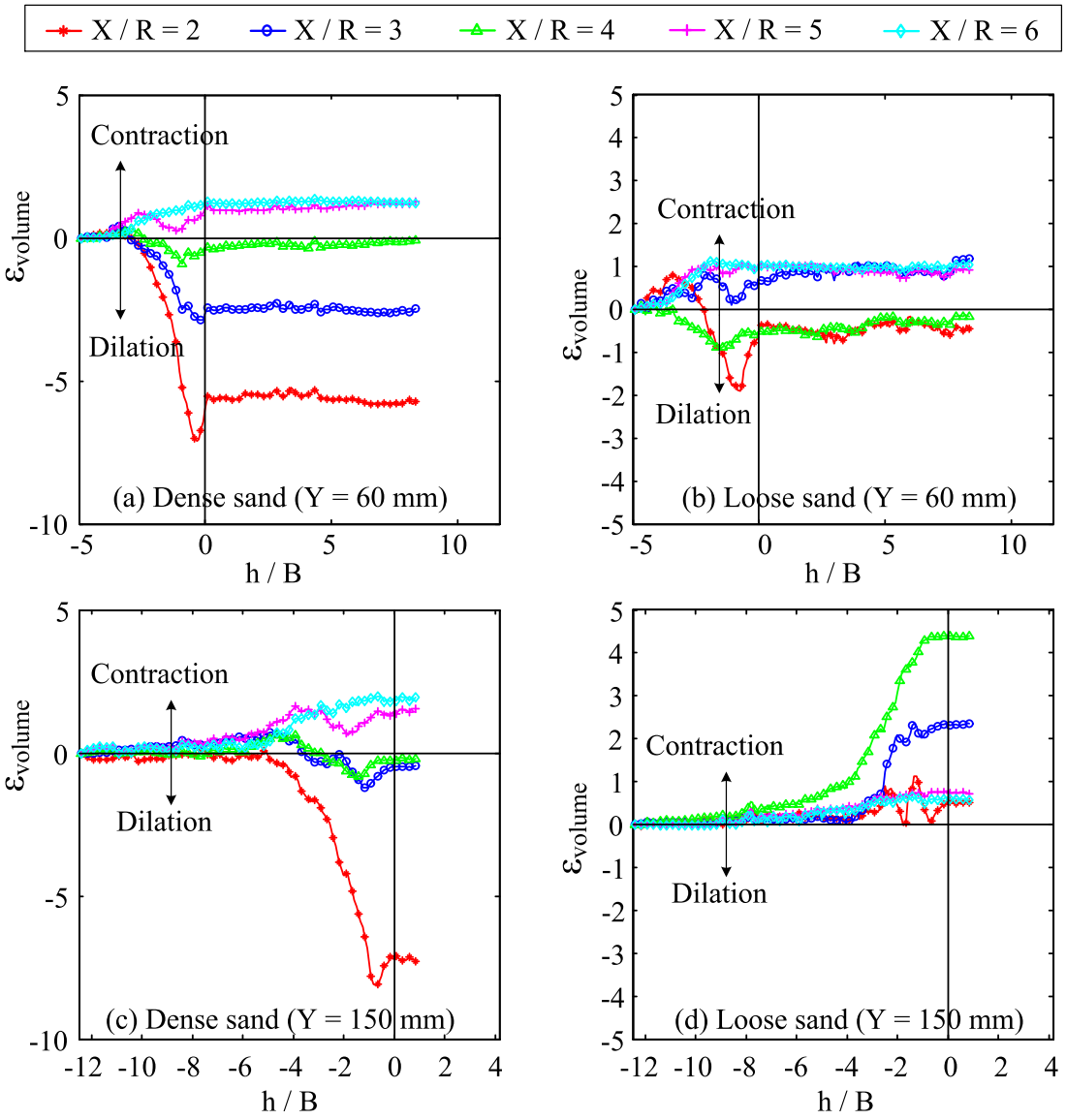

Figure 4.37 Volumetric strain paths of soil elements ($X/R = 2 \rightarrow 6$) against h/B: (a) Dense sand ($Y = 60\,mm$); (b) Loose sand ($Y = 60\,mm$); (c) Dense sand ($Y = 150\,mm$); (d) Loose sand ($Y = 150\,mm$)

the inclination of loose sand is about 10% less than that of dense sand; approximately 15% smaller values of θ_{ε_1} is observed for soil at 150 mm compared to soil at 90 mm.

Figure 4.37 reveals the developments of the volumetric strains during penetration; soil dilation is observed, especially for the dense sample. The dilation occurs associated with the shearing in the failure mode of penetration. After 160 mm of penetration, the cumulative volumetric strain (ε_{volume}) contours are show in Figure 4.39 for both dense and loose sand. The contours are plotted in gray-scale colourmap, indicating that the darker area has more effect of dilation. The distribution of ε_{volume} presents the changes of the soil density after probe installation. In dense sand, dilatant soil is ob-

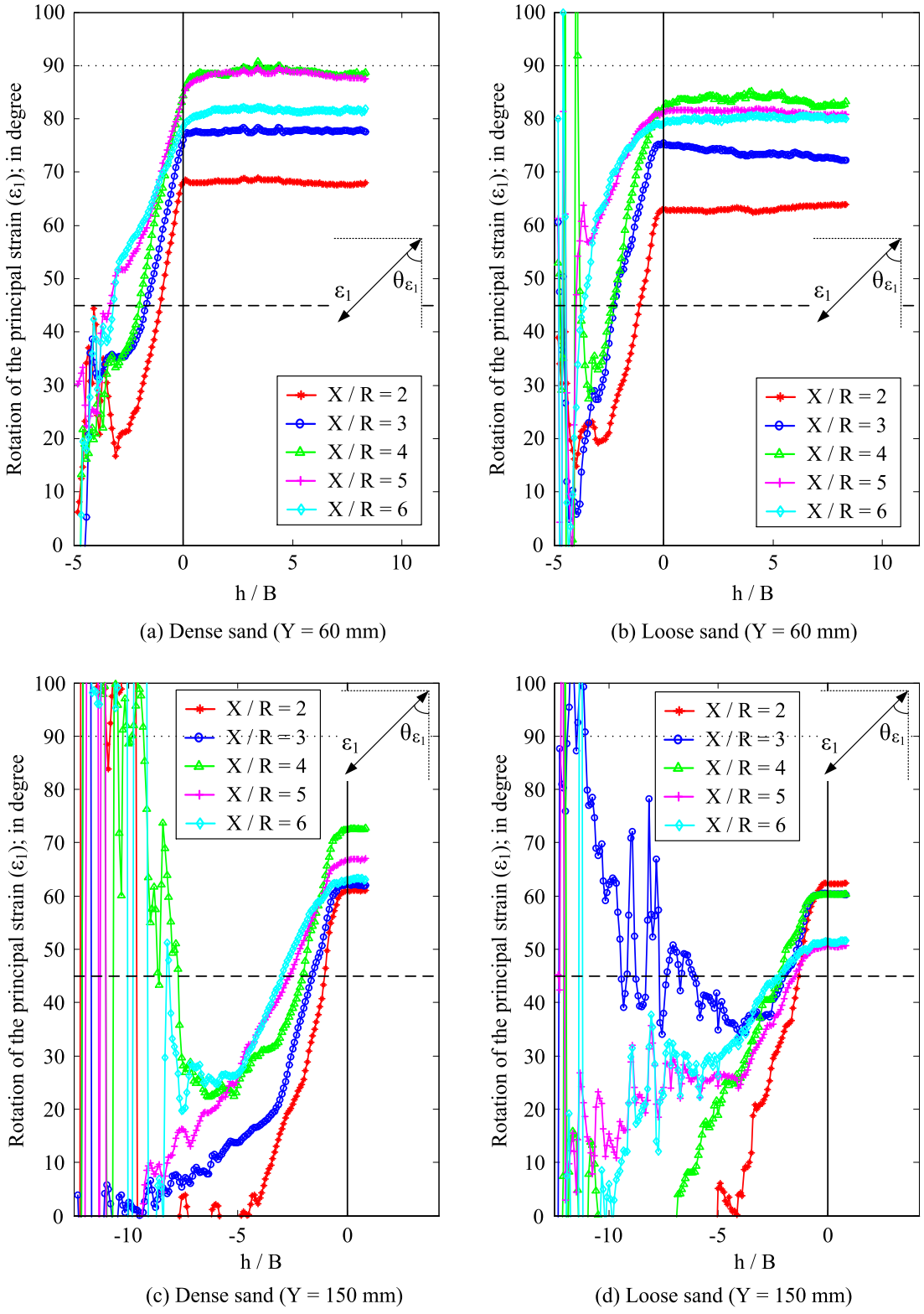

Figure 4.38 Rotations of the principal strain (ε_1) against h/B: (a) Dense sand ($Y = 60\,mm$); (b) Loose sand ($Y = 60\,mm$); (c) Dense sand ($Y = 150\,mm$); (d) Loose sand ($Y = 150\,mm$)

served within the area: $X/R < 4$; significant dilation ($\varepsilon_{volume} < -20\,\%$) occurs for soil adjacent to the probe ($X/R < 1$). For soil outside of this loosening area, contraction is observed indicating the effect of densification induced by the installation. Compared

with dense sand, the dilation area for loose sand is narrower, $X/R < 3$. The variation of dilation area with depth is not obvious for both dense and loose samples.

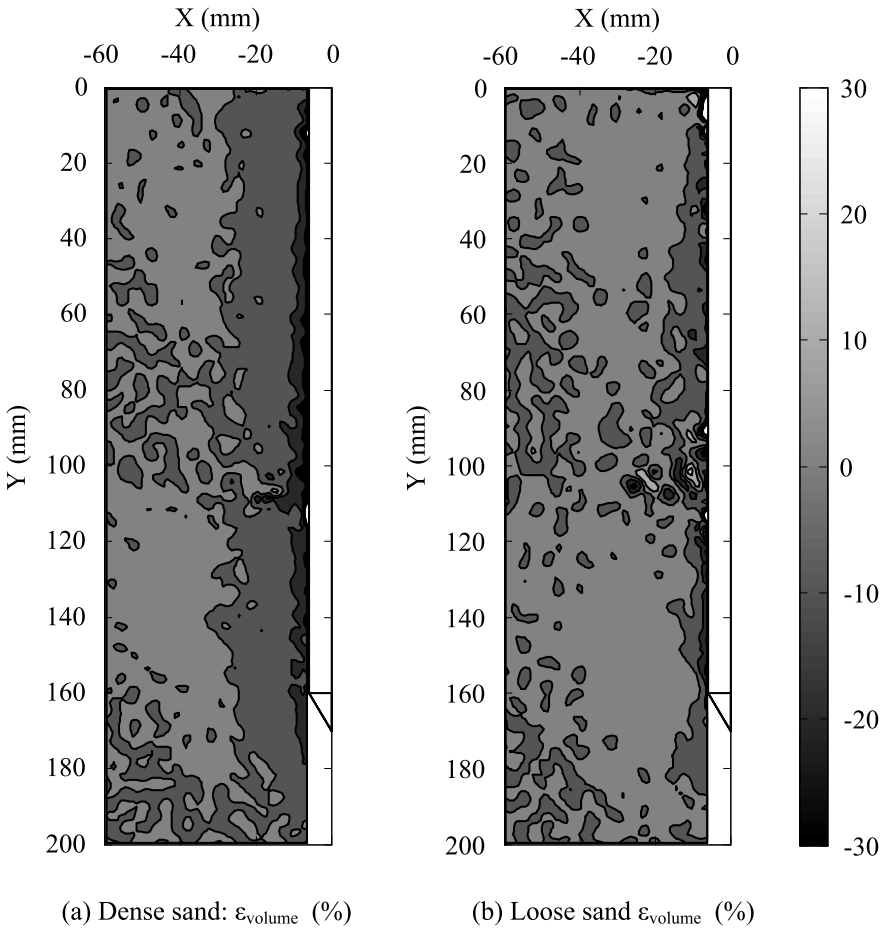

(a) Dense sand: ε_{volume} (%) (b) Loose sand ε_{volume} (%)

Figure 4.39 Cumulative volumetric strain (ε_{volume}) contours for: (a) Dense sand ($D_R = 91\%$); (b) Loose sand ($D_R = 50\%$)

To quantify the magnitude of dilation, the effect of shear strain is also included as illustrated in Equation (4.8) and (4.9). As incremental strains are used to calculate the mobilised dilation angle, the interval of penetration of $6\,mm$ (R) is considered here. Figure 4.40 offers the distribution of dilation angle through the interval for dense and loose sand at two different depths ($60\,mm$ and $150\,mm$). Because of the incremental calculation of the dilation angle, the error from the GeoPIV data is amplified, especially for soil with small strains. To minimise the scatter in the contours, smoothing was applied to the results and any dilation angle out of the range $-30^\circ < \psi < 30^\circ$ was eliminated. Thus the contours are strictly the representation of the dilation angle distribution, which provides the location and magnitude of the dilatant effect during the penetration interval. For soil at $Y = 60\,mm$ (subplots a and b), significant dilation area

is located ahead of the cone, where shear strain rate is high (see Figure 4.29 and Figure 4.30); contraction area is found around the probe shaft, indicating the relaxation when the soil flows over the probe shoulder, as reported by White (2002). Similar patterns are also shown when the probe is deeper ($Y = 150\,mm$), whereas dilation occurs in dense sand due to the shaft friction and nearly no contraction area is found around the shaft for loose sand.

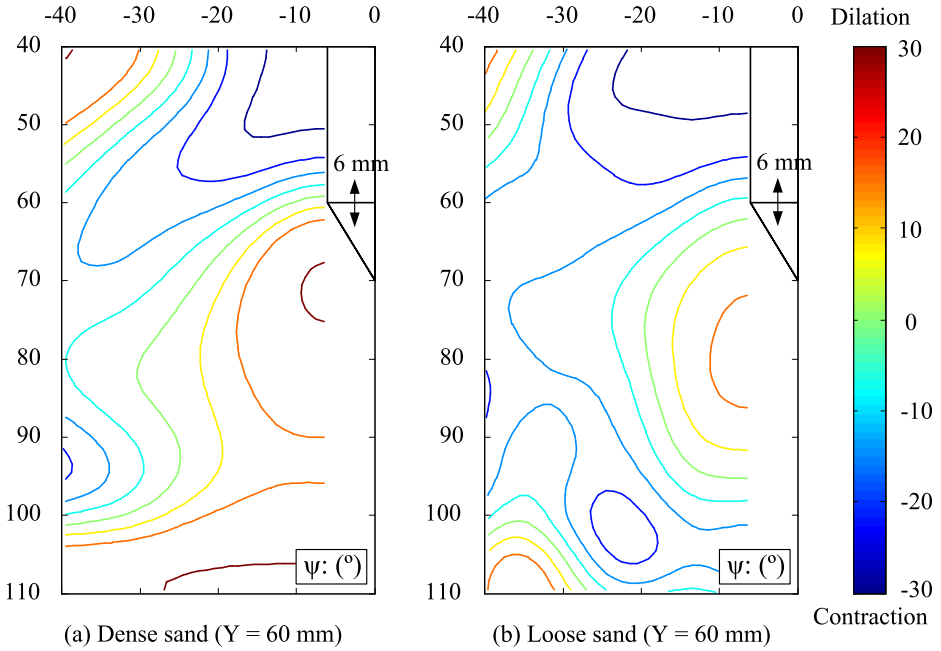

(a) Dense sand (Y = 60 mm) (b) Loose sand (Y = 60 mm)

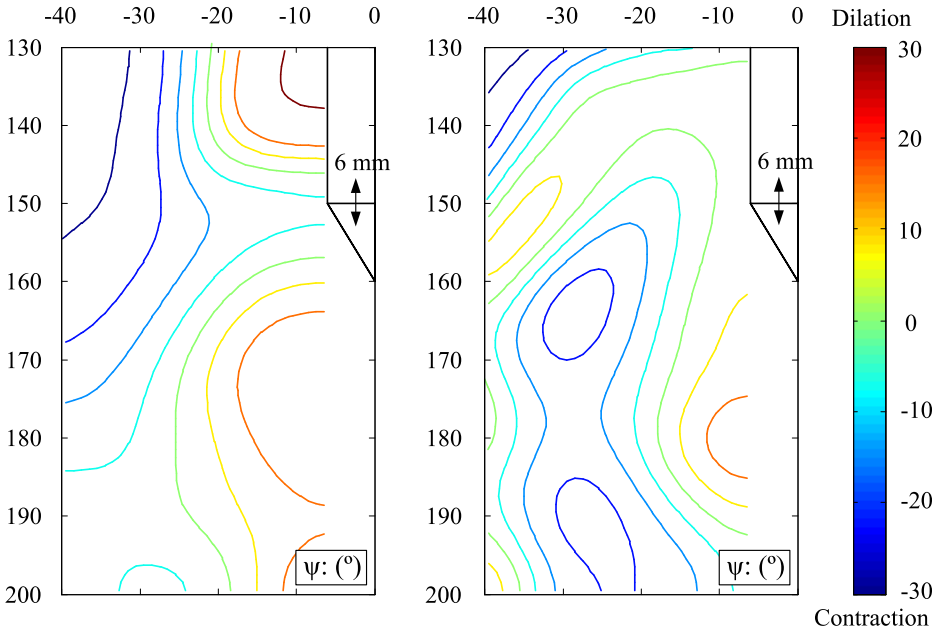

(c) Dense sand (Y = 150 mm) (d) Loose sand (Y = 150 mm)

Figure 4.40 Distributions of dilation angle over the interval of penetration ($6\,mm$): (a) Dense sand ($Y = 60\,mm$); (b) Loose sand ($Y = 60\,mm$); (c) Dense sand ($Y = 150\,mm$); (d) Loose sand ($Y = 150\,mm$)

4.5 Layered Effects on Soil Deformation

For penetrating in sand layers with different D_R, penetration resistance senses the effect of the approaching layer and is also affected by the upper soil when developing the resistance in a new-coming layer, as presented in Section 4.2.4. The differences of soil deformation for penetration in dense sand and loose sand are highlighted and illustrated throughout Section 4.3 and Section 4.4. It is also interesting to present the layered effects on soil deformation, which have not been found obviously shown in the literature. Therefore, this section focuses on the results of soil deformation for tests with layered soils (MP II-04 $\sim$ MP II-07), and the discussion attempts to provide the layered effects on soil deformation.

4.5.1 Contours of cumulative displacements

The cumulative displacement contours for dense sand (MP II-02) and loose sand (MP II-03) were provided in Figure 4.12 and Figure 4.13, in which smaller displacement zones were found in loose sand. Figure 4.41 offers the cumulative vertical displacement contours after 160 mm of penetration for all tests in layered soils. A concave shape of contours around the loose-dense interface is evident for Δy (Figure 4.41a), whereas the shape around the dense-loose interface is convex (Figure 4.41b). This concave shape shows that soil at the interface has relatively smaller vertical movement than both soil layers, resulting in two large displacement zones at some distances above and beneath the interface. The convex shape indicates the large deformation region concentrating around the soil interface. It can be explained by that the effect of compaction is increased in loose sand and the settlement of the lower sand layer is cumulated. Similar trends are also shown for tests with three-layers of sands: MP II-06 (Figure 4.41c) and MP II-07 (Figure 4.41d). The profiles with curvature are indicative of the layered effects with the concave and convex; large vertical displacement is mainly found around the interface from dense to loose. More details of the cumulative horizontal, vertical, and total displacement contours are also provided in Appendix A (Figures A.1 $\sim$ A.4).

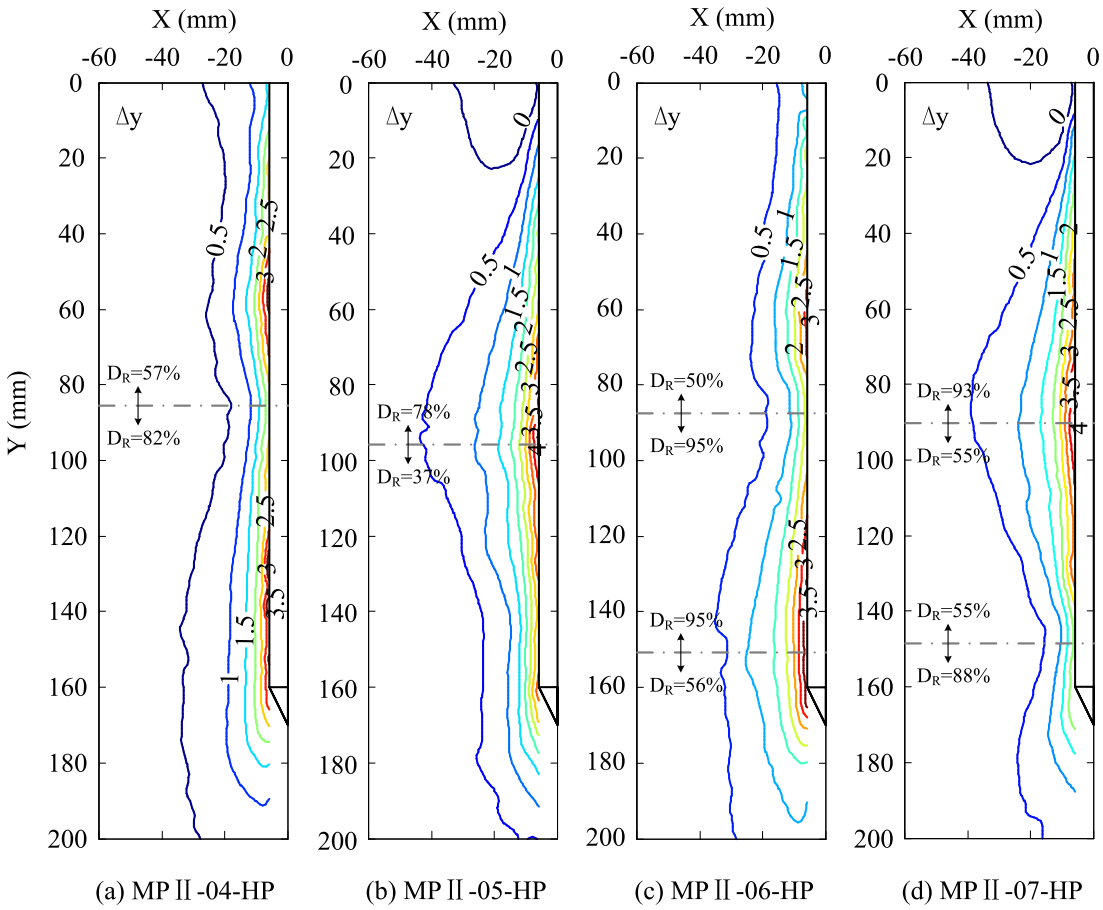

Figure 4.41 Cumulative vertical displacement contours of layered tests: (a) MP II-04; (b) MP II-05; (c) MP II-06; (d) MP II-07

4.5.2 Profiles of horizontal and vertical displacements

The profiles of the normalised cumulative displacements ($\Delta x/R$, $\Delta y/R$) for soil with different offset ($X/R = 2 \rightarrow 6$) in layered sand tests are provided in Figure A.5 and Figure A.6 (Appendix A), which can be compared with the results from the uniform sand tests (Figure 4.14). The observation from the contours in Figures A.1 $\sim$ A.4 (Appendix A) is clearly quantified from the profiles. Besides the larger displacements for soil closer to the probe, the effect of soil interface seems to be more distinct with considerable curvatured profiles.

Figure 4.42 shows the vertical displacement at $X/R = 2$ from the various uniform and layered tests in order to illustrate better the layered effects. From the results of $\Delta y/R$ in loose over dense sand, the peak above the interface occurs at around $2B$, where the penetration resistance starts to be affected, as shown in Figure 4.10 (Section 4.2.4). The influence zone beneath the interface is not obvious due to the smooth curves. For

the test with dense over loose sand, the peak occurs at the interface, and the influence zone in loose sand is about $4B$, based on the inflection point in the profile. By comparison, Z_w of MP II-05 in the penetration resistance curve is $\approx 1B$ (Figure 4.11a), indicating that a significantly larger influence zone of soil deformation exists in the lower soil layer than in results of penetration resistance. The reason can be attributed to the compaction effects below the probe tip with penetration; thus the layered effects on soil deformation are more obvious in the lower soil layer.

Similarly, for MP II-06-HP, the vertical displacement in the sandwiched dense layer increases until the cone tip is approaching the underlying loose sand layer. On the contrary, for MP II-07-HP, the vertical displacement in the sandwiched loose sand layer decreases further when the probe is close to the lower soil interface, and the lowest value is observed at the interface due to the influence of the underlying dense sand. The layered effects are also shown in the comparisons of $\Delta y/R$ profiles of two-layered and three-layered sand tests in Figure 4.42. Correspondingly, the developments of the profiles of the normalised cumulative displacements ($\Delta x/R$, $\Delta y/R$) are shown in Figure A.7 and Figure A.8 (Appendix A) with different depths of penetration for soil at $X/R = 2$.

4.5.3 Layered effects on displacement profiles

The profiles of soil displacements indicate that the soil around the interface is deformed with effects of both soil layers. After $160\,mm$ of penetration, the profiles of soil interfaces are described in Figure 4.43, in comparison with the profiles of soil at the same location in uniform sand tests. The profiles of uniform tests seem to be similar for both dense and loose sand, except for deeper soil ($Y \approx 150\,mm$) where dense sand experiences larger indentation. However, the displacements at the soil interfaces appear to fall outside of the range of displacement from the uniform sand tests. The deformation of loose-dense interface is less than the profiles of both dense and loose sand, whereas more downdrag movement is evident for the dense-loose interface. The deformed profiles of two types of interfaces interpret the concave and convex shapes in the displacement patterns shown in the previous sections.

Cone tip resistance ratio (η') was proposed in Section 4.2.4 to evaluate the transition of

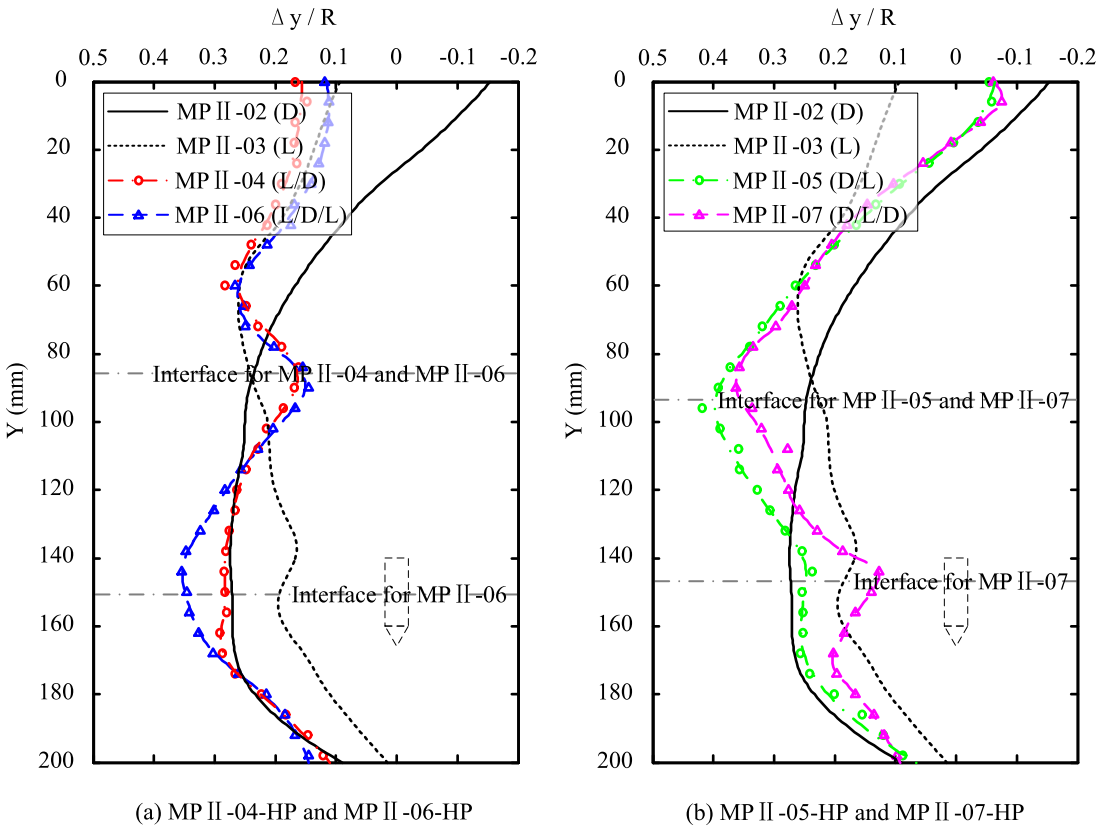

(a) MP II -04-HP and MP II -06-HP (b) MP II -05-HP and MP II -07-HP

Figure 4.42 Cumulative vertical displacement profiles for $X/R = 2$ after 160 *mm* of penetration: (a) MP II-04 and MP II-06; (b) MP II-05 and MP II-07

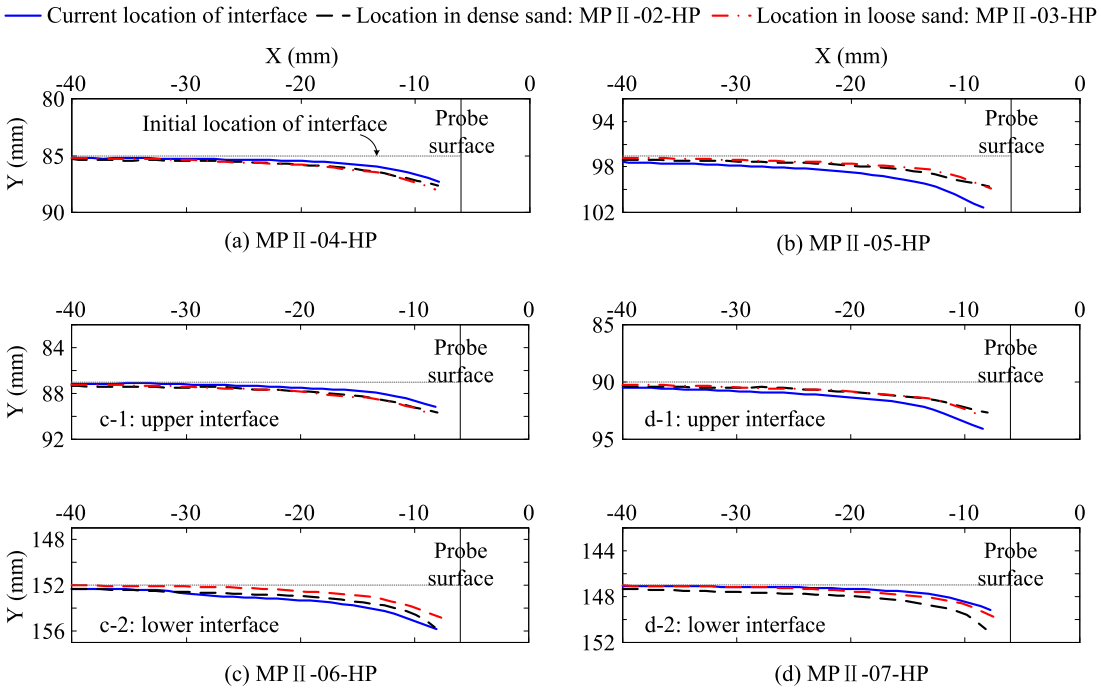

(a) MP II -04-HP (b) MP II -05-HP

(c) MP II -06-HP (d) MP II -07-HP

Figure 4.43 Profiles of soil interfaces after 160 *mm* of penetration for tests: MP II-04 ∼ MP II-07

q_c (or Q) when penetrating in layered soils. Similarly, the changes of soil deformation can also be treated as a ratio (ξ') transforming from weak soil into strong soil. Due to

the different trends of layered effects on horizontal and vertical displacements as described previously, ξ' is evaluated for Δx and Δy separately, as expressed in Equation (4.10).

$$\xi'_{\Delta x} = \frac{\Delta x - \Delta x|_{weak}}{\Delta x|_{strong} - \Delta x|_{weak}}$$
$$\xi'_{\Delta y} = \frac{\Delta y - \Delta y|_{weak}}{\Delta y|_{strong} - \Delta y|_{weak}} \tag{4.10}$$

Figure 4.44 presents the evaluation of layered effects on soil deformation for the test with loose over dense sand (MP II-04). The results of $\Delta x/R$ and $\Delta y/R$ for soil at $X/R = 2$ are shown in subplot (a) with reference lines of dense and loose sand (modified from tests: MP II-02 and MP II-03 respectively). Profiles of $\xi'_{\Delta x}$ and $\xi'_{\Delta y}$ are provided in subplots (b) and (c). The transition of $\xi'_{\Delta x}$ is believed to be similar with that of η', as shown in Figure 4.10; the ratio varies between 0 (loose sand) and 1 in dense sample, although the scatter in loose sand is large. $\xi'_{\Delta y}$ also transforms from 0 to 1, while the ratio around the interface ranges widely beyond the '$0 \sim 1$' zone. This is attributed to the layered effects on Δy and the crossing curves of the uniform sand profiles. $\xi'_{\Delta y}$ increases up to approximately 4 to the soil slightly below the interface, and drops dramatically to a negative $\xi'_{\Delta y}$ trough at $H/B \approx 2$. After that, $\xi'_{\Delta y}$ increases gradually to 1 with deformation of dense sand.

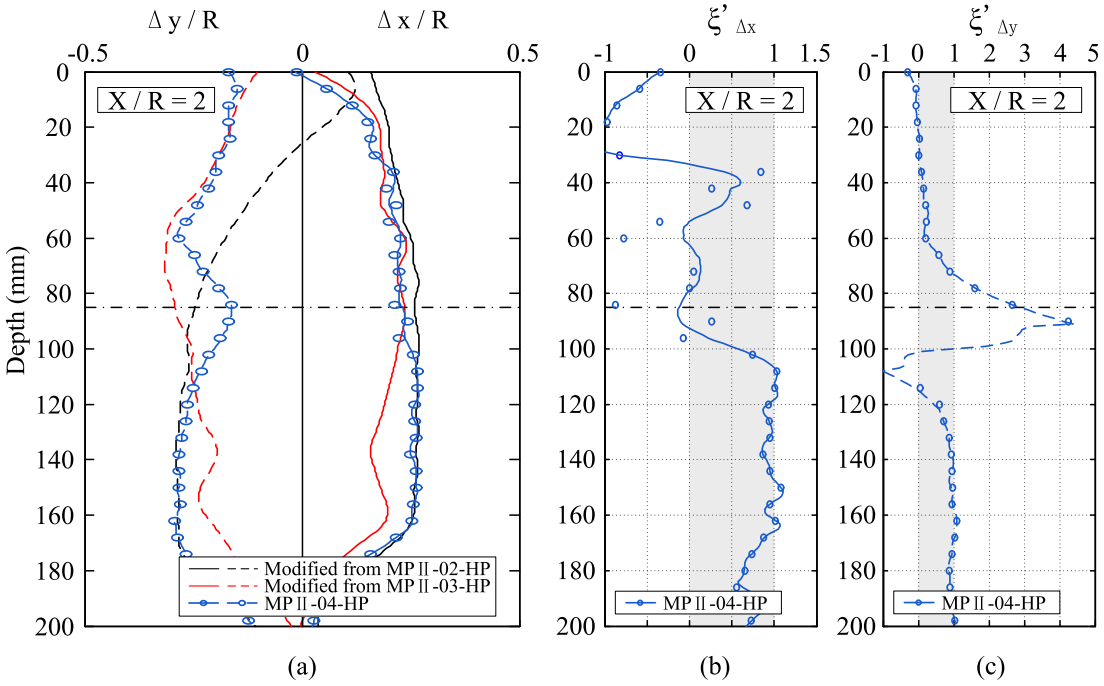

Figure 4.44 Layered effects on soil deformation ($X/R = 2$) for test: MP II-04

As smaller curvature of displacement profiles were observed for soil with larger offset from the probe, the soil deformation ratio ξ' is examined with variation of offset ($X/R = 2 \rightarrow 6$) in Figure 4.45. From the curves of $\xi'_{\Delta x}$ and $\xi'_{\Delta y}$, there is little systematic variation with offset. The large scatter in $\xi'_{\Delta x}$ curves is attributed to the similar horizontal displacement in dense and loose sand; the trends of $\xi'_{\Delta y}$ is relatively clear. The general tendency of layered effects is verified with less dependency on X/R.

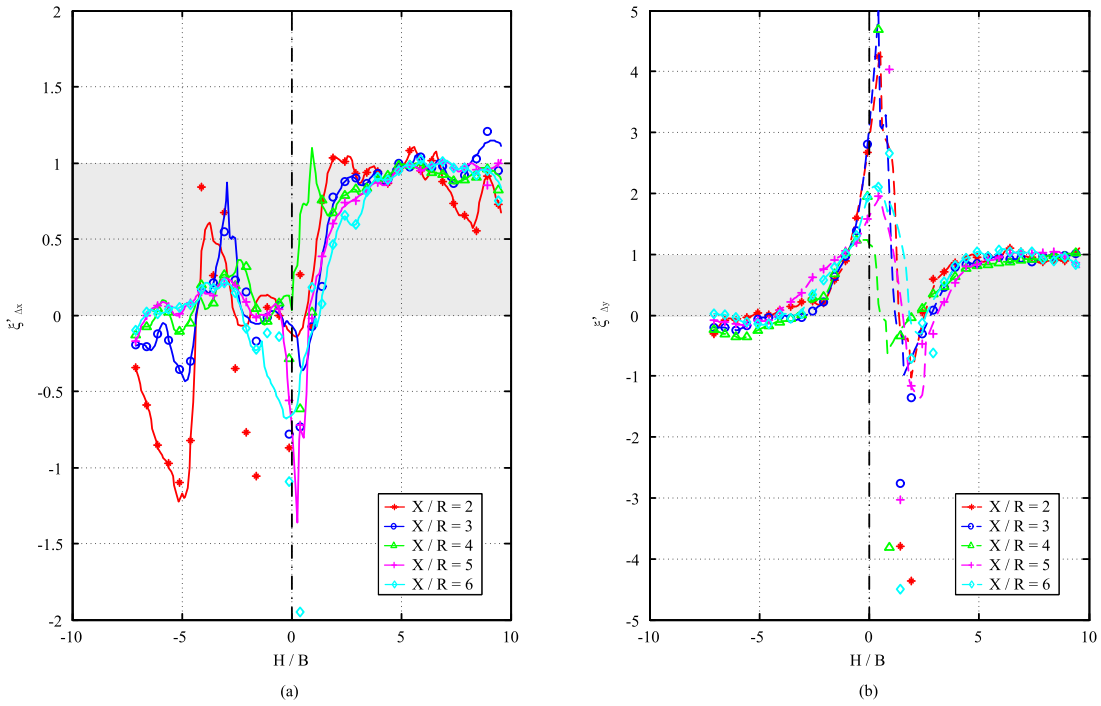

Figure 4.45 ξ' with variation of offset: $X/R = 2 \rightarrow 6$ (MP II-04)

The transition of $\xi'_{\Delta y}$ for all layered soil tests are provided in Figure 4.46 for two-layered soils (subplot a) and three-layered soils (subplot b, where H_t is the thickness of the sandwiched soil layer). With comparison of η' in Figure 4.11, the layered effects are obvious, while the thin-layer effect is shown with peak values occurring at the interfaces. The dramatic variation of $\xi'_{\Delta y}$ near the first soil interface seems to be attributed to the surface effects, whereas the transition around the second soil interface (Figure 4.46b) shows more smooth variation which occurs generally below the soil interface. Although the results of soil deformation are affected by the ground surface effects, the variation of soil displacement with different profiles of soil density and the trends of layered effects imply the layering mechanisms for penetration.

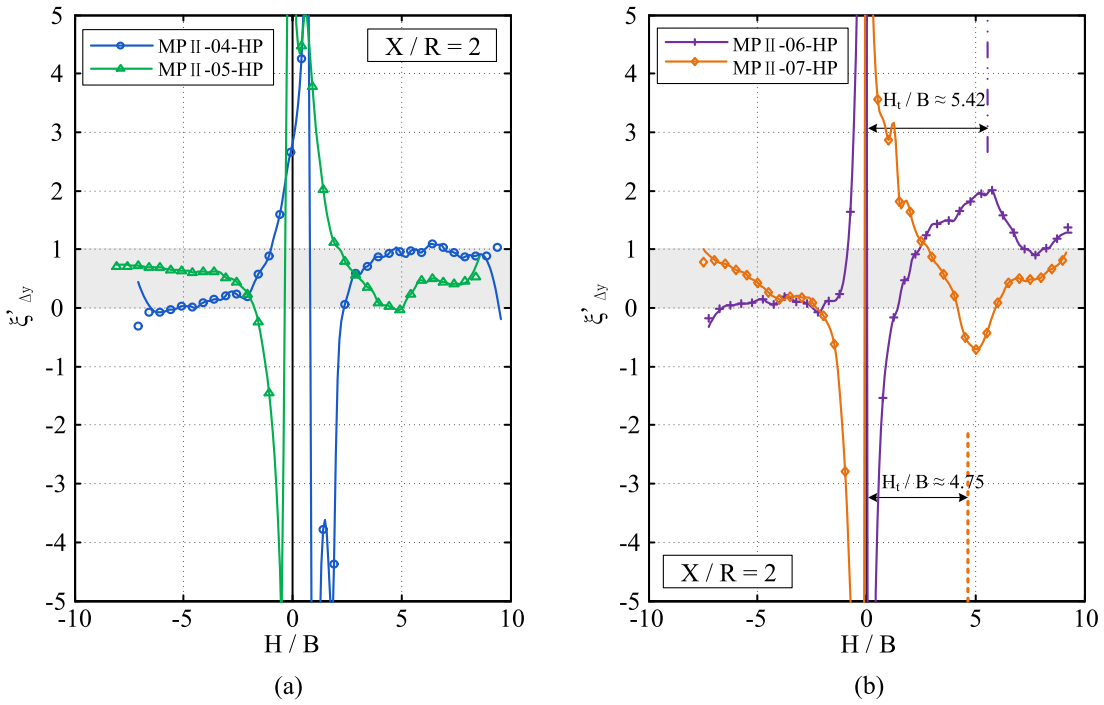

Figure 4.46 Layered effects on soil deformation ($X/R = 2$) for tests with: (a) two-layered soils; and (b) three-layered soils

4.6 Chapter Summary

The results of the centrifuge tests presented in this chapter provided an investigation of penetration in uniform and layered sands in an axisymmetric model. Both dense sand and loose sand had linear increases of tip resistance with depth. However, the value of tip resistance in the dense sand ($D_R = 90\,\%$) was found to be about $2 \sim 3$ times that for loose sand ($D_R = 50\,\%$). The magnitude of q_c for $50\,g$ tests was found to be $10 \sim 12$ times that from $1\,g$ tests, which implied that the resistances increased with stress level at a decreasing rate. The tip resistance ratio η' was proposed to illustrate the transition of q_c from one soil layer to another. The influence zone in stronger soil was larger than that in weak soil, and the size was likely dependent on the relative density of both soil layers, which led to the variation of thin-layer effect in different scenarios.

To analyse the displaced soil around the penetrometer, the half-probe tests together with the image-based measurement technique provided the results of displacements and the deduced strains during the process of penetration. The pattern of cumulative displacement showed reasonable similarity to cylindrical cavity expansion around the shaft, and spherical expansion around the cone. Comparing to loose sand, the size of

influence zone for dense sand was larger, and the heaving effect near the ground surface was more evident. The decay of displacement with offset from the pile implied that the lateral influence zone is about $5B$ wide for dense sand, and approximately $3.5B$ for loose sand. From the trajectories of soil elements, it was notable that the major proportion of the displacement occurred before the probe passed, and little contribution was made during $h > 0$. In addition, the directions of the principal strain rate provided some clues for estimation of directions and distributions of the principal stress rate. Strain reversal during penetration in the axisymmetric model was quantified to emphasise the severe distortion with rotation and dilation.

Parameters ($\xi'_{\Delta x}$ and $\xi'_{\Delta y}$) were proposed to evaluate the transition of displacement profiles for penetration in layered soils. The vertical displacement in loose sand overlying dense sand was affected within $2B$ above the interface, while the influence zone was $4B$ in an underlying loose sand. The deformation of loose-dense interface was less than the profiles of both dense and loose sand, and more downdrag movement was evident for the dense-loose interface. ξ' clearly indicated the layered effects on soil deformation, and did not appear to be affected by the offset.

Chapter 5

Cavity Expansion in Two Concentric Regions of Soil

5.1 Introduction

As discussed in Section 2.4, cavity expansion theory has been extensively developed and widely used for geotechnical applications. However, very little work has been done to consider the effect of distinct soil layers within the framework of cavity expansion analyses. Elastic solutions and assumptions of incompressibility are inadequate to describe soil behaviour, especially for problems with large deformation.

In this chapter, the analytical solution described in Yu and Houlsby (1991) is extended in order to consider a two concentric regions of soil. The soil is treated as an isotropic dilatant elastic-perfectly plastic material with a Mohr-Coulomb yield criterion and a non-associated flow rule. Large-strain quasi-static expansion of both spherical and cylindrical cavities is considered.

The chapter begins with a general definition of the problem and the necessary geometric parameters (Section 5.2). The following Section 5.3 considers the most general expansion problem within two concentric soils and derives expressions for stresses, strains, and displacements within elastic and plastic regions. In Section 5.4, the cavity expansion solution is then validated against results obtained using the Finite Element Method (FEM). Further results and parametric analyses are then presented in Section 5.5 with focus placed on the resulting pressure-expansion curves and the development

of plastic regions within the two regions of soil. A discussion of the application of the proposed method and its limitations is provided in Section 5.6, followed by concluding remarks.

5.2 Definitions of Cavity in Two Concentric Regions of Soil

The problem involves three concentric zones; (i) an inner zone representing the expanding cavity, (ii) a second zone representing Soil A, and (iii) a bounding region which extends to infinity and represents Soil B, as shown in Figure 5.1a. Initially, the cavity has a radius a_0 and the interface between Soils A and B is located at a radial distance b_0 from the centre of the cavity. The soils are assumed to be isotropic homogeneous media, therefore an initial hydrostatic stress P_0 acts throughout both Soils A and B as well as within the cavity. Note that a tension positive notation is used in this chapter, for consistency with Yu and Houlsby (1991).

When the cavity pressure P_a increases slowly from its initial value P_0, the radius of cavity and Soil A/B interface are expanded to a and b, respectively (Figure 5.1b). The pressure at the Soil A/B interface is given by P_b. Depending on material properties (and adopting the Mohr-Coulomb yield criterion), a plastic region may form within either of the soils A or B and extend to some radial distance c_A or c_B, respectively. For a given increment of cavity expansion, the initial plastic-elastic interfaces in soils A and B are given by c_{0A} and c_{0B}, respectively. The radial stresses at the plastic-elastic interfaces for soils A and B are defined as P_{c_A} and P_{c_B}, respectively.

As in the work of Yu and Houlsby (1991), the soils are modelled as an isotropic dilatant elastic-perfectly plastic material, obeying Hooke's law for elastic analysis and the Mohr-Coulomb yield criterion with a non-associated flow rule for plastic analysis. The properties of Soils A and B are denoted by subscripts 1 and 2, respectively: Young's modulus (E_1, E_2), Poisson's ratio (ν_1, ν_2), cohesion (C_1, C_2), friction angle (ϕ_1, ϕ_2), and dilation angle (ψ_1, ψ_2).

To combine both spherical and cylindrical analyses, the parameter k is used to indicate spherical analysis ($k = 2$) or cylindrical analysis ($k = 1$). It should be noted that for

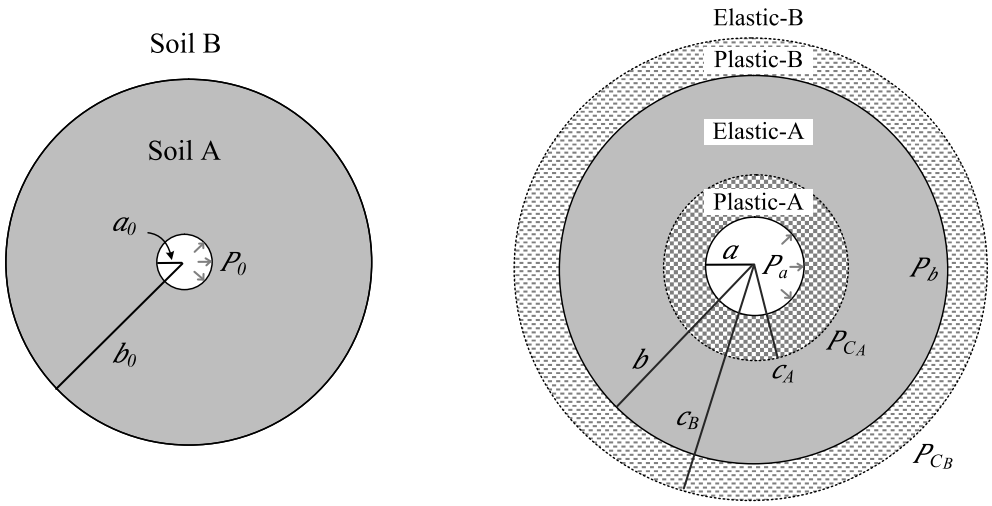

Figure 5.1 Schematic view of the model of cavity expansion in two concentric regions of soil

the cylindrical case, plane strain conditions in the z direction are assumed and the axial stress is assumed as the intermediate principal stress, which is satisfied for most realistic values of soil parameters, as discussed in Yu and Houlsby (1991). In accordance with Yu (2000), the following parameters are used for mathematical convenience (definitions apply separately to Soil A and B in current notations):

$$G_1 = \frac{E_1}{2(1+\nu_1)} \qquad G_2 = \frac{E_2}{2(1+\nu_2)} \tag{5.1a}$$

$$M_1 = \frac{E_1}{1-\nu_1^2(2-k)} \qquad M_2 = \frac{E_2}{1-\nu_2^2(2-k)} \tag{5.1b}$$

$$Y_1 = \frac{2C_1\cos\phi_1}{1-\sin\phi_1} \qquad Y_2 = \frac{2C_2\cos\phi_2}{1-\sin\phi_2} \tag{5.1c}$$

$$\alpha_1 = \frac{1+\sin\phi_1}{1-\sin\phi_1} \qquad \alpha_2 = \frac{1+\sin\phi_2}{1-\sin\phi_2} \tag{5.1d}$$

$$\beta_1 = \frac{1+\sin\psi_1}{1-\sin\psi_1} \qquad \beta_2 = \frac{1+\sin\psi_2}{1-\sin\psi_2} \tag{5.1e}$$

$$\gamma_1 = \frac{\alpha_1(\beta_1+k)}{k(\alpha_1-1)\beta_1} \qquad \gamma_2 = \frac{\alpha_2(\beta_2+k)}{k(\alpha_2-1)\beta_2} \tag{5.1f}$$

$$\delta_1 = \frac{Y_1+(\alpha_1-1)P_0}{2(\alpha_1+k)G_1} \qquad \delta_2 = \frac{Y_2+(\alpha_2-1)P_0}{2(\alpha_2+k)G_2} \tag{5.1g}$$

During cavity expansion, plastic regions in the two concentric soils are generated and develop depending on the relevant properties and profiles of soils A and B. Considering all possible situations, the expansion process would follow one of the routes in the flow chart illustrated in Figure 5.2, which also provides a definition of some notation. Generally, during expansion of the cavity from a_0 to a, an elastic stage ($A_E B_E$) appears initially, followed by plastic regions developing in both Soils A and B as a increases ($A_{PE} B_{PE}$). Ultimately, as a is increased further, Soil A becomes fully plastic ($A_P B_{PE}$) (Soil B extends to infinity and therefore never becomes fully plastic). The events at the circular nodes in the flowchart describe the situation of expansion and determine the appropriate state of soil to be considered. The solutions provided here are for the most general case of expansion ($A_{PE} B_{PE}$); all the scenarios described in Figure 5.2 can be deduced from this general solution.

5.3 Analytical Solutions for Cavity Expansion

5.3.1 Solutions in elastic regions

As illustrated in Figure 5.1, for an arbitrary radial distance r, the material is elastic in the zones where $r > c_B$ (Soil B) and where $c_A < r < b$ (Soil A). Under conditions of radial symmetry, the stresses within the soils around the cavity must satisfy the following equation of equilibrium:

$$\sigma_\theta - \sigma_r = \frac{r}{k} \frac{\partial \sigma_r}{\partial r} \tag{5.2}$$

where σ_r and σ_θ are stresses acting in the radial and tangential directions, respectively.

Correspondingly, the radial and tangential strain for small-strain analysis in the elastic regions can be expressed as a function of the radial displacement u:

$$\varepsilon_r = \frac{du}{dr} \tag{5.3}$$

$$\varepsilon_\theta = \frac{u}{r} \tag{5.4}$$

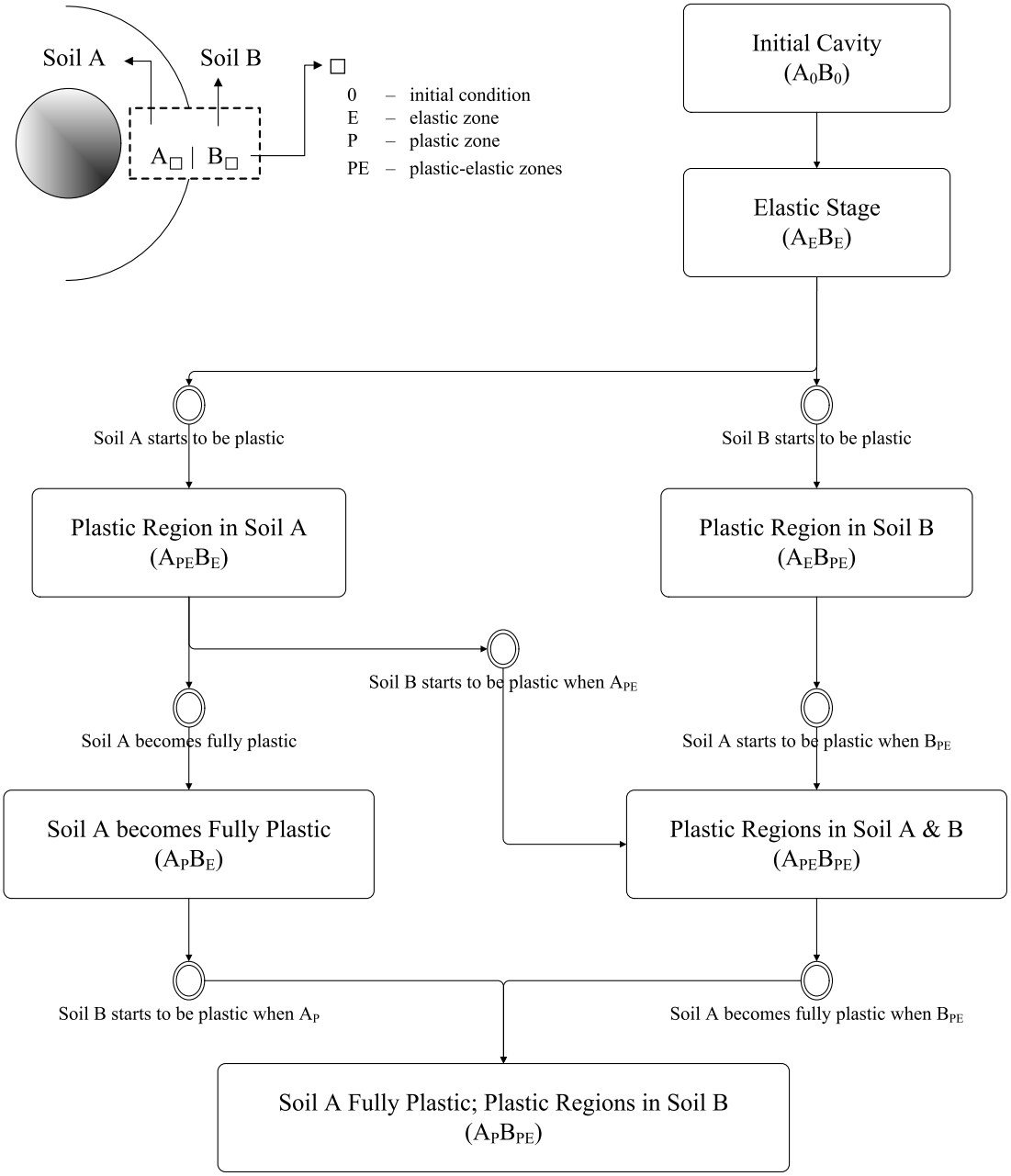

Figure 5.2 Flow chart of cavity expansion in two concentric regions of soil

5.3.1.1 Elastic region in Soil A

For the elastic region in Soil A ($c_A < r < b$), with Hooke's law, the solutions for the radial displacement and stresses are expressed as (Yu and Houlsby, 1991)

$$u = D_1 r + \frac{D_2}{r^k} \tag{5.5}$$

$$\sigma_r = \frac{M_1}{-k\left[\frac{\nu_1}{1-\nu_1(2-k)}\right]^2 + [1-\nu_1(k-1)]} \left\{[1-\nu_1(k-1)]\left(D_1 - k\frac{D_2}{r^{k+1}}\right) + k\frac{\nu_1}{1-\nu_1(2-k)}\left(D_1 + \frac{D_2}{r^{k+1}}\right)\right\} - P_0 \quad (5.6)$$

$$\sigma_\theta = \frac{M_1}{-k\left[\frac{\nu_1}{1-\nu_1(2-k)}\right]^2 + [1-\nu_1(k-1)]} \left[\frac{\nu_1}{1-\nu_1(2-k)}(D_1 - k\frac{D_2}{r^{k+1}}) + (D_1 + \frac{D_2}{r^{k+1}})\right] - P_0 \quad (5.7)$$

where D_1 and D_2 are integration constants defined as

$$D_1 = \frac{(c_A - c_{0A})\,{c_A}^k - (b - b_0)\,b^k}{{c_A}^{k+1} - b^{k+1}} \quad (5.8)$$

$$D_2 = \frac{(c_{0A}\,b - c_A\,b_0)\,{c_A}^k\,b^k}{{c_A}^{k+1} - b^{k+1}} \quad (5.9)$$

The solutions are subject to two stress boundary conditions:

$$\sigma_r|_{r=c_A} = -P_{c_A} \quad (5.10)$$

$$\sigma_r|_{r=b} = -P_b \quad (5.11)$$

5.3.1.2 Elastic region in Soil B

Similarly, the following solutions for the radial displacement and stress in Soil B ($r > c_B$) are obtained:

$$u = {c_B}^k\,(c_B - c_{0B})\,\frac{1}{r^k} \quad (5.12)$$

$$\sigma_r = \frac{M_2}{-k\left[\frac{\nu_2}{1-\nu_2(2-k)}\right]^2 + [1-\nu_2(k-1)]} \left\{k\left[\frac{\nu_2}{1-\nu_2(2-k)} - [1-\nu_2(k-1)]\right]\frac{{c_B}^k\,(c_B - c_{0B})}{r^{k+1}}\right\} - P_0 \quad (5.13)$$

$$\sigma_\theta = \frac{M_2}{-k\left[\frac{\nu_2}{1-\nu_2(2-k)}\right]^2 + [1-\nu_2(k-1)]} \left[\left(1 - k\frac{\nu_2}{1-\nu_2(2-k)}\right)\frac{{c_B}^k\,(c_B - c_{0B})}{r^{k+1}}\right] - P_0 \quad (5.14)$$

which is subject to the stress boundary condition:

$$\sigma_r|_{r=c_B} = -P_{c_B} \tag{5.15}$$

5.3.2 Solutions in plastic regions in Soil A

In order to account for the effect of large strain in the plastic regions, logarithmic strains are adopted, namely

$$\varepsilon_r = \ln\left(\frac{dr}{dr_0}\right) \tag{5.16}$$

$$\varepsilon_\theta = \ln\left(\frac{r}{r_0}\right) \tag{5.17}$$

Using the tension positive notation, the Mohr-Coulomb yield condition in Soil A during cavity expansion is

$$\alpha_1 \sigma_\theta - \sigma_r = Y_1 \tag{5.18}$$

where α_1 and Y_1 are functions related to friction angle and cohesion (Equation 5.1). It may be noted that when the friction angle is zero, the Mohr-Coulomb yield function reduces to the Tresca criterion.

The stress components in the plastic region of Soil A must satisfy equilibrium (Equation 5.2) and the yield condition (Equation 5.18) as follows:

$$\sigma_r = \frac{Y_1}{\alpha_1 - 1} + A_1 r^{-\frac{k(\alpha_1-1)}{\alpha_1}} \tag{5.19}$$

$$\sigma_\theta = \frac{Y_1}{\alpha_1 - 1} + \frac{A_1}{\alpha_1} r^{-\frac{k(\alpha_1-1)}{\alpha_1}} \tag{5.20}$$

where A_1 is a constant of integration and where σ_r has two stress boundary conditions:

$$\sigma_r|_{r=c_A} = -P_{c_A} \tag{5.21}$$

$$\sigma_r|_{r=a} = -P_a \tag{5.22}$$

Combining the expressions in Equation (5.21) and Equation (5.22) leads to

$$\frac{P_a + \frac{Y_1}{\alpha_1 - 1}}{P_{c_A} + \frac{Y_1}{\alpha_1 - 1}} = \left(\frac{c_A}{a}\right)^{\frac{k(\alpha_1 - 1)}{\alpha_1}} \tag{5.23}$$

$$A_1 = -(P_a + \frac{Y_1}{\alpha_1 - 1})\, a^{\frac{k(\alpha_1 - 1)}{\alpha_1}} = -(P_{c_A} + \frac{Y_1}{\alpha_1 - 1})\, c_A^{\frac{k(\alpha_1 - 1)}{\alpha_1}} \tag{5.24}$$

For the displacement analysis in the plastic region, total strain is considered as the sum of elastic and plastic contributions, using superscripts e and p respectively. Elastic strain (equivalent to strain rate $\dot{\varepsilon}$ for this case because initial strains are zero) can be derived from Equation (5.6) and Equation (5.7):

$$\dot{\varepsilon_r}^e = \frac{1}{M_1}\left[\dot{\sigma}_r - \frac{k\,\nu_1}{1 - \nu_1\,(2-k)}\,\dot{\sigma}_\theta\right] \tag{5.25}$$

$$\dot{\varepsilon_\theta}^e = \frac{1}{M_1}\left\{-\frac{\nu_1}{1 - \nu_1\,(2-k)}\,\dot{\sigma}_r + [1 - \nu_1\,(k-1)]\,\dot{\sigma}_\theta\right\} \tag{5.26}$$

where $\dot{(\,)}$ is the corresponding incremental form.

The non-associated Mohr-Coulomb flow rule for loading phase in Soil A can be expressed as

$$\frac{\dot{\varepsilon_r}^p}{\dot{\varepsilon_\theta}^p} = \frac{\dot{\varepsilon}_r - \dot{\varepsilon_r}^e}{\dot{\varepsilon}_\theta - \dot{\varepsilon_\theta}^e} = -\frac{k}{\beta_1} \tag{5.27}$$

where β_1 is a function of dilation angle. If $\beta_1 = \alpha_1$ (dilation angle = friction angle), then the flow rule for Soil A is said to be fully associated. This plastic-flow rule was proposed by Davis (1968), assuming that the soil dilates plastically at a constant rate to model the dilatant soil behaviour. The same flow rule is also applied to Soil B with the corresponding dilation angle (ψ_2).

Substituting elastic strain Equations (5.25) and (5.26) into the plastic-flow rule (Equation 5.27) results in

$$\begin{aligned}\beta_1\,\dot{\varepsilon}_r + k\,\dot{\varepsilon}_\theta =& \frac{1}{M_1}\left[\beta_1 - \frac{k\,\nu_1}{1 - \nu_1\,(2-k)}\right]\dot{\sigma}_r \\ &+ \frac{1}{M_1}\left[k\,(1 - 2\,\nu_1) + 2\,\nu_1 - \frac{k\,\nu_1\,\beta_1}{1 - \nu_1\,(2-k)}\right]\dot{\sigma}_\theta\end{aligned} \tag{5.28}$$

With logarithmic strain equations (5.16, 5.17), substituting equations (5.19, 5.20) and

applying the initial stress conditions into Equation (5.28) leads to

$$\ln\left[\left(\frac{r}{r_0}\right)^{\frac{k}{\beta_1}}\cdot\frac{dr}{dr_0}\right]=\ln\chi_1+\mu_1 A_1\left(\frac{1}{r}\right)^{\frac{k(\alpha_1-1)}{\alpha_1}} \tag{5.29}$$

where

$$\chi_1=exp\left\{\frac{(\beta_1+k)(1-2\nu_1)[1+(2-k)\nu_1][Y_1+(\alpha_1-1)P_0]}{E_1(\alpha_1-1)\beta_1}\right\} \tag{5.30}$$

$$\mu_1=\frac{1+\nu_1(2-k)}{E_1\alpha_1\beta_1}$$
$$\{[\beta_1+(k-2)\nu_1\beta_1-k\nu_1]\alpha_1+k(1-\nu_1-\nu_1\beta_1)\} \tag{5.31}$$

By means of transformation $\rho=-A_1\left(\frac{1}{r}\right)^{\frac{k(\alpha_1-1)}{\alpha_1}}$, Equation (5.29) can be integrated over the interval [c_A, r], leading to

$$\frac{\chi_1}{\gamma_1}\cdot(-A_1)^{-\gamma_1}\cdot\left({c_{0A}}^{\frac{\beta_1+k}{\beta_1}}-{r_0}^{\frac{\beta_1+k}{\beta_1}}\right)=\int_{P_{c_A}+\frac{Y_1}{\alpha_1-1}}^{\rho}e^{\mu_1\rho}\cdot\rho^{-1-\gamma_1}\,d\rho \tag{5.32}$$

By putting $r=a$, $r_0=a_0$ and $\rho\,|_{r=a}=P_a+\frac{Y_1}{\alpha_1-1}$, we find:

$$\frac{\chi_1}{\gamma_1}\left(P_a+\frac{Y_1}{\alpha_1-1}\right)^{-\gamma_1}\cdot\left[\left(\frac{c_{0A}}{a}\right)^{\frac{\beta_1+k}{\beta_1}}-\left(\frac{a_0}{a}\right)^{\frac{\beta_1+k}{\beta_1}}\right]$$
$$=\int_{P_{c_A}+\frac{Y_1}{\alpha_1-1}}^{P_a+\frac{Y_1}{\alpha_1-1}}e^{\mu_1\rho}\cdot\rho^{-1-\gamma_1}\,d\rho \tag{5.33}$$

With the aid of the series expansion

$$e^{\mu_1\rho}=\sum_{n=0}^{\infty}\frac{(\mu_1\rho)^n}{n!} \tag{5.34}$$

Equation (5.33) is found to be

$$\frac{\chi_1}{\gamma_1}\left(P_a+\frac{Y_1}{\alpha_1-1}\right)^{-\gamma_1}\cdot\left[\left(\frac{c_{0A}}{a}\right)^{\frac{\beta_1+k}{\beta_1}}-\left(\frac{a_0}{a}\right)^{\frac{\beta_1+k}{\beta_1}}\right]$$
$$=\sum_{n=0}^{\infty}\begin{cases}\frac{{\mu_1}^n}{n!}\ln\left[\frac{P_a+\frac{Y_1}{\alpha_1-1}}{P_{c_A}+\frac{Y_1}{\alpha_1-1}}\right] & \text{if } n=\gamma_1\\ \frac{{\mu_1}^n}{n!(n-\gamma_1)}\left[\left(P_a+\frac{Y_1}{\alpha_1-1}\right)^{n-\gamma_1}-\left(P_{c_A}+\frac{Y_1}{\alpha_1-1}\right)^{n-\gamma_1}\right] & \text{otherwise}\end{cases} \tag{5.35}$$

To calculate the distribution of displacements within the plastic region of Soil A, without imposing any boundary conditions, Equation (5.32) can be written as

$$\frac{\chi_1}{\gamma_1}\left(P_a+\frac{Y_1}{\alpha_1-1}\right)^{-\gamma_1}\cdot\left[\left(\frac{c_{0A}}{a}\right)^{\frac{\beta_1+k}{\beta_1}}-\left(\frac{r_0}{a}\right)^{\frac{\beta_1+k}{\beta_1}}\right]=\Lambda_1(r)$$
$$=\sum_{n=0}^{\infty}\begin{cases}\frac{{\mu_1}^n}{n!}\left[\ln\rho-\ln\left(P_{c_A}+\frac{Y_1}{\alpha_1-1}\right)\right] & \text{if } n=\gamma_1\\ \frac{{\mu_1}^n}{n!(n-\gamma_1)}\left[\rho^{\,n-\gamma_1}-\left(P_{c_A}+\frac{Y_1}{\alpha_1-1}\right)^{n-\gamma_1}\right] & \text{otherwise}\end{cases} \tag{5.36}$$

Hence displacement u is:

$$u=r-r_0$$
$$=r-\left[-\Lambda_1(r)\cdot\frac{\gamma_1}{\chi_1}\cdot\left(P_a+\frac{Y_1}{\alpha_1-1}\right)^{\gamma_1}+\left(\frac{c_{0A}}{a}\right)^{\frac{\beta_1+k}{\beta_1}}\right]^{\frac{\beta_1}{\beta_1+k}}\cdot a \tag{5.37}$$

To calculate the strain distribution, Equation (5.37) can be rewritten in terms of $\frac{r}{r_0}$ and derived to give an equation in terms of $\frac{dr}{dr_0}$. The final strain distribution is then obtained using logarithmic strains for large-strain analysis.

5.3.3 Solutions in plastic regions in Soil B

Similarly, by using the corresponding equilibrium equation and yield condition, the stress components in the plastic region of Soil B are shown to be in the form

$$\sigma_r=\frac{Y_2}{\alpha_2-1}+A_2\,r^{-\frac{k(\alpha_2-1)}{\alpha_2}} \tag{5.38}$$

$$\sigma_\theta=\frac{Y_2}{\alpha_2-1}+\frac{A_2}{\alpha_2}\,r^{-\frac{k(\alpha_2-1)}{\alpha_2}} \tag{5.39}$$

where A_2 is a constant of integration and radial stress has two boundary conditions:

$$\sigma_r|_{r=c_B}=-P_{c_B} \tag{5.40}$$

$$\sigma_r|_{r=b}=-P_b \tag{5.41}$$

From the stress in the elastic region in Soil B, we can find

$$\frac{c_B}{b}=\left\{\frac{(k+\alpha_2)\left[Y_2+(\alpha_2-1)P_b\right]}{(k+1)\,\alpha_2\left[Y_2+(\alpha_2-1)P_0\right]}\right\}^{\frac{\alpha_2}{k(\alpha_2-1)}}=R_2{}^{\frac{\alpha_2}{k(\alpha_2-1)}} \tag{5.42}$$

where R_2 is a parameter which is related to the pressure at the interface between Soils A and B (P_b). The solution for plastic displacements in Soil B can be obtained by the

equations of Yu and Houlsby (1991), which provides the following for the pressure-expansion relationship:

$$\left(\frac{b}{b_0}\right)^{\frac{\beta_2+k}{\beta_2}} = \frac{{R_2}^{-\gamma_2}}{(1-\delta_2)^{\frac{\beta_2+k}{\beta_2}} - \frac{\gamma_2}{\chi_2}\Lambda_2(R_2,\mu_2)} \tag{5.43}$$

in which Λ_2 is defined by

$$\Lambda_2(R_2,\mu_2) = \sum_{n=0}^{\infty} \begin{cases} \frac{{\mu_2}^n}{n!}\ln R_2 & \text{if } n=\gamma_2 \\ \frac{{\mu_2}^n}{n!(n-\gamma_2)}\left[(R_2)^{n-\gamma_2}-1\right] & \text{otherwise} \end{cases} \tag{5.44}$$

and

$$\chi_2 = \exp\left\{\frac{(\beta_2+k)(1-2\nu_2)[1+(2-k)\nu_2][Y_2+(\alpha_2-1)P_0]}{E_2(\alpha_2-1)\beta_2}\right\} \tag{5.45}$$

$$\begin{aligned}\mu_2 =& \frac{(k+1)\delta_2[1-{\nu_2}^2(2-k)]}{(1+\nu_2)(\alpha_2-1)\beta_2} \\ & \left[\alpha_2\beta_2+k(1-2\nu_2)+2\nu_2-\frac{k\nu_2(\alpha_2+\beta_2)}{1-\nu_2(2-k)}\right]\end{aligned} \tag{5.46}$$

It should be noted that the expressions of μ_1 (Section 5.3.2) and μ_2 are simplified for the cases that k only equals 1 or 2 (cylindrical or spherical). To calculate the distribution of displacements in the plastic region of Soil B, displacement (u) can be written as the following equation, which in-turn can be used to derive the strain distribution:

$$\begin{aligned}u &= r - r_0 \\ &= r - \left[-\int_1^{\rho} e^{\mu_2\rho}\cdot\rho^{-1-\gamma_2}\,d\rho\cdot\frac{\gamma_2}{\chi_2} + (1-\delta_2)^{\frac{\beta_2+k}{\beta_2}}\right]^{\frac{\beta_2}{\beta_2+k}}\cdot c_B\end{aligned} \tag{5.47}$$

5.4 Validation with Finite Element Simulations

The accuracy of the analytical model was initially confirmed against results obtained with the fundamental solutions from Yu and Houlsby (1991) for the case where the properties of Soils A and B were identical. To further validate the analytical model, two Finite Element numerical models were developed in Abaqus/Standard and used to simulate the expansion of both spherical and cylindrical cavities, as shown in Figure 5.3. The axis-symmetric option was used in Abaqus in order to achieve spherical and cylindrical analyses using the 2D models. The cavity was expanded from an initial radius of $6\,mm$ under an initial pressure of $1\,kPa$. The initial radius of the Soil A/B in-

terface (given by b_0) was $30\,mm$, while Soil B had a radius D which was large enough to make boundary effects negligible. In the numerical simulations, the properties of both soils A and B were set as follows: $\nu = 0.2$, $\phi = 10^\circ$, $\psi = 10^\circ$, $C = 10\,kPa$. The effect of a distinct change in soil stiffness (due to concentric regions of soil) on the pressure expansion curves and the development of plastic radius is shown to be significant in Figure 5.4 and 5.5.

A total of four expansion tests were carried out using the numerical model in which the Young's modulus (E) of Soils A and B was either $1\,MPa$ or $10\,MPa$ (results presented in Figure 5.4). The labels on the figure indicate the model (analytical = CEM; numerical = FEM), followed by the value of Young's modulus of Soil A and B, respectively. Hence, the label CEM-10-1 relates to the analytical cavity expansion analysis results in which Soil A has $E_1 = 10\,MPa$ and Soil B has $E_2 = 1\,MPa$. Figure 5.4 shows that very good agreement between analytical and numerical results was obtained.

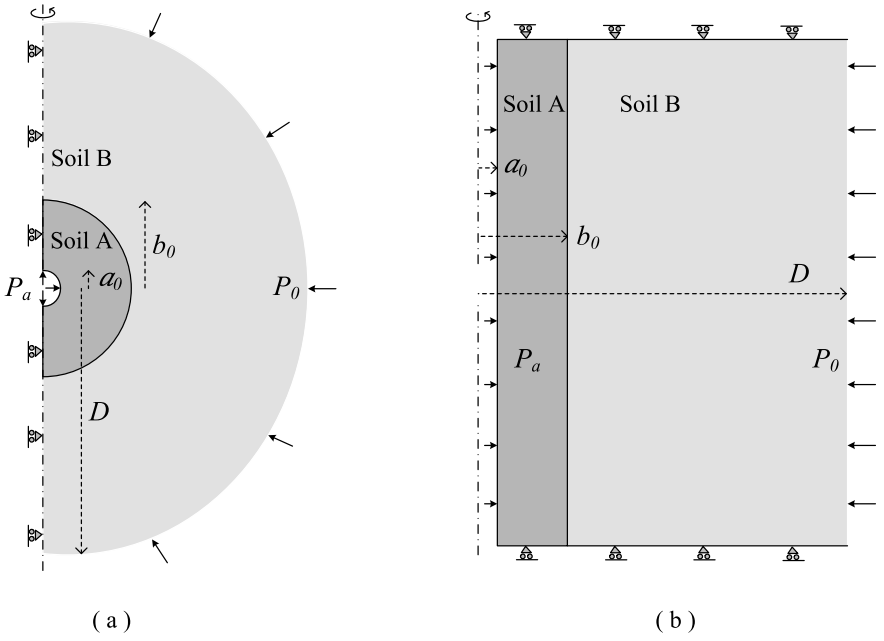

Figure 5.3 Finite element models for: (a) spherical cavity expansion; (b) cylindrical cavity expansion

As indicated in Figure 5.4a for spherical expansion, for the uniform soil tests ('-10-10' and '-1-1'), the cavity pressure (P_a) increases gradually with cavity displacement and asymptotically approaches a limit pressure. The limit pressure of the soil with $E = 10\,MPa$ is shown to be nearly twice as large as that with $E = 1\,MPa$. For the tests with two different soils (two-region tests), the pressure-expansion curves initially

follow the trend in which the E of the uniform soil tests matches the value of E in Soil A of the two-region tests (i.e. '-10-1' matches '-10-10' and '-1-10' matches '-1-1'). At a certain stage, the existence of Soil B begins to have an effect, and the pressure-expansion curve of the two-region analysis tends towards the limit pressure obtained from the uniform soil test in which E matches that of Soil B of the two-region test (i.e. ultimately '-10-1' approaches '-1-1' and '-1-10' approaches '-10-10'). Figure 5.4b shows equivalent results for cylindrical cavity expansion and illustrates that cylindrical pressures are about 60 % of those from the spherical analysis.

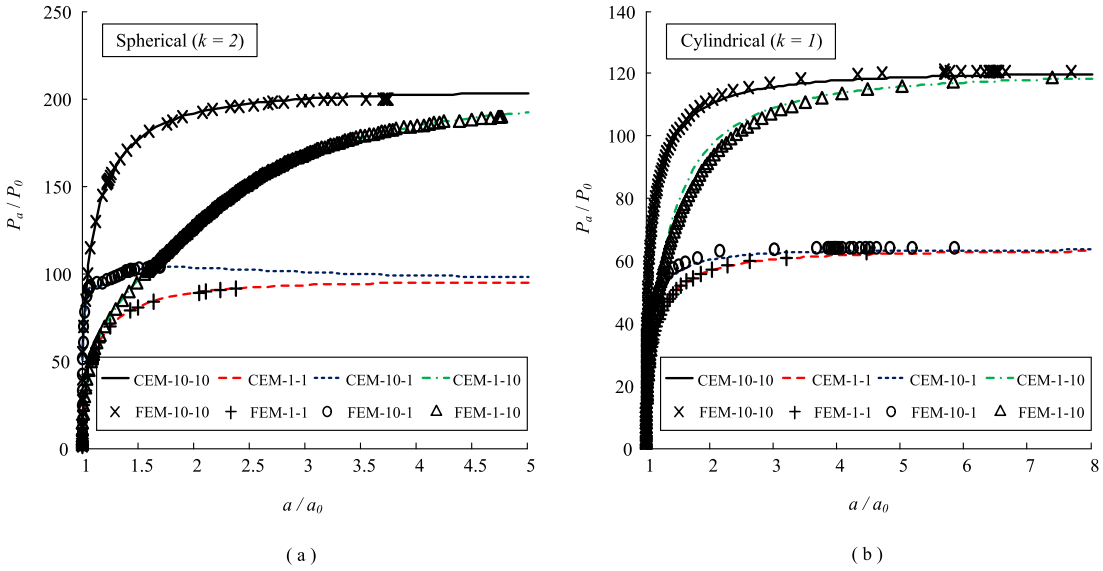

Figure 5.4 Comparison between numerical results and analytical solutions on cavity pressure: (a) spherical cavity expansion; (b) cylindrical cavity expansion

The development of plastic radius associated with cavity expansion is presented in Figure 5.5 with comparison of the analytical solutions. The plastic radius is focused on the outer plastic-elastic boundary (i.e. $max\{c_A; c_B\}$), when both soil regions have plastic zone. Figure 5.5a and b are results of uniform soil tests, showing that the plastic radius increases linearly with expansion after the early stage of non-linear development. The soil with higher stiffness is evident to have larger and faster development of plastic radius. It is obvious that the results of two-region tests presented in subplot (c) and (d) have a larger zone of non-linear development of plastic radius owing to the effects of two regions of soil. The numerical results again show good comparisons with analytical solutions. The scatter is found to be attributed to the quality of the mesh in the Finite element model. As the plastic radius is quantified according to the edges of the soil elements, finer mesh could make the scatter smaller. One of the drawbacks

of the numerical simulation is that soil element cannot be over-distorted with large expansion; thus the results are mainly focused on the initial stage of the expansion ($a/a_0 < 4$). By contrast, the proposed method can provide precise and robust solutions for expansion of an arbitrary cavity.

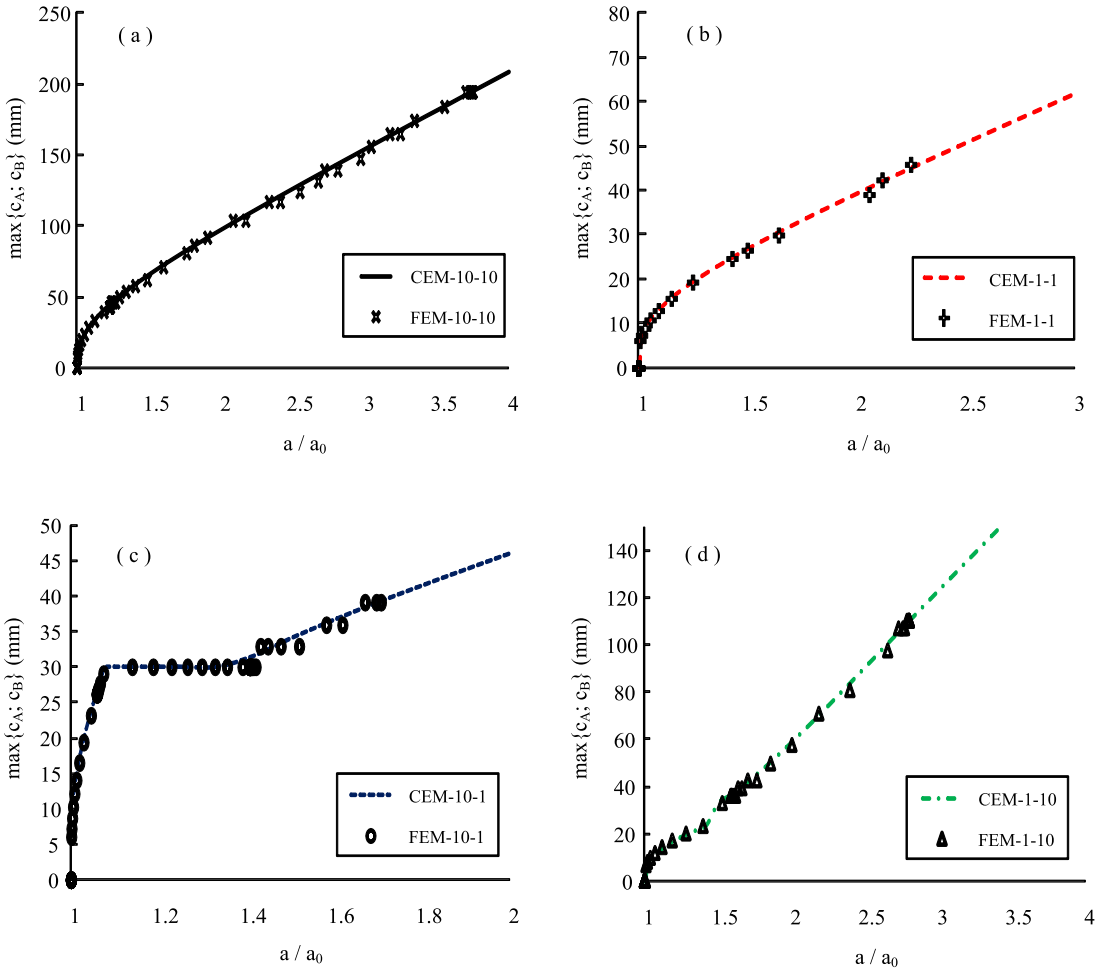

Figure 5.5 Comparison between numerical results and analytical solutions on plastic radius ($max\{c_A; c_B\}$) for spherical cavity expansion

5.5 Results of Parametric Study

This section considers the cavity expansion method in two concentric regions of different soils and investigates the effect of various parameters on model results. Results are based on the expansion of a cavity from $a_0 = 0.1\,mm$ to $a = 6\,mm$ ($a/a_0 = 60$). As illustrated in Figure 5.4 and Figure 5.5, the two-region tests are highly sensitive to the ratio a/a_0 (the value of a_0 has no effect on the normalised pressure expansion curves as long as the ratio of b_0/a_0 is maintained). The selection of these cavity pa-

rameters was based on geotechnical centrifuge experiments carried out as part of this research (see Chapter 3) in which a $6\,mm$ radius penetrometer is pushed into sand with an average grain size of approximately $0.14\,mm$ (a_0 is chosen close to $d_{50}/2$). The cavity expansion analysis was conducted with a Soil A/B interface at $b_0 = 30\,mm$ and initial hydrostatic stress $P_0 = 1\,kPa$. The following material parameters are taken for baseline comparison (note that subscripts 1 and 2 refer to soils A and B, respectively): $\nu_1 = \nu_2 = 0.2$; $\phi_1 = \phi_2 = 40^\circ$; $\psi_1 = \psi_2 = 10^\circ$; $C_1 = C_2 = 0\,kPa$. As in the previous section, results here focus mainly on the effect of varying the value of Young's modulus E of the two soils ($E_1 = 10$ or $1\,MPa$; $E_2 = 10$ or $1\,MPa$).

5.5.1 Distributions of stresses and displacements

Figure 5.6 shows the distribution of radial (a, b) and tangential (c, d) stresses respectively, for both spherical and cylindrical cavity expansion, as radial distance from the cavity (r) is increased. The results from tests with two regions of soil are bounded by the results from the uniform soil tests ('-10-10' and '-1-1'). A sharper decrease in stresses is noted for the spherical cases compared to the cylindrical cases. There is an interesting difference between the spherical and cylindrical analysis results. For the cylindrical tests, the results for the two-region analysis appear to be mainly controlled by the value of E of Soil B ('-10-1' effectively matches '-1-1' and '-1-10' is close to '-10-10'). For the spherical tests, however, the data from both the two-region tests are close to the uniform test '-1-1'. It is thought that the reason for this behaviour is due to the different degree of interaction between Soils A and B within the spherical and cavity expansion analyses, which is illustrated and discussed further using pressure-expansion curves later in Figure 5.9.

Normalized displacement distributions are presented in Figure 5.7 and show that results for all tests closely agree. This is due to the kinematic nature of the expansion problem; the differences between the lines shown in Figure 5.7 (for constant values of friction and dilation angles in Soils A and B) are due only to the effect of yielding. For purely elastic behaviour, the displacements are insensitive to the elastic parameters (as in the elastic half-plane analysis of Verruijt and Booker (1996) for displacements around tunnels). For two-region tests, the curves are seen to be located outside of the curves of uniform soil tests in Soil A, which approach the curves of tests with uniform

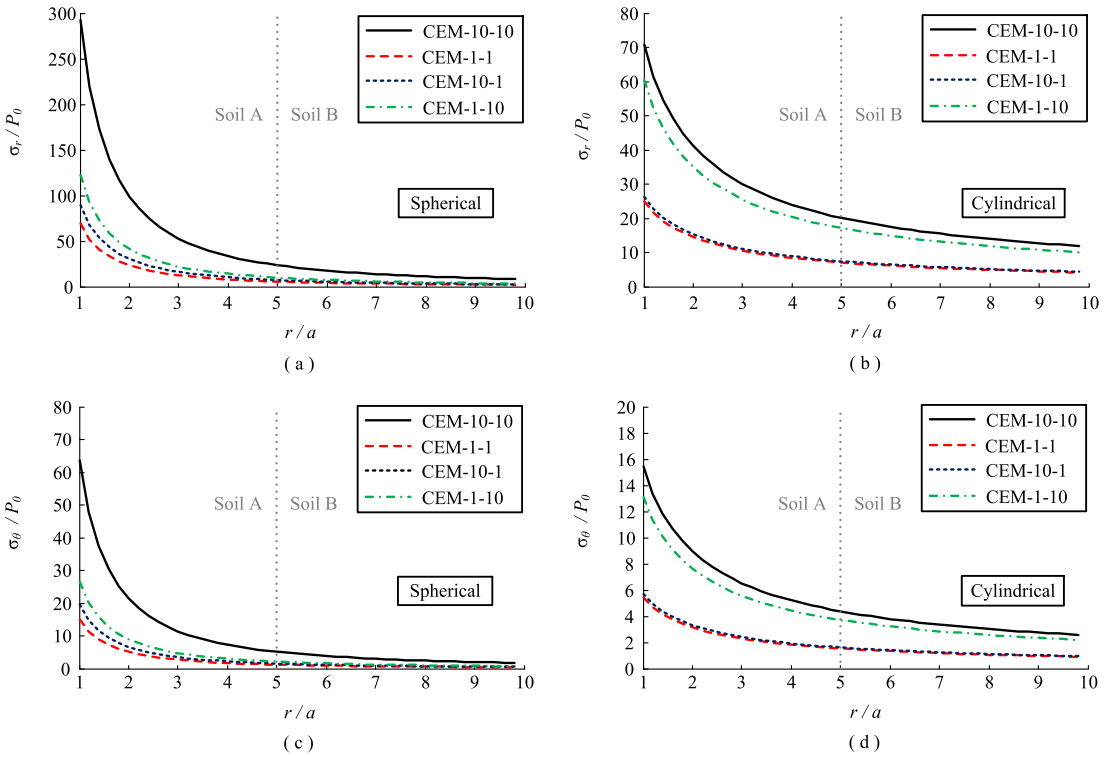

Figure 5.6 Radial (a, b) and tangential (c, d) stress distributions around cavity for both spherical and cylindrical cavity expansion (for $a/a_0 = 60$)

Soil B at some distance in Soil B. That implies the two-region effects on displacement of soils. Comparing the cylindrical expansion to spherical cases, the distributions decrease slower, and have larger deformation zones.

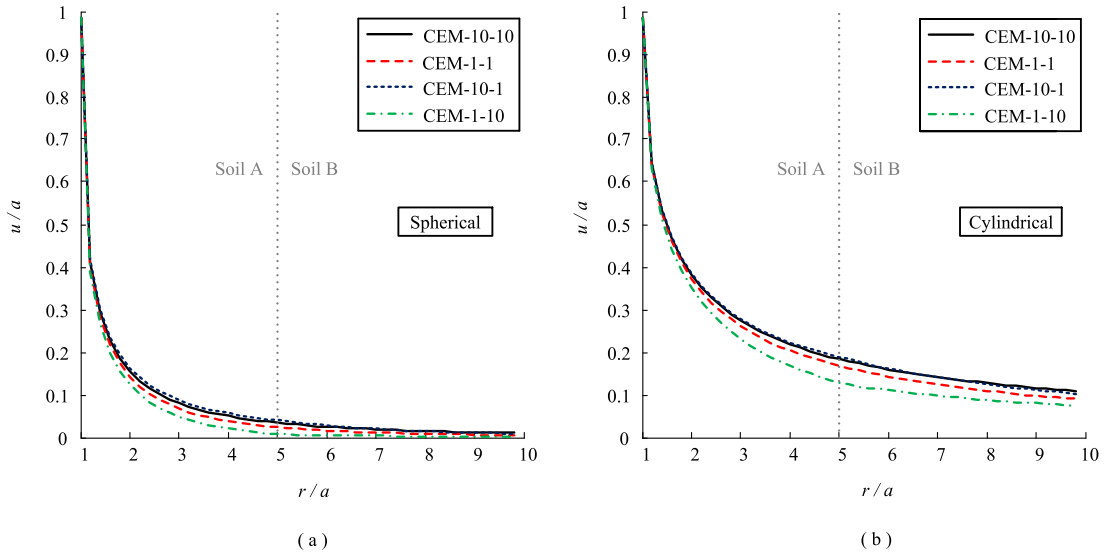

Figure 5.7 Displacement distribution around cavity: (a) spherical cavity expansion; (b) cylindrical cavity expansion (for $a/a_0 = 60$)

The distributions of strains (ε_r and ε_θ) are provided in Figure 5.8. All of the strains

are highly concentrated close to the cavity, resulting in significant strains in Soil A. By comparison, the results of the four tests appear to overlap with each other; the differences are even smaller than that in the displacement curves (Figure 5.7). These tiny offsets are magnified in the subplots to reveal the two-region effects, and are evident to have large influence to the cavity pressure and the stress field (Figure 5.6).

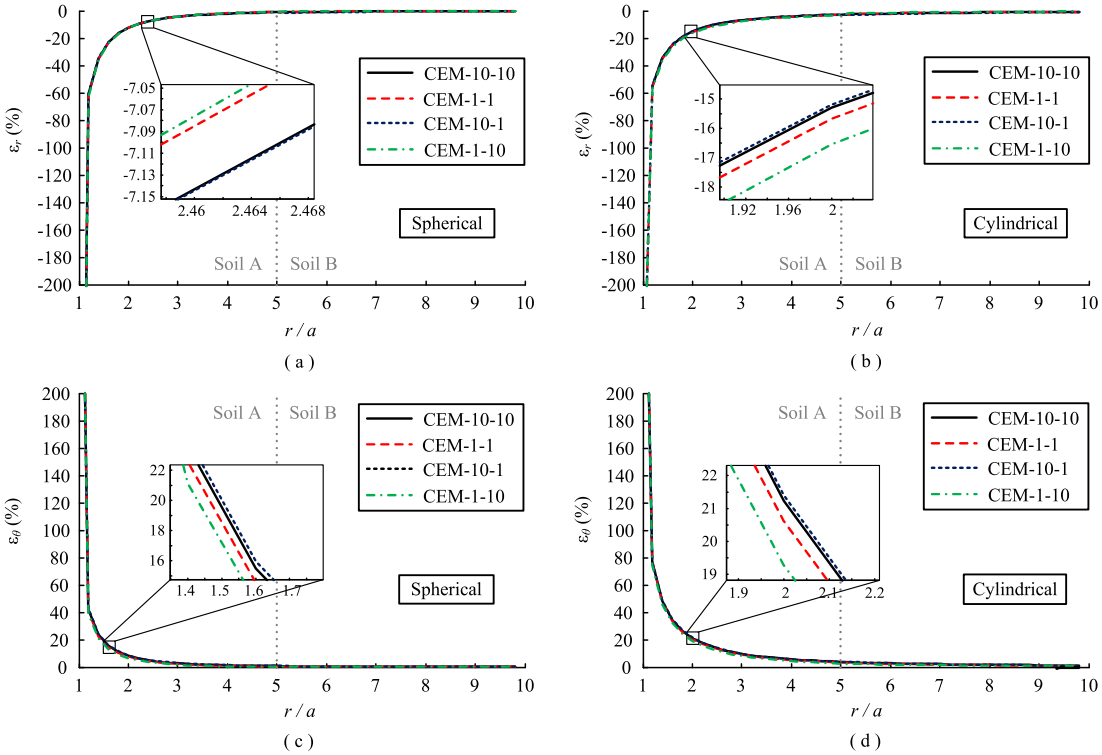

Figure 5.8 Radial (a, b) and tangential (c, d) strain distributions around cavity for both spherical and cylindrical cavity expansion (for $a/a_0 = 60$)

5.5.2 Variation with cavity radius

The pressure-expansion curves in Figure 5.9 show the effects of the two different concentric regions of soil, as discussed previously where analytical results were validated against FE simulations. As the cavity size (a/a_0) is increased, the curves from the uniform soil tests reach a limit pressure. The limit pressure is reached quite quickly (in terms of a/a_0) for the uniform soil tests ($a/a_0 < 20$ for spherical and cylindrical tests), while the two-region tests reach the limit pressure after a much greater expansion (a/a_0 ranging from 250 to > 500 for the spherical tests and from about 100 to 500 for the cylindrical tests).

The distinction between two-region effects in the spherical and cylindrical analyses mentioned in discussion of Figure 5.6 can be explained using Figure 5.9. For the analysis, in which $a/a_0 = 60$, Figure 5.9 shows that the cavity pressure is generally dominated by the stiffness of Soil B, except for the spherical test 'CEM-1-10'. The two concentric zones have a significant effect in this spherical expansion test at the considered expansion state, whereas in the cylindrical analysis the effect is minimal. This explains the difference in stress distributions between the spherical and cylindrical tests in Figure 5.6.

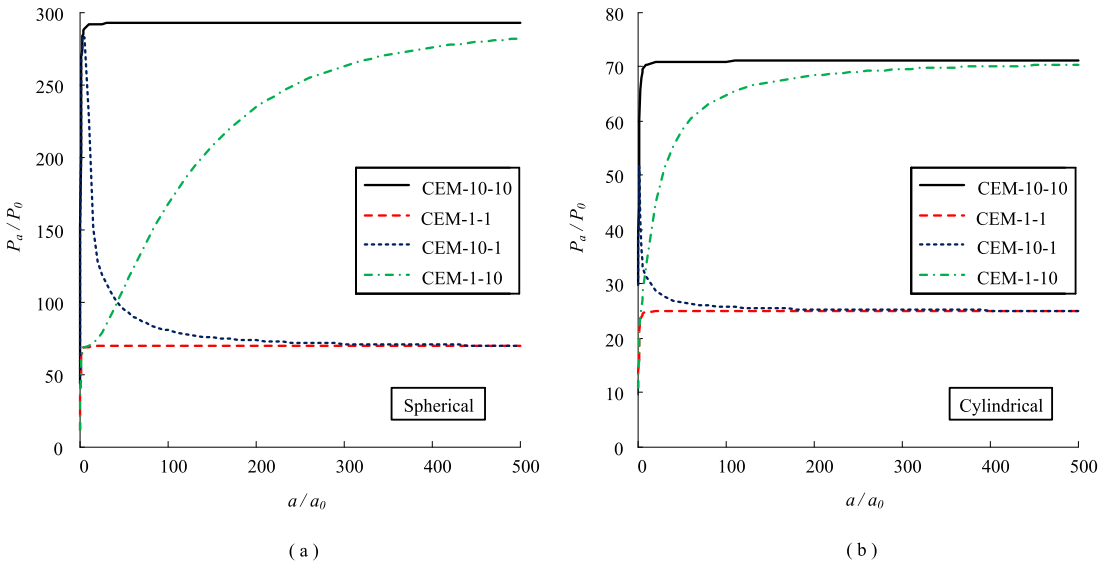

Figure 5.9 Variation of cavity pressure with cavity radius (a): (a) spherical cavity expansion; (b) cylindrical cavity expansion

In Figure 5.10, the development of normalized plastic radius (c_A/a, c_B/a) in soils A and B as the normalized cavity radius increases is presented for the case of spherical cavity expansion, as well as the Soil A/B interface b/a, plotted with dotted lines. The uniform soil test results in Figure 5.10a and b show that plastic radius increases linearly with expansion after a small initial stage of nonlinear development ($a/a_0 < 5$). The growth of the plastic region is noted to be much faster in the test with higher stiffness, resulting in Soil A becoming fully plastic (A_P) at a much lower expansion ratio in test '-10-10' ($a/a_0 = 12$) compared to test '-1-1' ($a/a_0 = 32$). For the two-region tests '-10-1' and '-1-10', the results in Figure 5.10c and d show the development of plastic radius within the different expansion stages (refer to Figure 5.2 for definition of labels). In test '-10-1', for a/a_0 between 11 and 22, Soil A is fully plastic while Soil B remains fully elastic ($A_P B_E$). In test '-1-10', there is a stage during which Soil B be-

comes partially plastic prior to Soil A becoming fully plastic ($A_{PE}B_{PE}$). The nonlinear behaviour of the plastic radius in the two-region tests is much more obvious compared to the uniform soil tests. All tests eventually tend towards an ultimate state in which further expansion generates a linear increase of the plastic radius (i.e. c_B/a levels off, which is discernible in the figures).

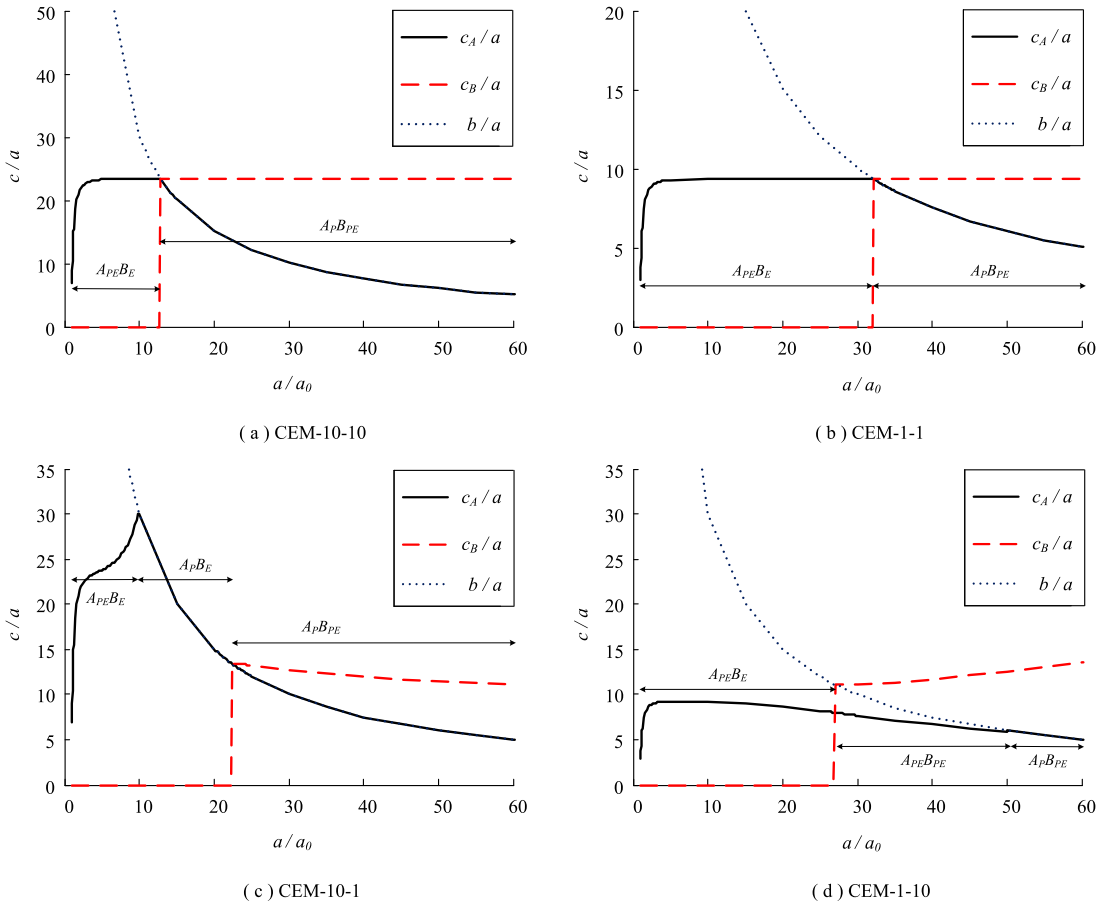

Figure 5.10 Development of plastic radii (c_A, c_B) in spherical tests: (a) CEM-10-10; (b) CEM-1-1; (c) CEM-10-1; (d) CEM-1-10

Figure 5.11 shows the equivalent results for the cylindrical cavity expansion. The cylindrical results show a significantly faster development (in terms of a/a_0) and higher value of plastic radius (c_A, c_B) compared to the spherical analysis results.

5.5.3 Variation with size of soil A

The results of the two-region analysis also depend to a large degree on the size of Soil A. Indeed, for some critical size of Soil A, Soil B should have no effect on the results of the analysis. Figure 5.12 shows the variation of cavity pressure with the size of

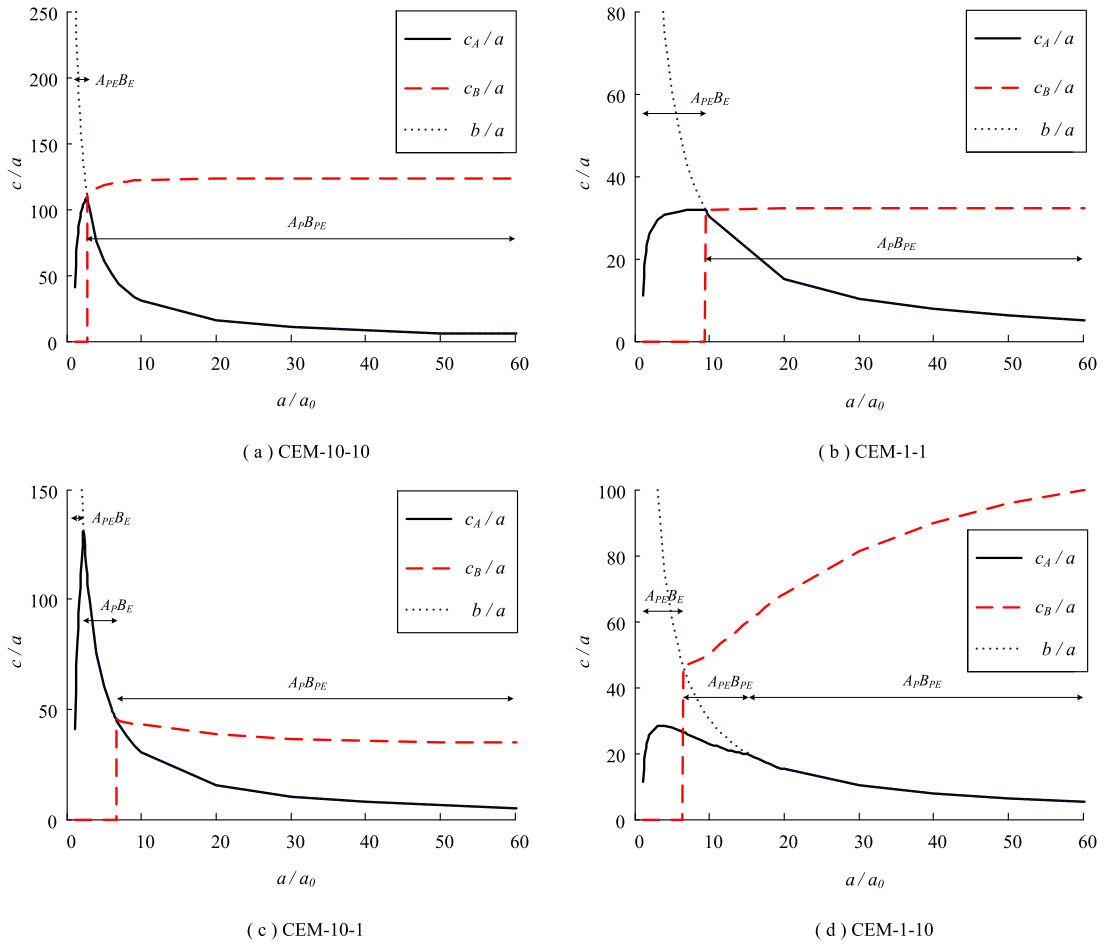

Figure 5.11 Development of plastic radii (c_A, c_B) in cylindrical tests: (a) CEM-10-10; (b) CEM-1-1; (c) CEM-10-1; (d) CEM-1-10

Soil A (given by b_0) for cavities expanded from $a_0 = 0.1\,mm$ to $a = 6\,mm$. The results for the uniform soil tests are, as expected, unaffected by the variation of b_0. For the two-region tests, when b_0 is small, the cavity pressure is close to the uniform soil test where E matches the value of E in Soil B of the two-region test. As b_0 increases, the two-region effects diminish and the cavity pressure approaches the uniform soil test pressure in which E matches the value of E in Soil A of the two-region test. The value of b_0 at this stage can be considered as defining the critical size of Soil A, referred to as $b_{0,crit}$; for Soil A larger than $b_{0,crit}$ there will be no effect of the outer region of soil. For example, for the spherical test '-1-10' in Figure 5.12a, the cavity pressure decreases from about $290\,kPa$ (equivalent to the '-10-10' test) and approaches the pressure of the '-1-1' test when b_0/a is about 25. This value of b_0/a defines the critical size of Soil A in order for the two regions to have an effect in the spherical cavity expansion analysis. In contrast, the critical size for test '-10-1' is about three times larger than that of test '-1-10' ($b_0/a \approx 90$ where '-1-10' line approaches '-10-10' line), illustrating the effect

of soil stiffness on the critical size. The cylindrical analysis results in Figure 5.12b show a much larger critical size compared to the spherical results.

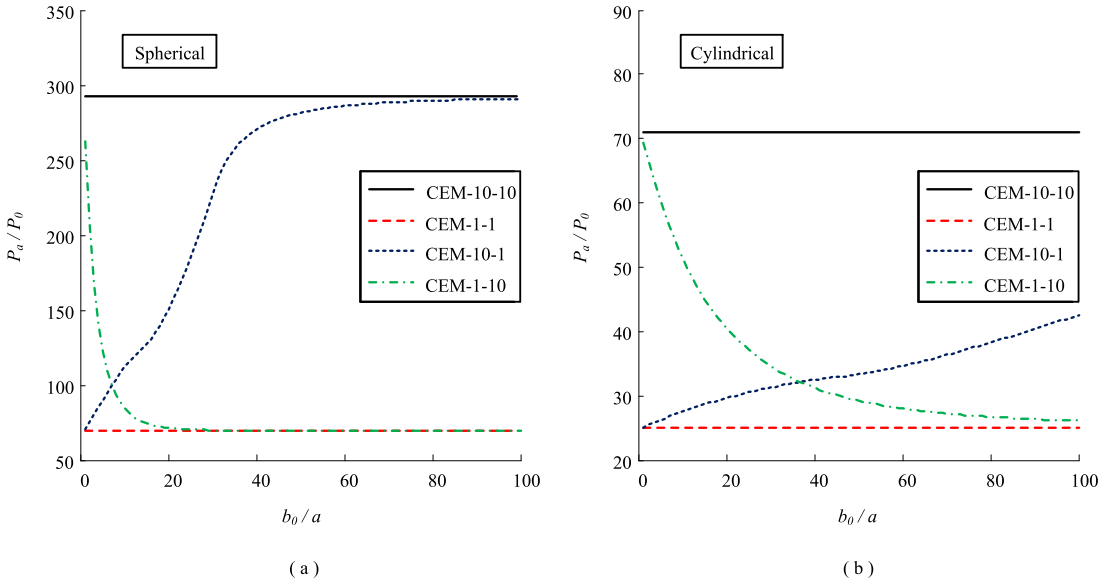

Figure 5.12 Variation of cavity pressure with size of Soil A (b_0): (a) spherical cavity expansion; (b) cylindrical cavity expansion

Figure 5.13 shows the variation of plastic radius (c_A, c_B) with b_0 for both spherical and cylindrical analyses for cavity expansion from $a_0 = 0.1\,mm$ to $a = 6\,mm$. The gray areas indicate values of the plastic radius in Soil B (c_B). The right-side boundary of the shaded area defines a line describing the linear increase of c_A with b_0 for all tests. The value of c_A eventually deviates from this line for all tests. Outside of the shaded area, c_B does not exist; the size of Soil A (defined by b_0) is great enough that plasticity does not commence within Soil B.

As expected, for the uniform soil tests, the plastic radius is unaffected by the variation of b_0. Considering the spherical test '-10-1' in Figure 5.13a, c_B increases initially with b_0, though at a lower rate than c_A. The plastic region in Soil B disappears when $b_0/a \approx 15$ (where the '10-1' line for c_B meets the right-side boundary of the shaded area). Soil A is fully plastic until $b_0/a \approx 30$, after which the value of c_A decreases towards and finally reaches the value obtained from the '-10-10' test at $b_0/a \approx 90$ (as the effects of Soil B gradually dissipate). In test '-1-10', c_B decreases initially with b_0 and c_A gradually increases and reaches the value from test '-1-1' at $b_0/a \approx 90$. This again defines the critical size of Soil A ($b_{0,crit}$) for the spherical analysis with the assumed

material parameters. The cylindrical results in Figure 5.13b show similar trends to the spherical test.

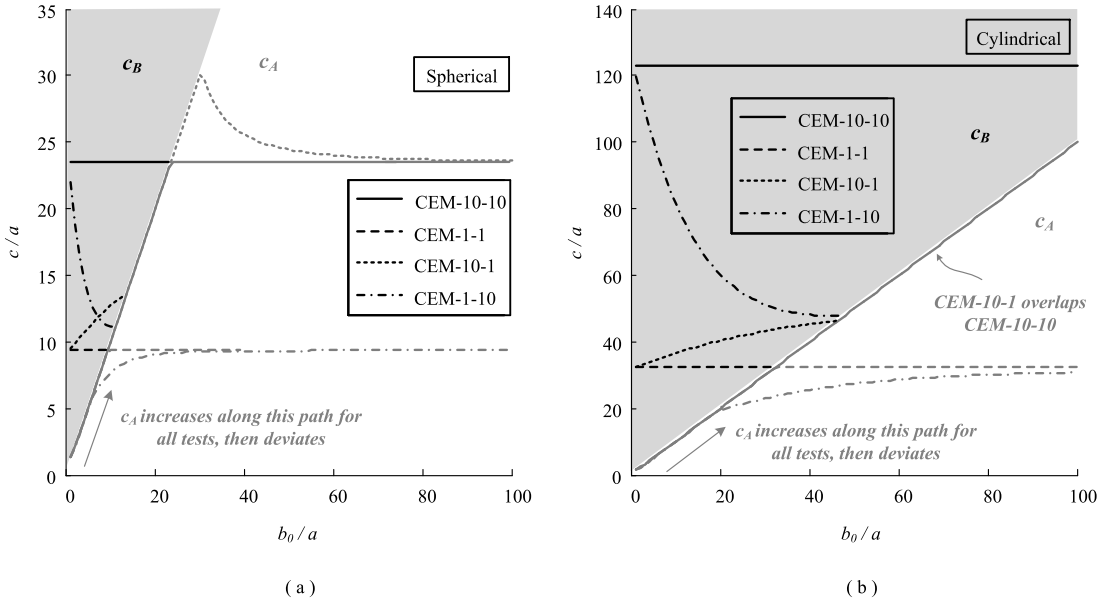

Figure 5.13 Variation of plastic radius (c_A, c_B) with thickness of Soil A (b_0): (a) spherical cavity expansion; (b) cylindrical cavity expansion

5.5.4 Variation with friction and dilation angles

The spherical test 'CEM-1-10' is selected to investigate the variation of displacement with strength and plastic-flow parameters (i.e. friction and dilation angles), as shown in Figure 5.14 and Figure 5.15. For tests with uniform parameters of ϕ and ψ in Soils A and B (Figure 5.14), the displacements increase with an increase in dilation angle (Figure 5.14b), whereas displacements decrease only marginally with an increase in friction angle (Figure 5.14a). The effect of varying friction angle between the two soils (Figure 5.15) is difficult to observe since the overall effect on displacements is small. The magnified zone in Figure 5.15a shows that the two-region effect of friction angle is bounded by the uniform tests. The magnitudes of the differences are of little practical concern. For dilation angle, the two-region soil behaviour is dominated by the value of dilation angle in Soil A, where the lines with equal values of ψ_1 are shown to overlap in Figure 5.15b.

For cases in Figure 5.15a, the spherical test 'CEM-1-10' is selected to study the effect of the variation of friction angle on the pressure-expansion curves and the development

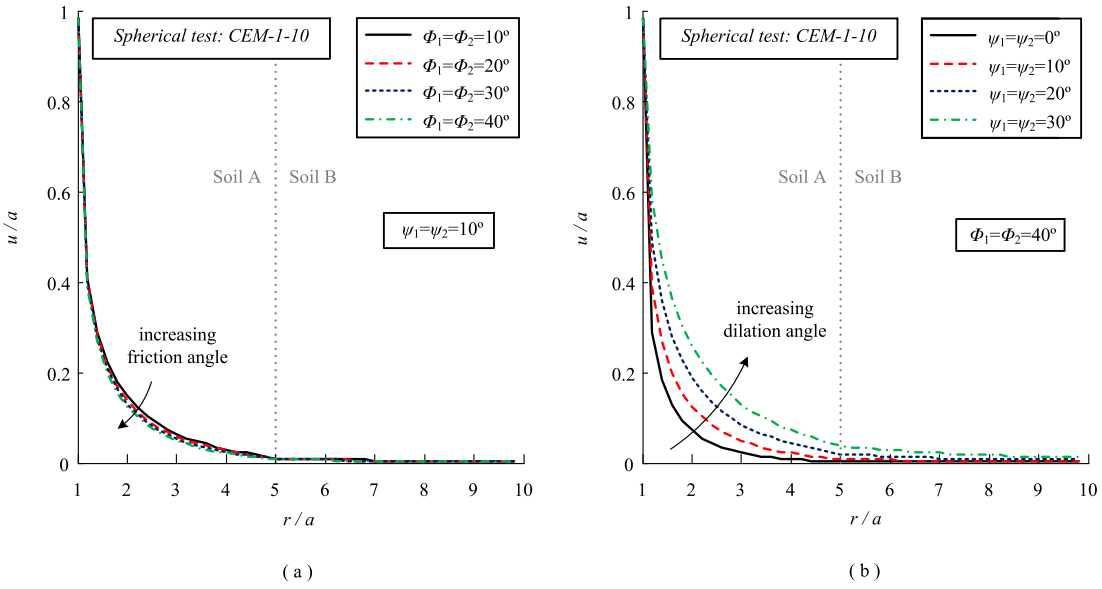

Figure 5.14 Variation of displacement distribution with (a) uniform friction angle and (b) uniform dilation angle for spherical test: CEM-1-10 (for $a/a_0 = 60$)

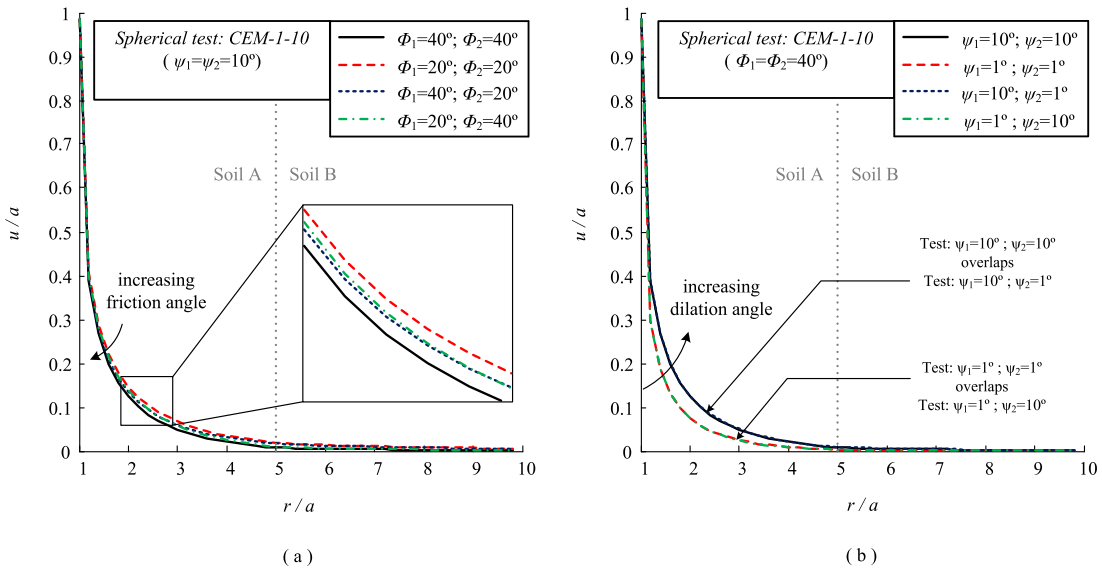

Figure 5.15 Variation of displacement distribution with (a) friction angle and (b) dilation angle for spherical test: CEM-1-10 (for $a/a_0 = 60$)

of cavity radius in Figure 5.16. The two-region effect on cavity pressure (Figure 5.16a) is clearly shown where cavity pressure is initially controlled by Soil A but is then controlled by Soil B at larger expansion ratios. Plastic radius of Soil A (c_A) is dominated by Soil A ('$\phi_1 = 40^\circ$; $\phi_2 = 40^\circ$' is close to '$\phi_1 = 40^\circ$; $\phi_2 = 20^\circ$', and '$\phi_1 = 20^\circ$; $\phi_2 = 20^\circ$' overlaps '$\phi_1 = 20^\circ$; $\phi_2 = 40^\circ$'), as shown in Figure 5.16b. The tests with a lower friction angle in Soil A have larger values of c_A, earlier appearance of c_B, and larger values of c_B.

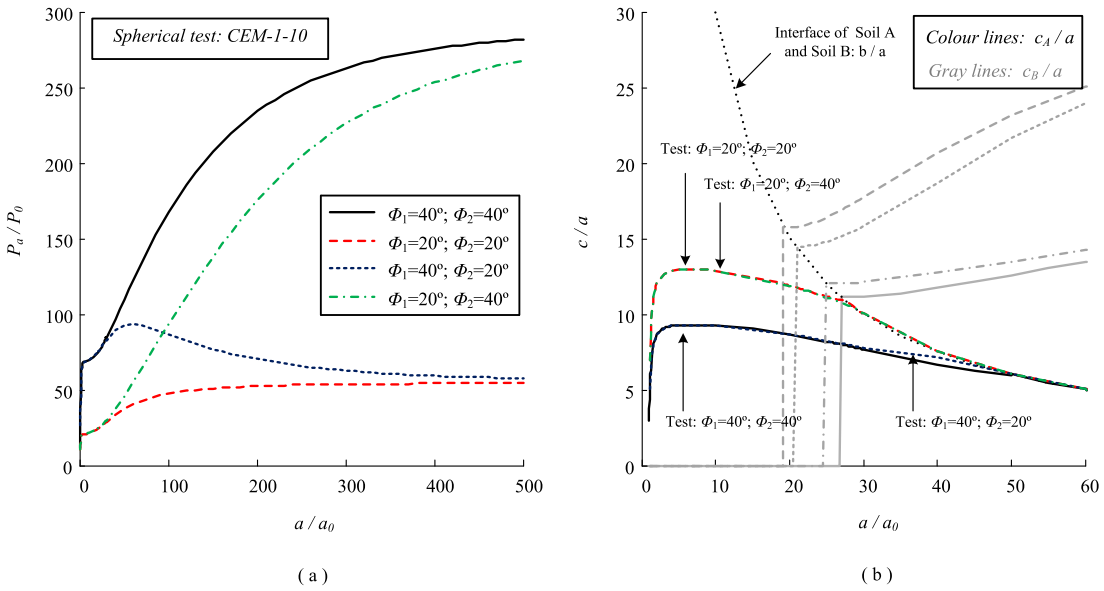

Figure 5.16 Developments of (a) cavity pressure, and (b) plastic radii (c_A, c_B) with variation of friction angle for spherical test: CEM-1-10 (for $\psi_1 = \psi_2 = 10^\circ$)

Figure 5.17 shows similar results for the effect of variation of dilation angle from spherical test 'CEM-1-10' (parameters are identical with Figure 5.15b). The development of plastic radius c_A and c_B are mainly controlled by Soil A, while a lower dilation angle in Soil A leads to a smaller value of c_A before Soil A becomes fully plastic (A_P).

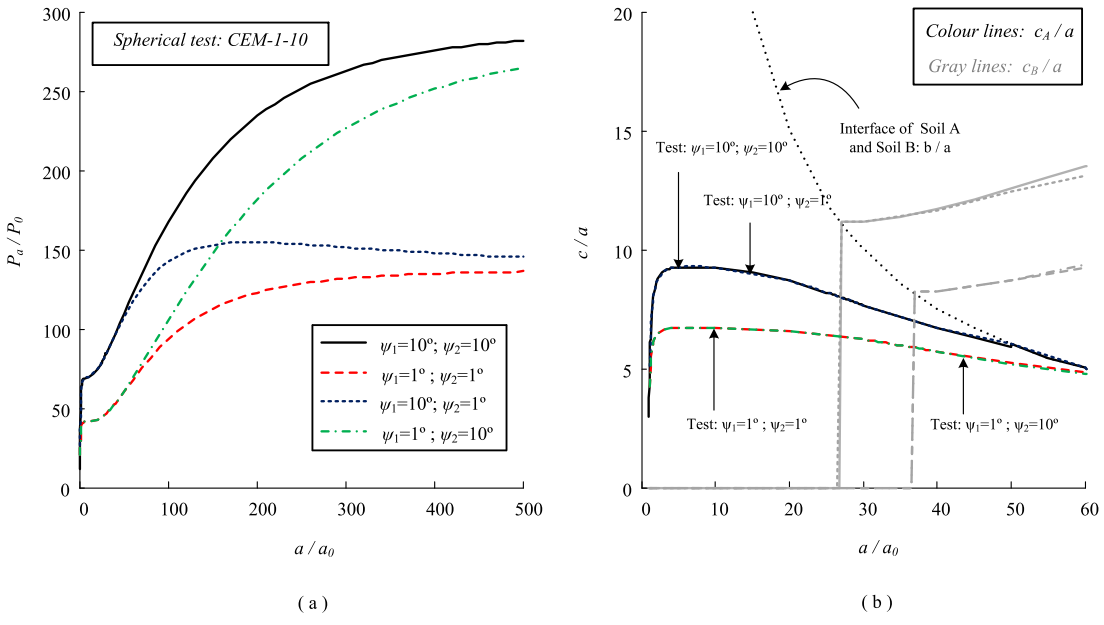

Figure 5.17 Developments of (a) cavity pressure, and (b) plastic radii (c_A, c_B) with variation of dilation angle for spherical test: CEM-1-10 (for $\phi_1 = \phi_2 = 40^\circ$)

The variations of cavity pressure with friction angle and dilation angle of Soil A for expansion from 0.1*mm* to 6*mm* are provided in Figure 5.18 (spherical tests) and Fig-

ure 5.19 (cylindrical tests). Four tests with different profiles of stiffness (10MPa and 1MPa) in each group are examined with $\phi_2 = 40^\circ$ and $\psi_2 = 10^\circ$. Cavity pressure (P_a) increases with soil stiffness, and appears to be dominated by the properties of Soil B. The curves are shown with nearly linear increasing with the friction ratio: ϕ_1/ϕ_2, and seem to be proportional to dilation angle of Soil A: ψ_1.

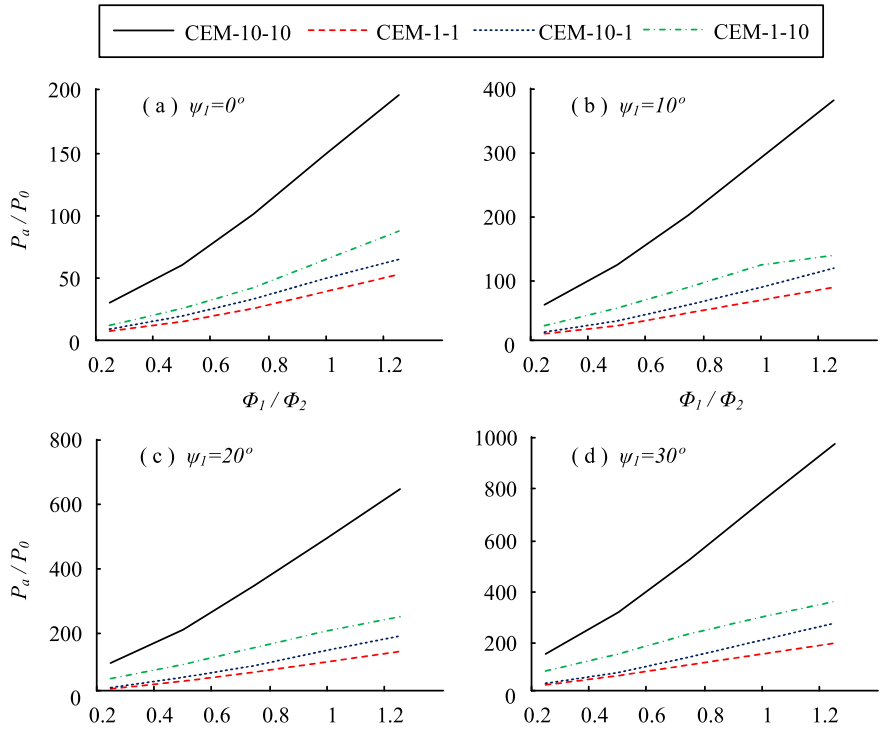

Figure 5.18 Variation of cavity pressure with friction angle and dilation angle of Soil A for spherical tests ($\phi_2 = 40^\circ$; $\psi_2 = 10^\circ$)

5.5.5 Variation with stiffness ratio

The effects of stiffness ratio have been investigated in Figure 5.20. Both E_1/E_2 and E_2/E_1 are examined for spherical and cylindrical tests at two stiffness levels. For spherical tests in Figure 5.20a, P_a increases exponentially with increase of E_1 (x axis is plotted in log scale) when $E_1/E_2 < 1$, whereas the effect of E_1 is negligible to development of P_a when $E_1/E_2 > 1$; the inflection point occurs earlier for test with larger E_2. For cylindrical tests, similar trends appear with inflection happening at $E_1/E_2 \approx 0.1$, indicating that the cylindrical cavity tends to be more dependent on the stiffness of Soil B. Correspondingly, Figure 5.20b shows the variation with E_2/E_1. Within the range of $10^{-2} \sim 10^2$, cavity pressure generally increase exponentially with E_2/E_1, especially for cylindrical tests.

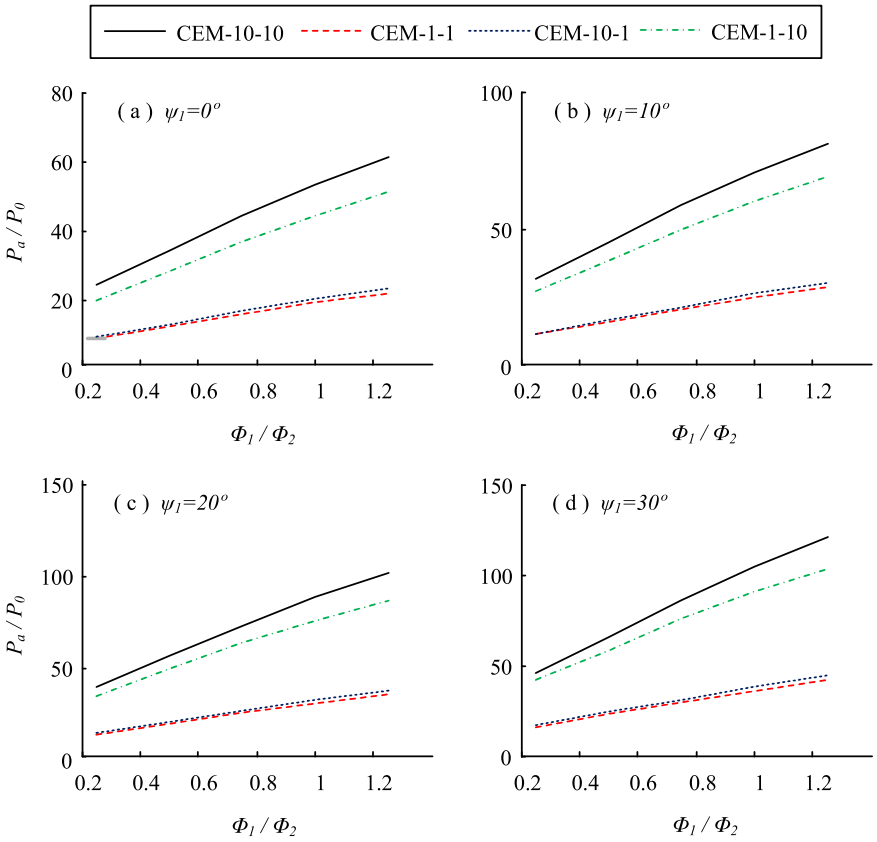

Figure 5.19 Variation of cavity pressure with friction angle and dilation angle of Soil A for cylindrical tests ($\phi_2 = 40^\circ$; $\psi_2 = 10^\circ$)

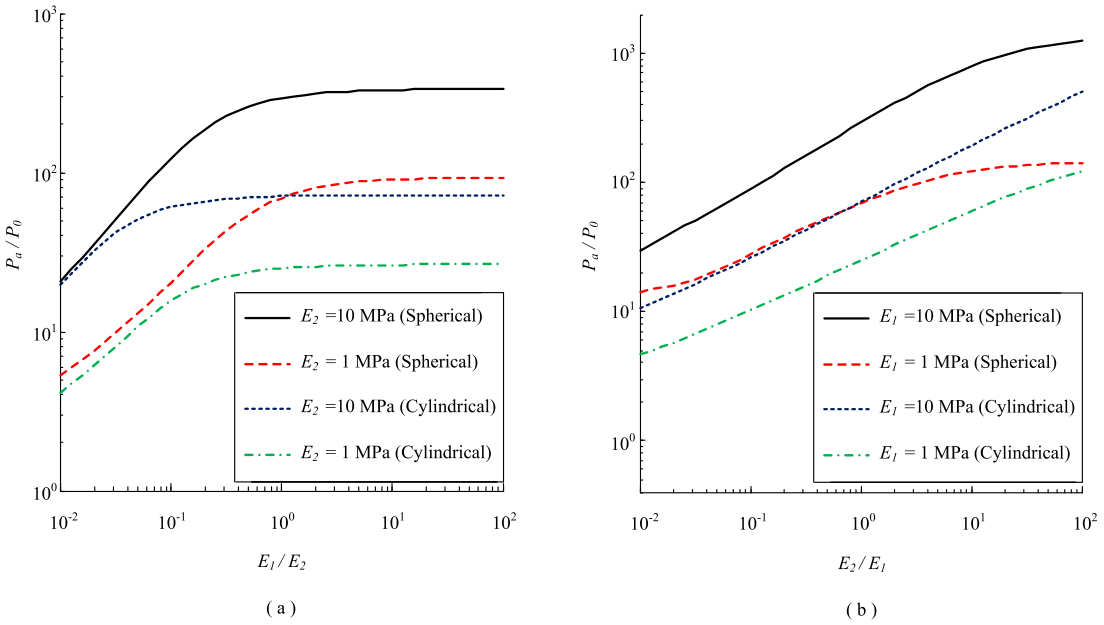

Figure 5.20 Variation of cavity pressure with stiffness ratio for both (a) spherical and (b) cylindrical tests

5.5.6 Variation with cohesion and Poisson's ratio

The effect of cohesion is examined for $C_1 = C_2$ varies from 0 to $10\,kPa$, as shown in Figure 5.21. Larger cavity pressure is found for higher soil cohesion. With increasing of cohesion, the cavity is more affected by the first soil region: Soil A. Compared with spherical tests, P_a with the effect of cohesion is close to the test with similar E_2 for cylindrical tests. In addition, the variation of P_a with Poisson's ratio is relatively not obvious, as shown in Figure 5.22. Very little increase of cavity pressure is shown, especially for tests with lower stiffness of Soil B ($E_2 = 1\,MPa$).

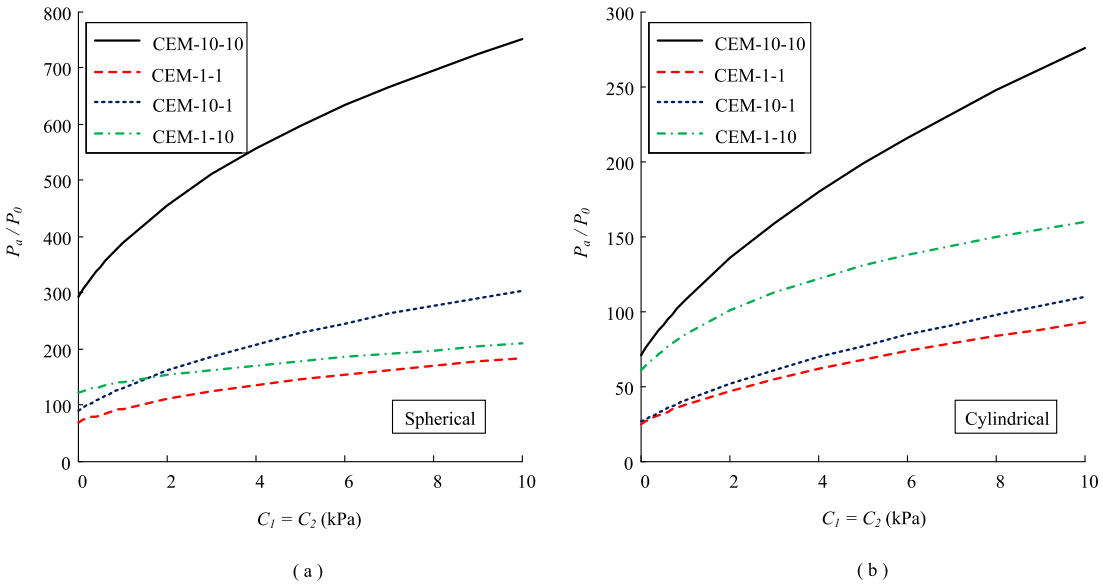

Figure 5.21 Variation of cavity pressure with cohesion for: (a) spherical tests; and (b) cylindrical tests

5.6 Comments on Geotechnical applications

The results presented in Section 5.5 illustrate that the cavity expansion method can be effectively used to study problems involving two concentric regions of soil. In reality, there are few geotechnical problems in which a true concentric condition exists. However, in some scenarios, the concentric assumption may prove to be of limited consequence to the application of the method to the more typical case of horizontally layered soils. The application of the method to the interpretation of CPT tip resistance or pile end bearing capacity in layered soils will be explored further in the next chapter (Chapter 6). The method may also have application to tunnelling and mining applications. Notably, the concentric assumption is directly applicable to the analysis of shaft

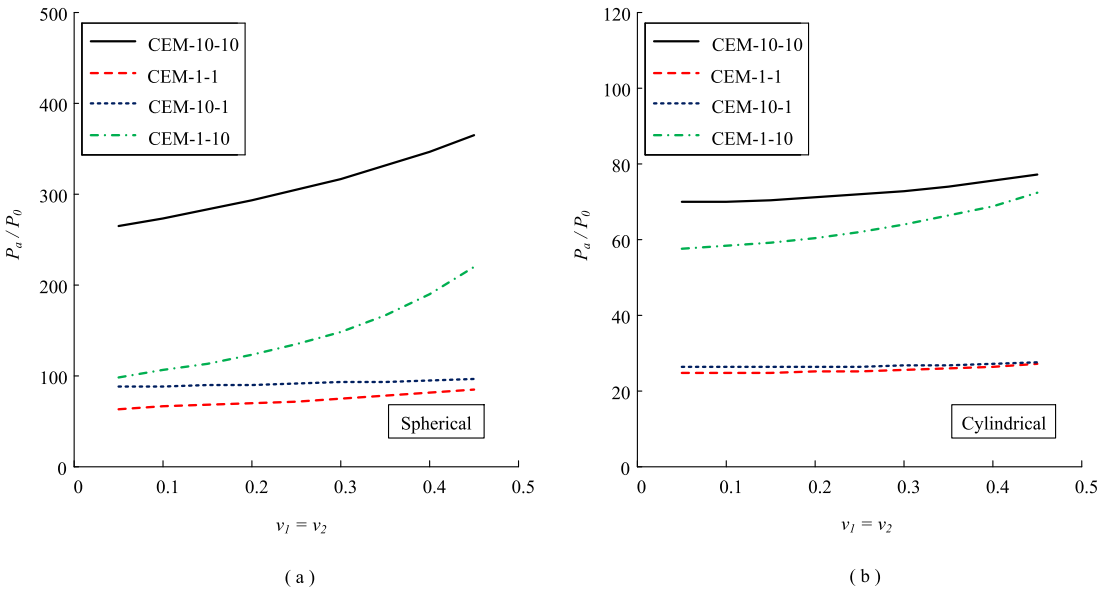

Figure 5.22 Variation of cavity pressure with Poisson's ratio for: (a) spherical tests; and (b) cylindrical tests

construction using ground-freezing techniques, where a cylinder of frozen ground is surrounded by a zone of less stiff and weaker un-frozen ground.

A limitation of the method presented here is that the material parameters (e.g. stiffness, cohesion, friction and dilation angles) are assumed constant within each soil region (A and B). To account for the variation of any parameters with shear strain (notably friction and dilation angles), a method similar to that used in Randolph et al. (1994) could be adopted, whereby the average values between the initial state (ϕ'_{max}) and critical state (ϕ'_{cs}) are used, as illustrated in Section 6.3.1.

5.7 Chapter Summary

An analytical solution for spherical and cylindrical cavity expansion in two concentric regions of soil was presented and validated against Finite Element simulations. The closed-form solutions are an extension of the cavity expansion solutions in an isotropic dilatant elastic-perfectly plastic material and provide the stress and strain distributions within the two soils for both elastic and plastic states using a Mohr-Coulomb yield criterion, a non-associated flow rule, and a large-strain analysis. The two-region effects were investigated by using pressure expansion curves and by studying the development of plastic radius in both soil regions (c_A and c_B). The effects of variation of stiffness,

strength, and plastic-flow parameters of both soils were illustrated and the results highlighted the capability of the analytical solution. Despite of the limitation of constant material properties, the proposed method is potentially useful for various geotechnical problems in layered soils, such as the interpretation of cone penetration test data, tunnelling and mining, and analysis of shaft construction using ground-freezing methods.

Chapter 6

Applications of Cavity Expansion Solutions to CPT

6.1 Introduction

The results presented in Section 5.5 illustrate that the cavity expansion method can be effectively used to study problems involving two concentric regions of soil. The provided analytical solutions have the potential to be applied to a range of geotechnical problems discussed in Section 2.4. For example, whereas the estimation of CPT tip resistance or pile end bearing capacity in layered soils has been evaluated numerically (Xu and Lehane, 2008; Ahmadi and Robertson, 2005), the analytical method provides a more efficient tool for studying the problem. The method may also be applicable to multi-layered soils using superposition methods, especially for thin layered profiles (Hird et al., 2003; Ahmadi and Robertson, 2005; Walker and Yu, 2010).

In this chapter, the cavity expansion solutions in two concentric regions of soil presented in Chapter 5 are applied to the analysis of cone penetration test data in two-layered and multi-layered soils. A discussion on the correlation between concentric and horizontal layering is provided first, aiming to reveal the analogue between cavity expansion in concentric soils and cone penetration in horizontally layered soils. After illustrating the methodology to relate the theoretical model to the penetration problem, cone tip resistance during penetration in layered soils are investigated using the analytical solutions. Results of interpretation of CPT measurements are then compared with experimental and numerical results from the literature. The layered and thin-layer

effects on penetration resistance are studied using the analytical solutions, with some parametric studies also provided.

6.2 Discussion on Concentric and Horizontal Layering

The use of cavity expansion in concentric media as an analogue to cone penetration in horizontal soil layers is discussed in this section before further investigation of this application is undertaken. For theoretical solutions, an infinite medium or circular/spherical boundary is generally preferred since the symmetric boundary conditions simplify the solutions significantly. Even for many half-space models, a semi-spherical boundary is usually applied to simplify the problems.

Equivalently, most cavity expansion methods employ similar assumptions that neglect the effects from different types of boundaries and the surface effects which are naturally horizontal. A direct application of a concentrically layered model of cavity expansion to pile foundations was proposed by Sayed and Hamed (1987) using elastic analyses. The comparison of cavity expansion in concentric layers and cone penetration in horizontal layers is shown in Figure 6.1, indicating the geometry differences between these two models.

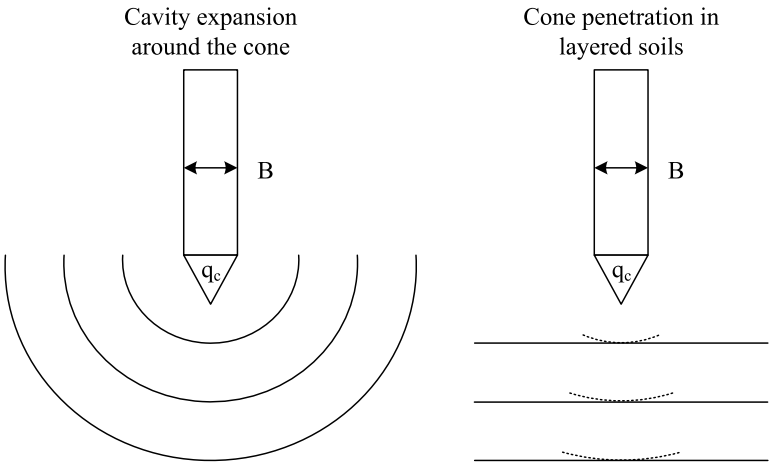

Figure 6.1 Comparison of cavity expansion in concentric layers and cone penetration in horizontal layers (after Sayed and Hamed, 1987)

In addition, the differences of cavity expansion in both models are further investigated by numerical simulations using Abaqus/Standard. The schematics of the two

models are shown in Figure 6.2, and the concentric model is the same with that used for validation of the analytical solutions (Figure 5.3a in Chapter 5). The dimensions, stress conditions, and soil properties are identical to that in Section 5.4. The cavities are expanded from an initial size of $a_0 = 6\,mm$, under an initial isotropic pressure of $P_0 = 1\,kPa$. The size of the two-soil interface b_0 varies from a_0 to infinity. The example of penetration problem presented here considers penetration from Soil 1 (weak soil) into Soil 2 (strong soil). The soil parameters are set as follows: $\nu = 0.2$, $\phi = 10^\circ$, $\psi = 10^\circ$, $C = 10\,kPa$; $E_{Soil1} = 1\,MPa$ and $E_{Soil2} = 10\,MPa$. The penetration process in the concentric model is simulated by varying b_0 from $-\infty$ to $+\infty$. Two stages of soil profiles are required, and the reversal of Soil A and Soil B happens when b_0 varies from negative to positive (b_0 indicates the distance to the soil interface). The cavity expansion in the horizontal model (Figure 6.2b) is simulated correspondingly by moving the position of the soil interface.

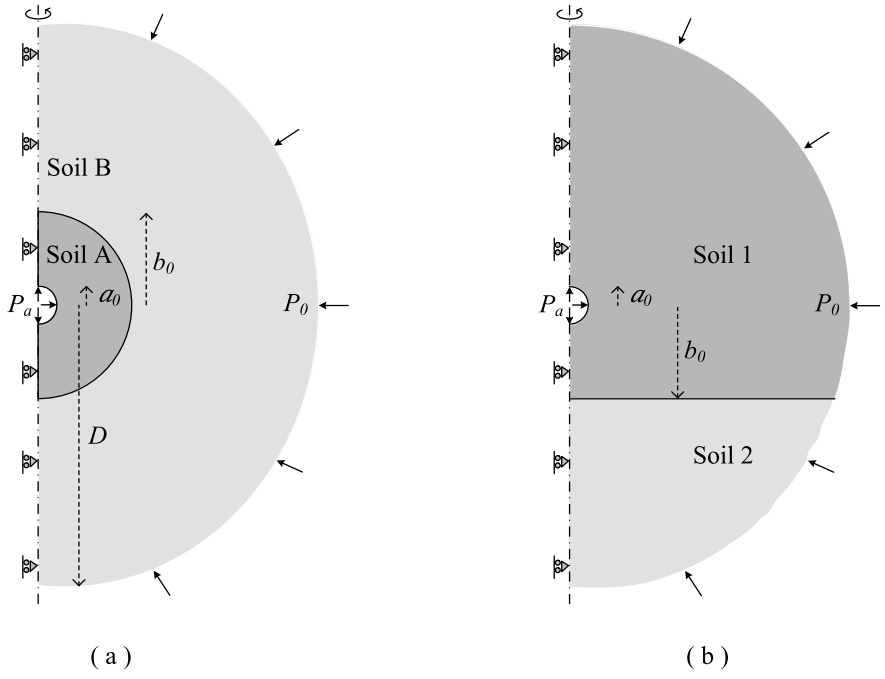

Figure 6.2 Numerical models for cavity expansion in: (a) concentric layers; and (b) horizontal layers

Figure 6.3 shows the pressure-expansion curves of cavities in concentric models with different soil profiles. When b_0 increases from -10 to -2, the curve moves from Soil 1 ($b_0/a_0 = -\infty$) to Soil 2 ($b_0/a_0 = -1$). Reversely, when b_0 increases from 2 to 10, the curve moves from Soil 1 ($b_0/a_0 = 1$) to Soil 2 ($b_0/a_0 = +\infty$) with different magnitude of the layering effects. On the other hand, expansion in the horizontal model trans-

forms smoothly from Soil 1 to Soil 2 when increasing b_0 from -10 to 10, as presented in Figure 6.4. It is worthwhile noting that the distribution of pressure on the cavity wall is not uniform owing to the asymmetry of soil conditions, and the pressure at the middle point of the cavity was selected for analysis. Comparing the pressure-expansion curves from concentric and horizontal models, the general trends of the variation in each stage are evident for both soil models, though the differences at the boundary are significant.

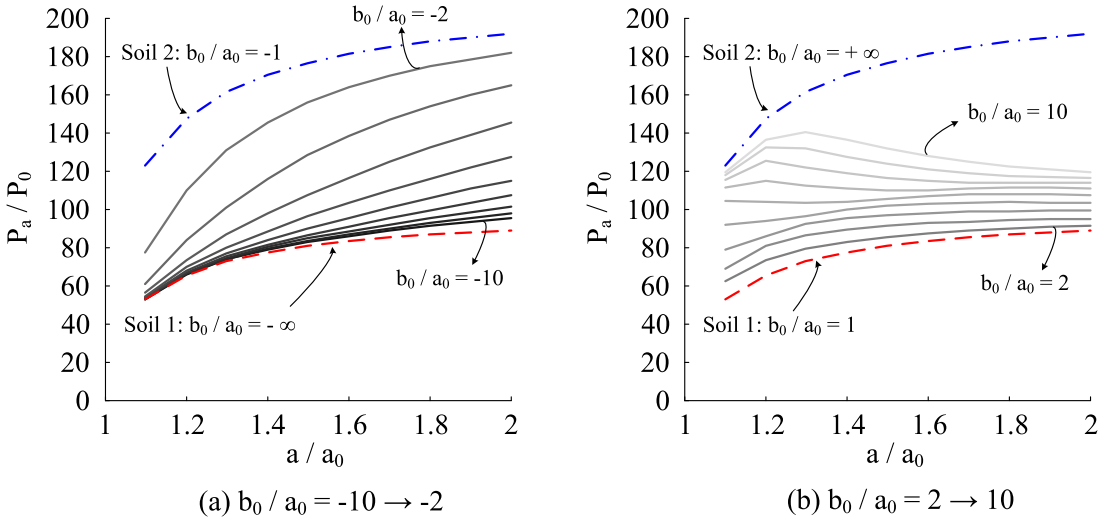

Figure 6.3 Pressure-expansion curves for cavities in two concentric layers: (a) cavity in Soil 1; and (b) cavity in Soil 2

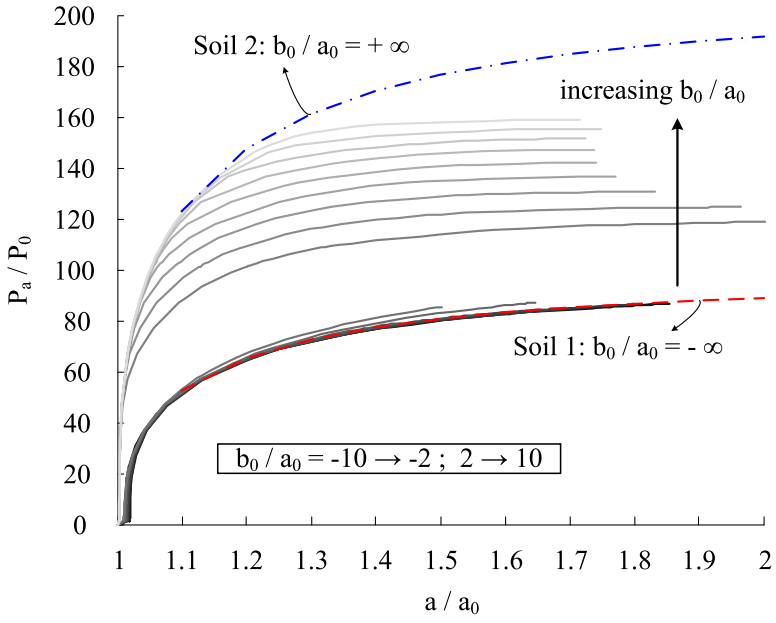

Figure 6.4 Pressure-expansion curves for cavities in horizontal two layers

A more visual comparison of the results is to integrate the values of cavity pressure at a certain expansion stage ($a/a_0 = 1.2$) with variation of b_0/a_0, as illustrated in Figure 6.5. The two horizontal reference lines are the cavity pressures in uniform weak and strong soils. The horizontally layered soil model provides a smoothed and realistic transition of cavity pressure and implies penetration resistance from one layer to the next. The results from the concentrically layered model illustrate a transition on each side of the interface. By combining the two stages from the concentric model, a prediction method for the transition of penetration resistance in layered soils can be provided (see Section 6.3.2). The size of the influence zone around the interface is related to the soil stiffness and strength, as shown in the results from both the concentrically and horizontal layered models.

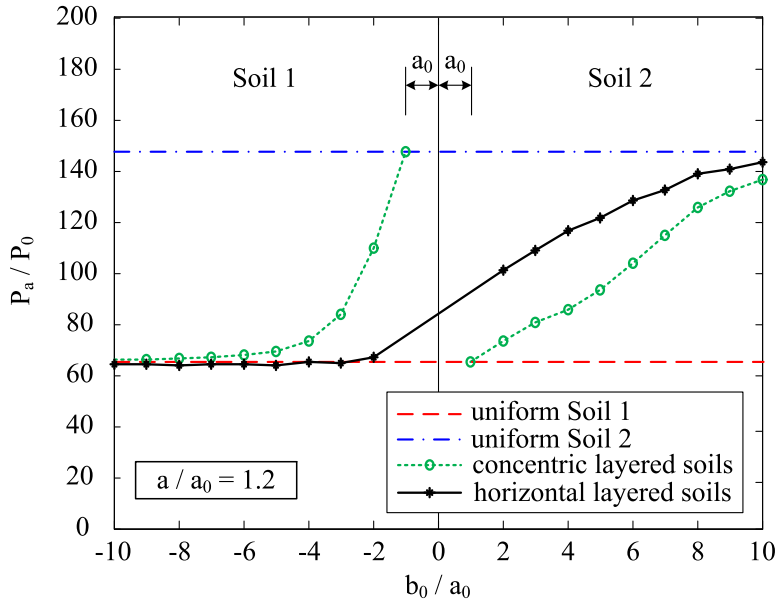

Figure 6.5 Cavity pressure with variation of b_0/a_0 in concentric and horizontal layered model when $a/a_0 = 1.2$

6.3 Penetration in Two-Layered Soils

6.3.1 Soil parameters

As non-associated Mohr-Coulomb soil model is used for analytical solutions, five parameters are required to represent the soil stress-strain relationship: Young's modulus (E); Poisson's ratio (ν); friction angle (ϕ); cohesion (C); dilatancy angle (ψ). The shear modulus (G) has the relationship between Young's modulus and Poisson's ra-

tio, based on Hooke's law: $G = E/[2(1+\nu)]$. Many analytical models have been proposed to predict the stress-strain behaviour for granular material (e.g. Santamarina and Cascante, 1996; Liao et al., 2000; McDowell and Bolton, 2001), especially for the evaluation of small-strain shear modulus (G_0). The Fahey-Carter model (Fahey and Carter, 1993) is a simple model to capture realistic non-linear stress-strain behaviour, which is also used in this chapter. For non-linear elastic behaviour, G_0 is defined as a function of in-situ confining stress (P_0), as follow:

$$\frac{G_0}{\sigma_{atm}} = c' \left(\frac{P_0}{\sigma_{atm}}\right)^{n'} \tag{6.1}$$

where c' and n' are soil-specific parameters (note that the dash mark $'$ is used to distinguish with the symbols appearing in Chapter 5), and σ_{atm} is the atmospheric pressure.

Shear stiffness degradation with increasing shear strain is not included in the analytical solutions, hence G_0 is used to represent the shear stiffness of the soil. Poisson's ratio is defined as 0.2, which is reasonable for many soils (Mitchell and Soga, 2005; Bolton, 1979). As the soil used in centrifuge tests is Fraction E silica sand, the triaxial test series carried out by Zhao (2008) is used to quantify the static soil stiffness. With curve-fitting using the Fahey-Cater model, the soil-specific parameters are suggested as $c' = 1000$ and $n' = 0.5$.

In terms of strength and dilatancy of sands, Bolton (1986) proposed a simple correlation between peak friction angle (ϕ'_{max}), critical state friction angle (ϕ'_{crit}) and peak dilatancy (ψ_{max}), with introducing a relative dilatancy index (I_R), based on triaxial tests of 17 sands:

$$\phi'_{max} - \phi'_{crit} = 0.8\,\psi_{max} = 3\,I_R{}^{\circ} \tag{6.2}$$

and I_R was also defined as a function of relative density (D_R) and in-situ confining stress (P_0):

$$I_R = D_R\,(Q' - \ln P_0) - R' \tag{6.3}$$

where Q' and R' are material constants; D_R is the relative density value in '%' and P_0 is in kPa.

For Leighton Buzzard sand, these material constants were obtained from triaxial tests by Wang (2005): $Q' = 9.4$ and $R' = 0.28$. In addition, the cohesion (C) was set as zero for cohesionless soil. Considering the assumption of constant material parameters for the analytical solution, a simple average method suggested by Randolph et al. (1994) is used for soil between the initial and critical state:

$$\phi = \frac{\phi'_{max} + \phi'_{crit}}{2} \tag{6.4}$$

$$\psi = \frac{\psi_{max}}{2} \tag{6.5}$$

6.3.2 Methodology

The effect of a distinct change in soil stiffness (due to soil layering) on the pressure expansion curves is shown to be significant in Chapter 5. The limit pressure is often applied to predict pile capacity or probe resistance in conventional cavity expansion solutions (e.g. Randolph et al., 1994). This approach is appropriate for uniform soils since the limiting pressure is only affected by the parameters of a single soil. In layered soils, Figure 5.4 and Figure 5.9 show that the limiting pressure depends only on the properties of Soil B (the outer layer or the lower layer). For penetration problems such as CPT or pile capacity analysis, the resistance of a probe located in Soil A depends in part on the properties of Soil A, so the limit pressure approach is not adequate for layered soils. A more suitable approach for layered soils, as suggested by Xu and Lehane (2008), is to consider a realistic increase in cavity size (given by a/a_0) and evaluate the cavity pressure required to achieve this expansion. Therefore, the penetration of a probe with diameter B into a sand sample with average particle size of d_{50} is suggested to be treated as a problem with an initial cavity ($a_0 = d_{50}/2$) expanding to the size of probe diameter (i.e. $a = B/2$).

To investigate cone tip resistance (q_c) in layered soils, the cone penetration process at a given depth is modelled as a spherical cavity expanded slowly from an initial diameter close in size to the average grain size of the soil to a final size corresponding to the diameter of the penetrometer. The cone tip resistance is then related to the corresponding cavity pressure that is calculated, as depicted in Figure 6.6. The penetration process is simulated by first considering an analysis point in Soil A (a weaker soil) sufficiently

far away from the Soil A/B interface such that Soil B has no effect, then considering points increasingly close to the interface, and finally moving into Soil B (a stronger soil). The distance to the soil interface is defined as H, which is equivalent to b_0 in the cavity expansion analysis.

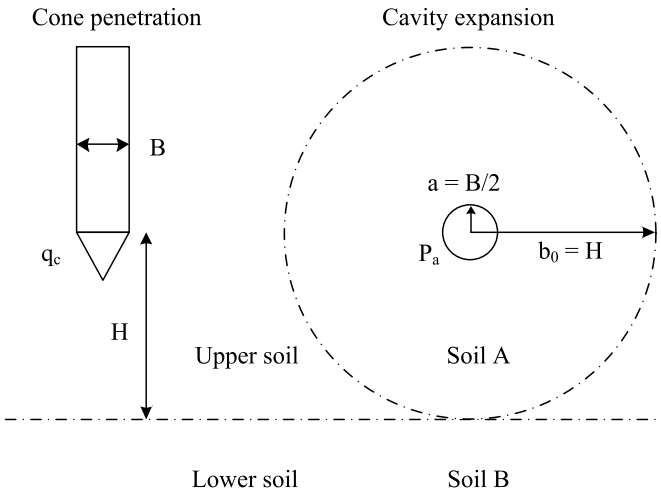

Figure 6.6 Schematic of cone penetration and cavity expansion in two-layered soils

As b_0 decreases from infinity to a_0 (i.e. cone tip approaches the interface), cavity pressure (P_a) transforms from $P_{a,A}$ to $P_{a,B}$, as shown in Figure 5.12 and Section 6.2. The cavity pressures at two stages provide the transition from Soil A to Soil B (blue dashed lines in Figure 6.7). However, these two lines do not give an adequate description of the transition of cavity pressure P_a between the soil layers, owing to the two extremes at the soil interface. To overcome this deficiency, the lines need to be combined to provide an interpolated transition of cavity pressure, $P_{a,int}$ (red line in Figure 6.7). A simple combination approach for the scenario of weak soil over strong soil is provided in Figure 6.7, which is based on the secant angles (θ_1 and θ_2) at $1B$ around the interface (i.e. a straight line on each side is formed by the two points at $|H| = 0$ and $|H| = B$ on the calculated lines). The corrected cavity pressure at the interface ($P_{a,interface}$) is then calculated by Equation (6.6), and the interpolated cavity pressure curve ($P_{a,int}$) is obtained using Equation (6.7) (the subscripts w and s relate to the weak and strong soil, respectively).

$$\frac{P_{a,interface} - P_{a,w}}{P_{a,s} - P_{a,interface}} = \frac{\tan\theta_1}{\tan\theta_2} \tag{6.6}$$

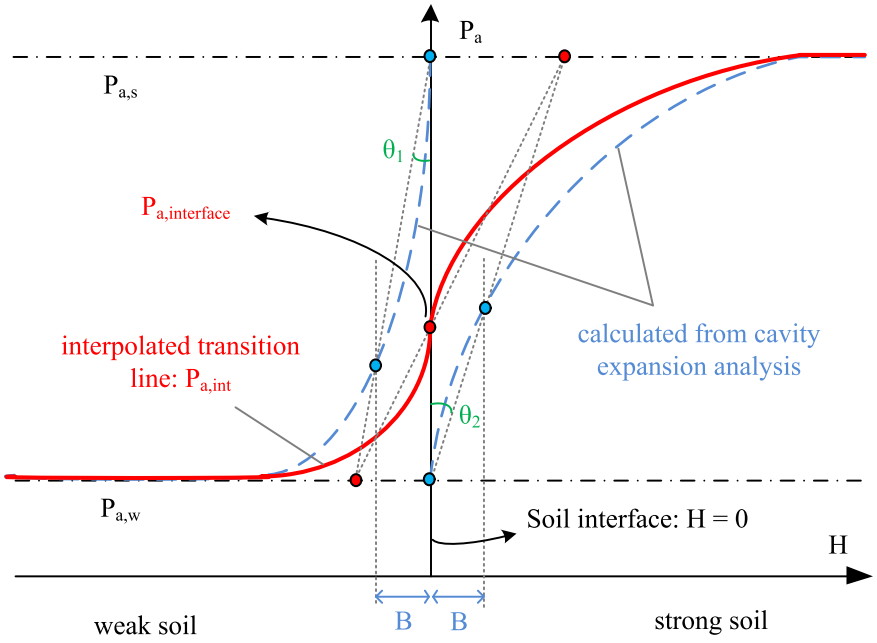

Figure 6.7 Schematic of combination of cavity pressures in two stages

$$P_{a,int} = \begin{cases} P_{a,w} + (P_a - P_{a,w}) \times \frac{P_{a,interface} - P_{a,w}}{P_{a,s} - P_{a,w}} & \text{(cavity in weak soil)} \\ P_{a,s} - (P_{a,s} - P_a) \times \frac{P_{a,s} - P_{a,interface}}{P_{a,s} - P_{a,w}} & \text{(cavity in strong soil)} \end{cases} \tag{6.7}$$

The cavity pressure ratio (η'_0) is defined as $(P_{a,int} - P_{a,w})/(P_{a,s} - P_{a,w})$, to represent the transfer proportion from weak soil ($\eta'_0 = 0$) to strong soil ($\eta'_0 = 1$), as shown in Figure 6.8a. This ratio η'_0 is also used to smooth the transition of soil properties (e.g. $\phi_{smooth} = \phi_w + \eta'_0 \times (\phi_s - \phi_w)$). The correlations for calculating cone resistance from spherical cavity pressure in cohesionless and cohesive soils proposed by Yasufuku and Hyde (1995) and Ladanyi and Johnston (1974), respectively, are used to estimate q_c (Equation 6.8).

$$q_c = \begin{cases} P_{a,int} \,/\, (1 - \sin\phi_{smooth}) & \text{(cohesionless soils)} \\ P_{a,int} + \sqrt{3} s_{u,smooth} & \text{(cohesive soils)} \end{cases} \tag{6.8}$$

where ϕ_{smooth} and $s_{u,smooth}$ are friction angle and undrained shear strength, respectively. The subscript *smooth* implies that the values have been smoothed between the two adjacent soil layers by using η'_0.

The transition of cone tip resistance, q_c, from the weak to the strong soil can now be described. The cone tip resistance ratio is defined as $\eta' = (q_c - q_{c,w})/(q_{c,s} - q_{c,w})$,

which also varies from 0 to 1. It needs to be noted that the definition of resistance ratio is different from η defined by Xu and Lehane (2008), which is $\eta = q_c/q_{c,s}$. Also, the correlation between the two definitions is: $\eta' = (\eta - \eta_{min})/(1 - \eta_{min})$. Correspondingly, the influence zones in weak and strong soil layers, referred to as Z_w and Z_s, respectively, are defined as areas where $0.05 < \eta' < 0.95$, as shown in Figure 6.8b.

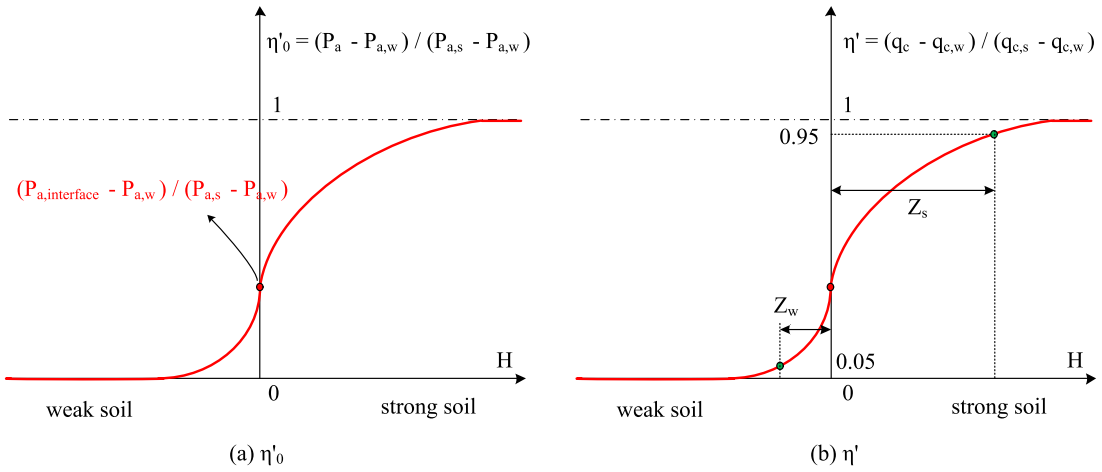

Figure 6.8 (a) Cavity pressure ratio: η'_0; (b) cone tip resistance ratio: η'

6.3.3 Interpretation of results

A series of cavity expansion tests in two-layered soils was carried out to explore the layered effects with variation of relative density (D_R). The cone penetration tests were simulated with initial condition of constant confining stress, as to replicate the environment in a calibration chamber test with no boundary effects. $P_0 = 1\,kPa$ was used in these tests, and the soil model parameters for different D_R are provided in Table 6.1, with estimated cone resistance in uniform soil layer using a penetrometer with diameter of $12\,mm$.

Figure 6.9 shows the example of combination of cavity expansion pressures in loose sand ($D_R = 10\,\%$) overlying dense sand ($D_R = 90\,\%$). The transformation curve (the red curve) is plotted against the normalised distance to the interface (H/B) and shows that the influence zone in the stronger layer is larger than in the weaker soil, which agrees with the observations from experiments (Chapter 4) and field tests (Meyerhof and Sastry, 1978a;b; Meyerhof, 1983).

Table 6.1 Soil model parameters and estimated cone resistance in uniform soil layer

D_R (%)	Soil parameters					Cone tip resistance q_c (kPa)
	G (MPa)	ν	C (kPa)	ϕ (°)	ψ (°)	
10	10.1	0.2	0	33.0	1.24	309.1
30	10.1	0.2	0	35.8	4.76	573.3
50	10.1	0.2	0	38.6	8.29	1063.8
70	10.1	0.2	0	41.5	11.81	1958.2
90	10.1	0.2	0	44.3	15.34	3542.4

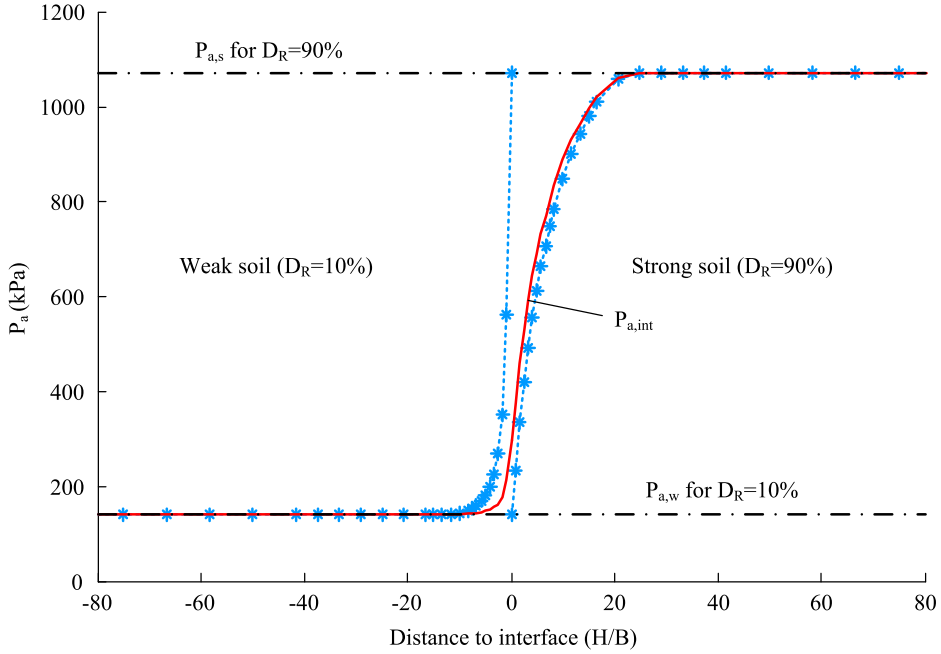

Figure 6.9 Combination of cavity expansion pressures in loose sand ($D_R = 10\%$) overlying dense sand ($D_R = 90\%$)

By varying the relative density of weaker soil overlying dense sand ($D_R = 90\%$), the cavity pressures are shown in Figure 6.10a. Figure 6.10b presents the results with loose sand ($D_R = 10\%$) overlying stronger soils with variation of relative density ($D_R = 30\%, 50\%, 70\%, 90\%$). The cavity pressure ratio curves, as defined before, are shown in Figure 6.11, and the smoothed friction angles (Figure 6.12) are calculated based on the cavity pressure ratio curves. With estimation of Yasufuku and Hyde (1995), the cone tip resistances and resistance ratio curves are shown in Figure 6.13 and Figure 6.14 respectively.

The studies of Meyerhof (1976) and Meyerhof (1977) provided constant influence regions around the soil interface: $10B$ in dense sand, and $2B$ in loose sand. A linear

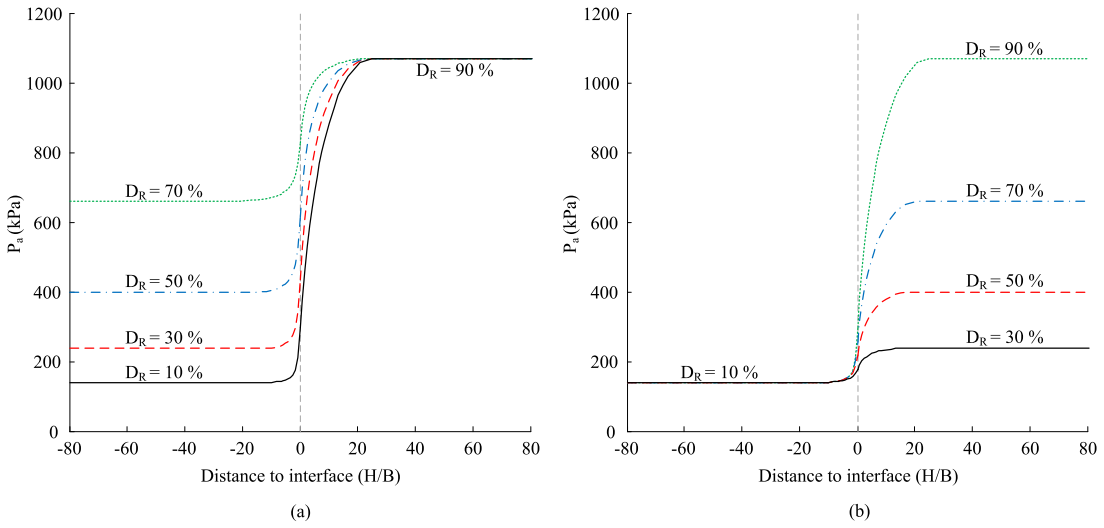

Figure 6.10 Cavity expansion pressures in two-layered soils: (a) variation of weaker soil; (b) variation of stronger soil

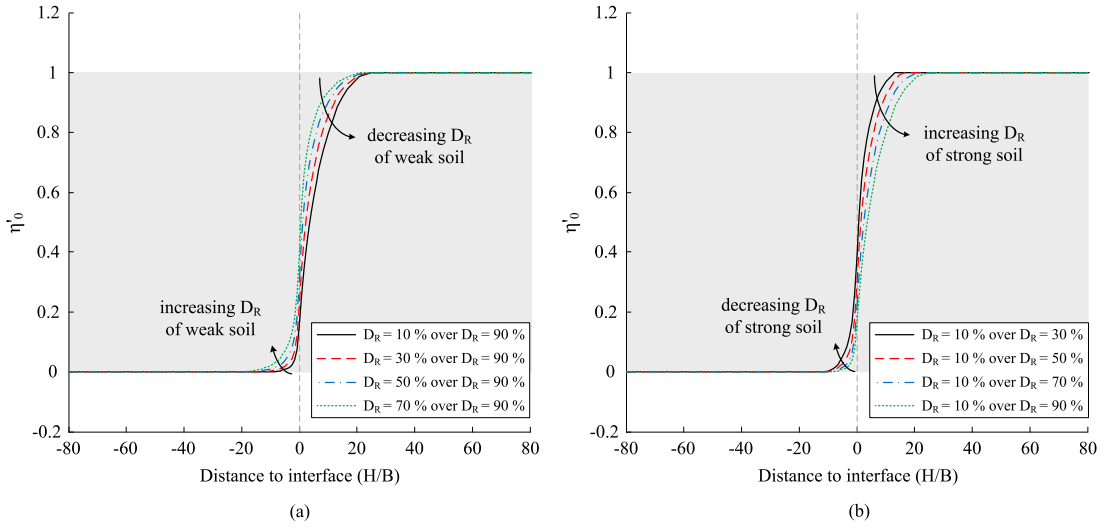

Figure 6.11 Cavity pressure ratio curves in two-layered soils: (a) variation of weaker soil; (b) variation of stronger soil

transition is generally used for pile design. However, from the resistance ratio curves presented previously, the transition zones on both sides of the soil interface are shown to be non-linearly dependent on the properties of both soil layers. The sizes of the influence zones vary with the relative density of each soil. The influence zones (Z_w and Z_s) are defined from resistance ratio curves where $\eta' = 0.05$ and 0.95. It can be seen that Z_w increases with relative density of the weaker soil and decreases with relative density of the stronger soil; whereas Z_s decreases with relative density of weaker soil and increases with relative density of stronger soil. In this study, the size of influence zones is suggested to be evaluated using the relative densities: $D_{R,w}$ and $D_{R,s}$, as shown in Figure 6.15. A surface fitting is applied to provide the expressions of normalised

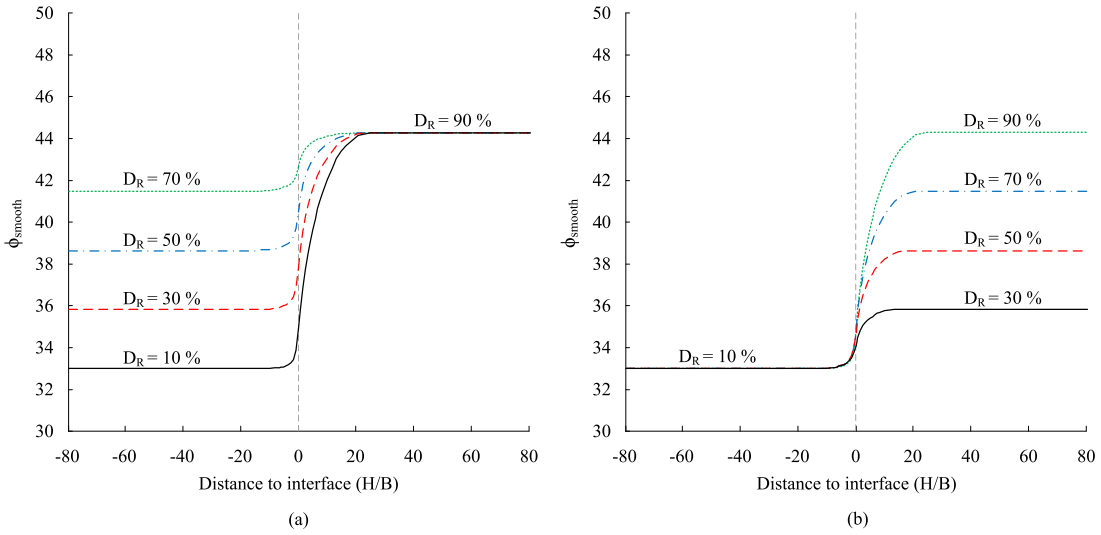

Figure 6.12 Smoothed friction angles based on cavity pressure ratio curves

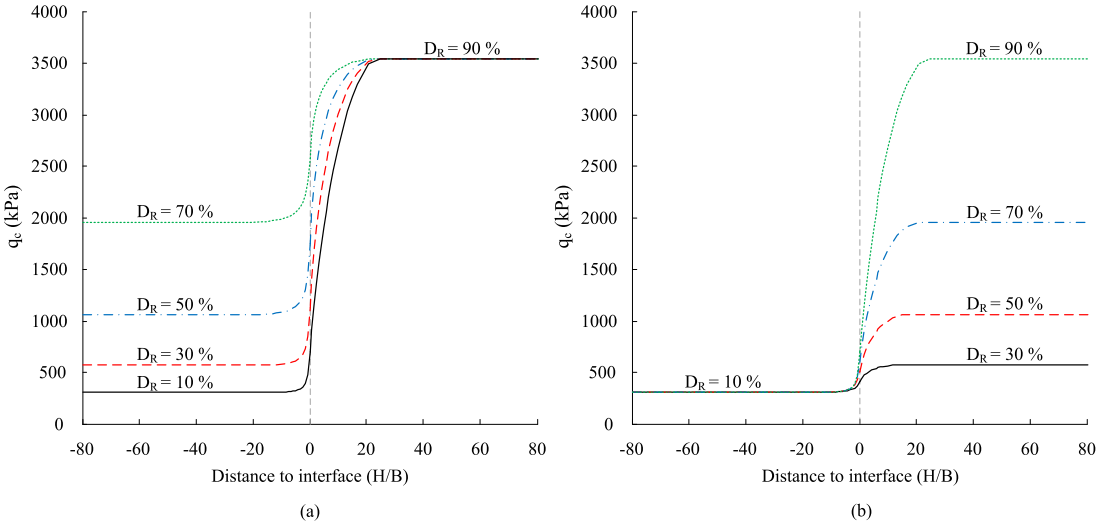

Figure 6.13 Cone tip resistance in two-layered soils: (a) variation of weaker soil; (b) variation of stronger soil

influence zones in Equation (6.9) and Equation (6.10) (D_R in '%'), with correlation coefficient R^2 of 0.9639 and 0.9955 respectively. The equations are only valid for this particular soil in a certain stress condition, however they imply a linear relationship between influence zone size and relative density.

$$Z_w/B = -0.0871 \times D_{R,w} + 0.0708 \times D_{R,s} - 5.8257 \tag{6.9}$$

$$Z_s/B = -0.1083 \times D_{R,w} + 0.1607 \times D_{R,s} + 5.1096 \tag{6.10}$$

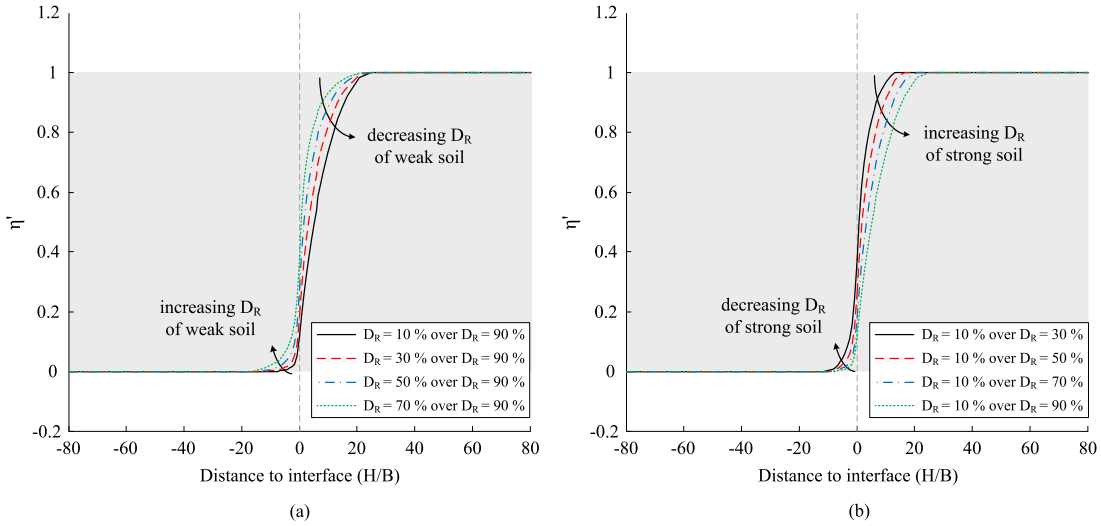

Figure 6.14 Cone tip resistance ratio curves in two-layered soils: (a) variation of weaker soil; (b) variation of stronger soil

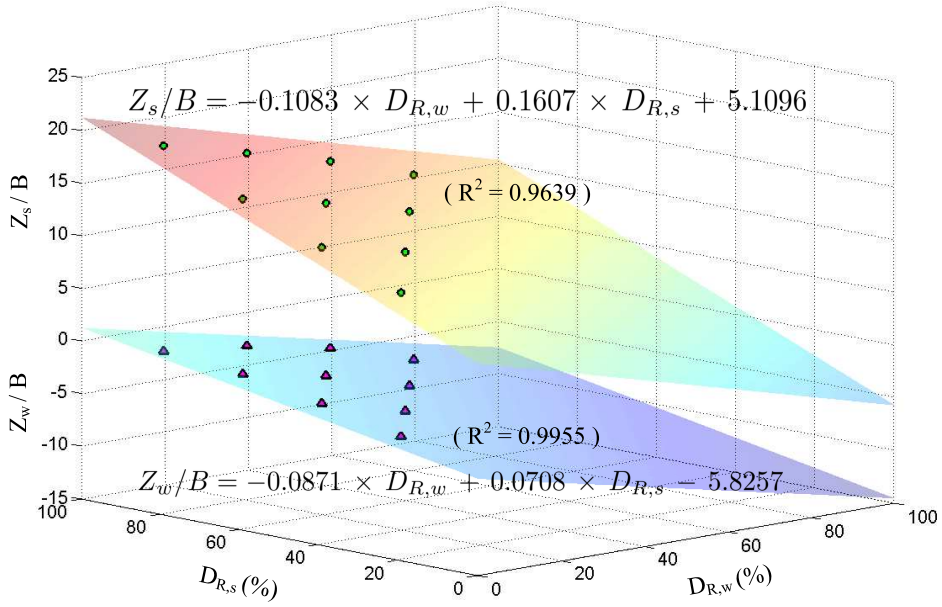

Figure 6.15 Influence zones in both weak and strong soils with variation of D_R

6.3.4 Comparisons with elastic solutions

Vreugdenhil et al. (1994) presented an approximate analysis for interpretation of cone penetration results in multi-layered soils, by representing a CPT by a circular uniform load, as shown in Figure 6.16. The vertical deflection in two soil layers caused by the uniform load was defined as Δ, given by Equation (6.11) and (6.12) (Vreugdenhil et al., 1994):

$$\Delta = \frac{P \times B}{4 G_A} \left(\frac{1-\lambda_0}{2-\lambda_0} \right) \tag{6.11}$$

$$\lambda_0 = \left(1 - \frac{G_A}{G_B} \right) \frac{1}{\sqrt{1+(2H/B)^2}} \tag{6.12}$$

where G_A and G_B are the stiffness in the two soil layers.

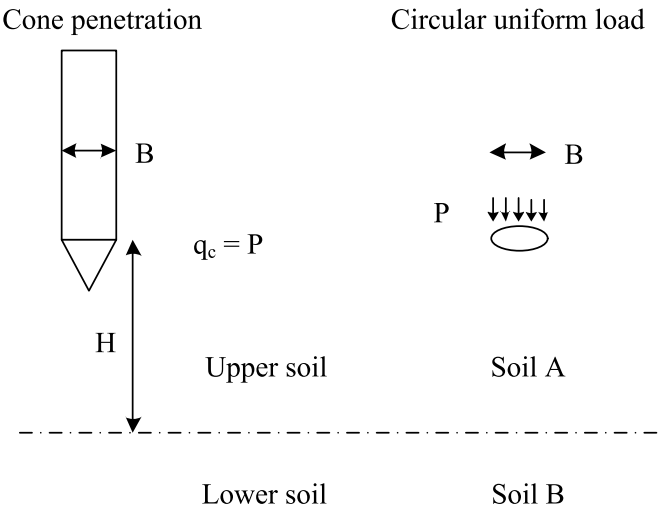

Figure 6.16 Representation of CPT by circular uniform load (after Vreugdenhil et al., 1994)

The derivation of Vreugdenhil et al. (1994) is extended here to combine the two loading stages (load in Soil A and load in Soil B) by using the integral of the Dirac delta function **Dirac(x)**, which is defined as:

$$s = \int_H^{+\infty} \mathbf{Dirac}(x) = \begin{cases} 0 & (\text{when } H > 0) \\ 1 & (\text{when } H < 0) \end{cases} \tag{6.13}$$

Then λ can be rewritten from λ_0, using a stiffness ratio $m = G_w/G_s \approx q_{c,w}/q_{c,s}$:

$$\lambda = (1 - m^{2s-1}) \frac{1}{\sqrt{1 + (2H/B)^2}} \tag{6.14}$$

With same vertical deflection generated from weak soil to strong soil, the CPT resistance and resistance ratio η' can be derived as shown in Equation (6.15) and Equation (6.16). The resistance ratio from the elastic solution is only dependent on the stiffness ratio (m) and distance to soil interface (H).

$$q_c = \frac{4\Delta}{B} \times \frac{2-\lambda}{1-\lambda} \times q_{c,s} \times \left(\frac{q_{c,w}}{q_{c,s}}\right)^s \tag{6.15}$$

$$\eta' = \frac{q_c - q_{c,w}}{q_{c,s} - q_{c,w}} = \frac{\frac{2-\lambda}{1-\lambda} \times m^s - 2m}{2\,(1-m)} \tag{6.16}$$

Comparison of the current analytical solution for q_c in two-layered soils and the elastic solution based on the extended elastic analysis are shown in Figure 6.17. For the test with loose sand ($D_R = 10\,\%$) overlying dense sand ($D_R = 90\,\%$), the influence zone in the dense sand for the elastic solution is much larger than that from the elastic-plastic solution, whereas the transition in the loose sand is similar. Smaller influence zones in both soil layers for elastic solution are obtained for tests with small variation of relative density (i.e. stiffness). The differences of the results are owing to elastic solution that excludes the effects of soil yielding. Also, the assumption of uniform circular load for the elastic penetration problem is believed to be over-simplified. On the other hand, the comparisons show the evolution of resistance ratio curve when considering the effects of soil strength with large strain analyses, and more comparisons will be provided in the next section with experimental and numerical results.

6.3.5 Comparisons with experimental and numerical results

Ahmadi et al. (2005) developed a numerical model of cone penetration using a Mohr-Coulomb elastic-plastic material and showed good comparisons with published experimental measurements from calibration chamber tests. Ahmadi and Robertson (2005) extended the numerical analyses to consider cone tip resistance in layered soils with varying soil properties (relative density of sand, undrained shear strength of clay) and geometric conditions. The results of η' from two of their tests are plotted in Figure

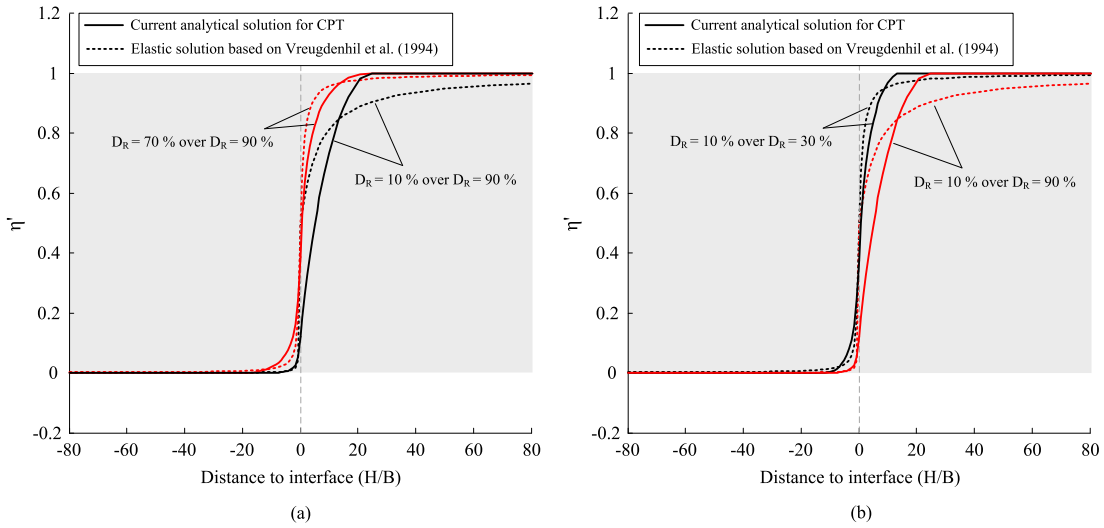

Figure 6.17 Comparisons of η' curves in two-layered soils between the current analytical solution and the elastic solution based on Vreugdenhil et al. (1994)

6.18: (a) loose sand ($D_R = 30\%$) overlying dense sand ($D_R = 90\%$); (b) soft clay ($s_u = 20\,kPa$) overlying dense sand ($D_R = 90\%$).

More recently, Xu and Lehane (2008) performed a series of numerical analyses of spherical cavity expansion to evaluate layered effects on the resistance of piles and penetrometers. They proposed Equation (6.17) for the resistance ratio (η') based on a parametric study and validated against centrifuge tests.

$$\eta' = exp\left[-exp\left(B_1 + B_2 \times H/B\right)\right] \tag{6.17}$$

where $B_1 = -0.22\ln\left(q_{c,w}/q_{c,s}\right) + 0.11 \leq 1.5$ and $B_2 = -0.11\ln\left(q_{c,w}/q_{c,s}\right) - 0.79 \leq -0.2$.

Figure 6.18 compares η' values from the above mentioned sources against results obtained using the analytical cavity expansion method for equivalent soil properties and stress conditions. The data illustrates that the results from this study compare very well with other published methods.

6.4 Penetration in Multi-layered Soils

The analytical cavity expansion solutions and their application to interpretation of CPT in two-layered soils have been presented and discussed in the previous section. The

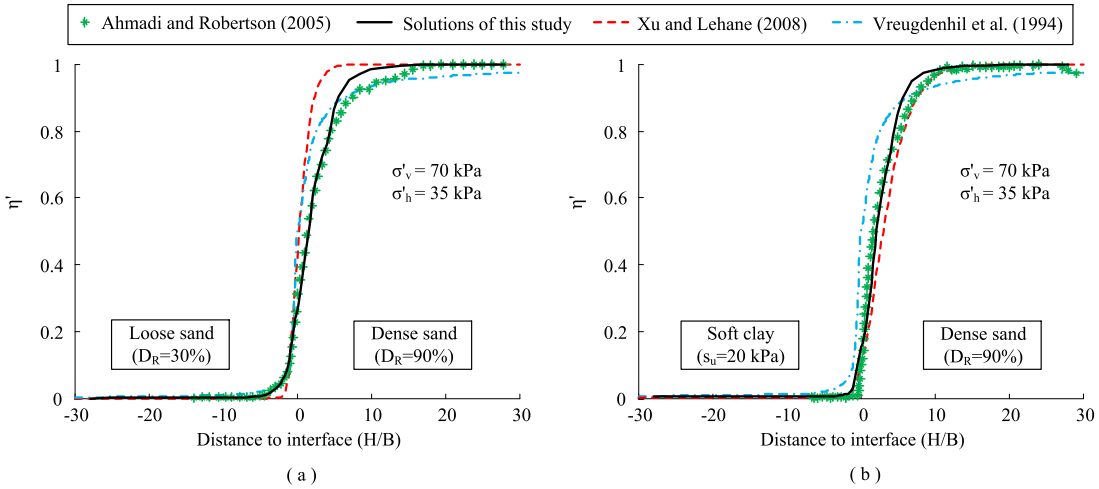

Figure 6.18 Comparison of cone tip resistance ratio (η') in two-layered soils

cone penetration resistance in multi-layered soils can be obtained by superposition of resistance ratios (η') in two-layer systems. Generally, the penetrometer senses soil layers some distance beneath and above the cone tip, which are referred to as influence zones (i.e. Z_w and Z_s). When the soil layer is very thin, the cone tip resistance would have been affected by the next soil layer before it reached the resistance in the local soil layer. Hence, interpretation of CPT data in thin layers may easily over-predict or under-predict soil properties. The effects of thin layer thickness and soil properties are investigated in this section.

6.4.1 Methodology

Figure 6.19 describes the cone penetration in multi-layered soils where a strong soil is embedded within a weak soil (assuming the layers of weak soil have the same properties). When the thickness of the strong soil (H_t) is thin enough ($< 2Z_s$), the cone tip resistance is always lower than the resistance in the uniform strong soil ($q_{c,s}$). The maximum resistance ($q_{c,max}$) is affected by the influence zones (Z_w and Z_s) and the thickness of the strong soil (H_t). The profile of cone tip resistance ratio (η') in the thin-layer of strong soil is shown in Figure 6.20a, with definition of maximum resistance ratio (η'_{max}). For the scenario of a thin-layer of weak soil in Figure 6.20b, penetration resistance in the strong soil ($\eta' = 1$) is influenced by the weak layer, and the thin-layer effect is evaluated by the minimum resistance ratio (η'_{min}). The gap between the peak resistance ratio with the uniform value ($1 - \eta'_{max}$ and $\eta'_{min} - 0$) implies the magnitude of thin-layer effects.

From the application of the analytical solution in two-layered soils presented in the previous section, the resistance ratio for multi-layered soils can be obtained by superposition of η' in multiple two-layered profiles. For example, when the strong soil is sandwiched by two layers of weak soil, the profile is a combination of 'weak-strong' (subscript *ws*) and 'strong-weak' (subscript *sw*), with resistance ratio of $\eta'_{ws} = \eta'(H)$ and $\eta'_{sw} = \eta'(H_t - H)$. This is based on the symmetric assumption, $\eta'_{ws}|_{H=0} = \eta'_{sw}|_{H=H_t}$ and $\eta'_{ws}|_{H=H_t/2} = \eta'_{sw}|_{H=H_t/2}$. When simply multiplying the resistance ratios, the maximum resistance ratio equals $\left(\eta'_{ws}|_{H=H_t/2}\right)^2$, and varies from $\left(\eta'_{ws}|_{H=0}\right)^2$ to 1 when increasing the thickness of the sandwiched soil layer (H_t) from 0 to infinity. In order to eliminate this inconsistency, a correction factor is integrated within the superposition of η'_{ws} and η'_{sw}. The generated resistance ratio and the maximum resistance ratio in the three-layered system with a thin layer of strong soil are expressed in Equation (6.18) and (6.19). Correspondingly, the system with a thin layer of weak soil can be produced in the same process for the calculation of η'_{min}.

$$\eta' = \eta'_{ws} \times \eta'_{sw} \times \frac{\left(\eta'_{ws}|_{H=H_t/2}\right)^2 - \left(\eta'_{ws}|_{H=0}\right)^2}{1 - \left(\eta'_{ws}|_{H=0}\right)^2} \tag{6.18}$$

$$\eta'_{max} = \left(\eta'_{ws}|_{H=H_t/2}\right)^2 \times \frac{\left(\eta'_{ws}|_{H=H_t/2}\right)^2 - \left(\eta'_{ws}|_{H=0}\right)^2}{1 - \left(\eta'_{ws}|_{H=0}\right)^2} \tag{6.19}$$

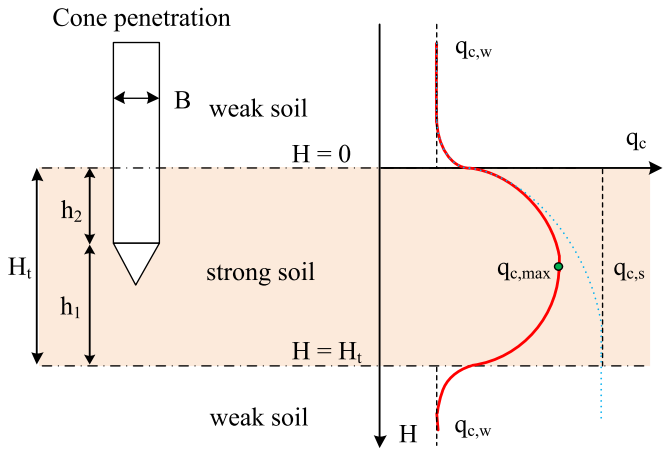

Figure 6.19 Schematic of cone penetration in multi-layered soils: strong soil embedded in weak soils

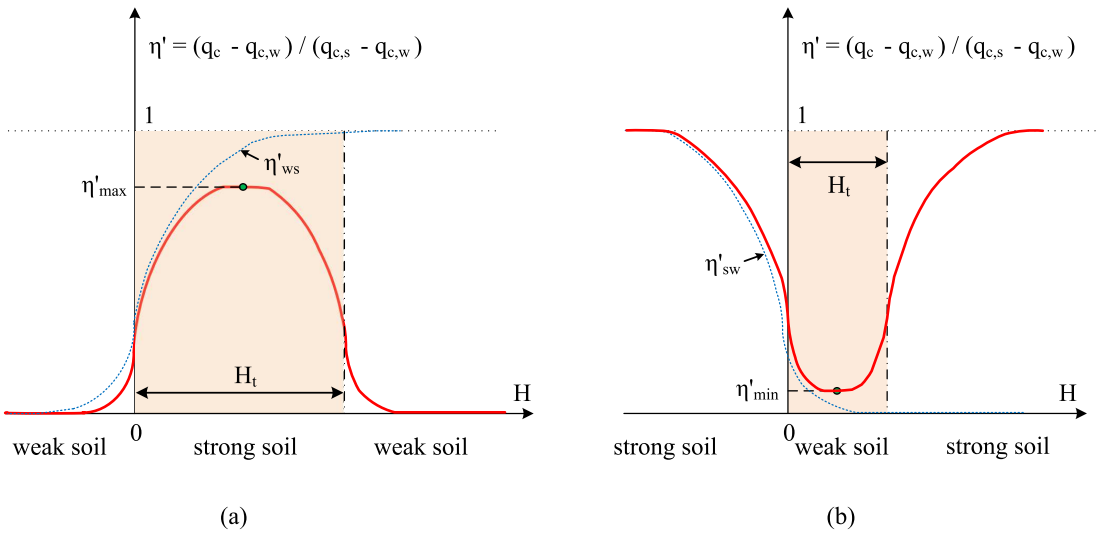

Figure 6.20 Schematic of cone tip resistance ratio (η') in thin-layered soils: (a) strong soil embedded in weak soils; and (b) weak soil embedded in strong soils

6.4.2 Thin-layer effects

6.4.2.1 Strong soil within weak soil layers

For thin-layer analysis, multi-layered solution is adopted, and the situation with thin layer of strong soil in weak soils is considered as depicted in Figure 6.20a. Cone tip resistance (q_c) transforms from $q_{c,w}$ to $q_{c,s}$ when penetrating from weak soil to strong soil. While the strong soil layer is a thin layer sandwiched by weak soils, q_c senses the lower weak soil before it reaches the resistance in strong soil ($q_{c,s}$). The maximum resistance, referred to as $q_{c,max}$, represents the resistance when the cone is around the centreline of the thin layer.

Figure 6.21 shows the resistance ratio curves for thin-layer of strong soil ($D_R = 90\%$) embedded within weak soil ($D_R = 10\%$) with variation of H_t/B from 10 to 50. Thin-layer effects increase significantly with decreasing layer thickness. When $H_t = 50$, the thickness is larger than two times Z_s ($Z_s \approx 20$ for test with $D_R = 10\%$ overlying $D_R = 90\%$) and the maximum value of η' reaches 1, indicating no thin-layer effect occurring.

The effects of relative density of strong soil (Figure 6.22a) and weak soil (Figure 6.22b) on the influence of thin-layer are investigated with a constant thin-layer thickness ($H_t = 20B$). η'_{max} seems to decrease linearly ($\Delta\eta'_{max} \approx -0.2$ for increasing D_R of 20%) when increasing D_R of strong soil from $D_R = 30\%$ to $D_R = 90\%$ embedded

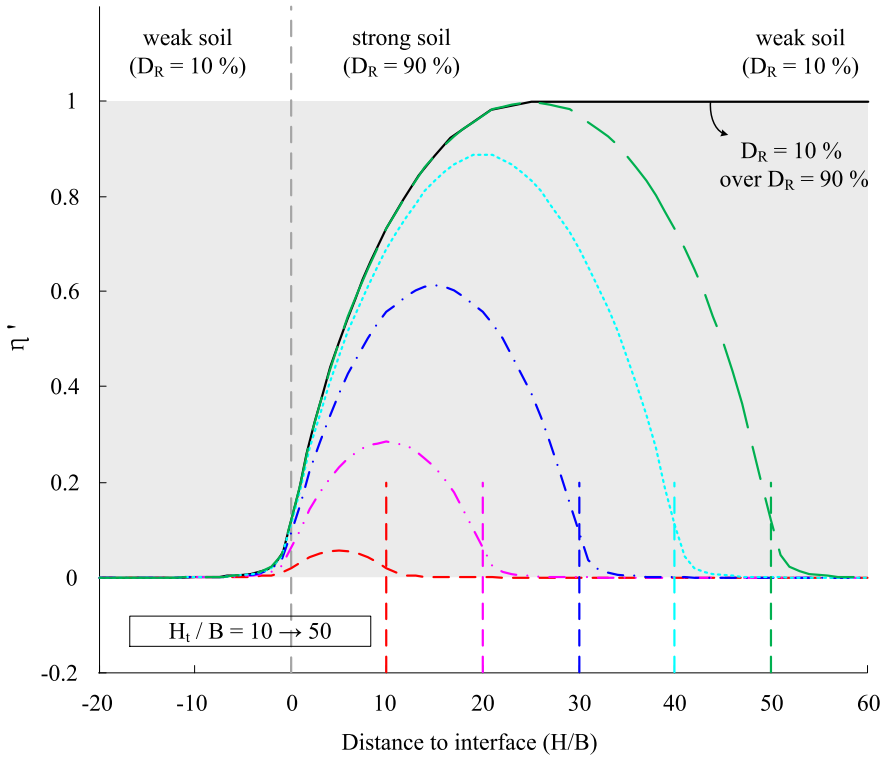

Figure 6.21 Resistance ratio curves for thin-layer of strong soil ($D_R = 90\,\%$) sandwiched by soils with $D_R = 10\,\%$, with variation of H_t/B from 10 to 50

within weak soil with 10 % relative density. On the other hand, a 20 % decrease of D_R in weak soil will enhance the thin-layer effect by approximately 15 %.

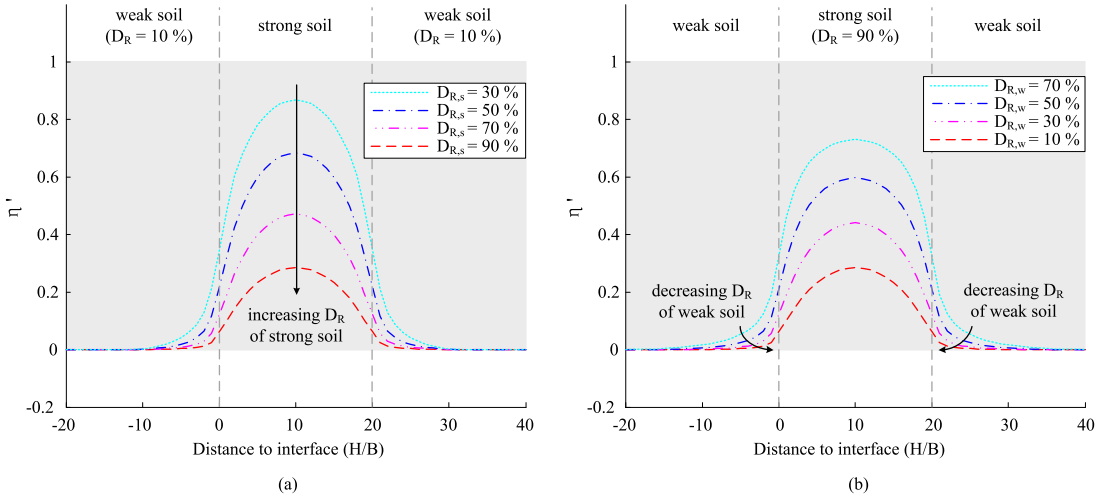

Figure 6.22 Resistance ratio curves for thin-layer of strong soil ($H_t/B = 20$): (a) varying D_R in strong soil; (b) varying D_R in weak soil

The variation of η'_{max} with the thickness of the thin-layer is examined by changing D_R in both strong and weak soil layer, as presented in Figure 6.23. The area between 1 and η'_{max} reveals the evidence and the magnitude of the thin-layer effects, which vanishes

gradually with increasing H_t. The curves also indicate the effects of $D_{R,s}$ and $D_{R,w}$; either increasing D_R of strong soil or decreasing D_R of weak soil would intensify the effects of the thin-layer.

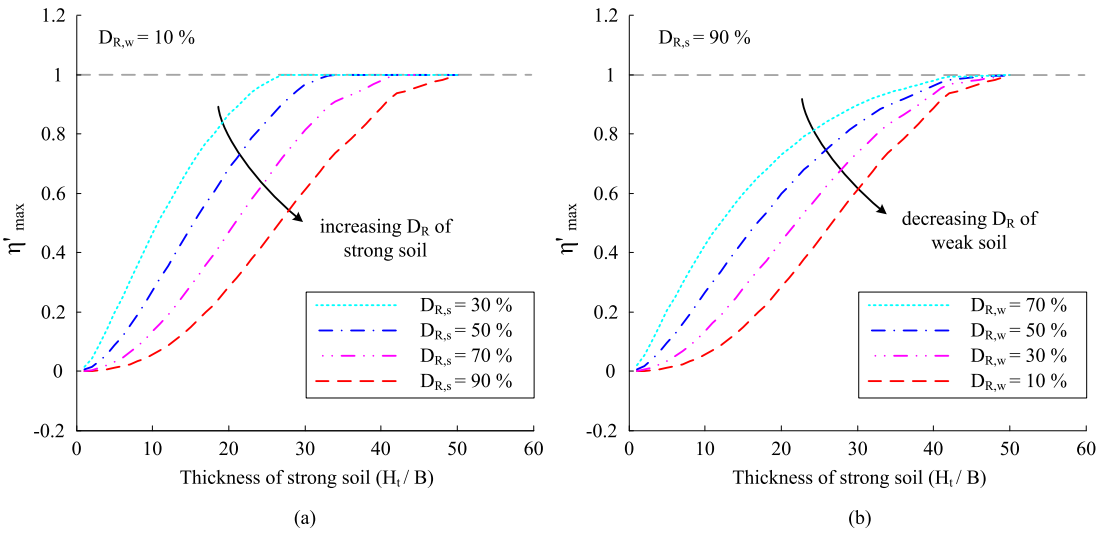

Figure 6.23 Variation of the maximum resistance ratio η'_{max} with the thickness of the thin-layer: (a) varying D_R in strong soil; (b) varying D_R in weak soil

6.4.2.2 Weak soil within strong soil layers

Correspondingly, for the scenario of thin layer of weak soil as illustrated in Figure 6.20b, the thin-layer effects are investigate in this section. The variation with weak soil thickness is provided in Figure 6.24. Compared to thin layer of strong soil, smaller size of H_t is required to show the layered effect, owing to the smaller size of the influence zone in the weak side. When $H_t < 15$, the minimum resistance ratio starts to be affected by the strong layers. However, the existence of the weak thin-layer significantly and extensively affect the measurements in both strong layers. When severe thin-layer effect is occurring, an estimation of the actual $q_{c,w}$ is required to prevent an over-predicted soil strength.

The variation of η' with D_R in each soil layer is shown in Figure 6.25, with a constant $H_t = 10\,B$. A larger thin-layer effect is observed for increasing density of the weak soil, while the effect means less influence induced by the layer of weak soil and smaller influence zones in strong soil layers. Inversely, when increasing D_R of the strong soil, the layers tend to be more affected by the thin-layer of weak soil, and η'_{min} decreases until the resistance is sufficiently developed in the weak layer.

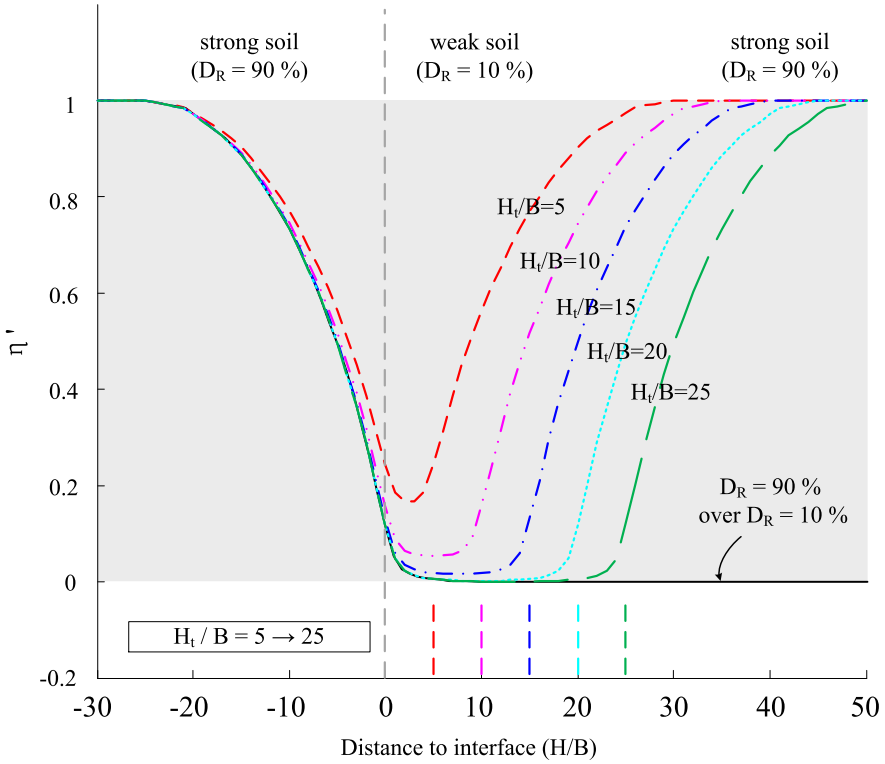

Figure 6.24 Resistance ratio curves for thin-layer of weak soil ($D_R = 10\%$) sandwiched by soils with $D_R = 90\%$), with variation of H_t/B from 5 to 25

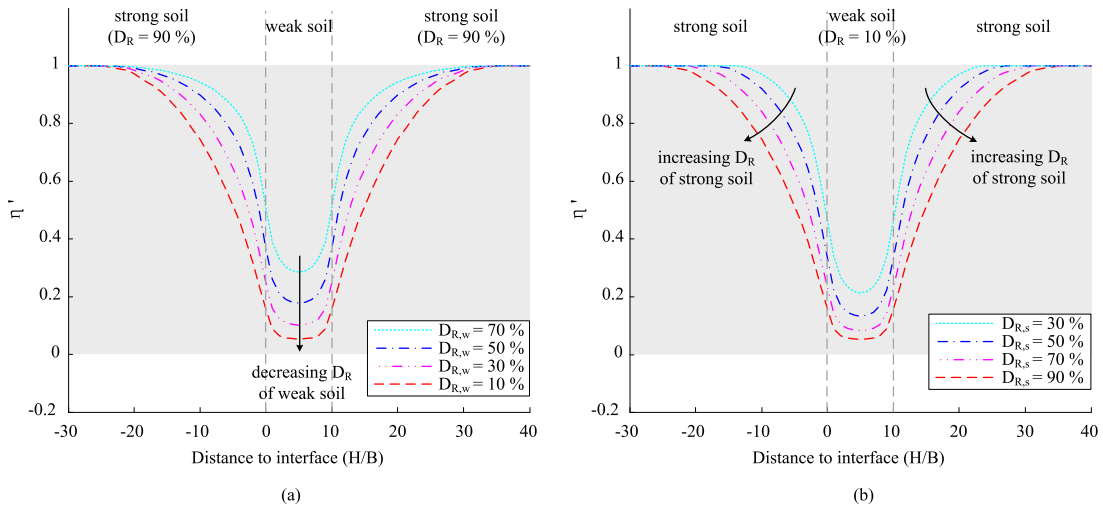

Figure 6.25 Resistance ratio curves for thin-layer of weak soil ($H_t/B = 10$): (a) varying D_R in weak soil; (b) varying D_R in strong soil

Consistent with the gradual reduction of the thin-layer effect from the curves of η'_{max} for thin-layer of strong soil (Figure 6.23), the minimum resistance ratio in the sandwiched weak soil decreases with the thickness H_t, but at a relatively sharper rate, as illustrated in Figure 6.26. Deceasing $D_{R,w}$ and increasing $D_{R,s}$ are also shown to prevent the thin-layer effect of the embedded weak soil.

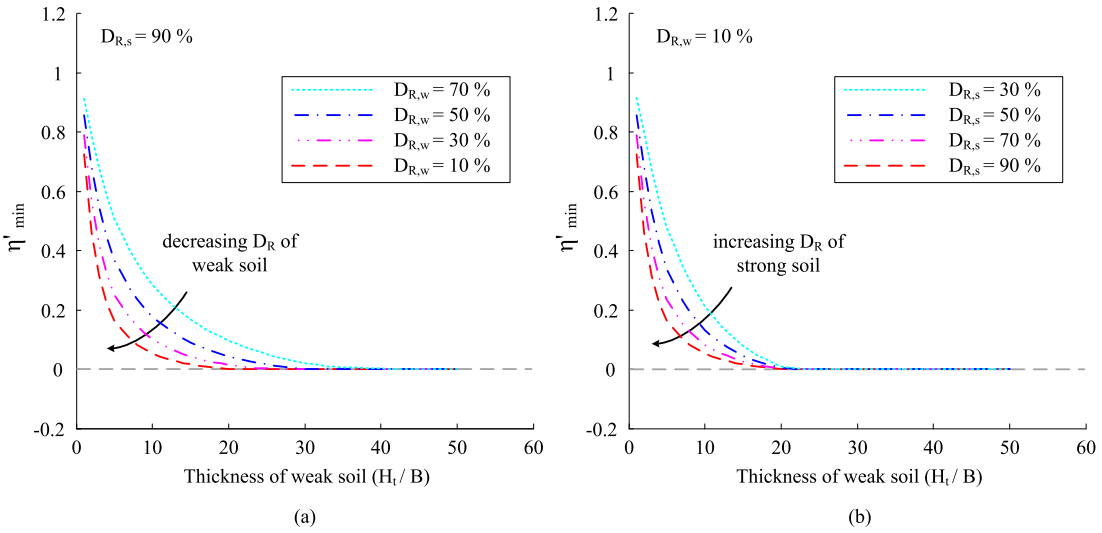

Figure 6.26 Variation of the minimum resistance ratio η'_{min} with the thickness of the thin-layer: (a) varying D_R in weak soil; (b) varying D_R in strong soil

6.4.3 Comparisons with field data and numerical results

For penetration in thin layered soils, most of the research and applications reported from the literature are based on the simplified elastic solution carried out by Vreugdenhil et al. (1994). Robertson and Fear (1995) proposed the parameter $K_H = q_{c,s}/q_{c,max}$ to correct the cone resistance from the field measurements. The degradation curves of K_H with H_t was investigated for different stiffness ratio G_s/G_w (i.e. $q_{c,s}/q_{c,w}$), based on the method of Vreugdenhil et al. (1994). After some field data reported by an unpublished work by Robertson and Castro, indicating the over-prediction of the thin-layer effects from the elastic solution, Youd and Idriss (2001) plotted this area with field data, and provided an empirical equation of K_H for the lower bound of the field observation.

A derivation of elastic solution based on the method of Vreugdenhil et al. (1994) is modified and provided here for a system with a thin layer of strong soil. The distances from the probe shoulder to the soil interfaces (Figure 6.19) are defined as h_1 and h_2, as expressed in Equation (6.20). The tip resistance q_c is then deduced for a probe at each soil layer in Equation (6.21); R_1 and R_2 are parameters related to h_1/B and h_2/B.

$$\begin{aligned} h_1 &= |H_t - H|; \qquad & R_1 &= 1/\sqrt{1+(2h_1/B)^2}; \\ h_2 &= |H - 0|; \qquad & R_2 &= 1/\sqrt{1+(2h_2/B)^2}; \end{aligned} \tag{6.20}$$

$$q_c = \begin{cases} q_{c,w} \times \frac{m-(m-1)(R_1+R_2)/2}{[m-R_1(m-1)][m-R_2(m-1)]} & (0 < H < H_t) \\ q_{c,w} \times \frac{2-(1-m)(R_1-R_2)}{2-2(1-m)(R_1-R_2)} & (others) \end{cases} \tag{6.21}$$

When the probe is at the depth with the centre of the thin layer $H = H_t/2$ (i.e. $h_1 = h_2 = H_t/2$), and $R_0 = R_1 = R_2 = 1/\sqrt{1+(H_t/B)^2}$, the maximum resistance is achieved (Equation 6.22), which is dependent with $q_{c,s}$, $q_{c,w}$, and H_t. As to the parameter K_H proposed by Robertson and Fear (1995), the expression is provided by Equation (6.23). K_H is a simple value to correct $q_{c,s}$; however the influence of the weak soil is neglected from the definition, and the value increases to infinity when the thin-layer effect is significantly large. The effects of thin layer have been investigated from the previous sections, showing the combination of the influences from both weak and strong soil layers. On the other hand, the maximum (or minimum) value of resistance ratio within the thin-layer system provides a more comprehensive parameter for evaluation of thin-layer effects. Therefore, η'_{max} for the elastic solution can be shown in Equation (6.24). More investigation of η'_{max} from the current elastic-plastic solution is presented later in this section.

$$q_{c,max} = q_{c,w} \times \frac{1}{m - R_0(m-1)} \tag{6.22}$$

$$K_H = \frac{q_{c,s}}{q_{c,max}} = 1 - R_0(1 - 1/m) \tag{6.23}$$

$$\eta'_{max} = \frac{q_{c,max} - q_{c,w}}{q_{c,s} - q_{c,w}} = \frac{1 - R_0}{1 - R_0(1 - 1/m)} \tag{6.24}$$

A series of numerical simulations was carried out by Ahmadi and Robertson (2005) to examine the variation of the correction factor K_H with thickness H_t. The sample was a thin sand layer embedded in soft clay layers under a relatively low confining stress ($\sigma'_{v0} = 70\,kPa$, $\sigma'_{h0} = 35\,kPa$). Loose sand ($D_{R,s} = 30\,\%$), medium dense sand ($D_{R,s} = 50\,\%$), and dense sand ($D_{R,s} = 90\,\%$) were investigated.

Figure 6.27 shows the comparisons of the parameters (K_H and η'_{max}) for investigation of the thin-layer effects. Again, the soil properties for the comparisons are equivalent to that from the simulations of Ahmadi and Robertson (2005). The value of K_H in Figure 6.27a decreases to 1 when the layer thickness is increased (i.e. $K_H = 1$ implies

no thin-layer effects). The field data provided by Robertson and Castro for the NCEER workshop is shown in the shaded area. Comparing with the field data, the analytical results show similar trends of K_H, and illustrate the effect of the relative soil properties. The results from this analysis signify that for a given thin layer thickness, a stronger thin layer soil has a larger correction factor of K_H. Unfortunately, details of the soil from the field data are not available so it is not possible to make a direct quantitative comparison. The analytical results also agree reasonably well with results of numerical simulations from Ahmadi and Robertson (2005) (also shown in Figure 6.27a), for the same assumed ground conditions.

Previous results in Section 6.4.2 have shown the comprehensive evaluation of thin-layer effects by using the proposed parameter (η'_{max}, η'_{min}), which is influenced by the tip resistance in both of the uniform soil layers ($q_{c,w}$, $q_{c,s}$). Similarly, the results of η'_{max} are compared with the numerical results (Ahmadi and Robertson, 2005) and the elastic solutions (Vreugdenhil et al., 1994), in Figure 6.27b. Although similar trends are found for the general curves with variation of $D_{R,s}$, much larger thin-layer effects are shown for the elastic solutions, and the current analytical elastic-plastic solutions provide a more reasonable evaluation of the thin-layer effects, which have a better agreement with the numerical results.

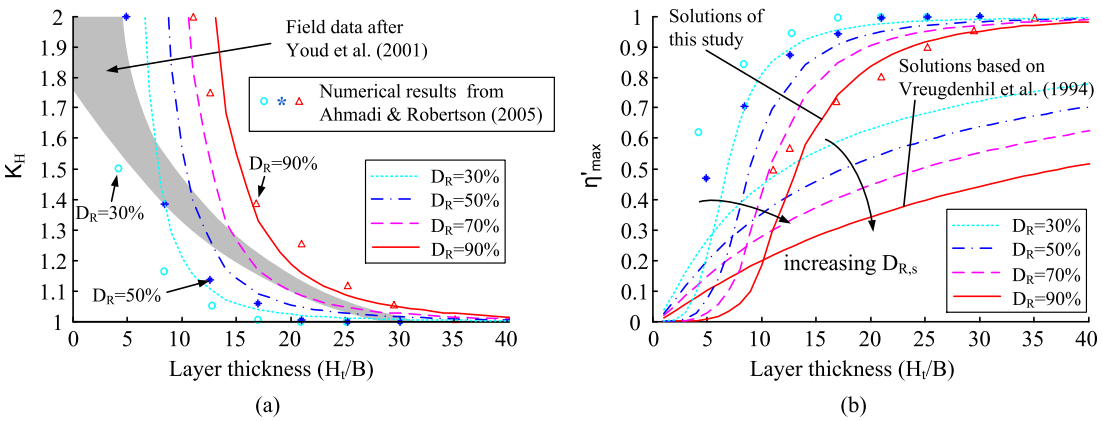

Figure 6.27 Comparisons of the parameters for investigation of thin-layer effects: (a) K_H; (b) η'_{max}

It should also be noted that the values of the parameters (Z_s and Z_w; K_H and η'_{max}) were calculated for specific situations and should not be taken as generally applicable. The influence zones depend not only the soil properties and profiles, but also on the stress state and probe diameter, which are included in the analytical calculations. The

magnitude of in situ confining stress has an impact on the size of the influence zones. A higher stress condition is found to result in smaller values of Z_s and Z_w, though the impact was found to be relatively small. All of the results with distance to the interface has been normalised by the probe diameter. The size of influence zones are proportional to the probe diameter, and thus a smaller penetrometer has a less significant layer effect and is more effective at detecting thin layers, as mentioned in Ahmadi and Robertson (2005) and Xu and Lehane (2008). Similarly, the thin-layer effects are also influenced by stress condition and probe diameter. The analytical solutions presented here used the mean stress as the in-situ hydrostatic stress. The effect of the coefficient of at-rest earth pressure (K_0) was not considered. The effects related to the cone surface friction and shaft friction on the influence zones were also not included in this study of application.

6.5 Chapter Summary

Analytical cavity expansion solutions in two concentric regions of soil were applied to the interpretation of CPT results, with specific focus on the layered effects during penetration. A discussion on concentric and horizontal layering was provided to validate the relevance between the two types of models. The analogy between the CPT and cavity expansion in two-layered soils was described, and the combination approach for predicting tip resistance in two-layered soils was applied. The analyses of CPT in two-layered soils highlighted the effect of respective soil properties (strength, stiffness) on CPT measurements within the influence zones around the two-soil interface. The resistance ratios and influence zones in the weak and strong soils were found to be affected by the soil properties of both layers. The results were compared with elastic solutions and provided good comparisons with experimental and numerical results. A simple superposition method of the two-layered analytical results was applied for the analysis of penetration in multi-layered soils. The thin-layer effects were investigated by analysing thin layer of both strong and weak soils. The correction factor (K_H) showed a good comparison with field data and numerical results, and the proposed parameters (η'_{max}, η'_{min}) effectively presented the thin layered effects, which are influenced by soil properties in each layer and soil profiles. It is also clear that the results of η'_{max} show better agreement with the numerical results, compared with the elastic solutions.

Chapter 7

Analysis and Discussion

7.1 Introduction

An analysis based on the results of this research is provided in this chapter, and the discussion involves many aspects of penetration problems, which rise up the potential areas for further investigation. The back analysis from the penetration resistance is first presented in Section 7.2, for the small-strain stiffness, shaft friction, relative density, and the soil state parameter. The analysis of soil deformation is given in Section 7.3 to investigate the effects of boundary and stress level. Comparisons of the soil displacements with the solutions of cavity expansion and previous experimental results are also provided in the same section. In addition, the analogy between the cone tip resistance and the pile end-bearing capacity is discussed in Section 7.4, and the scale effects are attributed to the soil layering and ground surface effects, which are predicted by the proposed cavity expansion methods. Finally, the penetration mechanisms are summarised through aspects of soil stress-strain history, particle breakage, soil patterns, and penetration in layered soils (Section 7.5).

7.2 Back analysis from penetration resistance

7.2.1 Back analysis of small-strain stiffness

Small-strain stiffness G_0 is a soil state variable, that is conventionally measured for the strains ranging from 10^{-6} to 10^{-5} for sands in the laboratory using resonant column tests or bender element tests. Seismic techniques for in-situ testing also provide the magnitude of G_0 in the field, based on the elastic relationship: $G_0 = \rho \cdot (V_s)^2$,

where ρ is the mass density and V_s is the measured propagating shear wave velocity. In general, experimental data shows that G_0 is proportional to the square-root of the effective stress state (Houlsby and Wroth, 1991; McDowell and Bolton, 2001; O'Loughlin and Lehane, 2003; Mitchell and Soga, 2005). A simple model described in Chapter 6, the Fahey-Cater model, also shows a similar dimensionless relationship: $G_0/\sigma_{atm} \propto (P_0/\sigma_{atm})^{0.5}$. In addition to Fahey and Carter (1993), some other empirical relationships relate G_0 with confining pressure and either soil density or void ratio (Hardin and Black, 1966; Jamiolkowski et al., 1985; Lo Presti, 1987; Santos, 1999). For instance, Lo Presti (1987) proposed a correlation as expressed in Equation (7.1), where the variables were suggested as $S' \approx 600$, $c' \approx 0.7$, and $n' \approx 0.43$. However, Randolph et al. (1994) suggested that S' is about 400 and $n' = 0.5$ for clean silica sand, and S' decreases for compressible and silty materials. Note that the dash mark $'$ is used to distinguish with the symbols appearing previously.

$$\frac{G_0}{\sigma_{atm}} = S' exp(c' D_R) \left(\frac{P_0}{\sigma_{atm}}\right)^{n'} \tag{7.1}$$

In-situ soil testing has been widely used to evaluate soil properties under in-situ conditions. Many correlations between G_0 and q_c have been proposed, despite the fact that the small-strain property is predicted by a large-strain measurement, which is controlled non-linearly by large-strain stiffness/strength. The CPT rigidity ratio is defined as $\frac{G_0}{q_c}$, which is usually adopted to present the correlation between G_0 and q_c. When the tip resistance is taken to be proportional to σ'_{v0}, as presented in the results of centrifuge tests in Chapter 4, a simple estimation of $\frac{G_0}{q_c}$ turns out to be proportional to ${\sigma'_{v0}}^{-0.5}$.

Robertson and Campanella (1983) proposed a relationship in Equation (7.2), which was modified from Imai and Tonouchi (1982) by converting the SPT blow count N into tip resistance q_c. As the definition of the normalised tip resistance q_{c1N} in Equation (4.4), many correlations were proposed with comparing data on a $\frac{G_0}{q_c}$-q_{c1N} space (Schnaid and Yu, 2007). Rix and Stokoe (1991) suggested a modified correlation for uncemented quartz sands in Equation (7.3) from calibration chamber tests. Schnaid et al. (2004) proposed the lower and upper bounds for both uncemented and cemented sands, and the expression is shown in Equation (7.4). For uncemented sands, $\alpha = 110$ for lower bound, and $\alpha = 280$ for upper bound.

$$\frac{G_0}{q_c} = 50 \times \left(\frac{\sigma_{atm}}{q_c}\right)^{0.389} \tag{7.2}$$

$$\frac{G_0}{q_c} = 291 \times {q_{c1N}}^{-0.75}; \quad q_{c1N} = \frac{q_c/\sigma_{atm}}{\left(\sigma'_{v0}/\sigma_{atm}\right)^{0.5}} \tag{7.3}$$

$$\frac{G_0}{q_c} = \alpha \times {q_{c1N}}^{-\frac{2}{3}} \tag{7.4}$$

A comparison between these correlations on $\frac{G_0}{q_c}$-q_{c1N} space is provided in Figure 7.1. The model of Fahey and Carter (1993) for Fraction E sand is derived as $\frac{G_0}{q_c} = 1000 \times \left(\frac{1+2K_0}{3}\right)^{0.5} \times {q_{c1N}}^{-1}$, and K_0 is taken as 0.5. Correlation of Lo Presti (1987) is expressed as $\frac{G_0}{q_c} = S' exp\,(c' D_R) \times \left(\frac{1+2K_0}{3}\right)^{0.5} \times {q_{c1N}}^{-1}$ for $n = 0.5$; sand is shown with higher rigidity ratio for larger D_R. Back-analysis using the correlation of Robertson and Campanella (1983) provides nonlinear curves on $\frac{G_0}{q_c}$-q_{c1N} space (Figure 7.1b) for three tests with uniform sand samples (MP II-01-FP-1g, MP II-02-FP, MP II-03-FP). The results show that the $1g$ test has a higher rigidity ratio, and stress level has a greater influence to the value than the relative density.

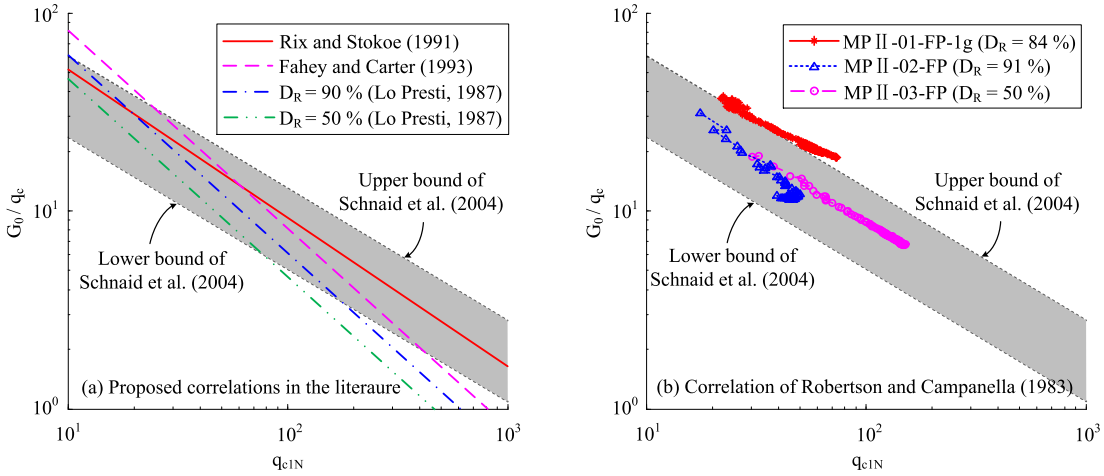

Figure 7.1 Comparison of the correlations on $\frac{G_0}{q_c}$-q_{c1N} space

As also noted by Schnaid and Yu (2007), the CPT rigidity ratio $\frac{G_0}{q_c}$ is a useful parameter for soil characterisation, which is not sensitive to changes in mean stress, relative density or sand compressibility; which also increases with sand age and cementation. The back-analysis of G_0 for the three tests with uniform sand samples has been provided in Figure 7.2 with comparisons of the estimated G_0. The variation of G_0 with depth is provided by the predictions from the various methods, and the lower and upper bounds

proposed by Schnaid et al. (2004) generally involve the variation of G_0.

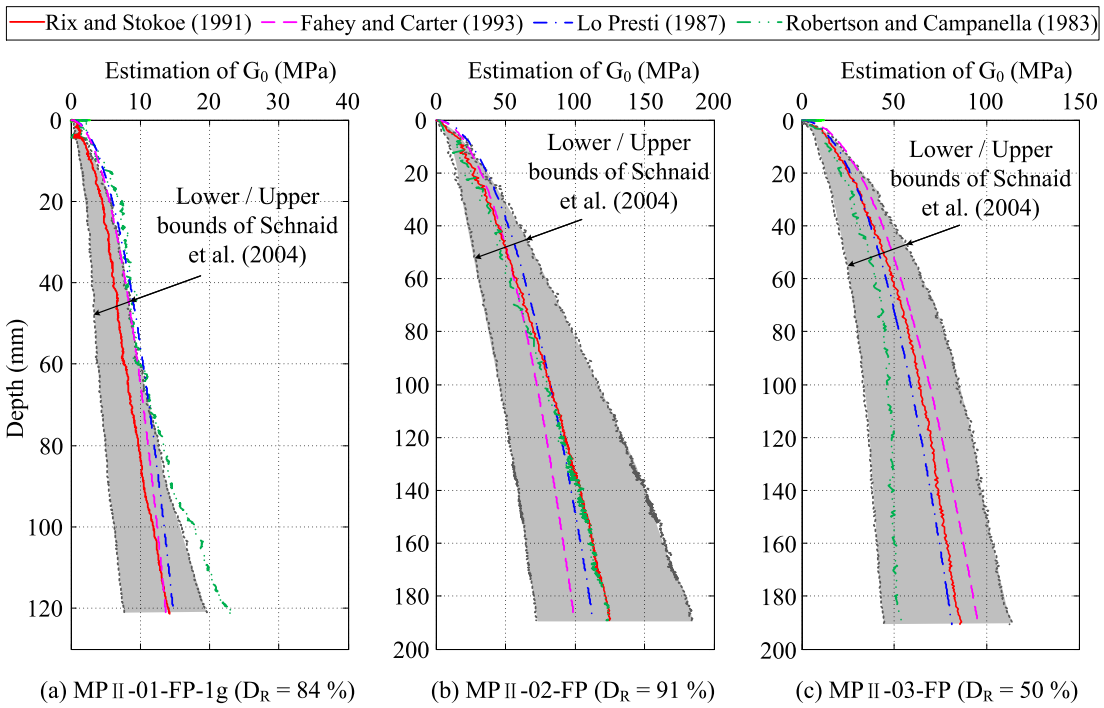

Figure 7.2 Back-analysis of small-strain stiffness using tip resistance

7.2.2 Estimation of shaft friction

The results of shaft friction shown in Section 4.2.2 were obtained from the difference between the total load and the tip load. Q_s or $\overline{\tau_s}$ shown in Figure 4.8 did not consider the variation of τ_s along the shaft, though Q_s is implicitly the integration of τ_s over the embedded length. A precise measurement of τ_s or sleeve friction f_s for a miniature probe is extremely difficult and unreliable due to the restriction of instrumentation and the local variation around the shaft (e.g. soil coated with the shaft has a significant influence to the measurements); probe verticality and inherent sample variation also have large impacts on the results of shaft friction.

A conventional design method relates τ_s with $\tan\delta \times \sigma'_{v0}$; δ is the interface friction angle. However, the shaft friction is governed by the adjacent soil, which is deformed by the probe, rather than the in-situ soil (i.e. σ'_{v0}). Therefore, with the development of the in-situ soil testing, τ_s tends to be associated with the tip resistance q_c, for interpretation of CPT and pile design (Randolph et al., 1994; Jardine and Chow, 1996; Lehane et al., 2005; Kolk et al., 2005); and Q_s is found to be proportional to q_c. Fleming (1992)

suggested that: $\tau_s = 0.02\, q_b \times \tan \phi_{cv}$, which generally overestimates the shaft capacity for long piles.

The UWA-05 is a CPT-based design method proposed by Lehane et al. (2005) for driven piles in siliceous sand which was developed using the UWA database of static load pile tests (Schneider et al., 2008). The correlation between τ_s and q_c, modified from the UWA-05 method for cone penetration test, is expressed in Equation (7.5), where δ is assumed as 15° for the tests (it is the mean value from centrifuge tests and ring shear tests for Leighton Buzzard sand, as reported by Klotz and Coop, 2001). 'a' was suggested to be 33, in light of the general friction ratio: $F_s = f_s/q_c = 0.5 \sim 1.5\%$ (provided by Robertson, 1990). The component ${A_r}^b$ was used in consideration of open-ended piles, and $A_r = 1$ for closed-ended piles; 'c' was about -0.5 to account for the friction fatigue. $\Delta\sigma'_{rd}$ was the change in radial stress during pile loading ($\Delta\sigma'_{rd} = 4\frac{G}{B} \times \Delta t$; $G \approx 185\, q_c \times {q_{c1N}}^{-0.7}$ for the operational shear modulus; $\Delta t \approx 0.02\, mm$ for radial displacement during pile loading). For application, the value of Δt is modified here with consideration of the miniature probe in fine sand; Δt is assumed as $0.1\% \times B \approx 12\, \mu m$ (according to Lehane and White, 2005).

$$\tau_s = \left\{ \frac{1}{a} \times q_c \times {A_r}^b \times \left[max\left(\frac{|h|}{B}, 2 \right) \right]^c + \Delta\sigma'_{rd} \right\} \times \tan\delta \tag{7.5}$$

Figure 7.3a presents the prediction of friction distribution along the shaft for penetration $z = 150\, mm$ based on the design method: UWA-05. The distribution shows the decrease of τ_s with the distance to probe shoulder, attributed to the degradation of the operative horizontal stress. The integration of τ_s provides the estimation of total friction load Q_s, which can be compared with measurements from centrifuge tests, as illustrated in Table 7.1. It is found that the calculated Q_s is about 37% underestimated for dense sand and 51% overestimated for loose sand. This is believed to be because of the constant assumption of soil-probe interface friction angle. Centrifuge tests by Klotz and Coop (2001) showed that δ varied between $10^\circ \sim 20^\circ$. It was also noted by Cavalieri (2000) that δ increases with stress condition and reduced particle size; the relative surface roughness R_n controls the magnitude of δ. Comparing with the test of loose sand, penetration load or tip resistance in dense sand is significantly larger, which increases the mobilised confining stress. On the other hand, the potential particle crushing in dense sand is more likely to increase the value of R_n, which in

turn results in a higher interface friction angle. Therefore, it can be concluded that the magnitude of δ for dense sand is relatively larger than that of loose sand. According to the discrepancy between the measured and calculated Q_s, the operative δ can be back analysed for both dense and loose sand, showing that $\delta = 23^\circ$ for dense sand ($D_R = 91\%$) and $\delta = 10^\circ$ for loose sand ($D_R = 50\%$). A good prediction of Q_s is presented in Table 7.1 and Figure 7.3b, which also illustrates the comparisons with the profiles of Q_s during penetration for tests: MP II-02-FP and MP II-03-FP.

Table 7.1 Prediction of Q_s and back analysis of δ

Measured Q_s when $z = 150\,mm$	Calculated Q_s for $\delta = 15^\circ$	Back calculated δ	Prediction of Q_s for modified δ	Error
$956.4\,N$	$604.1\,N$	$\delta = 23^\circ$	$956.9\,N$	0.052%
$210.8\,N$	$318.8\,N$	$\delta = 10^\circ$	$209.7\,N$	-0.522%

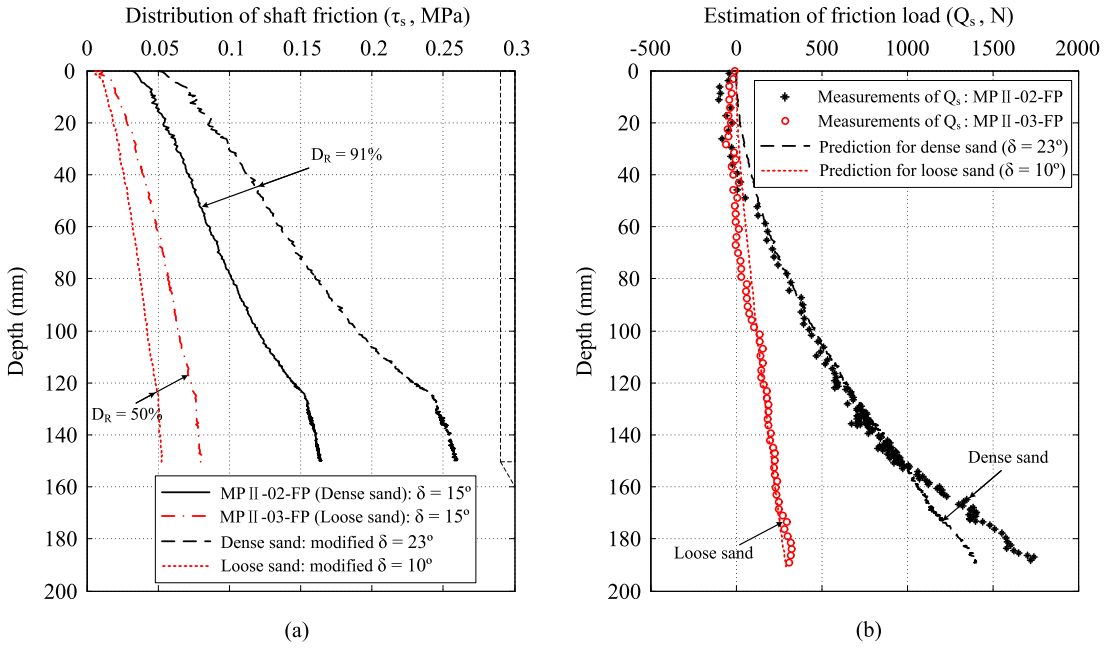

Figure 7.3 Prediction of: (a) shaft friction distribution and (b) friction load for centrifuge tests, using back-analysed interface friction angle

Alternatively, the interface friction angle δ is assumed as 11.2° for loose sand and 14.8° for dense sand based on penetration resistance. The values are interpolated from the proposed correlation between δ and pile end resistance (q_b here is estimated as the tip resistance at $z = 150\,mm$) for Leighton Buzzard sand by Klotz and Coop (2001). Figure 7.4 presents the prediction of friction distribution along the shaft and the total friction load Q_s with the comparison of the centrifuge results. It is found that the

estimation of friction load for the loose sand test has a good agreement with the experimental measurement, whereas the prediction of Q_s underestimates the friction load for dense sand. This is believed to be because of the assumption of soil-probe interface friction angle using the method of Klotz and Coop (2001), which does not include the effects of particle size and soil relative density. In addition, the method based on UWA-05 assumed a constant friction degradation parameter c, and the increased radial stress $\Delta\sigma'_{rd}$ was related to tip resistance and a constant radial displacement Δt, which could be attributed for the underestimation of shaft friction for dense sand. Further study needs to be carried out to evaluate the design method, and provide better prediction of the mobilised shaft friction.

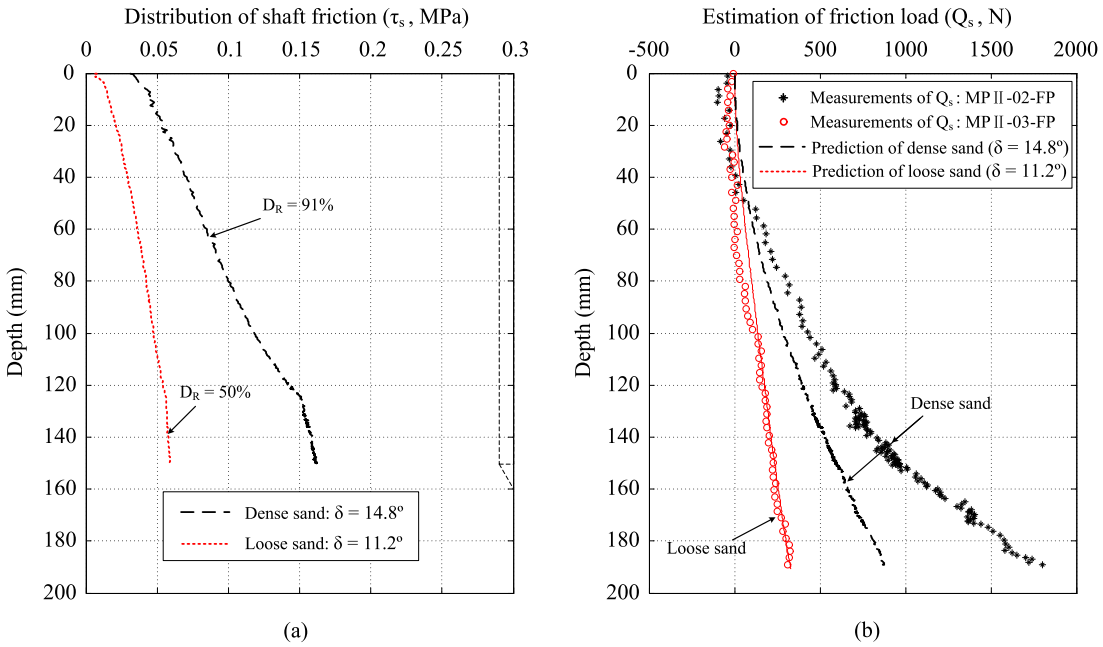

Figure 7.4 Prediction of: (a) shaft friction distribution and (b) friction load for centrifuge tests, using estimated interface friction angle

7.2.3 Back analysis of relative density

D_R is an important indication to assess G_0 for normally-consolidated sands, as reported by Lo Presti (1987); Jamiolkowski et al. (1988); Salgado and Prezzi (2007) and shown in the seismic relationship. A linear relationship between D_R and $\log_{10}\left[q_c/\left(\sigma'_{v0}\right)^{\alpha}\right]$ was postulated by Vesic (1977) from pile load tests, and $\alpha = 0.5$ was generally suggested by Baldi et al. (1986); Robertson and Wride (1998); Jamiolkowski et al. (2003) (the units of q_c and σ'_{v0} are *MPa*; alternatively dimensional analysis replaces the expression $q_c/\left(\sigma'_{v0}\right)^{0.5}$ by the normalised tip resistance q_{c1N}).

According to Jamiolkowski et al. (1985), Lancellotta (1983) proposed a correlation in Equation (7.6) from calibration chamber tests for five types of quartz sands, and Jamiolkowski et al. (2001) modified the correlation to Equation (7.7). Relationships from centrifuge tests were also provided by Tatsuoka et al. (1990) (Equation 7.8) and Bolton and Gui (1993) (Equation 7.9).

$$D_R\,(\%) = -98 + 66 \times \log_{10} q_{c1N} \tag{7.6}$$

$$D_R\,(\%) = -67.5 + 26.8 \times \ln q_{c1N} \tag{7.7}$$

$$D_R\,(\%) = -85 + 76 \times \log_{10} Q \;; \qquad Q = \frac{q_c - \sigma'_{v0}}{\sigma'_{v0}} \tag{7.8}$$

$$D_R\,(\%) = 32.964 + 0.2831 \times Q \tag{7.9}$$

The comparisons of the back-analysed D_R using tip resistance are presented in Figure 7.5. The first two correlations from calibration chamber tests underestimate the relative density, while the correlations based on centrifuge tests have better agreement with the measured density. Nevertheless, the variation between the prediction and the measurement is still notable, thereby further calibration is required to investigate the relationship between tip resistance and the relative density.

7.2.4 Effects of soil state

The CPT data varies significantly with soil density as discussed in Section 7.2.3, owing to the behaviour of cohesionless soils which is strongly dependant on the density. However, the relative density D_R is not a useful indicator for soil classification, since different sand types with same D_R are evident to have various soil properties (Klotz and Coop, 2001). Hence it is difficult to propose a correlation between q_c and D_R for many types of sand. As an alternative, the state parameter (ψ) was developed by Been and Jefferies (1985) to describe the soil state, that is defined as the difference in void ratio between the current state and the critical state at the same mean stress (Figure 7.6a). The influence of soil state variable to cone tip resistance was also emphasised by Salgado et al. (1997) and Schnaid and Yu (2007), other than the intrinsic soil prop-

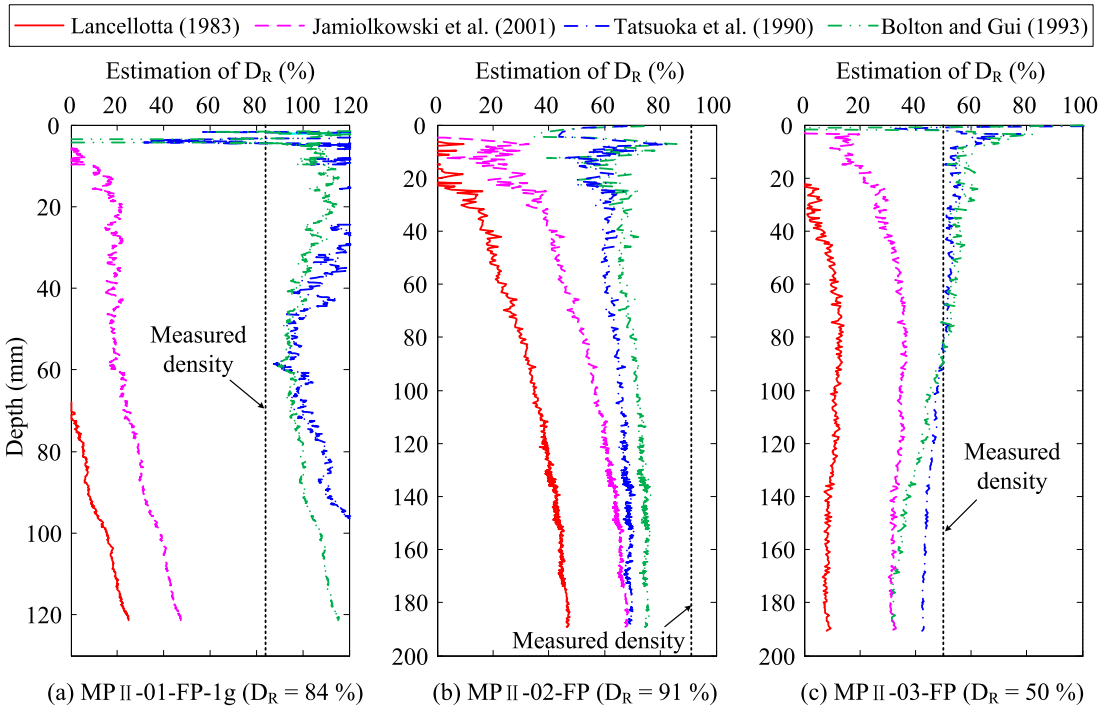

Figure 7.5 Back-analysis of relative density using tip resistance

erties. Nevertheless, Klotz and Coop (2001) suggested that a ratio of stresses rather than a volume difference provided a better and more effective approach to quantify the state of sands. The state parameter was defined as $R_s, = p_0'/p_{cs}'$, as also depicted in Figure 7.6a.

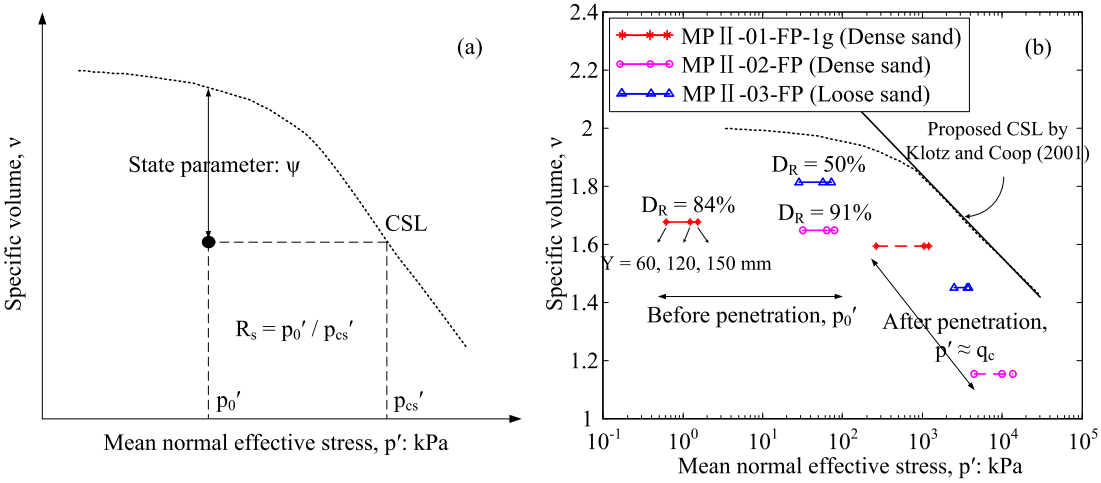

Figure 7.6 Soil state: (a) definitions of state parameters; (b) prediction of variation with penetration

The variation of soil state during penetration is predicted in Figure 7.6b for three of the uniform soil tests, with the assumption of $K_0 = 0.5$. The tip resistance at a given level is regarded as the mean stress after penetration, and the change of specific volume is

derived from the volumetric strain adjacent to the probe. The distance to the proposed critical state line by Klotz and Coop (2001) is presumably caused by the variation of K_0 and the significantly increased shear stress around the cone. Nevertheless, the state parameter R_s is used to analyse the cone factor N_q and the averaging β ($\overline{\beta} = \overline{\tau_s} / \overline{\sigma'_{v0}}$, after Klotz and Coop, 2001), and the resulting trends of the three tests are compared with the proposed trends by Klotz and Coop (2001) in Figure 7.7. As expected, the variations of N_q with R_s agree well with the line of Klotz and Coop (2001), whereas the direction with penetration crosses against the line for dense sand samples. Figure 7.7b shows the development of $\overline{\beta}$ is closer to the field data reassembled in Klotz and Coop (2001), and stable values of $\overline{\beta}$ are achieved for $50g$ tests.

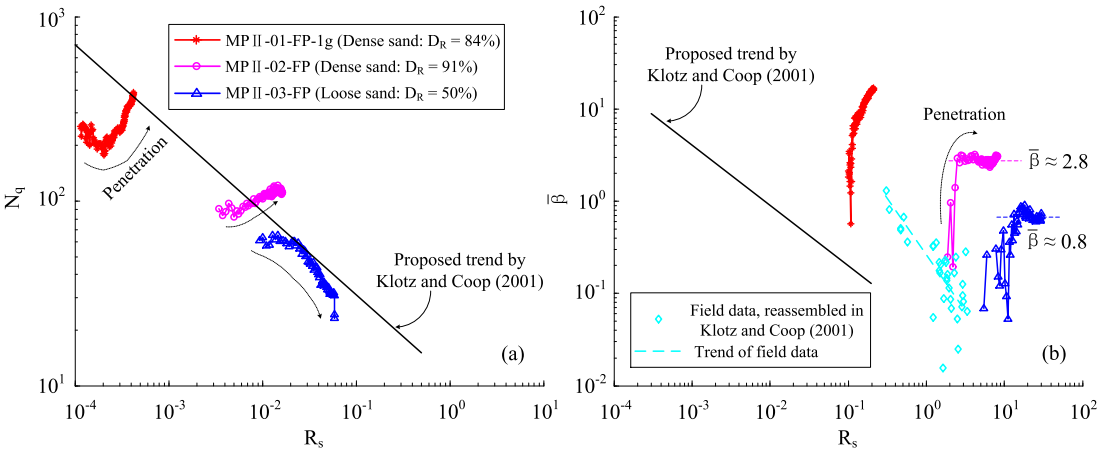

Figure 7.7 Variation of (a) N_q and (b) $\overline{\beta}$ with state parameter R_s

7.3 Analysis of soil deformation

7.3.1 Boundary effects

For physical modelling, the effects of boundary are inevitable and it is important to understand their influence. The cone penetration in centrifuge model is affected by the container walls (confining wall and base wall). Gui et al. (1998) proposed that the container to probe diameter ratio D/B should be > 40 to eliminate the boundary effects, based on a series of centrifuge tests of CPT in dense Fontainebleau silica sand.

Klotz and Coop (2001) and White (2002) conducted pile tests in both silica and carbonate sands. No significant influence of boundary for carbonate sand and loose samples of quartz sand was reported by Klotz and Coop (2001), after centrifuge tests with

$D/B = 19$ under different g-level (varied from 50 to 200). More influence was observed for dense silica sand from the bottom boundary, and the effect on shaft friction was negligible.

Plane strain calibration chamber tests were undertaken by White (2002), and the diameter ratio was selected as $D/B = 31$ for a pile with breadth of $32.2\,mm$. The boundary effects were $20 \sim 30\,\%$ larger than an axisymmetric model, owing to the restriction condition with higher stress distribution around the penetrometer. Base boundary effects were also observed for silica sand tests from the chamber base load cell and the penetration resistance curves, while little influence was found for Dogs Bay carbonate sand.

The centrifuge tests conducted in this research also provide an examination of boundary effects from the results of penetration resistance and soil deformation. For half-probe tests, the diameter ratio is $D/B = 42$. The results in Chapter 4 showed that the boundary effect for both loose and dense sand was negligible, while the bottom boundary effect was evaluated according to the correlation of Lee (1990), and the concave shape of the resistance curve for dense sand (Figure 4.6) was attributed to the container base.

On the other hand, full-probe tests are expected to have larger boundary effects, since $D/B \approx 20$, which is half that suggested by Gui et al. (1998) and similar to that of Klotz and Coop (2001). The boundary effects can be evaluated by the deformation field at the Perspex window when the penetration was carried out at about $120\,mm$ of offset from the Perspex window (Figure 3.14).

Results of MP II-01-FP-1g and MP II-02-FP from GeoPIV data are shown in Figure 7.8. The contours of total displacements are small, indicating the little influence from the boundary. The displacement in the $1g$ test is largely attributed to the sample settlement or indentation from the penetration, whereas the deformation in the $50g$ test is even smaller and negligible ($< 0.05\,mm$, which is likely from the PIV error). In addition, the boundary effects for loose sand is less than that of dense sand, since the influence zone of penetration for loose sample is smaller and sand contraction occurs

adjacent to the probe. Hence, the boundary effects from the confining wall are relatively small for both half-probe and full-probe tests; and small effect to penetration resistance from the base wall for dense sand has been discussed in Section 4.2.2 with Lee (1990)'s empirical relationship.

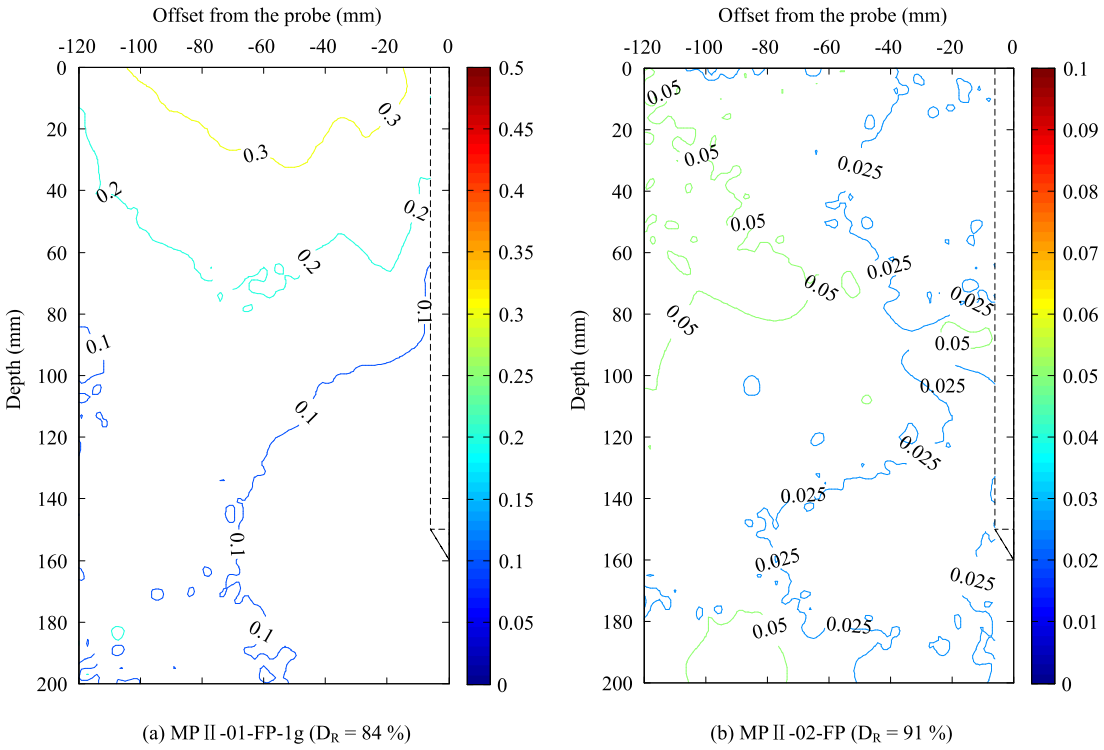

(a) MP II -01-FP-1g (D_R = 84 %) (b) MP II -02-FP (D_R = 91 %)

Figure 7.8 Deformation fields on the Perspex window for full-probe tests

7.3.2 Effects of stress level

The boundary effects for tests at different g-level as discussed in Section 7.3.1 show a significant difference on the displacement contour, and the stress level has a significant impact on the results of penetration resistance (Section 4.2.3). Results of half-probe tests with dense sand samples at different g-level (MP II-01-HP-1g and MP II-02-HP) are presented in this section, showing the effects of stress level on soil deformation.

Figure 7.9 provides the contours of cumulative and instantaneous displacements for both tests. The total displacement after 120 mm of penetration from 1 g test shows a slightly larger deformation zone. The soil near the surface is dominated by the heaving effect, and the dense sand under a lower confining stress shows more dilatancy. Similar trends are also presented in the cumulative contours ($\Delta z = 6\,mm$ in subplots c and d),

where the heaving effect in 50g test is more constrained by the increased gravity.

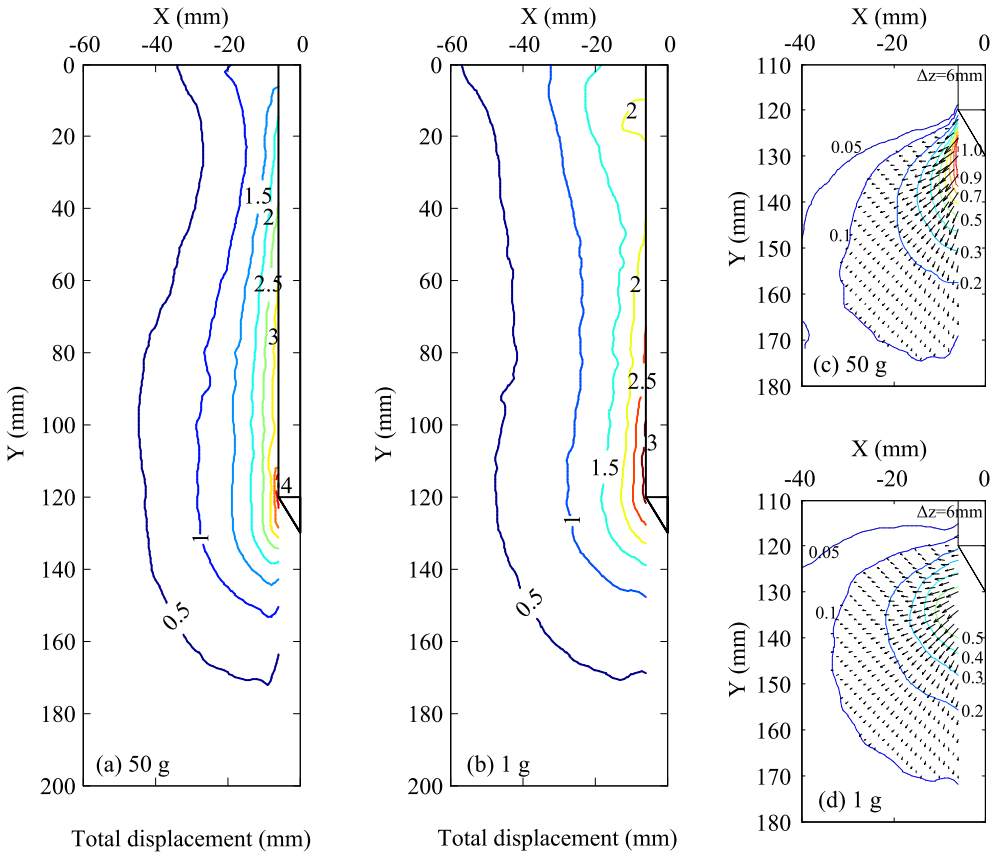

Figure 7.9 Deformation fields after 120mm of penetration in dense sand: cumulative displacements: (a) 50g, (b) 1g; instantaneous displacements: (c) 50g, (d) 1g

The comparisons of the distributions of the normalised displacements ($\Delta x/R$, $\Delta y/R$) are provided in Figure 7.10. The horizontal displacement for 1g test again shows larger distribution than that of 50g test. The significant heave near the ground surface is evident in the distribution of Δy. When the penetration goes deeper, the vertical displacement in 1g test increases steeper to a larger profile. Hence, the sand in lower stress condition has a larger deformation field with penetration.

7.3.3 Comparisons with cavity expansion methods

The results of instantaneous displacement field presented in Section 4.3.2 showed the nearly spherical contours around the cone tip, which had similar shapes with the failure modes of penetration as illustrated in Figure 2.27 $\sim$ 2.30. The deformation field from the cavity expansion field is also useful for the evaluation of displacements around the cone (e.g. Liu, 2010).

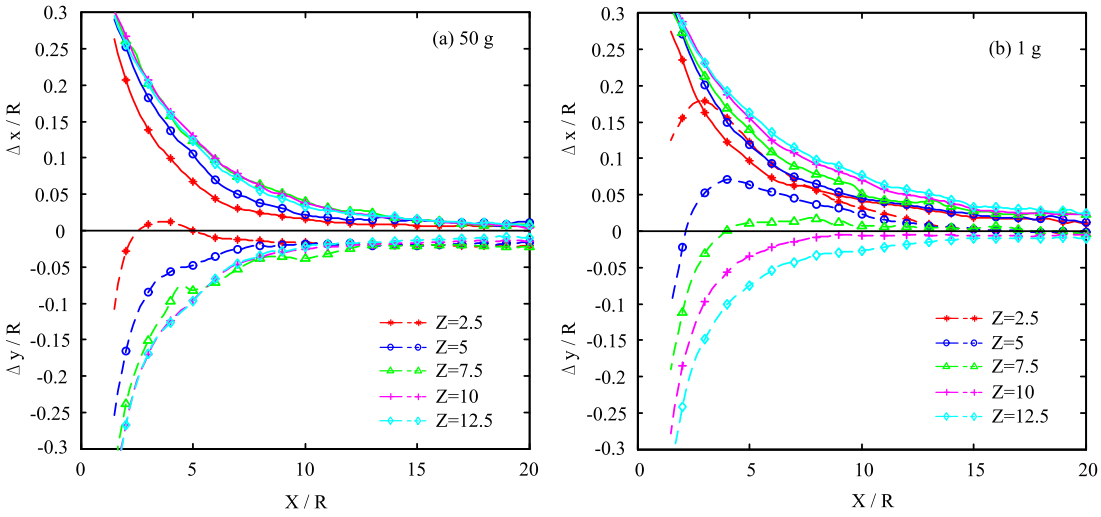

Figure 7.10 Displacement distributions ($h = 0$) with variation of penetration depth: (a) $50\,g$: $D_R = 91\%$; (b) $1\,g$: $D_R = 84\%$

The distributions of horizontal and vertical displacements at depth of $120\,mm$ from the centrifuge tests for different g-level and densities are shown in Figure 7.11a. The results of total displacement fields are then compared with the corresponding results based on the cavity expansion method in Figure 7.11b. The comparisons show that the centrifuge results have significantly larger distributions, since the results of total displacement include a large component of soil settlement by the compaction effects from the probe. However, the general trends of the tests have been replicated within the results of cavity expansion; the distribution of displacement and the size of deformation zone increase with relative density and decrease with stress level. Therefore, the effects of these two factors are investigated based on the cavity expansion method, as presented in Figure 7.11c and d. The stress condition is selected for soil at $120\,mm$ depth in a centrifuge model, and the soil parameters are determined by the approach described in Section 6.3.1. The results show that the spherical cavity expansion is a good method to describe the soil deformation after penetration, and the effects of relative density and stress level on the soil deformation are effectively examined.

7.3.4 Comparisons with other results

The results of soil deformation by penetration are compared with previous studies in this section. Soil displacements presented in Section 4.3 provided the general trends as a probe is inserted, and similar displacement profiles were also shown by Allersma

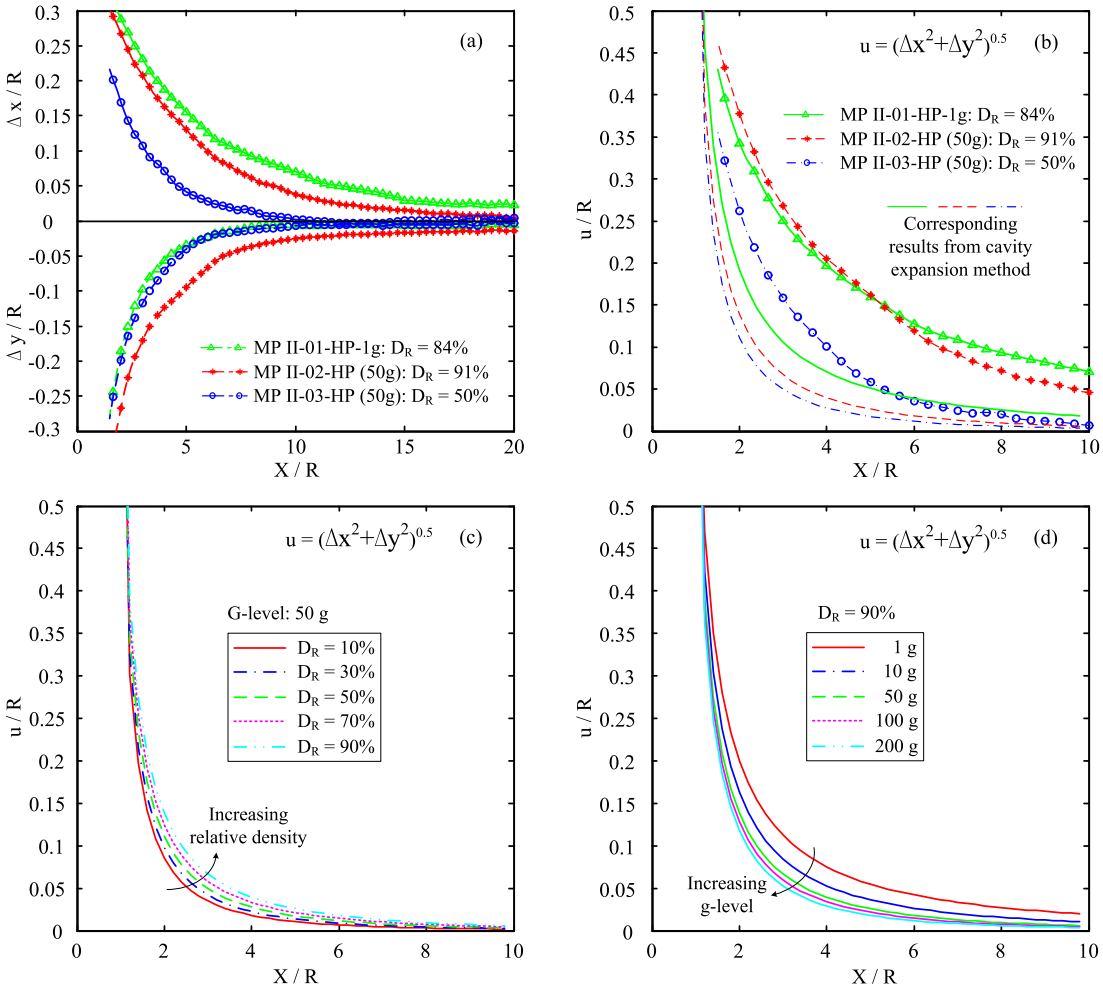

Figure 7.11 Displacement distributions for penetration depth $= 120\,mm$: (a) centrifuge tests; (b) comparisons with cavity expansion results; (c) variation with soil density; (d) variation with stress level

(1987); White and Bolton (2004); Liu (2010). The strain reversals from the results of strain paths (Figure 4.35 $\sim$ 4.36) are evident in accordance with the prediction from the strain path method (Baligh, 1985).

Figure 7.12a shows the distributions of displacements in Fraction E sand and Fraction C sand (provided by Liu, 2010) at both $1\,g$ and $50\,g$. The experimental conditions are quite similar between the tests; only the grain size of Fraction C sand is relatively larger, ranging from $0.3\,mm$ to $0.6\,mm$. The profiles of Δy have a good comparison for both sand at a similar depth, while the distribution of Δx in Fraction C sand in $1\,g$ test is smaller than the $50\,g$ test, which is in contrast with the results from the Fraction E sand tests and the cavity expansion analysis. Although Liu (2010) reported that the horizontal displacement has a similar tendency and the vertical displacement increases with stress level, a more convincing explanation is that soil deformation is somehow

controlled by the kinematic behaviour and vertical movement under higher gravity is produced by the compaction of the sample. Thus, it is believed that the decreasing distribution of displacement is generated with increasing g-level as presented previously, when considering the soil compressibility.

The strain paths with penetration are compared with Fraction C sand test by Liu (2010) and Fraction B sand test by White (2002) in Figure 7.12b. Both Fraction E sand test and Fraction C sand test were undertaken in centrifuge under $50\,g$ using a miniature probe ($B = 12\,mm$), whereas the Fraction B sand test was conducted in a plane-strain calibration chamber by penetrating a pile with diameter of $32.2\,mm$. The ratios of probe diameter to average grain size (B/d_{50}) for the tests are 86, 24, and 38, respectively. All of the soil elements were selected at a similar distance to the probe centreline ($X/R = 2$, 1.9, and 1.99). The results of axisymmetric models from the first two tests are comparable, and the Fraction C sand experienced higher vertical compression before probe passed and had larger horizontal strain after penetration. Significant differences between the axisymmetric tests and the plane-strain test are shown, though the general trends of strain reversals were also captured from the Fraction B sand test. The much higher tensile-horizontal and compressive-vertical strains with larger influence zones for the plane-strain Fraction B test are directly attributed to the boundary conditions that the out-of-plane strain was strictly constrained.

Alternative comparisons of strains are the distributions of maximum and minimum strains, as provided in Figure 7.12c ($\varepsilon_{xx,max}$ and $\varepsilon_{xx,min}$) and d ($\varepsilon_{yy,max}$ and $\varepsilon_{yy,min}$). Compared with the results of Fraction E sand test, slightly larger maximum strains are shown in the Fraction C sand test. The results of the Fraction B sand test again show differences of the variation of strain with the offset from the pile, which is mainly caused by the plane-strain condition.

7.4 Probe Resistance and Pile Capacity

7.4.1 Cone tip resistance and pile end-bearing capacity

Since CPT was originally developed as a scale model of a pile (van den Berg, 1994), the analogy between CPT and displacement piles contributes to the establishment of

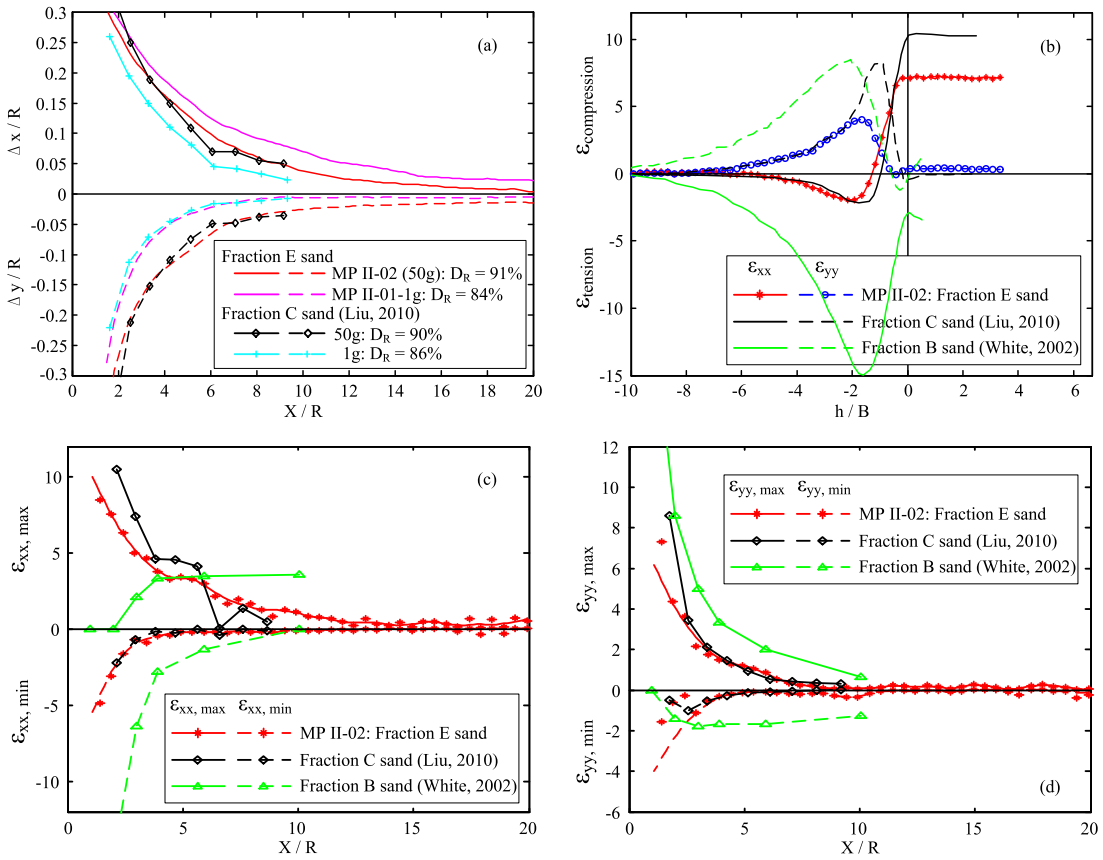

Figure 7.12 Comparisons of displacements and strains for different types of sand using different experimental models

the correlations between cone tip resistance q_c and pile end bearing capacity q_b. A simple relationship: $q_c = q_b$ was usually suggested for designs, though some field tests denoted that the pile capacity was slightly smaller than q_c by various factors and pile capacity was found to decrease with pile diameter. The MTD design method proposed by Jardine and Chow (1996) has included the effects of pile size (B), and suggested a correlation: $q_b = q_c\,[1 - 0.5 \log{(B/B_{cone})}]$, based on the database of load test results reassembled by Chow (1997).

More databases of load tests have been re-examined by White (2003) and White and Bolton (2005) to investigate the relationship between q_c and q_b. The main factors about the reduction of q_b were examined, $q_b/q_c = 0.9$ was suggested by White and Bolton (2005) with consideration of partial embedment, local inhomogeneity, absolute pile diameter, partial mobilisation, and residual stresses. White and Bolton (2005) claimed that the variation of q_b/q_c with B was not clear when reassembling the available databases in the literature. $q_b/q_c = 0.6$ was assumed for closed-end driven piles according to design method 'UWA-05' (Lehane et al., 2005), and a modified value

($q_b/q_c = 0.9$) was proposed for jacked piles when considering the field tests from White and Bolton (2005).

Regarding to the scale effect between a CPT penetrometer and a pile, the differences between q_c and q_b come from the surface effect and the layered effect. As presented in Chapter 4 and Chapter 6, the influence zones around the soil interfaces are proportional to probe diameter, which is also illustrated in White and Bolton (2005). Hence, pile end base resistance is more affected by the ground surface and a wider range of soil above and below the pile end. When the penetration is in a sufficient deep and uniform ground, the scale effect is believed to be limited, if ignoring the effects of grain size.

Conventional cavity expansion solutions provide an identical limit pressure and a resulting penetration resistance for probes with various diameters (i.e. $q_c = q_b$). However, the scale effects on the reduction of penetration resistance with pile diameter can not be evaluated. The cavity expansion solutions presented in Chapter 5 provide the results of cavity expansion in two concentrically layered soils, and this method has the potential to examine the scale effects. In contrast to relate pile capacity with the limit pressure, the application of the solutions in Chapter 5 to the penetration problem is regarded as an expansion from an initial cavity to a final size of pile ($a = B/2$), and the proposed smoothing approach is required as described in Chapter 6.

One of the main factors of scale effects is the ground surface effect, since larger piles at a given depth tend to be more affected by the ground surface. For cavity expansion analysis, the surface is treated as an extremely weak soil layer. The parameters of Soil B are set as: $E_2 = 0.01Pa$, $\nu_2 = 0.2$, and only elastic behaviour is considered in this layer, representing the ground surface. Figure 7.13a shows the results of cavity pressure ($a_{cone} = B_{cone}/2$, $B_{cone} = 12\,mm$) which increase with depth, and soil parameters under $50g$ are estimated based on the procedure in Section 6.3.1. The results of tests with surface effects are compared with the cavity expansion in uniform soil. As expected, the significant reduction of cavity pressure is obvious when the cavity is close to the surface, and the surface effect is larger for soil with higher relative density. Figure 7.13b shows the results for cavities expanded to a variety of sizes (B equals 1, 2, 5, 10 times of B_{cone}). It is evident that the larger cavity expansion is more affected

by the ground surface, which indicates a larger pile with smaller end bearing capacity. It should be noted that the assumptions of the extremely weak soil layer and the concentric regions of soil are not quite realistic to provide the quantitative analysis of the ground surface effect, whereas the trends of scale effects are captured qualitatively from the results of the two-region cavity expansion analysis.

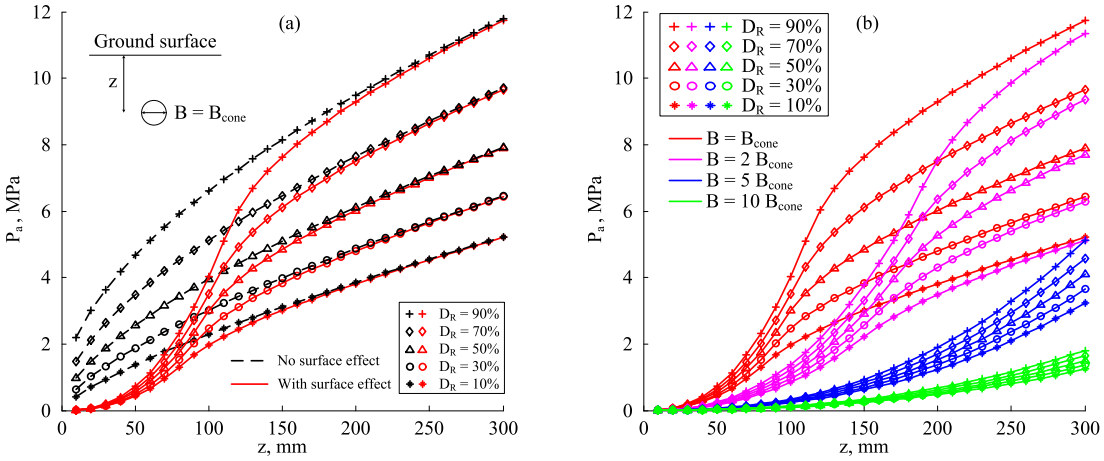

Figure 7.13 Scale effects from the ground surface: (a) comparing with no surface effect; (b) variation of surface effect with cavity size or pile diameter

Some experimental evidences (Plantema, 1948; Begemann, 1963; De Beer et al., 1979) showed the scale effects on layered soils, and White and Bolton (2005) also elucidated the profiles of q_c and q_b in layered soils (Figure 7.14a). The influence zones in both soil layers are dependent on the size of probe, and the results with distance to soil interface in Chapter 6 are normalised with probe diameter (H/B). When considering the effects of probe size, the results of Figure 7.14b show that the larger pile is more affected by the soil above and below it, and the sizes of the influence zones decrease with the stress condition. The analyses using the cavity expansion in two-layered soils cannot represent the actual surface and soil layering, but provide qualitative assessments to the scale effects between probes and piles.

7.4.2 Penetration resistance and cavity pressure

Comparing the cone probes and the displacement piles, there are some other differences other than the geometry, though the scale effects have the influence to the penetration resistance. Driving method for displacement pile installation is an important factor for pile foundation design. Soil stress state and soil disturbance vary with the

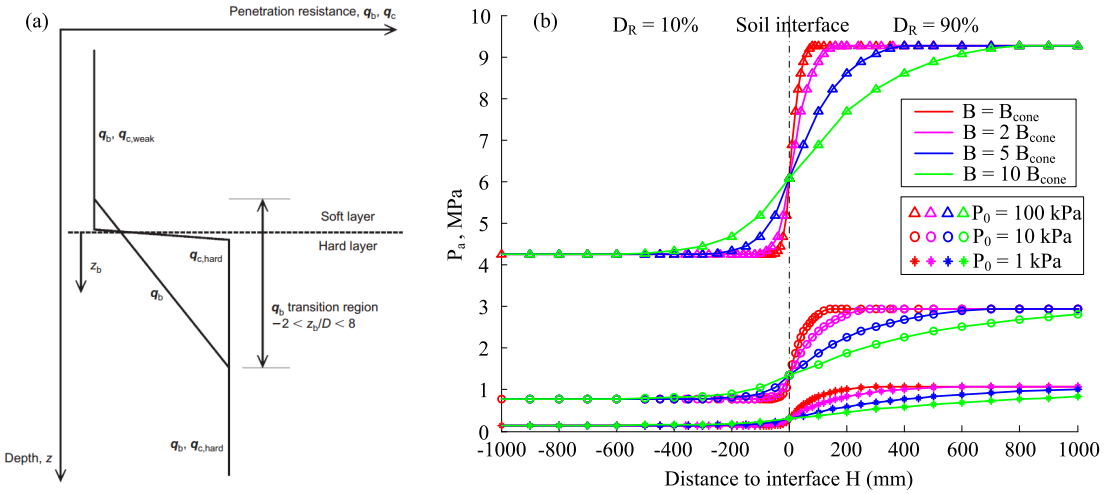

Figure 7.14 Scale effects on layer soils: (a) schematic of White and Bolton (2005); (b) results of cavity expansion solutions

installation method, thereby affecting the foundation stiffness and strength, as emphasised by Deeks (2008). Pile monotonic installation, jacking or conventional vibration driving also generates different types of cyclic loading to the ambient soil, resulting in a decrease of shaft friction at a given depth. This phenomenon is prevalently referred to as friction fatigue, and was investigated by White and Bolton (2002); White and Lehane (2004); Gavin and O'Kelly (2007). The effects of penetration rate have significant influence for soil with partial drainage condition and partial consolidation, and the effects have been studied by Chung et al. (2006); Silva et al. (2006); Kim et al. (2010). Another difference lies in the post-installation effects for pile capacity. The effects of time on shaft resistance is regarded as 'set-up', which was mostly attributed to the soil creep and ageing by Chow (1997); Bowman and Soga (2005); Jardine et al. (2006).

As presented in Section 2.4, cavity expansion methods provide effective analytical approaches for prediction of both pile bearing capacity and cone tip resistance. The results of instantaneous displacement field in Section 4.3.2 and the direction of principal strain rate in Section 4.4.3 also give support to a spherical cavity expansion mechanism around the cone tip. Although the correlation between the cavity pressure and penetration resistance has been examined by many researchers (e.g. Vesic, 1977; Randolph et al., 1994; Yasufuku and Hyde, 1995), the mechanism relating the cone and the probe is not available, and the solution of stress/strain field is suggested only for soil in the far-field. The limitations of the cavity expansion theory for penetration problems stem from the boundary value. The spherical boundary creates spherically symmetric

soil deformation, which is not strictly the pattern around the cone. The variation of soil displacement is also distorted by the severe shear strain with penetration, that is neglected by the cavity expansion analysis. The variation of soil properties, particle breakage, soil heterogeneity and anisotropy make the analytical solutions extremely difficult. Therefore, numerical approaches have the potential to develop the cavity expansion methods, and the correlation between the penetration resistance and the cavity pressure still needs to be investigated. In addition, the effects of shaft friction are not considered in a conventional cavity expansion analysis, which have an inevitable influence on the penetration resistance and the performance of a piled foundation. The combination of cavity expansion and shearing has a potential to become an effective approach for the analysis of penetration problem, according to the one-dimensional finite element analysis of shaft resistance of jacked piles by Basu et al. (2011).

7.5 Summary of Penetration Mechanisms

As presented in the literature and the results in this research, cone penetration involves severe soil straining and drastic changes in the soil stress, as well as particle breakage, cyclical loading, and friction fatigue (van den Berg, 1994; Yu, 2006; Jardine et al., 2013*b*). A summary of the penetration mechanisms is provided in this section to illustrate the soil stress-strain history, particle breakage, soil patterns, and penetration in layered soils.

7.5.1 Soil stress-strain history

The process of penetration causes the generation of radial pressure and leads to the impact on adjacent subsurface structures. The investigation of soil stress-strain behaviour is essential to understand the penetration mechanism, albeit the soil nonlinearity makes it a complex process. Many attempts have been made to predict and measure the local stress around the cone or closed-ended displacement pile (e.g. Lehane, 1992; White and Bolton, 2005; Jardine et al., 2013*b*). A typical stress path during loading of a pile is presented in Figure 7.15a, after Lehane (1992). It is thought that the initial reduction of radial stress is due to the rotation of principal stress direction, with initial contraction and strain softening. After that, the radial and shear stresses are in-

creased significantly, owing to the compaction, shearing, and interface dilation. The failure pattern is then emerged through the soil remoulding and formation of shear planes around the cone and the shaft. However, the measurement of stress field is extremely difficult and highly dependent on the quality of the instrumentation, which needs to be further investigated in the future.

The results of soil displacements in Chapter 4 demonstrate the soil strain history during penetration. The decay of displacement against the offset from the probe matches the trends of the degradation of stress field measured by Jardine et al. (2013*a*) (Figure 7.15b). The reduction of stresses after the probe passes (Jardine et al., 2013*a*;*b*) also provides an explanation for the trends of strain paths around the probe shoulder. The postulated stress-strain paths in Lehane and White (2005) elucidated the large increase of stress-strain with penetration, unloading as tip passes, and dilation during monotonic shear for soil elements close to a pressed-in probe.

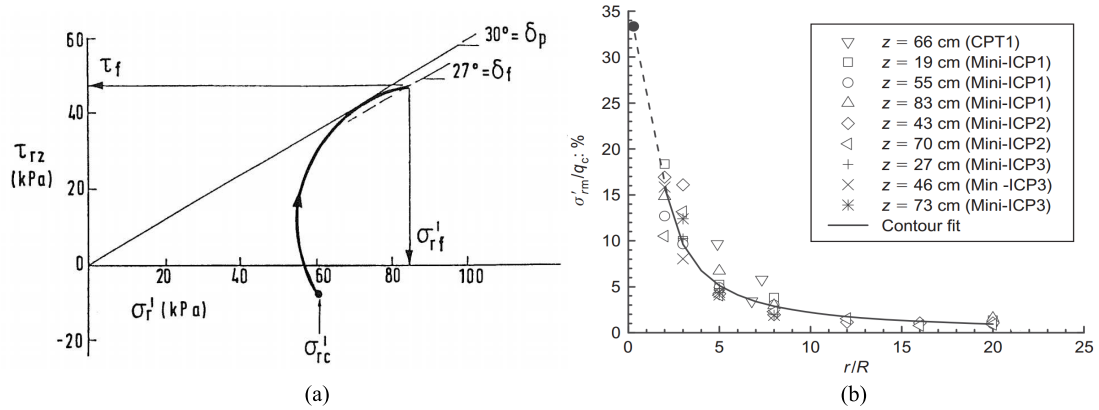

Figure 7.15 Stress history: (a) stress path during loading of pile (after Lehane, 1992); (b) distribution of radial stress (after Jardine et al., 2013*a*)

The probe-soil interaction depends on the interface friction angle, probe surface roughness, and particle crushing; and the shearing effects enhance the dilation and crushing in the shear zone, which is located adjacent to the loaded probe shaft (Klotz and Coop, 2001; Lehane and White, 2005). The thickness of shear zone t_{shear} is about $10 \sim 20$ times d_{50} for a large level of shear displacement (Uesugi et al., 1988), and varies with pile roughness, stress level and soil properties. The penetration forms the shear zone, and the created dilation increases the normal stress in the confinement. The change of normal stress $\Delta\sigma'_{rd}$ was extrapolated by the elastic cylindrical cavity expansion surrounding the probe, as shown in Figure 7.16, which was also integrated within the

UWA-05 method (Lehane et al., 2005). The change of lateral stress and shaft friction for piles in sand was investigated by Lehane and White (2005), through a series of constant normal stiffness (CNS) interface shear tests by analogy. The stiffness of soil and dilation in the shear zone control the probe-soil interaction. However, the operational shear modulus is largely degraded with the soil deformation imposed by penetration; and the variation of soil strength and dilatancy with stress-strain paths influences the shearing effects around the probe shaft. Thus, further analysis of stress-strain life of soil around the penetrometer is required to enhance the understanding of the penetration mechanisms.

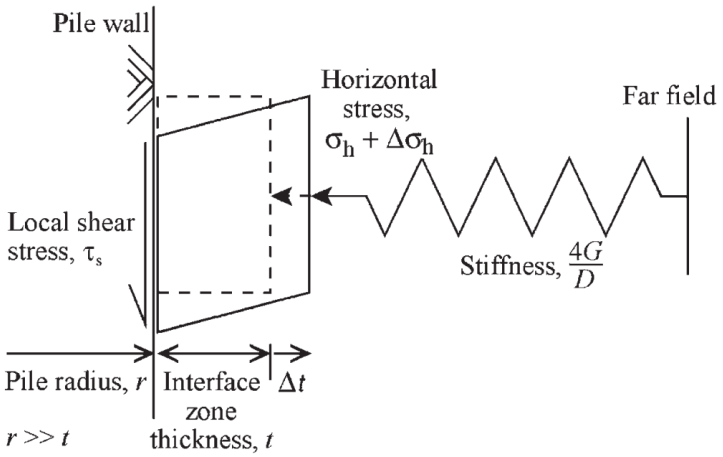

Figure 7.16 The mechanism of probe-soil interface with dilation in shear zone, after Lehane and White (2005)

7.5.2 Particle breakage

Particle size and the crushability have a significant influence to the mechanical behaviour of sands; the soil compressibility is reflected by the particle breakage and rearrangement. The centrifuge tests were designed with consideration that the effect of particle breakage was negligible, and the samples were prepared with pouring the reused sand. However, the high stress condition in the centrifuge and the significant increase of stress level around the inserting penetrometer would have an impact to the sand particles, as observed by some researchers (e.g. Klotz and Coop, 2001; White, 2002; Deeks, 2008). Therefore, the effects of particle breakage associated with penetration are discussed in this section.

McDowell and Bolton (2000) conducted centrifuge tests of cone penetration in calcareous Quiou sand with different particle size distribution. Significant crushing was found by retrieving the sand around the probe, though the breakage was not noticeable for sand at depth shallower than the critical depth (i.e. the depth where the peak tip resistance occurs). The results of calibration chamber tests by White (2002) indicated that high compression and particle breakage had occurred below the pile for both carbonate and silica sands. The initial vertical stress σ'_{v0} is around $50\,kPa$, and the base resistance during penetration reached up to $5\,MPa$ for carbonate sand and $25\,MPa$ for silica sand. The crushing of silica sand particles was attributed to the high stress level and shear strains around the pile, whereas the effect of breakage was small from a triaxial test at a comparable stress level. Particle crushing is localised only in the vicinity of the cone tip (Klotz and Coop, 2001; White and Bolton, 2004), due to the greater stress-strain level adjacent to the probe. Additionally, the particle breakage decreases the average of particle size, and the resulting relative roughness increases with the interface friction angle. This is supported by the prediction of δ for dense and loose sand in Section 7.2.2, indicating that the magnitude of particle crushing in dense sand is much greater. Strain reversal during penetration was also attributed to soil crushing (White, 2002), since the crushing induced radial contraction and resulted in the stress reduction around the probe shoulder.

The sand used in this research was Leighton Buzzard sand, which is a typical silica sand with high volumetric stiffness. The parameter σ_0, defined by McDowell and Bolton (1998), is the tensile stress when 37% of the tested particles survives in the particle tensile strength test. The values for Fraction A and Fraction D sands were provided as $26\,MPa$ and $54\,MPa$, respectively. For Fraction E sand, the Weibull 37% tensile strength can be derived as $68\,MPa$, based on the relationship: $\sigma_0 \propto d_{50}^{b}$ ($b = -0.357$ was suggested by Lee, 1992 for Leighton Buzzard sand, based on the particle tensile strength tests; assuming $b = -\frac{3}{m}$ based on McDowell and Bolton, 1998, thus the Weibull modulus m equals 8.403 for this analysis). When assuming this microscopic stress value relates to the macroscopic failure stress and the possibility of particle crushing represents the macro percentage of grain breakage, the back analysis could illustrate the magnitude of particle breakage around the penetrating probe. In considering the soil at $150\,mm$ depth, the penetration resistances for dense sand and loose

sand at $50g$ tests are approximately $13.5MPa$ and $3.8MPa$, respectively. Therefore, the survival probability $P_s \approx \exp\left[-\left(\frac{q_c}{\sigma_0}\right)^m\right]$, and the calculation shows that very little sand particle is crushed by penetration ($< 2\times10^{-4}\%$ for dense sand; $< 3\times10^{-9}\%$ for loose sand). The little crushing is presumably due to the smaller particle size compared to the previous penetration tests (Klotz and Coop, 2001; White and Bolton, 2004). Alternatively, the analysis underestimates the magnitude of crushing for penetration, as the significant shearing around the probe largely enhances the possibility of particle crushing, as noted by Vesic and Clough (1968). Therefore, it is believed that the effect of particle breakage is limited in the centrifuge tests, while particle compression and abrasion are experienced by the insertion of probes.

7.5.3 Soil patterns

The penetrating probe generates a complex deformation field near the penetrometer. The most comprehensive illustration of soil patterns in the literature is based on the deformation measurement by White (2002). The schematic in Figure 7.17 followed by Deeks (2008) presents the streamlines of soil flow and stress profile at the base of a pile during installation based on White and Bolton (2004) and White et al. (2005), though the pressed-in pile was installed in a plane strain model. The pattern of soil element deformation was illustrated and the stress reduction above the pile end was interpreted by cavity contraction when pile passes.

The general trends in this schematic are replicated in this study with penetration in a 180° axisymmetric model, as presented in Chapter 4. For the cumulative total displacements in Figure 4.12 $\sim$ 4.13, penetration leads to a cylindrical deformation zone around the probe shaft and a spherical deformation region ahead of the cone. With regards to a surrounding soil element, the movement is initially tending to downwards, and then becomes outwards as the probe is approaching, ultimately reaching a similar vertical and horizontal movement (Figure 4.21). Additionally, most of the deformations are developed before $h = 0$, while a tiny outwards and downwards movement occurs after $h > 0$ (Figure 4.22). Although the deformation fields of dense and loose sand are similar, dense sand has larger influences due to stiffer confinement, and loose sand close to the probe has larger strains owing to the greater compressibility and the unrestricted dilation. Soil strain paths (Figure 4.35 $\sim$ 4.37) provide the development

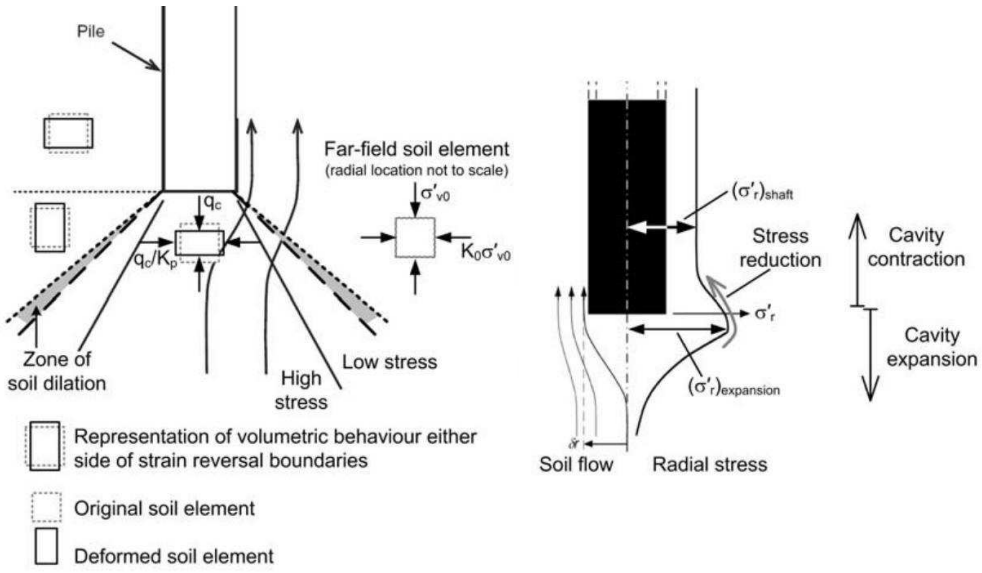

(a) after White and Bolton (2004) (b) after White et al. (2005)

Figure 7.17 Schematic of soil stress-strain profiles during pile installation (Deeks, 2008)

of soil strains during the penetration. The soil element experiences a complex transformation of strains until $h \approx 0$, due to large deformation, significant rotation of principal stresses and different types of failure mechanisms occurring around the cone. The distribution of volumetric strain in Figure 4.39 reveals that the soil loosening appears close to the probe rather than densification due to dilation, which is consistent with the measurements of Chong (1988) and Dijkstra et al. (2012).

7.5.4 Penetration in layered soils

The effect of layered soils on in-situ test results was not addressed sufficiently, and plays a key role for precise interpretation, as mentioned by Yu (2006). The examination of layered effects in this research provides the data on penetration resistance (Section 4.2.4) and soil deformation (Section 4.5). In general, the effect of layered soils results from the difference of influence zones in adjacent layers, since the influence zone is determined by the soil stiffness / strength, relative density, mobilised friction angle, and stress condition (Yang, 2006). A more compressible sand has a smaller influence zone, and the size of the influence zone also decreases with depth due to the increase in stiffness of the soil that results from the increased confining stress.

The proposed parameter η' indicates the transition of penetration resistance in layered soils; Z_w and Z_s represent the influence zones in both soil layers. For the scenario of

weak soil over strong soil (Figure A.5a), as the probe approaches the interface, it is conceivable that the problem can be regarded as a pressure applied on top of a two-layered soil, with the top being less stiff than the bottom. For a given stress, it would therefore be expected that the displacement in the upper, less stiff, zone would be greater than in the lower. In addition, the strength of the lower dense soil will be greater than that of the loose soil. The zone of yielded soil around the probe in the loose soil is therefore expected to be larger than in the dense soil. The dense soil would not be expected to yield until the probe was very close or within the dense soil layer. Displacements within a yielding soil will be greater than in a non-yielding soil. This effect of soil strength can therefore help to explain the trend in displacement data observed in the tests. Similarly, for the scenario of strong soil over weak soil (Figure A.5b), the compaction effect for the underling weak soil is enhanced by the increase of vertical stress. The increase of vertical displacement in the strong soil is mainly cumulated from the lower soil layer, while the displacement induced by the local soil is dominated by the shearing effect with soil drag-down.

The analytical solution based on cavity expansion is also evident to be an effective approach to ascertain the layered effects relating to soil properties and layering profiles (Chapter 6). The comparisons of the resistance ratio in layered soils between centrifuge tests and cavity expansion calculations are provided in Figure 7.18, showing the essentially identical trends of the transitions of q_c. Despite the experimental uncertainties, the differences are mainly from the effects of ground surface, stress gradient and penetration direction, which have not been considered in the cavity expansion analysis. Although the number of centrifuge tests is limited, it is clear that the proposed analytical method has the potential to examine the effects of soil layering for penetration problems.

In terms of the variation of CPT data in layered profile, many averaging techniques were proposed for pile design. LCPC method (Bustamante and Gianeselli, 1982) suggested the average tip resistance was calculated from CPT measurement within the region $\pm 1.5B$, and corrected by eliminating the random data over $\pm 30\,\%$. The Schmertmann method (Schmertmann, 1978) proposed another averaging approach (also referred to as the 'Dutch' cone averaging technique) in considering the zones with $8B$

above the tip and $0.7B \sim 4B$ below the tip. A more comprehensive method suggested in this research is to apply the transition curve of q_c in layered soils with consideration of the scale effect caused by the soil layering, as investigated in Section 7.4.1.

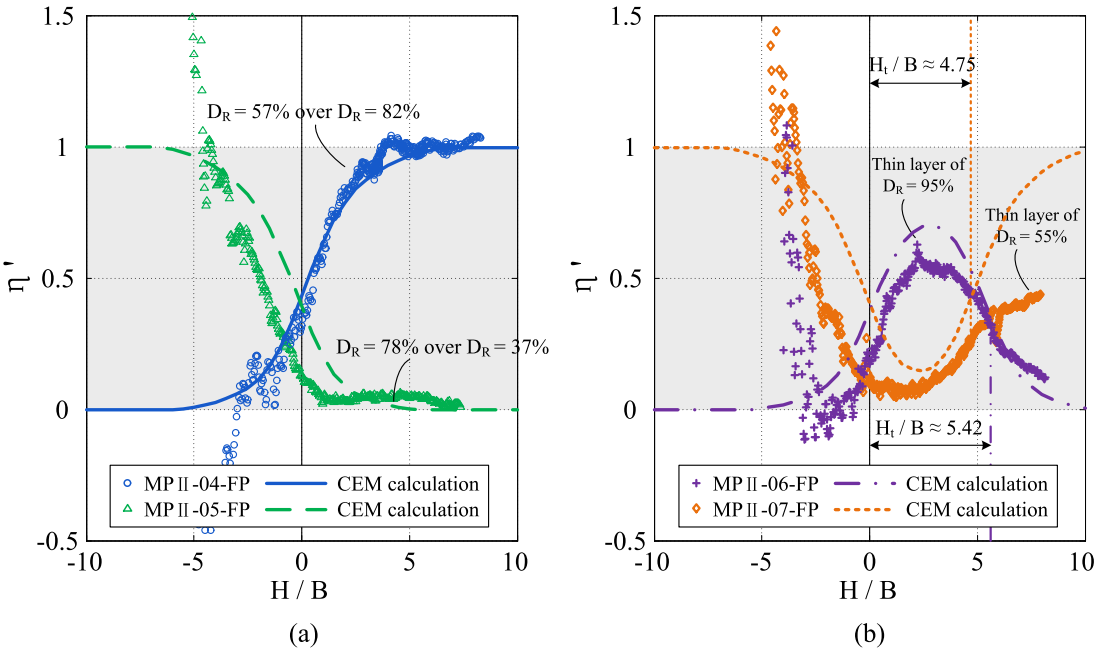

Figure 7.18 Comparisons of η' between centrifuge tests and cavity expansion calculations

Chapter 8

Conclusions and Further Research

Cone penetration testing, as one of the in-situ tools for site characterisation, provides data for soil classification and stratification, on the basis that the subsoil consists of layered deposits rather than being homogeneous. The behaviour of layered soils during installation of probes was investigated, and this research focused on both centrifuge experiments and cavity expansion analysis. This chapter presents the main conclusions drawn from each part of the research (Section 8.1), and provides recommendations for further possible areas of research on the penetration problems and possible implications (Section 8.2).

8.1 Conclusions

8.1.1 Centrifuge modelling

As one of the objectives of this research, the testing methodology for CPT modelling within the geotechnical centrifuge has been improved.

- Two series of cone penetration tests were performed in stratum configurations of silica sand in a constructed 180° axisymmetric model. For half-probe tests, a strain gauge near the cone tip and a load cell at the head of the probe were installed to measure the penetration resistance. Additionally, digital image analysis was used to investigate the soil response around the advancing probe. A full probe was also manufactured with the same dimension of the half-probe and more reliable readings of the cone tip resistance were obtained, aiming to validate the results of penetration resistance and examine the boundary effects.

- With respect to the half-cylinder axisymmetric model, an attempt was made to maintain continual contact between the probe and the Perspex window using a steel guiding bar attached to the penetrometer in parallel to the probe, and an aluminium channel fixed into the middle of the Perspex window (Figure 3.3). As the penetrometer was inserted along the Perspex face, the guiding bar slid into the aluminium channel to maintain contact between the half-probe and the window. The arrangements also addressed to the connection between the actuator and the probe, and the half-bridge circuit of strain gauges in Section 3.3.1 to eliminate the influence of bending effect.

- The soil model was prepared by multiple-sieving air pluviation of Fraction E sand. The density of the sand sample was controlled by the pouring height and the average flow rate, which was proved to provide a high quality and repeatable soil preparation. For each sample of layered soils, centrifuge tests ($50\,g$) of half-probe and full-probe penetration were performed at a constant speed of approximately $1\,mm/s$, followed by the '$1\,g$' test using the full-probe. The tests were designed for investigation of the effects of relative density, stress level, layering, and thin-layering.

8.1.2 Results of centrifuge tests

It was evident that the centrifuge penetration tests, together with the soil deformation measurement, provided an effective approach for investigation of penetration mechanisms around the probe. The results presented in Chapter 4 also served as a base for applications of cavity expansion solutions, back analyses and further studies.

- The magnitude of compression and tension recorded by the load cell of the full-probe was essentially identical with the results provided by Deeks and White (2006) under similar test conditions. The results of half-probe test and full-probe test were comparable with each other, for both penetration and pull-out processes. The resistance of full-probe was slightly larger than that of half-probe, which is likely due to the boundary effects at the centre of the sample and the slightly densified sample caused by the insertion of the half-probe and spin-down / up of the centrifuge. The magnitude of penetration resistance for $50\,g$ tests was found around $10 \sim 12$ times that from $1\,g$ tests, which implied that the resistances increased with stress level at a decreasing rate, and was thought to be attributed to

the restrained dilatancy at high stress level.

- The results from tests with similar D_R exhibited essential consistency, illustrating the repeatability of penetration and the homogeneity of the sample. Both dense sand and loose sand had linear increases of total load and tip resistance with depth. However, the value of total load in the dense sand ($D_R = 90\,\%$) was found to be about $2 \sim 3$ times that for loose sand ($D_R = 50\,\%$). The dimensional analysis appeared to indicate that Q (Bolton et al., 1993) provided a more appropriate normalisation for tip resistance in centrifuge model, which varied between $90 \sim 110$ for dense sand. The magnitude of shaft friction showed to be about $20 \sim 40\,\%$ of total load for both dense and loose sand. The tip resistance ratio η' was proposed to illustrate the transition of q_c from one soil layer to another. The influence zone in stronger soil was larger than that in weak soil, and the size was likely dependent on the relative density of both soil layers, which led to the variation of thin-layer effect in different scenarios.

- As a probe was advanced into the ground, soil particles were pushed away to accommodate the probe and were simultaneously dragged downwards owing to shearing at the soil-probe interface. The pattern of cumulative displacement showed reasonable similarity to cylindrical cavity expansion around the shaft, and spherical expansion around the cone. Comparing to loose sand, the size of influence zone for dense sand was larger, and the heaving effect near the ground surface was more evident. The decay of displacement with offset from the pile implied that the lateral influence zone is about $5B$ wide for dense sand, and approximately $3.5B$ for loose sand. The spherical cavity expansion method for penetration problems was also supported by the observation of the instantaneous soil displacement around the cone tip, and the upper boundary of the influence zone in dense sand was close to an inclination line of 60° from vertical, whereas the loose sand had a boundary that inclined at approximately 45° from vertical.

- From the trajectories of soil elements, it was notable that the major proportion of the displacement occurred before the probe passed, and little contribution was made during $h > 0$. More specifically, the displacement in stage $h > 0$ went slightly further away from the probe, which was in contrast with that observed by White (2002). Dense sand tended to have more horizontal displacement than vertical, whereas loose sand experienced lower magnitudes of displacements. The

streamlines and the displacement vectors provided the magnitude and the direction of displacement in soil with different relative density, and the shape of the deformed soil element was also illustrated alternatively by the soil element path. In brief, the distributions of soil deformation around the penetrometer provided insights into the mechanisms.

- Soil strains were derived from the results of the incremental displacements. The soil below the probe shoulder underwent vertical compression and horizontal extension, whereas the soil around the probe shaft experienced vertical extension and horizontal compression. The magnitude of strains in loose sand seemed to be greater, attributed to the higher compressibility of the loose sample. The contour of shear strain rate was a bulb shaped zone extending down to $3B$ below the probe; a little negative zone existed as the soil was rolled up around the probe shoulder. It was also notable that dilation with significant shear occurred below the cone and the contraction zone close to the probe shoulder was relatively small, while loose sand showed to be less sheared and dilated than dense sand. In addition, the directions of the principal strain rate provided some clues for estimation of directions and distributions of the principal stress rate. Strain reversal during penetration in the axisymmetric model was quantified to emphasise the severe distortion with rotation and dilation.

- The mechanism of deformation of layered soils around the probe was described and highlighted in Section 4.5 through the displacement profiles and the transition of deformation ratio: $\xi'_{\Delta x}$ and $\xi'_{\Delta y}$. The influence of layering on the displacement profiles was evident. The vertical displacement in loose sand overlying dense sand was affected within $2B$ above the interface, while the influence zone was $4B$ in an underlying loose sand. The deformation of loose-dense interface was less than the profiles of both dense and loose sand, and more downdrag movement was evident for the dense-loose interface. ξ' clearly indicated the layered effects on soil deformation, and did not appear to be affected by the offset. The variation of soil displacement with different profiles of soil density implied that the illustration of layered effects on soil deformation was essential to reveal the layering mechanisms for penetration.

8.1.3 Cavity expansion analyses of CPT in layered soils

- Analytical solutions for cavity expansion in two concentric regions of soil were developed and investigated based on Yu and Houlsby (1991) in Chapter 5. The soils were modelled by a non-associated Mohr-Coulomb yield criterion, and the solutions were extended to obtain large strain analysis for both spherical and cylindrical scenarios. The distributions of stress-strain around the cavities were provided, as well as the development of the plastic region. The solutions were also validated against Finite Element simulations, and the effects of varying geometric and material parameters were studied with the layered effects on the cavity-pressure curves. Despite of the limitation of constant material properties, the proposed method is potentially useful for various geotechnical problems in layered soils, such as the interpretation of cone penetration test data, tunnelling and mining, and analysis of shaft construction using ground-freezing methods.

- In order to apply the analytical solutions of cavity expansion to the penetration problem, a discussion on the concentric and horizontal layering was first addressed. The comparison showed that the horizontal layered soils provided a smooth and realistic transition curve, whereas the results from the concentric layered soils seemed to represent the transition in each side of the interface. A simple combination method was required to provide the prediction of the transition in layered soils, since the influence of the soil stiffness and strength was included in the results from the analytical solutions.

- An approach based on the Fahey-Carter model (Fahey and Carter, 1993) was adopted to estimate the soil properties for analyses. The penetration of a probe with diameter B into a sand sample with average particle size of d_{50} was suggested to be treated as a problem with an initial spherical cavity ($a_0 = d_{50}/2$) expanding to the size of probe diameter (i.e. $a = B/2$). By analogy, penetration in layered soils corresponded to the cavity in concentric layers, when the distance to the soil interface was set as the size of Soil A (b_0). The combination approach for the scenario of weak soil over strong soil was suggested based on the cavity pressure at $1\,B$ around the interface (Figure 6.7).

- The interpretation of penetration in two-layered soils implied that Z_s decreased with relative density of weaker soil and increased with relative density of stronger

soil, and vice versa. The correlations of the influence zones were also derived based on the relative densities, indicating the linear relationship with both $D_{R,w}$ and $D_{R,s}$. Compared with the elastic solution by Vreugdenhil et al. (1994), the derived transition of resistance ratio showed more realistic results when considering the effects of soil strength with large strain analysis. The comparisons with numerical and experimental results indicated that the cavity expansion analysis could provide essentially identical results more effectively.

- The penetration in multi-layered soils was also considered to investigate the thin-layer effects for interpretation of CPT data. The analysis was conducted by the superposition of two scenarios with 'two-layer' profiles. After the correction of the superposed resistance ratio, the extremes η'_{max} and η'_{min} were used to indicate the magnitude of thin-layer effects. The variation with relative density and thin-layer thickness was also investigated, showing that η'_{max} decreased with increasing relative density of the thin-layer strong soil, and increased to 1 when the thickness was enlarged. The examinations showed that the thin-layer effects were enhanced when the difference of D_R was increased and the thickness of thin-layer was narrowed. The comparisons with field data and numerical results provided essential consistency, and the proposed method improved the prediction of thin-layer effects when comparing with the elastic results.

8.1.4 Back analyses and the summarised penetration mechanisms

- A comparison of the previous correlations on CPT rigidity ratio and normalised tip resistance (Lo Presti, 1987; Rix and Stokoe, 1991; Fahey and Carter, 1993; Schnaid et al., 2004) was illustrated to show similar linear relationship in log-log space. Back-analysis using correlation of Robertson and Campanella (1983) showed that $1g$ test had a higher rigidity ratio, and stress level had a greater influence to the value than the relative density. The prediction of G_0 using previously proposed relationships was provided, and the lower and upper bounds proposed by Schnaid et al. (2004) generally involved the variation of G_0. The estimation of shaft friction was provided by the UWA-05 design method, and the operative value of pile friction was back analysed as $\delta = 23^\circ$ for dense sand and $\delta = 10^\circ$ for loose sand. Although the variation between the back-analysed relative density and the measured value was obvious, soil state parameter was suggested to

evaluate the tip resistance, and also showed good agreement with Klotz and Coop (2001) and field data.

- Boundary effects for centrifuge tests were discussed and verified by the soil deformation at the window, showing that the effect from the confining wall was limited and the influence of the base was small for dense sand. The effects of stress level on soil deformation were also examined to illustrate the larger deformation zone for penetration at '1g' condition, which was attributed to the enhanced heaving effect near the surface and the dense sand under a lower confining stress showed more dilatancy. After comparing the distribution of displacement with results of cavity expansion, the larger component of displacement in centrifuge tests was due to the compaction and shearing, and the cavity expansion analysis effectively showed that the distribution of displacement and the size of deformation zone increase with relative density and decrease with stress level. The results of deformation were also compared with White (2002) and Liu (2010) to examine the effect of particle size, and to emphasise the necessity of an axisymmetric model.

- By analogy, the correlation between the cone tip resistance and the pile bearing capacity was discussed, and the scale effects were examined through the ground surface effect and the layering effect by the developed cavity expansion solutions in Chapter 5. The ground surface was evident to have more influence for denser sand and larger penetrometer. Additionally, the influence zones around the soil interfaces were proved to be proportional to the probe diameter and decrease with stress level. On the other hand, the correlation between the penetration resistance and the cavity pressure was also revised, and the difference was emphasised for further investigation on soil shearing, anisotropy and particle crushing.

- Penetration mechanisms were finally summarised from the aspects of soil stress-strain history, particle breakage, soil patterns, and penetration in layered soils. The measurement of soil deformation presented the strain paths and soil patterns induced by penetration, and provided some insights for the examination of soil stress-strain history and probe-soil interaction. The effect of particle breakage was presumably limited in the centrifuge tests for fine silica sand, while particle compression and abrasion were experienced by the insertion of probes. The trends in results of displacement in layered soil were explained in terms of the effect of both soil stiffness and strength. The layered effects emphasised in this

research indicated that the penetration resistance was strongly dependent on the soil properties within the influence zones above and below, and also related to the in-situ stress gradient along the penetration. Hence, it was suggested that the correlations from the calibration chamber tests using uniform soil and constant stress field could not be used directly for interpretation of CPT data. The averaging technique for pile design was suggested based on the transition curve of q_c in layered soils with consideration of the scale effects caused by the soil layering.

8.2 Recommendations for Further Research

Based on the benefits of the developed physical model in this research, there are several aspects where further research on penetration in soils could be undertaken. For penetrometer, the instrumentation of the probe needs to be improved to depict the distribution of normal stress and friction along the shaft, though the space within the miniatured probe is limited. Moreover, different types of foundation are also of interest to examine the comparisons between close-ended pile, open-ended pile, square pile, H-section pile.

This study is only concerned with penetration in dry sand. Therefore, to widen the scope of the investigation, further study of saturated / unsaturated sand and clay is warranted to provide the effects of water and drainage condition. Meanwhile, the actuator could be upgraded to robustly control the penetration speed for static load tests, and enable more types of installation method (e.g. monotonic loading, jacking, and pseudo-dynamic installation). Precise measurement of stress and pore water pressure is required with developed and miniature stress sensors and pore pressure transducers. In addition, the soil deformation measurement would be improved when the rotation and strains of soil patch can be directly measured, together with the high-speed photography for analysis of dynamic problems.

With respect to the analytical solutions, a detailed investigation of concentric and horizontal layering is suggested for penetration, although the solutions can be directly applied to mining problems and shaft constructions. There is certainly scope for further work involving the development of cavity expansion with more sophisticated soil models that include the variation of soil properties with expansion. Although there is

reasonable consistency between the cavity pressure and the cone tip resistance, further research should be done to investigate the correlation which is appropriate for more types of soil. Numerical approaches are also encouraged to simulate the penetration and cavity expansion problems.

There is always a need to improve the interpretation of CPT data for G_0, soil strength, state parameters, and subsoil profiles. Further investigations are also needed for the implications to pile design, which is one of the main design tasks in geotechnical engineering. Additionally, more research on the sophisticated framework needs to be established to properly describe the penetration mechanisms before the association between the probe measurements and the soil stress-strain behaviour is more clearly understood.

Appendix A

The details of the displacement contours and profiles are presented in this Appendix, which provide additional information for the analysis of layered effects on soil deformation in Section 4.5. The figures are only for the tests in layered soils, and they can be directly compared with the results of tests in uniform dense and loose sand (MP II-02 and MP II-03), as presented in Figures 4.12 $\sim$ 4.15 (Section 4.3.1).

Figures A.1 $\sim$ A.4 provide the corresponding displacement contours of 'Δx', 'Δy' and 'Total displacement' after 160 mm of penetration for tests in layered soils: MP II-04, MP II-05, MP II-06, and MP II-07.

Figure A.5 and Figure A.6 show the profiles of the normalised cumulative displacements ($\Delta x/R$, $\Delta y/R$) for soil with different offset ($X/R = 2 \rightarrow 6$) in layered sand tests.

Figure A.7 and Figure A.8 present the developments of the profiles of the normalised cumulative displacements ($\Delta x/R$, $\Delta y/R$) with different depths of penetration for soil at $X/R = 2$.

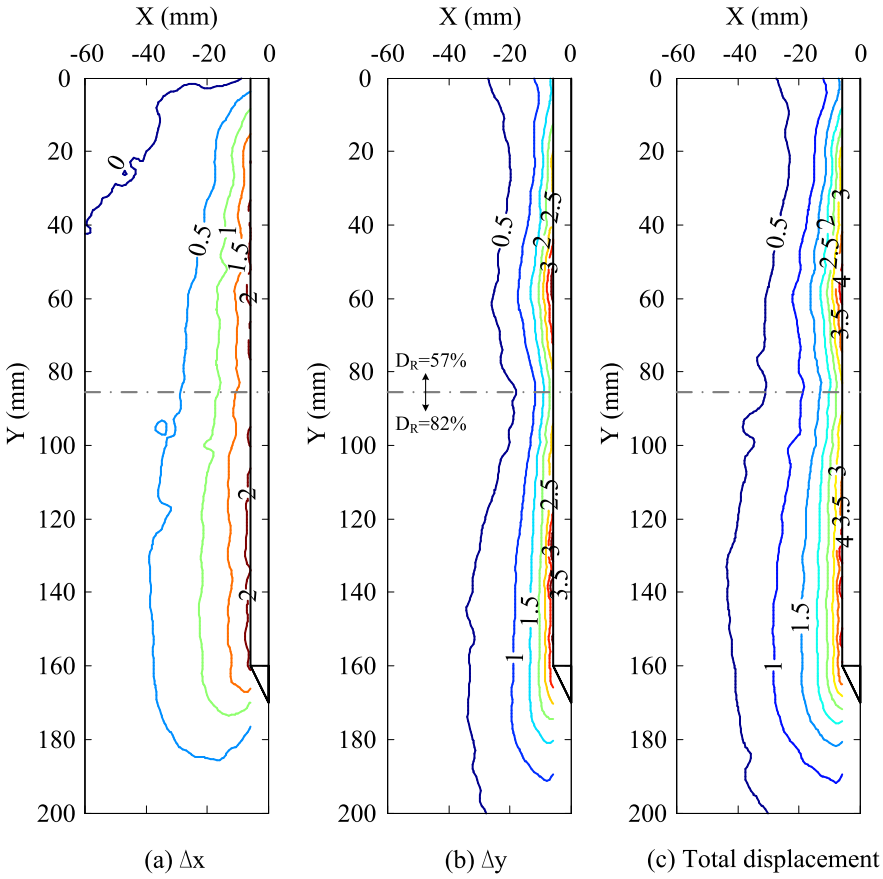

Figure A.1 Cumulative displacement contours of MP II-04 (loose sand over dense sand): (a) Δ*x*; (b) Δ*y*; (c) total displacement

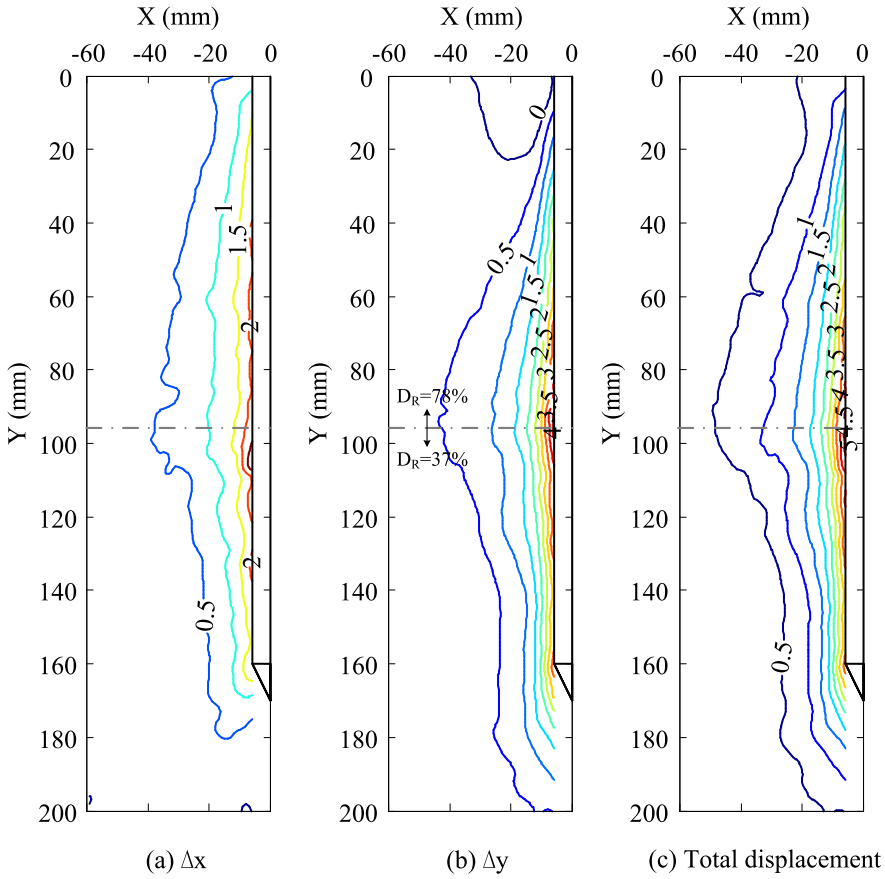

Figure A.2 Cumulative displacement contours of MP II-05 (dense sand over loose sand): (a) Δ*x*; (b) Δ*y*; (c) total displacement

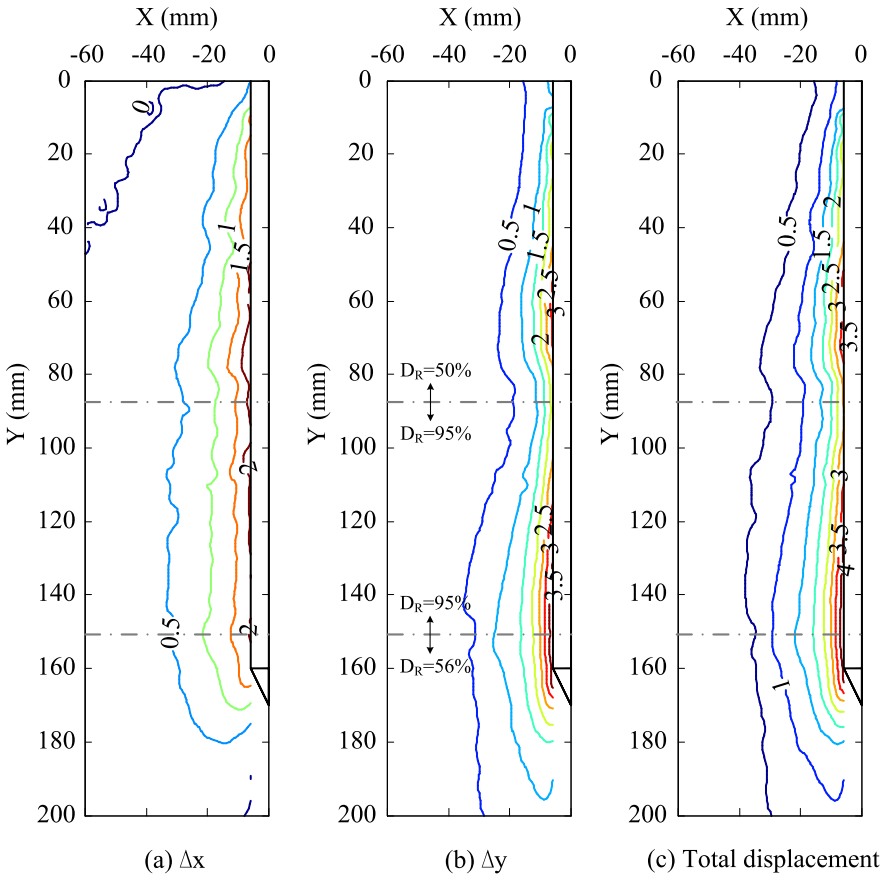

Figure A.3 Cumulative displacement contours of MP II-06 (dense sand sandwiched by loose layers): (a) Δx; (b) Δy; (c) total displacement

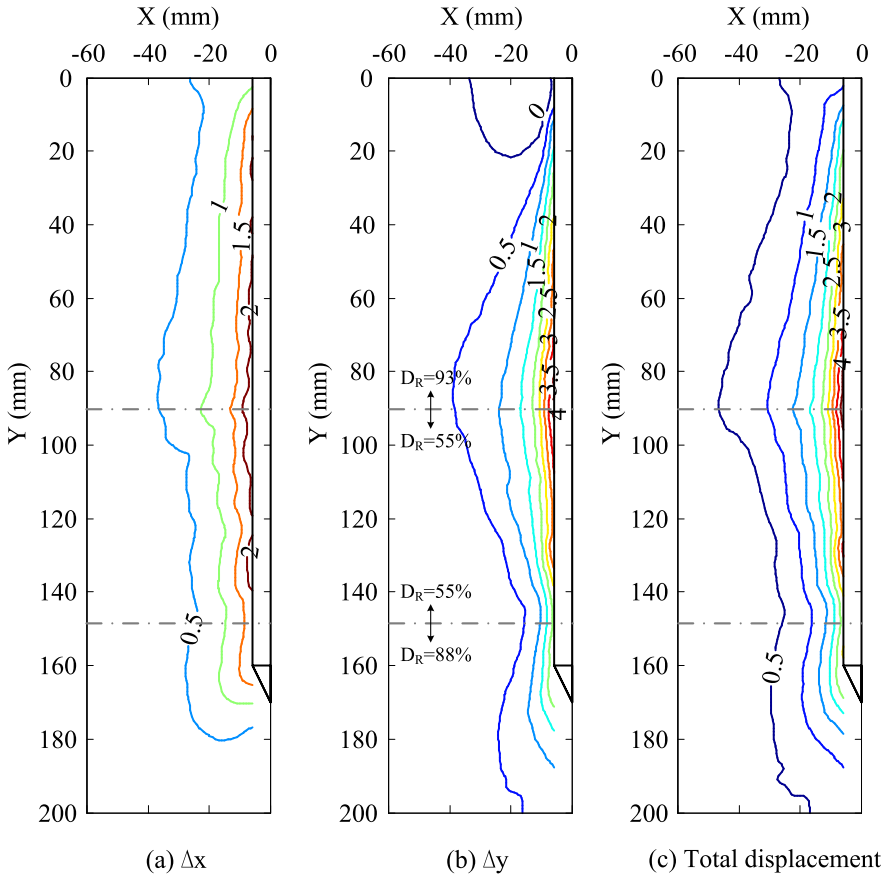

Figure A.4 Cumulative displacement contours of MP II-07 (loose sand sandwiched by dense layers): (a) Δx; (b) Δy; (c) total displacement

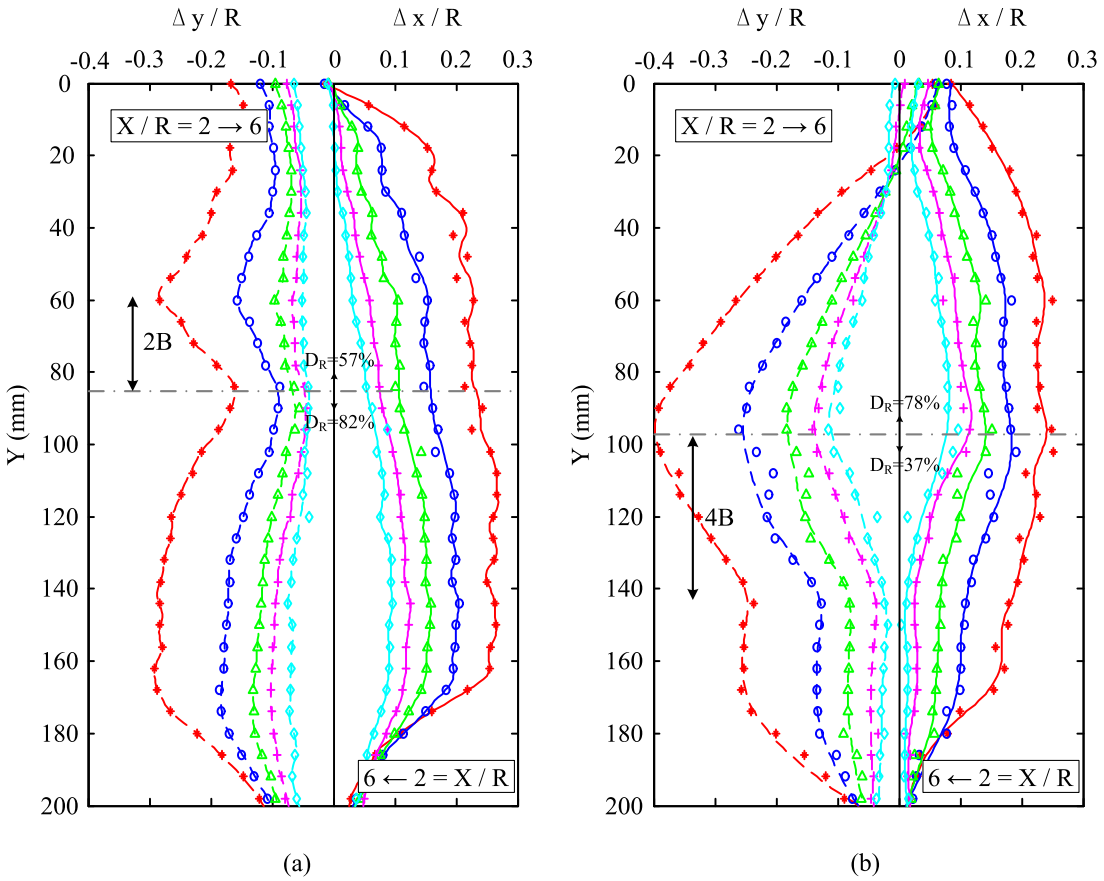

Figure A.5 Cumulative displacement profiles with variation of horizontal distance to the probe after 160 *mm* of penetration: (a) MP II-04; (b) MP II-05

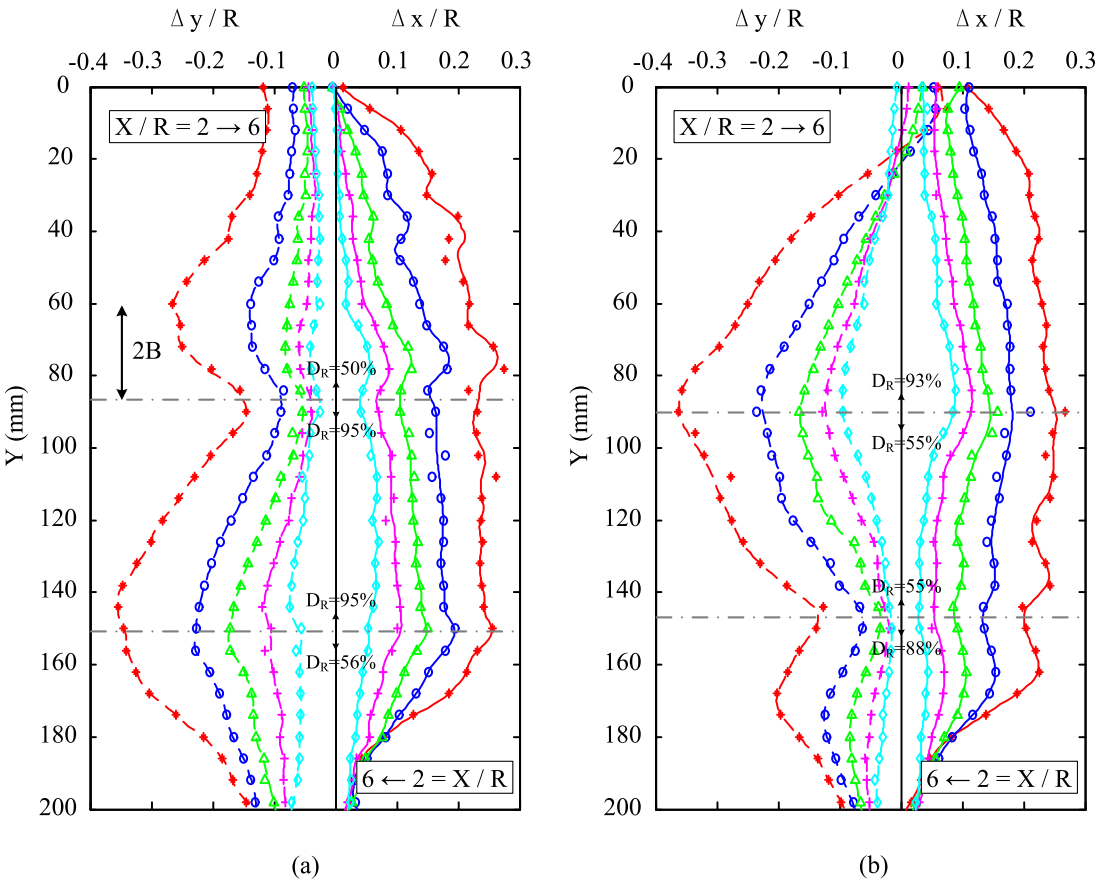

Figure A.6 Cumulative displacement profiles with variation of horizontal distance to the probe after 160 *mm* of penetration: (a) MP II-06; (b) MP II-07

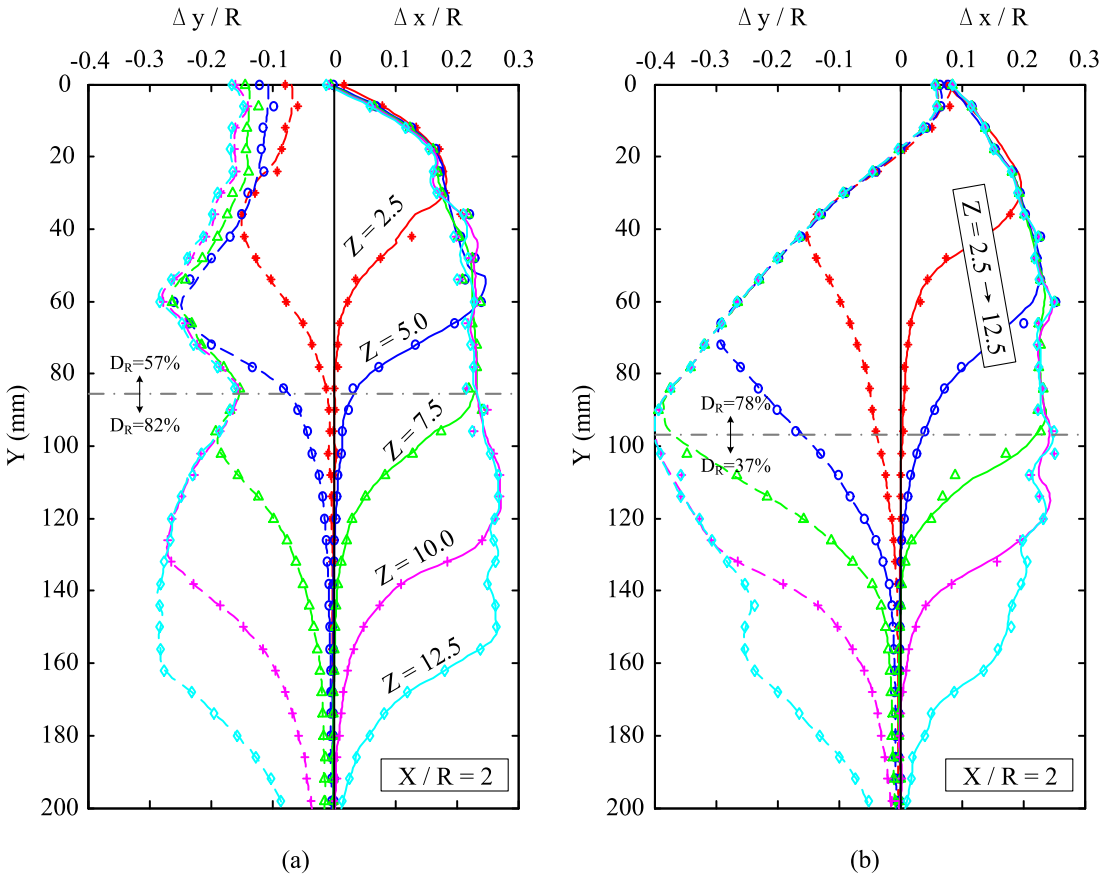

Figure A.7 Cumulative displacement profiles with variation of penetration depth for $X/R = 2$: (a) MP II-04; (b) MP II-05

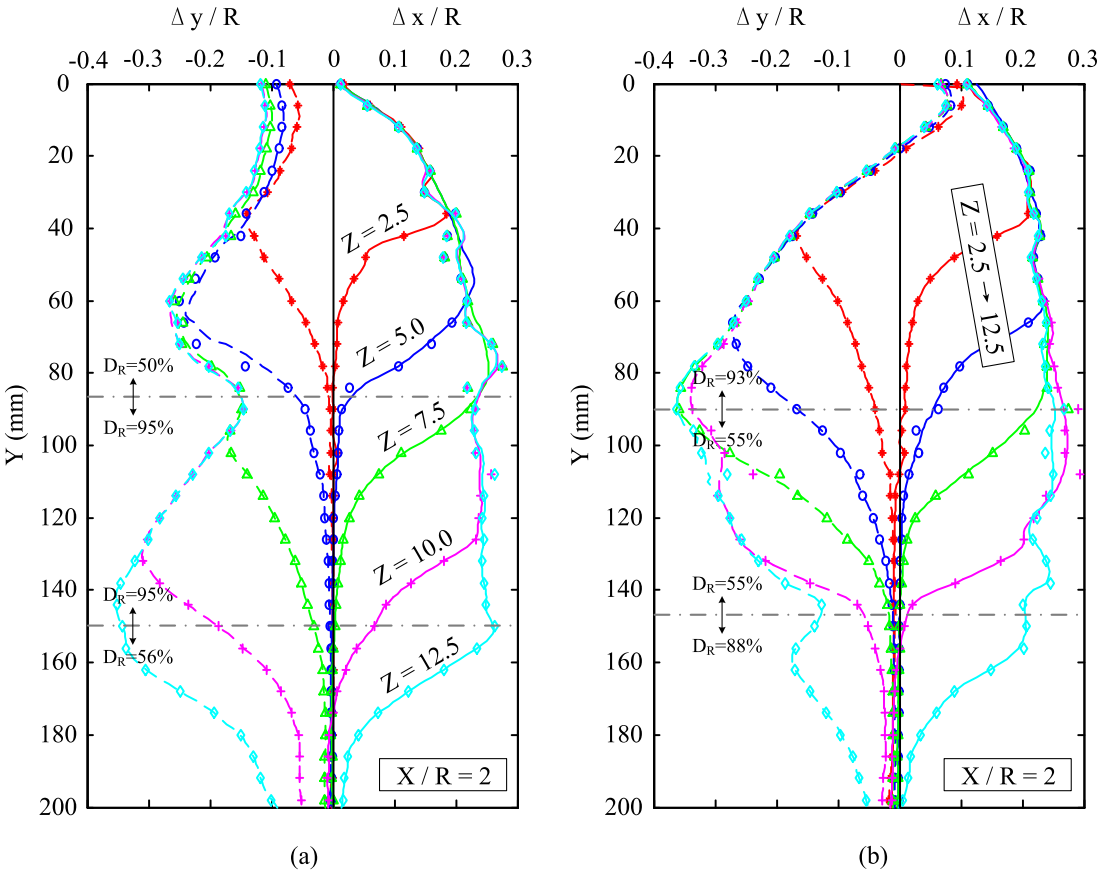

Figure A.8 Cumulative displacement profiles with variation of penetration depth for $X/R = 2$: (a) MP II-06; (b) MP II-07

References

Ahmadi, M. M., Byrne, P. M. and Campanella, R. G. (2005), 'Cone tip resistance in sand: modeling, verification, and applications', *Canadian Geotechnical Journal* **42**(4), 977–993.

Ahmadi, M. M. and Robertson, P. K. (2005), 'Thin-layer effects on the CPT q(c) measurement', *Canadian Geotechnical Journal* **42**(5), 1302–1317.

Ajalloeian, R. and Yu, H. S. (1998), 'Chamber studies of the effects of pressuremeter geometry on test results in sand', *Géotechnique* **48**(5), 621–636.

Allersma, H. (1987), Optical analysis of stress and strain in photoelastic practicle assembles, PhD thesis, Delft University of Technology.

Baldi, G., Bellotti, R., Ghionna, V. N., Jamiolkowski, M. and Pasqualini, E. (1986), Interpretation of CPTs and CPTUs; 2nd part: drained penetration of sand, *in* 'Proceedings of the 4th International Geotechnical Seminar', Singapore, pp. 143–156.

Baligh, M. (1985), 'Strain path method', *ASCE Journal of Geotechnical Engineering* **111**(9), 1108–1136.

Basu, P., Loukidis, D., Prezzi, M. and Salgado, R. (2011), 'Analysis of shaft resistance of jacked piles in sands', *International Journal for Numerical and Analytical Methods in Geomechanics* **35**(15), 1605–1635.

Been, K. and Jefferies, M. G. (1985), 'A state parameter for sands', *Géotechnique* **35**(2), 99–112.

Begemann, H. K. S. P. (1963), 'Use of static soil penetrometer in holland', *New Zealand Engineering* **18**(2), 41–49.

Berezanysev, V. G., Kristoforov, V. S. and Golubkov, V. N. (1961), Load bearing capacity and deformation of piled foundations, *in* 'International Conference on Soil Mechanics and Foundation Engineering', Vol. 2, Paris, France, pp. 11–15.

Bernard, R. S. (1976), Development of a projectile penetration theory. Report 2: Deep

penetration theory for homogeneous and layered targets, Technical Report S-75-9, U.S. Army Engineering Waterways Experiment Station.

Bernard, R. S. and Hanagud, S. V. (1975), Development of a projectile penetration theory. Report 1:penetration theory for shallow to moderate depths, Technical Report S-75-9, U.S. Army Engineering Waterways Experiment Station.

Bishop, R. F., Hill, R. and Mott, N. F. (1945), 'The theory of indentation and hardness tests', *Proceedings of the Physical Society of London* **57**(321), 147–159.

Bolton, M. D. (1979), *A guide to soil mechanics*, Macmilan, London.

Bolton, M. D. (1986), 'The strength and dilatancy of sands', *Géotechnique* **36**(1), 65–78.

Bolton, M. D. and Gui, M. W. (1993), The study of relative density and boundary effects for cone penetration tests in centrifuge, Technical Report CUED/D-SOILS/TR256, University of Cambridge.

Bolton, M. D., Gui, M. W., Garnier, J., Corte, J. F., Bagge, G., Laue, J. and Renzi, R. (1999), 'Centrifuge cone penetration tests in sand', *Géotechnique* **49**(4), 543–552.

Bolton, M. D., Gui, M. W. and Phillips, R. (1993), Review of miniature soil probes for model tests, *in* 'Proc. 11th South East Asia Geotechnical Conf.', pp. 85–91.

Bowman, E. T. and Soga, K. (2005), 'Mechanisms of setup of displacement piles in sand: laboratory creep tests', *Canadian Geotechnical Journal* **42**(5), 1391–1407.

Bui, M. T. (2009), Influence of some particle characteristics on the small strain response of granular materials, PhD thesis, University of Southampton.

Bustamante, M. and Gianeselli, L. (1982), Pile bearing capacity predictions by means of CPT, *in* 'European Symposium on Penetration Testing', Vol. 2.

Butterfield, R., Harkness, R. M. and Andrawes, K. Z. (1970), 'A stereophotogrammetric method for measuring displacement fields', *Geotechnique* **20**(3), 308–314.

Cabalar, A. F., Cevik, A. and Guzelbey, I. H. (2010), 'Constitutive modeling of leighton buzzard sands using genetic programming', *Neural Computing & Applications* **19**(5), 657–665.

Carter, J. P., Booker, J. R. and Yeung, S. K. (1986), 'Cavity expansion in cohesive frictional soils', *Géotechnique* **36**(3), 349–358.

Cavalieri (2000), The interface friction behaviour of sands, PhD thesis, University of Trento, Italy.

Chadwick, P. (1959), 'The quasi-static expansion of a spherical cavity in metals and ideal soils', *Quarterly Journal of Mechanics and Applied Mathenatics* **12**, 52–71.

Chen, J., Robson, S., Cooper, M. A. R. and Taylor, R. N. (1996), An evaluation of three different image capture methods for measurement and analysis of deformation within a geotechnical centrifuge, *in* 'International archieves of photogrammetry and remote sensing', Vol. 31, pp. 70–75.

Chong, M. K. (1988), Density changes of sand on cone penetration resistance, *in* S. G. Wright, ed., 'Proceedings of the conference on geotechnical practice in offshore engineering', pp. 181–202.

Chow, F. C. (1997), Investigations into the behaviour of displacement piles for offshore foundations, PhD thesis, University of London (Imperical College).

Chung, S. F., Randolph, M. F. and Schneider, J. A. (2006), 'Effect of penetration rate on penetrometer resistance in clay', *Journal of Geotechnical and Geoenvironmental Engineering* **132**(9), 1188–1196.

Clarke, B. G. (1995), *Pressuremeter in Geotechnical Design*, Chapman and Hall, London.

Collins, I. F., Pender, M. J. and Wang, Y. (1992), 'Cavity expansion in sands under drained loading conditions', *International Journal for Numerical and Analytical Methods in Geomechanics* **16**(1), 3–23.

Collins, I. F. and Yu, H. S. (1996), 'Undrained cavity expansions in critical state soils', *International Journal for Numerical and Analytical Methods in Geomechanics* **20**(7), 489–516.

Cundall, P. A. and Strack, O. D. L. (1979), 'Discrete numerical-model for granular assemblies', *Géotechnique* **29**(1), 47–65.

Davis, E. H. (1968), Theories of plasticity and the failure of soil masses, *in* I. Lee, ed., 'Soil Mechanics', London, Butterworths.

Davis, R. O., Scott, R. F. and Mullenger, G. (1984), 'Rapid expansion of a cylindrical cavity in a rate-type soil.', *International Journal for Numerical and Analytical Methods in Geomechanics* **8**(2), 125–140.

De Beer, E. E., Lousberg, D., De Jonghe, A., Carpentier, R. and Wallays, M. (1979),

Analysis of the results of loading tests performed on displacement piles of different types and sized penetrating at a relatively small depth into a very dense layer, *in* 'Proceedings of the Conference on Recent Development in the Design and Construction of Piles', ICE, pp. 199–211.

Deeks, A. D. (2008), An investigation into the strength and stiffness of jacked piles in sand, PhD thesis, University of Cambridge.

Deeks, A. D. and White, D. J. (2006), Centrifuge modelling of jacked piles, *in* 'Proceedings of the 6th International Conference on Physical Modelling in Geotechnics', Hong Kong, pp. 821–826.

Dijkstra, J., Broere, W. and Van Tol, A. F. (2012), 'Electrical resistivity method for the measurement of density changes near a probe', *Géotechnique* **62**(8), 721–725.

Ellis, E. A., Cox, C., Yu, H. S., Ainsworth, A. and Baker, N. (2006), A new geotechnical centrifuge at the university of nottingham, uk, *in* C. W. W. Ng, L. M. Zhang and Y. Wang, eds, 'Physical Modelling in Geotechnics - 6th ICPMG '06', pp. 129–133.

Fahey, M. and Carter, J. P. (1993), 'A finite-element study of the pressuremeter test in sand using a nonlinear elastic-plastic model', *Canadian Geotechnical Journal* **30**(2), 348–362.

Fioravante, V. (2002), 'On the shaft friction modelling of non-displacement piles in sand', *Soils and Foundations* **42**(2), 23–33.

Fleming, W. G. K. (1992), 'A new method for single pile settlement prediction and analysis', *Géotechnique* **42**(3), 411–425.

Gavin, K. G. and O'Kelly, B. C. (2007), 'Effect of friction fatigue on pile capacity in dense sand', *Journal of Geotechnical and Geoenvironmental Engineering* **133**(1), 63–71.

Geng, Y. (2010), Discrete element modelling of cavity expansion in granular materials, PhD thesis, University of Nottingham.

Geng, Y., Yu, H. S. and McDowell, G. R. (2013), 'Discrete element modelling of cavity expansion and pressuremeter test', *Geomechanics and Geoengineering: An International Journal* **8**(3), 179–190.

Gerber, E. (1929), Untersuchungen uber die Druck-verteilung im Oerlick Belasteten Sand, PhD thesis, Dissertation Technische Hochschule.

Gibson, R. and Anderson, W. (1961), 'In situ measurement of soil properties with the

pressuremeter', *Civil Engineering and Public Works Review* **56**(658), 615–618.

Gibson, R. E. (1950), 'Correspondence', *J. Inst. Civ. Engrs* **34**, 382–383.

Gui, M. and Bolton, M. D. (1998), Geometry and scale effect in cpt and pile design, *in* P. Robertson and P. Mayne, eds, 'Geotechnical Site Characterization: Proceedings of the First International Conference on Site Characterization, ISC'98', Vol. 2, Balkema, Rotterdam, Atlanta, Georgia, pp. 1063–1068.

Gui, M., Bolton, M. D., Garnier, J., Corte, J. F., Bagge, G., Laue, J. and Renzi, R. (1998), Guidelines for cone penetration tests in sand, *in* 'International Conference on Centrifuge Modelling (Centrifuge '98)', Vol. 1, Balkema, pp. 155–160.

Gui, M. W. and Jeng, D. S. (2009), 'Application of cavity expansion theory in predicting centrifuge cone penetration resistance', *The Open Civil Engineering Journal* **3**, 1–6.

Hardin, B. O. and Black, W. L. (1966), 'Sand stiffness under various triaxial stresses', *Journal of Soil Mechanics and Foundation Engineering Division, ASCE* **92**(2), 27–42.

Hill, R. (1950), *The Mathematical Theory of Plasticity*, Oxford University Press.

Hird, C. C., Johnson, P. and Sills, G. C. (2003), 'Performance of miniature piezocones in thinly layered soils', *Géotechnique* **53**(10), 885–900.

Hoek, E. and Brown, E. T. (1980), *Underground excavations in rock*, The Institution of Mining and Metallurgy, London.

Holden, J. C. (1971), Laboratory research on static cone penetrometers, Technical Report CE-SM-71-1, Department of Civil Engineering, University of Florida, Gainesville, Fla.

Houlsby, G. T. and Hitchman, R. (1988), 'Calibration chamber tests of a cone penetrometer in sand', *Géotechnique* **38**(1), 39–44.

Houlsby, G. T. and Wroth, C. P. (1991), 'The variation of shear modulus of a clay with pressure and overconsolidation ratio', *Soils and Foundations* **31**(3), 138–143.

Houlsby, G. T. and Yu, H. S. (1980), Finite element analysis of the cone pressuremeter test, *in* 'Proceedings of the 3rd International Symposium on Pressuremeters', pp. 201–208.

Huang, A. B. and Ma, M. Y. (1994), 'An analytical study of cone penetration tests in granular material', *Canadian Geotechnical Journal* **31**(1), 91–103.

Huang, W., Sheng, D., Sloan, S. W. and Yu, H. S. (2004), 'Finite element analysis of

cone penetration in cohesionless soil', *Computers and Geotechnics* **31**(7), 517–528.

Hughes, J. M. O., Wroth, C. P. and Windle, D. (1977), 'Pressuremeter tests in sands', *Géotechnique* **27**(4), 455–477.

Imai, T. and Tonouchi, K. (1982), Correlation of n-values with s-wave velocity, *in* 'Proceedings of Second European Symposium on Penetration Testing', Vol. 2, pp. 67–72.

IRTP (1994), International reference test procedure (IRTP) for the Cone Penetration Test (CPT) and the Cone Penetration Test with pore pressure (CPTU), *in* 'Proceedings of the XIIth ECSMGE', Balkema, pp. 2195–2222.

Itasca (2005), 'FLAC-3D user's manual'.

Jacobs, P. (2004), Cone Penetration Testing (CPT), Technical report, Fugro Engineering Services Ltd.

Jamiolkowski, M., Ghionna, V. N., Lancellotta, R. and Pasqualini, E. (1988), New correlations of penetration test for design practice. Invited Lecture, *in* 'ISOPT-1', pp. 196–263.

Jamiolkowski, M., Ladd, C. C., Germaine, J. T. and Lanellotta, R. (1985), New developments in field and laboratory testing of soils, *in* 'Theme Lecture, Proc. 11th Int. Conf. on Soil Mechanics and Foundation Engineering', San Francisco., pp. 57–156.

Jamiolkowski, M., Lo Presti, D. C. F. and Manassero, M. (2001), Evaluation of relative density and shear strength of sands from CPT and DMT, *in* 'Soil Behaviour and Soft Ground Construction: proceedings of the symposium'.

Jamiolkowski, M., Lo Presti, D. C. F. and Manassero, M. (2003), 'Evaluation of relative density and shear strength of sands from CPT and DMT', *Soil Behavior and Soft Ground Construction* **7**(119), 201–238.

Jardine, R. J. and Chow, F. C. (1996), New design methos for offshore piles, Technical Report MTD96/103, Marin Tech. Directorate.

Jardine, R. J., Standing, J. R. and Chow, F. C. (2006), 'Some observations of the effects of time on the capacity of piles driven in sand', *Géotechnique* **56**(4), 227–244.

Jardine, R. J., Zhu, B. T., Foray, P. and Yang, Z. X. (2013*a*), 'Interpretation of stress measurements made around closed-ended displacement piles in sand', *Géotechnique* **63**(8), 613–627.

Jardine, R. J., Zhu, B. T., Foray, P. and Yang, Z. X. (2013*b*), 'Measurement of stresses around closed-ended displacement piles in sand', *Géotechnique* **63**(1), 1–17.

Jiang, M. J., Yu, H. S. and Harris, D. (2006), 'Discrete element modelling of deep penetration in granular soils', *International Journal for Numerical and Analytical Methods in Geomechanics* **30**(4), 335–361.

Keer, L. M., Xu, Y. L. and Luk, V. K. (1998), 'Boundary effects in penetration or perforation', *Journal of Applied Mechanics-Transactions of the Asme* **65**(2), 489–496.

Kim, K., Prezzi, M., Salgado, R. and Lee, W. (2010), Penetration rate effects on cone resistance measured in a calibration chamber, *in* '2nd International Symposium on Cone Penetration Testing (CPT'10)'.

Klotz, E. U. and Coop, M. R. (2001), 'An investigation of the effect of soil state on the capacity of driven piles in sands', *Géotechnique* **51**(9), 733–751.

Kokturk (1993), Interpretation von Drucksondierungen in Zentrifugen-modellversuch, PhD thesis, Diplomarbeit, Ruhr University Bochum, Germany.

Kolk, H. J., Baaijens, A. E. and Senders, M. (2005), 'Design criteria for pipe piles in silica sands'.

Kurup, P. U., Voyiadjis, G. Z. and Tumay, M. T. (1994), 'Calibration chamber studies of piezocone test in cohesive soils', *Journal of Geotechnical Engineering-ASCE* **120**(1), 81–107.

Ladanyi, B. (1963), Evaluation of pressuremeter tests in granular soils, *in* 'Proceedings of the 2nd Pan American Conference on Soil Mechanics', Vol. 1, pp. 3–20.

Ladanyi, B. and Johnston, G. H. (1974), 'Behaviour of circular footings and plate anchors embedded in permafrost', *Canadian Geotechnical Journal* **11**, 531–553.

Lancellotta, R. (1983), Analisi di affidabilita in ingegneria geotechnica, Technical Report 625, Politernico di Torino.

Lee, D. M. (1992), The angles of friction of granular fills, PhD thesis, University of Cambridge.

Lee, S. (1990), Centrifuge modelling of cone penetration testing in cohesionless soils, PhD thesis, University of Cambridge.

Lehane, B. (1992), Experimental investigations of pile behaviour using instrumented field piles, PhD thesis, Imperial College.

Lehane, B. M., Schneider, J. A. and Xu, X. (2005), The UWA-05 method for prediction of axial capacity of driven piles in sand, *in* 'International Symposium on

Frontiers in Offshore Geotechnics', pp. 683–689.

Lehane, B. M. and White, D. J. (2005), 'Lateral stress changes and shaft friction for model displacement piles in sand', *Canadian Geotechnical Journal* **42**(4), 1039–1052.

Lekhnitskii, S. G. (1963), *Theory of Elasticity of an Anisotropic Elastic Body*, Holden-Day, Inc.

Liao, C. L., Chan, T. C., Suiker, A. S. J. and Chang, C. S. (2000), 'Pressure-dependent elastic moduli of granular assemblies', *International Journal for Numerical and Analytical Methods in Geomechanics* **24**(3), 265–279.

Liu, W. (2010), Axismmetric centrifuge modelling of deep penetration in sand, PhD thesis, University of Nottingham.

Lo Presti, D. C. F. (1987), Mechanical behaviour of Ticino sand from resonant column tests, PhD thesis, Politecnico di Torino.

Lunne, T., Robertson, P. K. and Powell, J. J. M. (1997), *Cone Penetration Testing in Geotechnical Practice*, Blackie Academic and Professional, London.

Mair, R. J. and Taylor, R. N. (1993), *Prediction of clay behaviour around tunnels using plasticity solutions*, Thomas Telford, London, pp. 449–463.

Marshall, A. M. (2009), Tunnelling in sand and its effect on pipelines and piles, PhD thesis, Cambridge University.

Marshall, A. M. (2012), 'Tunnel-pile interaction analysis using cavity expansion methods', *ASCE Journal of Geotechnical and Geoenvironmental Engineering* **138**(10), 1237–1246.

Marshall, A. M. (2013), 'Closure to "Tunnel-pile interaction analysis using cavity expansion methods" by Alec M. Marshall', *ASCE Journal of Geotechnical and Geoenvironmental Engineering* **139**(11), 2002–2004.

McDowell, G. and Bolton, M. D. (2001), 'Micro mechanics of elastic soil', *Soils and Foundations* **41**(6), 147–152.

McDowell, G. R. and Bolton, M. D. (1998), 'On the micromechanics of crushable aggregates', *Géotechnique* **48**(5), 667–679.

McDowell, G. R. and Bolton, M. D. (2000), 'Effect of particle size distribution on pile tip resistance in calcareous sand in the geotechnical centrifuge', *Granular Matter* **2**(4), 179–187.

Meyerhof, G. G. (1951), 'Ultimate bearing capacity of foundations', *Géotechnique*

2(4), 301–330.

Meyerhof, G. G. (1976), 'Bearing capacity and settlement of pile foundations', *Journal of the Geotechnical Engineering Division-ASCE* **102**(3), 195–228.

Meyerhof, G. G. (1977), Bearing capacity of piles in layered soils, *in* 'Proceedings of the 8th International Conference on SOil Mechanics and Foundation Engineering', pp. 645–650.

Meyerhof, G. G. (1983), 'Scale effects of ultimate pile capacity', *Journal of Geotechnical Engineering-ASCE* **109**(6), 797–806.

Meyerhof, G. G. and Sastry, V. V. R. N. (1978a), 'Bearing capacity of piles in layered soils.1. clay overlying sand', *Canadian Geotechnical Journal* **15**(2), 171–182.

Meyerhof, G. G. and Sastry, V. V. R. N. (1978b), 'Bearing capacity of piles in layered soils.2. sand overlying clay', *Canadian Geotechnical Journal* **15**(2), 183–189.

Mitchell, J. K., Bonita, J. A. and Brandon, T. L. (1998), Development of a piezovibrocone penetrometer for in-situ evaluation of soil liquefaction potential, Technical report, United States Geologic Survey.

Mitchell, J. K. and Soga, K. (2005), *Fundamentals of soil behaviour*, 3rd edn, John Wiley and Sons.

Miura, S. and Toki, S. (1982), 'A sample preparation method and its effect on static and cyclic deformation-strength properties of sand', *Soils and Foundations* **22**, 61–77.

Moss, R. E. S., Seed, R. B., Kayen, R. E., Stewart, J. P., Kiureghian, A. D. and Cetin, K. O. (2006), 'CPT-based probabilistic and deterministic assessment of in situ seismic soil liquefaction potential', *Journal of Geotechnical and Geoenvironmental Engineering* **132**(8), 1032–1051.

O'Loughlin, C. D. and Lehane, B. M. (2003), Measurement and prediction of deformation patterns beneath strip footings in sand, *in* 'Proc., Int. BGA Conf. on Foundations', Thomas Telford, pp. 705–714.

Palmer, A. C. (1972), 'Undrained plane-strain expansion of a cylindrical cavity in clay - simple interpretation of pressuremeter test', *Géotechnique* **22**(3), 451–457.

Palmer, A. C. and Mitchell, R. J. (1971), Plane strain expansion of a cylindrical cavity in clay, *in* 'Proceedings of the Roscoe Memorial Symposium', pp. 588–599.

Parkin, A. and Lunne, T. (1982), Boundary effects in the laboratory calibration of a cone penetrameter in sand, *in* 'Proc., 2nd Eur. Symp. on Penetration Testing',

Vol. 2, pp. 761–768.

Plantema, G. (1948), Results of a special loading-test on a reinforced concrete pile, a so-called pile sounding; interpretation of the results of deep-soundings, permissible pile loads and extended settlement observations, *in* 'The 2nd International Conference on Soil Mechanics and Foundation Engineering', pp. 112–117.

Pournaghiazar, M., Russell, A. R. and Khalili, N. (2012), 'Linking cone penetration resistances measured in calibration chambers and the field', *Géotechnique Letters* **2**, 29–35.

Prakongkep, N., Suddhiprakarn, A., Kheoruenromne, I. and Gilkes, R. J. (2010), 'SEM image analysis for characterization of sand grains in thai paddy soils', *Geoderma* **156**(1-2), 20–31.

Prandtl, L. (1921), 'Uber die Eindringungsfestigkeit (Harte) plastischer Baustoffe und die Festigkeit von Schneiden', *Z. Angew. Math. Mech.* **1**(15-20).

Randolph, M. F., Dolwin, J. and Beck, R. (1994), 'Design of driven piles in sand', *Géotechnique* **44**(3), 427–448.

Rix, G. J. and Stokoe, K. H. (1991), Correlation of initial tangent modulus and cone penetration resistance, *in* 'Calibration Chamber Testing', Elsevier, pp. 351–361.

Robertson, P. K. (1982), In-situ tesing of soil with emphasis on its application to liquefaction assessment, PhD thesis, The University of British Columbia.

Robertson, P. K. (1990), 'Soil classification using the cone penetration test', *Canadian Geotechnical Journal* **27**(1), 151–158.

Robertson, P. K. and Campanella, R. G. (1983), 'Interpretation of cone penetration tests.1. sand', *Canadian Geotechnical Journal* **20**(4), 718–733.

Robertson, P. K. and Fear, C. E. (1995), Liquefaction of sands and its evaluation, *in* 'Proceedings of the 1st International Conference on Earthquake Geotechnical Engineering', Vol. 3, pp. 1253–1289.

Robertson, P. K. and Wride, C. E. (1998), 'Evaluating cyclic liquefaction potential using the cone penetration test', *Canadian Geotechnical Journal* **35**(3), 442–459.

Roscoe, K. H. (1970), 'The influence of strains in soil mechanics', *Géotechnique* **20**(2), 129–170.

Roscoe, K. H. and Burland, J. B. (1968), On generalised stress strain behaviour of wet clay, *in* 'Engineering Plasticity', pp. 535–609.

Rosenberg, Z. and Dekel, E. (2008), 'A numerical study of the cavity expansion process and its application to long-rod penetration mechanics', *International Journal of Impact Engineering* **35**(3), 147–154.

Salgado, R. (1993), Analysis of penetration resistance in sands, PhD thesis, University of California, Berkeley, Calif.

Salgado, R., Mitchell, J. K. and Jamiolkowski, M. (1997), 'Cavity expansion and penetration resistance in sand', *Journal of Geotechnical and Geoenvironmental Engineering* **123**(4), 344–354.

Salgado, R., Mitchell, J. K. and Jamiolkowski, M. (1998), 'Calibration chamber size effects on penetration resistance in sand', *Journal of Geotechnical and Geoenvironmental Engineering* **124**(9), 878–888.

Salgado, R. and Prezzi, M. (2007), 'Computation of cavity expansion pressure and penetration resistance in sands', *International Journal of Geomechanics* **7**(4), 251–265.

Santamarina, J. C. and Cascante, G. (1996), 'Stress anisotropy and wave propagation: A micromechanical view', *Canadian Geotechnical Journal* **33**(5), 770–782.

Santos, J. A. (1999), Soil characterisation by dynamic and cyclic torsional shear tests. Application to the study of piles under lateral static and dynamic loadings, PhD thesis, Technical University of Lisbon, Portugal.

Sayed, S. M. and Hamed, M. A. (1987), 'Expansion of cavities in layered elastic system', *International Journal for Numerical and Analytical Methods in Geomechanics* **11**(2), 203–213.

Schanz, T., Vermeer, P. A. and Bonnier, P. G. (1999), The hardening soil model: formulation and verification, *in* 'Beyond 2000 in Computational Geotechnics - 10 years of Plaxis'.

Schmertmann, J. H. (1978), Guidlines for cone test, performance, and design, Technical Report FHWATS-78209, U. S. Federal Highway Administration.

Schnaid, F. and Houlsby, G. T. (1990), An assessment of chamber size effects in the calibration of in situ tests in sand, Technical Report OUEL 1849/90, Department of Engineering Science, University of Oxford.

Schnaid, F. and Houlsby, G. T. (1991), 'An assessment of chamber size effects in the calibration of it situ tests in sand', *Géotechnique* **41**(3), 437–445.

Schnaid, F., Lehane, B. M. and Fahey, M. (2004), In situ test characterisation of un-

usual soils. Keynote Lecture, *in* 'Proc. 2nd Int. Conf. Geotech. Geophys. Site Characterisation', Vol. 1, pp. 49–74.

Schnaid, F. and Yu, H. S. (2007), 'Interpretation of the seismic cone test in granular soils', *Géotechnique* **57**(3), 265–272.

Schneider, J. A., Xu, X. T. and Lehane, B. M. (2008), 'Database assessment of cpt-based design methods for axial capacity of driven piles in siliceous sands', *Journal of Geotechnical and Geoenvironmental Engineering* **134**(9), 1227–1244.

Schofield, A. N. and Wroth, C. P. (1968), *Critical state soil mechanics*, McGraw-Hill, England.

Silva, M. F. and Bolton, M. D. (2004), 'Centrifuge penetration tests in saturated layered sands', *Geotechnical and Geophysical Site Characterization Vols 1 and 2* pp. 377–384.

Silva, M. F., White, D. J. and Bolton, M. D. (2006), 'An analytical study of the effect of penetration rate on piezocone tests in clay', *International Journal for Numerical and Analytical Methods in Geomechanics* **30**(6), 501–527.

Take, W. A. (2003), The influence of seasonal moisture cycles on clay slopes, PhD thesis, Cambridge University.

Tan, F. S. C. (1990), Centrifuge and theoretical modelling of conical footings on sand, PhD thesis, University of Cambridge.

Tatsuoka, F., Zhou, S., Sato, T. and Shibuya, S. (1990), Evaluation method of liquefaction potential and its application, Technical report, Ministry of Education of Japan.

Taylor, R. N. (1995), *Geotechnical Centrifuge Technology*, Blackie Academic and Professional, London.

Teh, C. I. (1987), An analytical study of the cone penetration test, PhD thesis, University of Oxford.

Teh, C. I. and Houlsby, G. T. (1991), 'An analytical study of the cone penetration test in clay', *Géotechnique* **41**(1), 17–34.

Terzaghi, K. (1943), *Theoretical soil mechanics*, John Wiley & Sons, Inc., New York, N. Y.

Tolooiyan, A. and Gavin, K. (2011), 'Modelling the cone penetration test in sand using cavity expansion and arbitrary lagrangian eulerian finite element methods', *Computers and Geotechnics* **38**(4), 482–490.

Treadwell, D. D. (1976), The influence of gravity, prestress, compressibility, and layering on soil resistance to static penetration, PhD thesis, University of California at Berkeley.

Tseng, D. J. (1989), Prediction of cone penetration resistance and its application to liquefaction assessment, PhD thesis, University of California, Berkeley, Calif.

Uesugi, M., Kishida, H. and Tsubakihara, Y. (1988), 'Behavior of sand particles in sand-steel friction', *Soils and Foundations* **28**(1), 107–118.

van den Berg, P. (1994), Analysis of soil penetration, PhD thesis, Delft University of Technology.

van den Berg, P., de Borst, R. and Huetink, H. (1996), 'An eulerean finite element model for penetration in layered soil', *International Journal for Numerical and Analytical Methods in Geomechanics* **20**, 865–886.

Verruijt, A. and Booker, J. R. (1996), 'Surface settlements due to deformation of a tunnel in an elastic half plane', *Géotechnique* **46**(4), 753–756.

Vesic, A. S. (1972), 'Expansion of cavities in infinite soil mass', *ASCE Journal of Soil Mechanics and Foundations Division* **98**(SM3), 265–290.

Vesic, A. S. (1977), Design of pile foundations, Technical report, Transport Research Board.

Vesic, A. S. and Clough, G. W. (1968), 'Behaviour of granular materials under high stresses', *J. Soil Mech. Fdns Div. Am. Soc. Civ. Engrs 94* **SM3**, 661–688.

Vreugdenhil, R., Davis, R. and Berrill, J. (1994), 'Interpretation of cone penetration results in multilayered soils', *International Journal for Numerical and Analytical Methods in Geomechanics* **18**(9), 585–599.

Walker, J. (2007), Adaptive finite element analysis of the cone penetration test in layered clay, PhD thesis, University of Nottingham.

Walker, J. and Yu, H. S. (2010), 'Analysis of the cone penetration test in layered clay', *Géotechnique* **60**(12), 939–948.

Wang, J. (2005), The stress-strain and strength characteristics of portaway sand, PhD thesis, University of Nottingham.

White, D. J. (2002), An investigation into the behaviour of pressed-in piles, PhD thesis, Cambridge University.

White, D. J. (2003), Field measurements of CPT and pile base resistance in sand, Technical Report CUED/D-SOILS/TR327, University of Cambridge.

White, D. J. and Bolton, M. D. (2002), 'Observing friction fatigue on a jacked pile', *Constitutive and Centrifuge Modelling: Two Extremes* pp. 347–354.

White, D. J. and Bolton, M. D. (2004), 'Displacement and strain paths during plane-strain model pile installation in sand', *Géotechnique* **54**(6), 375–397.

White, D. J. and Bolton, M. D. (2005), 'Comparing CPT and pile base resistance in sand', *Proceedings of the Institution of Civil Engineers-Geotechnical Engineering* **158**(1), 3–14.

White, D. J. and Lehane, B. M. (2004), 'Friction fatigue on displacement piles in sand', *Géotechnique* **54**(10), 645–658.

White, D. J., Schneider, J. A. and Lehane, B. M. (2005), The influence of effective area ratio on shaft friction of displacement piles in sand, *in* 'International Symposium on Frontiers in Offshore Geotechnics', pp. 741–749.

White, D. J., Take, W. A. and Bolton, M. D. (2003), 'Soil deformation measurement using particle image velocimetry (PIV) and photogrammetry', *Géotechnique* **53**(7).

Wood, D. M. (1990), *Soil behaviour and critical state soil mechanics*, Cambridge University Press.

Wroth, C. P. (1984), 'Interpretation of in situ soil tests.', *Géotechnique* **34**(4), 449–489.

Xu, X. T. (2007), Investigation of the end bearing performance of displacement piles in sand, PhD thesis, The University of Western Australia.

Xu, X. T. and Lehane, B. M. (2008), 'Pile and penetrometer end bearing resistance in two-layered soil profiles', *Géotechnique* **58**(3), 187–197.

Yang, J. (2006), 'Influence zone for end bearing of piles in sand', *Journal of Geotechnical and Geoenvironmental Engineering* **132**(9), 1229–1237.

Yasufuku, N. and Hyde, A. F. L. (1995), 'Pile end-bearing capacity in crushable sands', *Géotechnique* **45**(4), 663–676.

Yi, J. T. (2009), Centrifuge and numerical modelling of sand compaction pile installation, PhD thesis, National University of Singapore.

Youd, T. L. and Idriss, I. M. (2001), 'Liquefaction resistance of soils: Summary report from the 1996 NCEER and 1998 NCEER/NSF workshops on evaluation of liquefaction resistance of soils', *Journal of Geotechnical and Geoenvironmental Engineering* **127**(4), 297–313.

Yu, H. S. (1993), Cavity expansion in heavily OC clays under fully drained loading conditions, Technical report, The University of Newcastle, Australia.

Yu, H. S. (2000), *Cavity expansion methods in geomechanics*, Kluwer Academic Publishers.

Yu, H. S. (2006), 'The first james k. mitchell lecture in situ soil testing: from mechanics to interpretation', *Geomechanics and Geoengineering: An International Journal* **1**(3), 165–195.

Yu, H. S., Herrmann, L. R. and Boulanger, R. W. (2000), 'Analysis of steady cone penetration in clay', *Journal of Geotechnical and Geoenvironmental Engineering* **126**(7), 594–605.

Yu, H. S. and Houlsby, G. T. (1991), 'Finite cavity expansion in dilatant soils: loading analysis', *Géotechnique* **41**(2), 173–183.

Yu, H. S. and Mitchell, J. K. (1998), 'Analysis of cone resistance: Review of methods', *Journal of Geotechnical and Geoenvironmental Engineering* **124**(2), 140–149.

Yu, H. S. and Rowe, R. K. (1999), 'Plasticity solutions for soil behaviour around contracting cavities and tunnels', *International Journal for Numerical and Analytical Methods in Geomechanics* **23**(12), 1245–1279.

Yu, H. S., Schnaid, F. and Collins, I. F. (1996), 'Analysis of cone pressuremeter tests in sands', *Journal of Geotechnical Engineering-ASCE* **122**(8), 623–632.

Zhao, Y. (2008), In situ soil testing for foundation performance prediction, PhD thesis, University of Cambridge.